Atomic-Scale Imaging and Spectroscopy using Scanning Tunneling Microscopy

Thesis by

Michael George Youngquist

In partial fulfillment of the requirements for
the degree of Doctor of Philosophy

Department of Chemistry
California Institute of Technology
Pasadena, California
1993

Submitted February 11, 1993

Acknowledgments

This thesis was shaped by my interactions with many individuals. John Baldeschwieler hooked me with his ideas about how the STM could be used and then freed me in the laboratory; his patience, confidence and encouragement were appreciated. Bill Kaiser often acted as a co-thesis advisor, sharing time, guidance, and ideas. Rich Colton gave me my first project and first atoms. Rick LeDuc let me use his cryogenic STM and taught me the basics of superconductor spectroscopy. Bob Jaklevic shared his tunneling spectroscopy experience. Michael Weimer injected rigor and sage advice into my life. John Kramar and Bob Driscoll introduced me to STM in UHV. Bob and I collaborated on many projects, spending long days and nights with the STM, music, plots, and philosophy. Terry Coley helped me understand tunneling theory. Shenda Baker's work led me in new directions. David Baselt provided software that was both functional *and* fast. Steve Clark shared Minnesotan humor and helped me build, debug, and understand electronics. Charles Spence helped with the electronics, and together with Joe Meier talked me and Bob into imaging DNA. Joe prepared an ultraclean DNA solution. Steve O'Connor helped install the new UHV tunneling and field ion microscopes. Marty Gould taught me how to machine whatever I needed. I thank everyone in The Group and all of my other friends and acquaintances for providing help, insight, discussion, exposure to interesting things, idle banter, and fun times. I thank my family for their encouragement and shared excitement. I especially thank Stephanie for standing by me for the 30 month 'year' I spent finishing this work and for saying "yes."

Abstract

Advances in scanning tunneling microscopy (STM) instrumentation and applications are presented. An ultrahigh vacuum (UHV) scanning tunneling microscope incorporating computer-controlled two-dimensional sample translation and *in vacuo* tip and sample transfer was developed. Its performance is documented through large-area and atomic-resolution imaging of highly stepped Si(111) 7x7 reconstructed surfaces and physisorbed clusters on graphite. An STM with automated approach and intra-Dewär spring suspension was developed for operation in cryogenic liquids. A high performance digital signal processor (DSP) based control system was constructed, and software with advanced spectroscopic imaging and data processing capabilities was developed.

The feasibility of individual-molecule vibrational spectroscopy via STM-detected inelastic electron tunneling is assessed. In preliminary experiments, a low-temperature STM was used for energy gap and phonon spectroscopy of superconducting Pb films. The first STM observation of phonon density of states effects in a superconductor is reported.

A systematic UHV STM imaging and spectroscopy study of *2H*-MoS_2 was conducted. Atom-resolved images from three distinct imaging modes are presented. Occasional appearance of negative differential resistance (NDR) in I vs. V measurements is traced to changing tip electronic structure rather than localized surface states. Other potential NDR mechanisms are discussed including electron trap charging and resonant tunneling through a

double-barrier quantum well structure arising from layer separation in the MoS_2 crystal.

DNA was imaged at atomic resolution with a UHV STM. Images show double-helical structure, base pairs, and atomic-scale substructure. Experimental STM profiles have atom-for-atom correlation with the A-DNA van der Waals surface. This work demonstrates the potential of the STM for characterization of large biomolecular structures.

Impurity-pinned steps on silicon and gold surfaces were imaged by STM. Pinned gold steps have short linear coherence lengths and form step loops at impurities by an Orowan-type bypassing mechanism. Step loops were not observed at Si(111) pinning sites; step contours seem to be correlated with the degree of order in the Si surface reconstruction.

Table of Contents

List of Figures

Chapter 1: Introduction

Scanning Tunneling Microscopy

The scanning tunneling microscope (STM) is an elegantly simple instrument capable of producing stunning three-dimensional images of surfaces showing the position of each atom.[1] It was invented by Heinrich Rohrer and Gerd Binnig who shared the 1986 Nobel prize in physics for their work.[2] (Ernst Ruska, who fifty years earlier had invented the electron microscope, also shared the prize.) While the earliest studies showed that the STM could image monatomic steps on surfaces,[3] the real potential of the instrument became clear with its elucidation of the 7x7 atomic reconstruction of the Si(111) surface for which many competing models had been proposed.[4] The 7x7 reconstruction has since become the standard test surface for STMs operating under ultrahigh vacuum. Figure 1.1 shows an STM image of the 7x7 reconstruction.

There are now numerous examples of STM imaging not only in ultrahigh vacuum but also in air and under liquids. In addition, several related scanned probe microscopies have been developed. The voluminous proceedings of the international conferences on scanned probe microscopy illustrate the rapid development and breadth of the field.[5]

The STM's capability to probe a surface with atomic scale resolution in real space stems from a highly localized current of quantum-mechanically tunneling electrons. When a metal "tip" is brought sufficiently near (usually within a few angstroms of) a conducting "sample" with a small voltage bias applied across the gap (typically 0.01-2 V), a measurable current of tunneling electrons is established (typically 0.1-2 nA). The essential properties of the

tunneling current are embodied in the expression given by the one-dimensional square-barrier tunneling approximation for low voltage bias,

$$I \propto (V / s)\exp(-ks\sqrt{\phi}), \tag{1}$$

where I is the tunnel current, V is the voltage bias, s is the separation between the tip and the sample, $k = \hbar^{-1}\sqrt{2m_e} = 1.025(eV)^{-1/2}\,\text{Å}^{-1}$, and ϕ is the effective local work function, also referred to as the barrier height. For a typical work function of 4 eV, a decrease in separation of only one angstrom increases the tunneling current by an order of magnitude. This exponential dependence of current on separation associated with vacuum tunneling can be measured in the scanning tunneling microscope as shown in Figure 1.2. Because of this strong dependence of electron tunneling probability on electrode separation, almost all of the current flows through the single atom on the tip which is nearest the conducting surface.[6]

A schematic diagram of a scanning tunneling microscope is shown in Figure 1.3. The heart of the instrument is a sharpened wire "tip" mounted on a piezoelectric actuator which precisely controls its position in three orthogonal directions. An electronic feedback system serves to adjust the tip height in order to maintain a constant tunneling current or resistance. "Topographic" images are made either by rastering the tip over the sample while monitoring the vertical motion of the tip (indicated by the feedback voltage applied to the Z-actuator) required to maintain a constant tunnel current or by measuring the current variation while scanning the tip over the surface at constant average height. "Barrier height" images can be made by measuring the dependence of the current on separation, since

$\phi \approx (kd(\ln I)/ds)^2$. Examples of these modes of imaging are given in Chapter 4.

Theory of Tunneling Microscopy

A good review of STM theory has been given by Kuk and Silverman.[7] While the one-dimensional square-barrier analogy used above is a good starting approximation for the operation of the STM, a three-dimensional tunneling theory facilitates understanding of its imaging capabilities. The electronic structure of the tip and surface must be considered in interpreting STM data. The transfer Hamiltonian approach[8] can be used to derive the tunneling current. The method treats the sample and tip as independent systems with weak coupling and the gap as a perturbing Hamiltonian. The net current is described by

$$I \approx \int_{-\infty}^{\infty} dE \rho_s(E+eV)\rho_t(E)|M(E)|^2[f(E)-f(E+eV)], \tag{2}$$

where M is the tunneling matrix element, $f(E)$ is the Fermi function, and ρ_s and ρ_t are the densities of electronic states of the sample and tip, respectively. Tersoff and Hamann[9] simplified the expression in the low-voltage limit to

$$I \propto V\rho_s(\mathbf{r}_o, E_F)\rho_t(E_F), \tag{3}$$

where $\rho_s(\mathbf{r}_o, E_F)$ is the surface density of states at the center of the tip and $\rho_t(E_F)$ is the density of states of the tip at the Fermi level. Thus, at low voltages, only states near the Fermi levels of the sample and the tip contribute to the tunneling current, and at constant current the STM tip follows a contour of a constant density of electronic states. In evaluating equation (3) Tersoff and Hamann showed that the lateral resolution of the STM is related

to the gap distance, s, and tip radius , R, roughly as $\left[(2\mathring{A})(R+s)\right]^{1/2}$. A more accurate expression of equation (3) valid at higher voltages ($\phi > V > 1V$) can be written as[10]

$$I \propto \int_0^{eV} \rho(E) D(E,V) dE \tag{4}$$

where $D(E,V)$ is the transmission coefficient of the barrier at voltage V. $D(E,V)$ can be calculated using the WKB approximation.[11] Because the tip and surface densities of electronic states are energy dependent, the tunneling image is voltage dependent. Thus, a complete picture of the surface requires imaging at several different voltages.[12] The voltage bias determines the sign of eV in equation (4) and determines whether empty or filled states are imaged. (When the sample bias is positive relative to the tip, electrons tunnel from the tip into unoccupied states in the sample.) As can be surmised from equation (3) or (4), the local density of states at voltage V is directly related to the differential conductance G as given by[13]

$$G \equiv dI / dV \propto \rho_s(\mathbf{r}_o, V) D(V). \tag{5}$$

At low voltages, a plot of G vs. V has been shown to be proportional to the density of states.[14] Plotting $d(\ln I) / d(\ln V)$ vs$V$ removes the exponential shape of D; peaks then correspond to resonances in the tip and sample densities of states.

Tunneling Spectroscopy

Tunneling spectroscopy measures the electron tunneling probability (current) as a function of electron energy (voltage). Electrons tunnel across a

junction with a range of energies $0 \leq E \leq eV$ determined by the voltage, V, between the two electrodes. Electrons tunnel from filled states in one electrode to empty states in the opposite electrode. Both elastic and inelastic tunneling contribute to the measured current. The elastic contribution (final energy = initial energy) is a direct probe of the electronic density of states. Examples of tunneling spectroscopy with the STM will be given in Chapters 3 and 4. Sufficiently energetic electrons can also tunnel inelastically by exciting vibrational or electronic modes of the electrodes or material in the barrier. Inelastic tunneling is further discussed in Chapter 3.

Thesis Organization

This thesis presents advances in scanning tunneling microscopy instrumentation and applications. It begins with an introduction to the basic principles of STM (Chapter 1), describes developments in instrumentation (Chapter 2), and then discusses applications of the STM in spectroscopy and imaging of clean surfaces (Chapters 3 and 4), imaging of macromolecular adsorbates (Chapter 5), and imaging of surfaces with impurity inclusions (Appendix A). Finally, additional details of instrumentation development are provided (Appendices B - E.)

Chapter 1 provides a brief introduction to scanning tunneling microscopy which will be drawn on in the following chapters. It summarizes the development of the field, capabilities of the instrument, principles of STM operation, and STM theory for imaging and spectroscopy.

Chapter 2 describes instrumentation developed in the course of this work. The chapter is subdivided into sections describing (1) a new

microscope design for ultrahigh vacuum studies which incorporates a piezoelectric tube scanner, a computer-controlled sample translation stage, and *in situ* sample and tip exchange, (2) the development of new microscope designs for operation in liquid helium, and (3) tip preparation, tip effects in imaging, and tip characterization using field emission microscopy.

Chapter 3 describes applications of the STM inspired by tunneling spectroscopy in solid-state tunnel junctions. The first half assesses the feasibility of using the STM for vibrational spectroscopy of individual adsorbed molecules via inelastic electron tunneling spectroscopy (IETS). The second half presents tunneling spectroscopy measurements of thin superconducting lead films at 4.2 Kelvin, experiments conducted as a first step toward IETS with the STM. Superconducting energy gap spectra and the first superconducting phonon spectra obtained with an STM are described.

Chapter 4 comprises imaging and spectroscopy studies on molybdenum disulfide. The primary focus is on the occasional observation of negative differential resistance (NDR) and its possible origins.

Chapter 5 details ultrahigh vacuum imaging studies of DNA adsorbed on highly oriented pyrolytic graphite (HOPG). It is demonstrated that under certain conditions the scanning tunneling microscope can resolve the atomic contours of the surface of a DNA double-helix.

Appendix A shows impurity-mediated pinning of steps on both silicon surfaces electrically annealed under UHV and gold surfaces flame-annealed in air. Similar mechanisms appear to be active. Several additional

appendices are included describing (B) enhancements of an existing UHV STM system used for the experiments described in chapters 4 and 5, (C) construction and limitations of digital control electronics for STM and adaptation of scanned probe operating system software for tunneling microscopy and spectroscopy, (D) control system hardware performance, and (E) software considerations for a digital signal processor (DSP) based control system.

Figures -- Chapter 1

Figure 1.1. STM image of the Si(111) 7x7 reconstruction. The pattern of adatoms forming the top layer of the reconstructed surface was revealed for the first time by the newly developed scanning tunneling microscope in 1982. The image led to the rapid acceptance of the STM by the scientific community. The 60x80 Å image of the 7x7 reconstruction shown here was taken with the new UHV STM described in Chapter 2. Brightness corresponds to topographic height -- maxima are white. The silicon crystal was annealed at 1100° C by resistive heating with a direct current flowing through the sample. Imaging was done with an electrochemically etched tungsten tip held at -2.0 V relative to the sample with a 1 nA constant current.

Figure 1.1

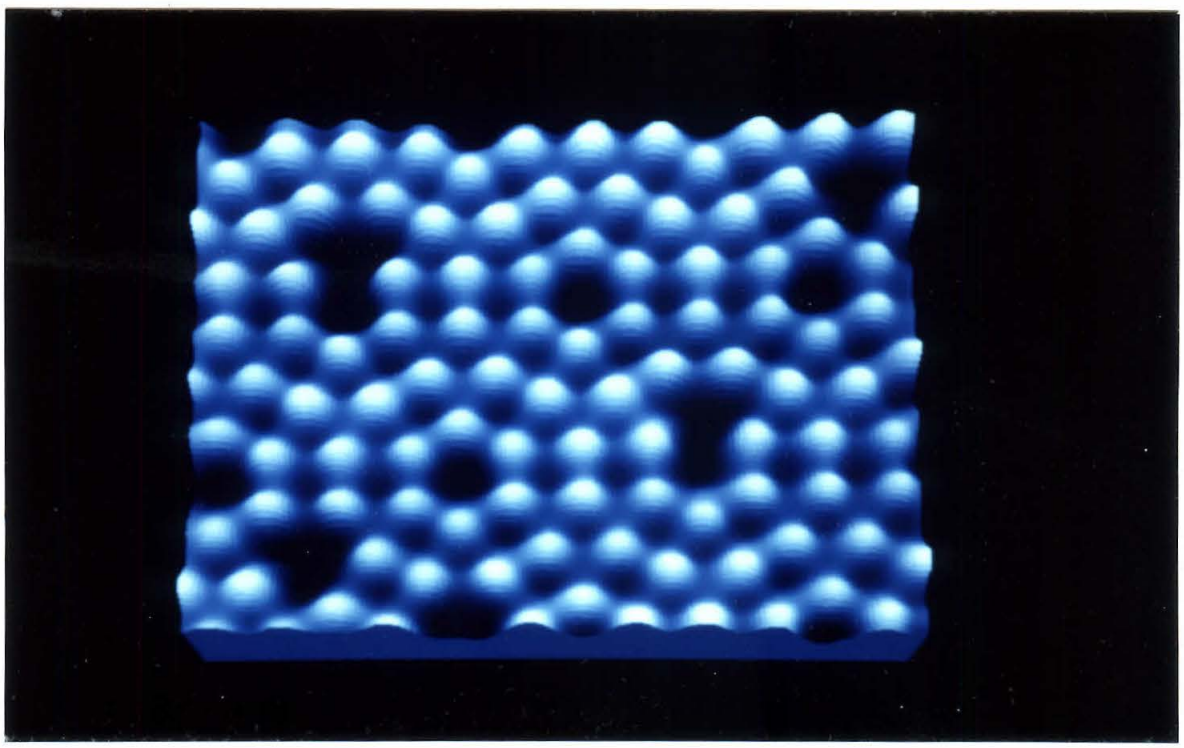

Figure 1.2. Exponential dependence of electron tunneling probability on tip-sample separation. A Si (111) 7x7 reconstructed surface was approached with an electrochemically etched tungsten tip. After feedback stabilized tunneling was established at 1 nA, feedback was interrupted. The tip was retracted ~3 Å and then moved toward the sample ~6 Å while the current was recorded. The exponential dependence of tunneling probability on tip-sample separation is evident in the linear change of the log of the current with change in Z. The flat region at the left corresponds to the noise floor of the logarithmic amplifier circuit used for the measurement; the flat region at the right is due to signal clipping. The local effective barrier height inferred from the slope is 2.3 eV calculated using a Z-piezo response of 40Å/V estimated from factory calibration data.

Figure 1.2

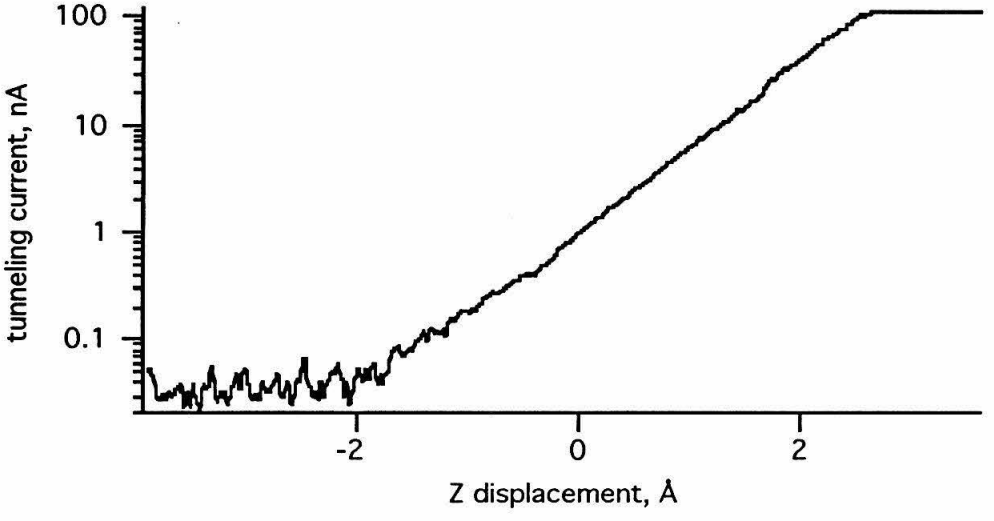

Figure 1.3. Schematic view of an STM. The tip, shown as a rounded cone, is mounted on a three-dimensional scanner made of piezoelectric ceramic. As the tip is moved across a conducting sample, the shape of the surface can be revealed down to the atomic level. Two contours are shown giving paths the tip might follow as constant current is maintained with different bias voltages. The varying trajectories over a foreign atom illustrate the microscope's dependence on the chemical nature of the surface. The contours could also illustrate the current magnitude which would be observed if the tip were moved across the surface at constant z, an alternative imaging mode. (After Hansma *et al.*)[15]

Figure 1.3

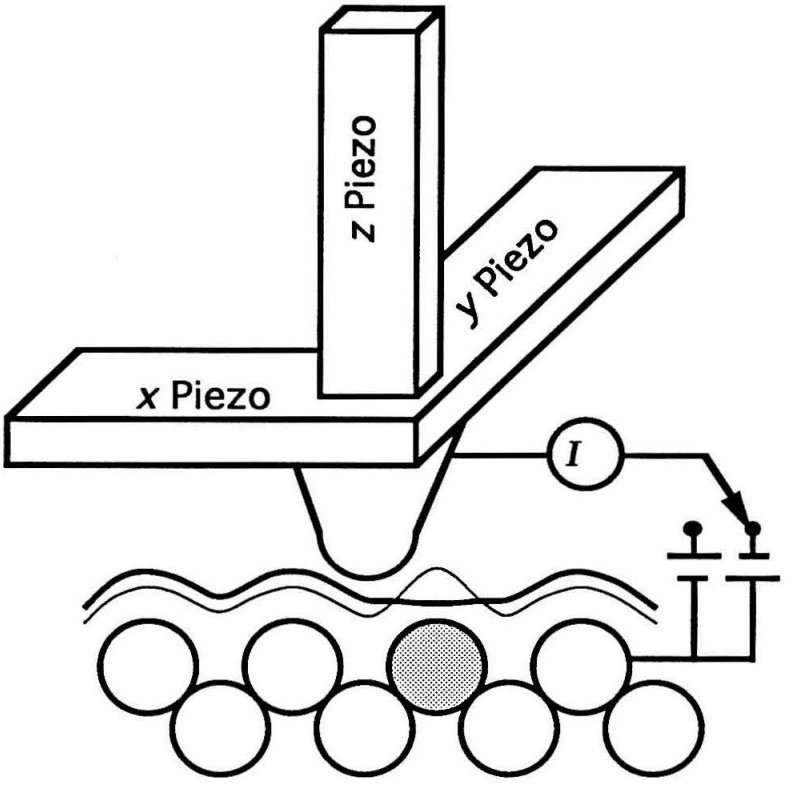

References

1. G. Binnig, H. Rohrer, Ch. Gerber, and E. Weibel, *Phys. Rev. Lett.* **49,** 57 (1982).
2. G. Binnig and H. Rohrer *in* Les Prix Nobel 1986, Almqvist & Wiksell International, Stockholm-Sweden, 85-111 (1986).
3. G. Binnig and H. Rohrer, *Helv. Phys. Acta* **55,** 726 (1982).
   G. Binnig and H. Rohrer, *Surf. Sci.* **126,** 236 (1983).
4. G. Binnig, H. Rohrer, Ch. Gerber and E. Weibel, *Phys. Rev. Lett.* **50,** 120 (1983).
5. Proceedings of international conferences on scanned probe microscopy. 6th: *Ultramicrosc.* **42 (July),** (1992). 5th: *J. Vac. Sci. Technol.* B **9(2),** (1991). 4th: *J. Vac. Sci. Technol. A* **8(1),**(1990). 3rd: *J. Microsc.* **152 pt 1,** (1988). 2nd: *J. Vac. Sci. Technol. A* **6(2),**(1988). 1st: *Surface Science* **181,** (1987).
6. E. Stoll, A. Baratoff, A. Selloni, and P. Carnevali, *J. Phys. C* **17,** 3073 (1984). N. D. Lang, *Phys. Rev. Lett.*. **56,** 1164 (1986).
7. Y. Kuk and P. J. Silverman, *Rev. Sci. Instrum.* **60,** 165-180 (1989).
8. J. Bardeen, *Phys. Rev. Lett.* **6,** 57 (1961); W. A. Harrison, *Phys. Rev.* **123,** 85 (1961).
9. J. Tersoff and D. R. Hamann, *Phys. Rev. Lett.* **50,** 25 (1983); *Phys. Rev. B* **31,** 805 (1985).
10. R. M. Feenstra, J. A. Stroscio, and A. P. Fein, *Surf. Sci.* **181,** 295 (1987).
11. L. I. Schiff, Quantum Mechanics, McGraw-Hill, New York p. 184 (1955).
12. R. Feenstra, J. Stroscio, and A. P. Fein, *Phys. Rev. Lett.* **58,** 1192 (1987).
13. A. Selloni, P. Carevali, E. Tosatti, and C. D. Chen, *Phys. Rev. B* **34,** 994 (1986).
14. C. B. Duke, Tunneling in Solids, Academic, New York (1969).
15. P. K. Hansma, V. B. Elings, O. Marti, and C. E. Bracker, Science 242, 209-216 (1988).

Chapter 2: Instrumentation

This chapter describes instrumentation developed in the course of this work. The chapter begins with an overview of the components making up a scanning tunneling microscopy system and fundamental principles of STM design. Following are sections describing (1) a novel microscope for ultrahigh vacuum studies which incorporates a piezoelectric tube scanner, a computer-controlled sample translation stage, and *in vacuo* sample and tip exchange, (2) the development of new microscopes for operation in liquid helium, and (3) tip preparation, tip effects in imaging, and tip characterization using field emission microscopy. Tips made using different procedures were characterized, and a method was developed for making sharp tips. A simple field emission microscope (FEM) was designed and implemented for tip evaluation and modification.

Instrumentation for Scanning Tunneling Microscopy

Components of a scanning tunneling microscopy system include a microscope head, a tip, vibration isolation, electronics for instrument control and data acquisition, and data processing facilities. The head consists of a three-dimensional actuator for raster-scanning the tip (the X and Y axes defined as the fast and slow raster directions, respectively) and adjusting tip-sample separation (the Z axis), an approach mechanism for bringing the sample within range of the Z-actuator, and optionally a sample translator for moving the sample laterally relative to the tip. The tip is a sharpened wire, in the best case terminating with a single atom at its apex. Vibration isolation, necessary to maintain a stable tunneling current between the tip and sample,

is achieved both through careful head design and by external means. Control electronics comprise a raster generator, a feedback circuit to maintain constant tunneling current by adjusting the tip-sample separation, and controllers for any other input signals such as tip-voltage (V) ramps and V- or Z-modulation. Data acquisition electronics record Z, I (current), ø (work function), and/or other observables as functions of X, Y, and/or other input signals. The control and acquisition electronics are often fully integrated to allow interruption of the feedback and raster for spectroscopy, lithography, panning, zooming, or other operations. The data processing facility is used for visual presentation of the data as well as post-processing for noise reduction or enhancement of specific features.

The three-dimensional actuator for raster-scanning the tip is usually made of a piezoelectric ceramic, a material that expands or contracts under the influence of an electric field. With the different formulations of the lead-zirconate-titanate (PZT) materials most commonly used, responses are in the range of 10-100 Å/V for ~0.5 mm thickness, so subangstrom precision in positioning can be easily achieved. Some popular types are PZT-4, PZT-5A, and PZT-5H from Vernitron[1] and the corresponding EBL #1, #2, and #3 from Staveley Sensors.[2]

Principles of Vibration Isolation

Vibration isolation is critical for tunneling microscopy and spectroscopy because of the exponential dependence of tunneling current on tip-sample separation and the fact that atomic corrugations observed in constant-current STM can be 0.1Å or smaller. Small fluctuations in separation

caused by vibration can lead to large fluctuations in current. When these fluctuations are within the feedback bandwidth, the feedback circuit can compensate and maintain a constant tip-sample separation, but the vibration amplitude will appear as structure in images. When the vibration is out of the feedback bandwidth or the feedback is disabled for spectroscopy, vibration noise is observed as periodic structure on the tunneling current; in the worst case it can cause the tip to oscillate into contact with the surface, usually damaging the tip.

Two complementary approaches are used to eliminate the effects of vibration on the tunneling gap. The first is to make the mechanical path between the tip and sample as rigid as possible so that the lowest resonance frequency is as high as possible; careful head design can substantially reduce (but not eliminate) the need for external vibration isolation.[3] The other is to isolate the instrument from vibration sources by using damped spring-and-mass systems, pneumatically supported tables (sometimes with active vibration compensation), sound-proof enclosures, and/or a floor isolated from building foundations.

The relative motion between the tip and sample (assuming simple harmonic motion) can be calculated using the transfer function for a rigid body given by

$$T_h = \frac{(\nu/\nu_h)^2}{\left(\left(1-(\nu/\nu_h)^2\right)^2 + (\nu/\nu_h Q_h)^2\right)^{1/2}}, \qquad (1)$$

where ν is the driving frequency, ν_h is the resonance frequency of the STM head, and Q_h is the quality factor of the tip-sample junction. When $\nu \ll \nu_h$, which is typical, equation (1) can be simplified to

$$T_h \approx \frac{\nu^2}{\nu_h^2}. \tag{2}$$

The amplitude transfer function for a mass on a spring (again assuming simple harmonic motion) is

$$T_s = \left(\frac{1 + (2\xi\nu/\nu_s)^2}{(1 - \nu^2/\nu_s^2)^2 + (2\xi\nu/\nu_s)^2} \right)^{1/2} \tag{3}$$

where ξ is the ratio of the system damping coefficient to the critical, damping coefficient, ν is the driving frequency, and ν_s is the resonance of the spring-mass system. For $\nu \gg \nu_s$, this reduces to

$$T_s \approx \nu_s/\nu. \tag{4}$$

The applicability of these formulas in the design of STM systems will be demonstrated below. Kuk and Silverman provide a detailed treatment of vibration isolation and electronic control characteristics desirable for STM.[4]

New UHV Scanning Tunneling Microscope

Design

Motivation and Requirements

A scanning tunneling microscope head for operation in ultrahigh vacuum (UHV) was designed and built to replace the "tripod and louse STM"

of the Kramar system (described in Appendix B.) The unreliable performance of the louse and its low resonant frequency were the primary incentives for building a new instrument. Design requirements were facile *in vacuo* tip and sample exchange, reliable normal and lateral sample translation with step size < 1000Å, improved rigidity, increased scan range, and compatibility with the existing UHV chamber, wobble-stick manipulators, and vibration isolation stage.

Execution

The new microscope head is shown in Figure 2.1. The design was based on a customized version of a commercially available 2-dimensional translation stage from Micro Pulse Systems, Inc.[5] The sample is mounted on a stub which is secured on a mounting block on the translation stage with a set-screw (T-shaped for wobble-stick tightening and loosening). A piezoelectric tube scanner is cemented with Torr-Seal into a Macor slab attached to the side of the translation stage base-plate. The tip is mounted in a titanium clip mounted on top of the scanning tube for accessibility with a wobble-stick. A Macor ring is cemented into the end of the tube to minimize distortion during scanning. The lowest resonance of the structure was designed to be ~5 kHz giving approximately 25 times improvement in vibration immunity over the louse-based STM which had a resonance at ~1 kHz.

Characteristics

Translator

The translator range is 6.4 mm in X and Z (scanner axes). It is based on Micro-Pulse actuators as illustrated in Figure 2.2. The moving platform (35 x 44 x 6.4 mm) is supported by three alumina feet on a fixed base-plate. It is held rigidly in place by two rare-earth magnets mounted on the moving platform. Although it moves freely in air with a 12 V power supply, it was necessary to use a 15 V supply for reliable performance in vacuum. There are 8 drive elements driven by a single resonant circuit. It was somewhat challenging (but possible) to find a frequency which functioned well for all four translator directions during vacuum operation, perhaps because of the asymmetric loading of the drivers. Some resonant modes tend to lift the moving stage or driver assembly off the base-plate and should be avoided.

The original NdFeB magnets depoled on baking; the SmCo magnetic material for the replacements was selected to ensure tolerance to sustained bakeouts at 120° C, which is the limit imposed by the Torr-Seal used in mounting several components. It was necessary to harden the base-plate with a titanium nitride coating to prevent galling by the alumina feet during UHV operation. The stage was originally equipped with LED/shark-fin displacement sensors, but they were not reinstalled after the instrument was cleaned for installation and testing in UHV; tests in air showed better than 1 μm differential displacement resolution, and the sensors should be quite useful if reinstalled.

Scanner

Several different scanners were used during the development process, and atomic resolution was achieved even with long-range EBL #2 scanners having sensitivities of 80 Å/V. The best combination of sensitivity and low hysteresis was found in a 25.4 x 12.7 x 0.51 mm EBL #1 tube. The active length is approximately 18 mm, the length extending from the Macor slab. The sensitivities[6] are 40 Å/V in Z, 37 Å/V in X, and 29 Å/V in Y giving respective ranges of 1.5, 1.4, and 1.1 μm for 375 V drivers and two-quadrant rastering. (The X and Y ranges can be approximately doubled by driving all four quadrants). The louse-STM had a sensitivities of ~10 Å/V and 0.30 μm ranges with its 300 V drivers. The increased sensitivity of the new scanner required the use of improved drive electronics to achieve atomic resolution capability over the full image-window (see Appendices C and D). Position resolutions at 18-bits are 0.057, 0.053, and 0.042 Å in X, Y, and Z. The Z resolution can be improved to 0.014 Å by selecting the low-voltage range option on the DAC module. The displacement hysteresis was significantly less for EBL #1 than for EBL #2 or EBL #3, a performance improvement which outweighed the 25 and 50% relative reductions in scan range.

Since the tip is mounted on top of the tube, its motion is coupled directly to one of the quadrants. If that quadrant is used for scanning (*i.e.*, as the X or Y raster), a strong coupling with Z is observed. Normal operation is with two quadrants grounded, the X-raster on the quadrant adjacent the tip, and the Y raster on a quadrant opposite the tip. It was found with some tubes that, contrary to finite-element analysis predictions,[7] the end of the tube must

be constrained to a circular shape with a rigid disk or significant distortion can occur during rastering, hence the use of the Macor disk mentioned above.

Tip Mount

Figure 2.3 shows the tip mounting block, tip shape, and tip mounting procedure. The titanium tip-mount was designed for low mass at the end of the scanning tube. It accommodates 0.25 mm wire tips. The tips are shaped specifically for wobble-stick manipulation and hanging in storage or transport racks in the vacuum system. The tip acts as a spring and holds itself in the mounting block.

Sample Stubs

The sample stubs were designed with a hole for wobble-stick manipulation and a grooved pin to force the stub downward against the mounting block when a set screw is tightened against it. The stub may be altered to suit specific samples as long as the wobble-stick hole and pin are conserved. Flat cubes of stainless steel are adequate for samples like HOPG which can be soldered in place. Crystals to be cleaved *in vacuo* can be mounted in a vertical slit machined into a stub. Silicon studies require a multiple piece refractory metal stub such that the crystal can complete an electrical circuit for ohmic heating.

Sample Heating Considerations

Sample stubs and a complementary heater assembly for silicon are shown in Figures 2.4 and 2.5, respectively. They are made of molybdenum or

tantalum to withstand high temperature and avoid sample contamination (especially by nickel which is present in stainless steel and diffuses readily through hot silicon, segregating to the surface and interfering with surface studies). Figure 2.4a shows the prototype stub used in testing the new system. The top of the stub is held against the silicon crystal on one side and a triangular quartz-glass spacer on the other by an 0-80 screw made from tantalum compressing a small steel spring. The prototype stub was designed to accommodate two samples; this led to poorly controlled annealing, so one sample was replaced by the glass spacer. A better design would use a kinematically mounted alumina or sapphire sphere as the spacer as shown in Figure 2.4b; this would be simpler to use and be more rigid. The steel spring is a potential contamination source, but it remains cool relative to the rest of the stub during sample heating; a spring could be made from Ta to eliminate this potential contamination source. A Macor spacer insulates the top piece of the mounting block from the spring and screw.

For sample heating, the stub is placed in the heater assembly shown in Figure 2.5. The tantalum base is at ground potential. A tantalum plate connected to an electrical feed-through is lifted and turned into place with a wobble-stick and held against the top of the stub by a spring. Alternating or direct current is passed through the sample while its temperature is monitored with an optical pyrometer. For the silicon work presented in this thesis, a Hewlet Packard Harrison 6274A (0-60 V, 0-15 A) DC power supply was used.

The stub assembly remains relatively cool during low-temperature (~600° C) outgassing of the silicon and gets sufficiently hot to desorb most contamination only when the sample is at high-temperature. If silicon is to be the object of an ongoing project, the cylindrical boron nitride heater used by Kramar *et al.* for MoS_2 studies should be reinstalled in the system and used for outgassing the stub assembly before it is transferred to the silicon heater for annealing.[8] For a good silicon 7x7 preparation recipe, the reader is referred to the work of Swarzentruber *et al.*[9] In the present system, sample contamination from stub outgassing can be minimized by using short annealing times and carefully monitoring the pressure with the mass spectrometer; if the pressure approaches $2x10^{-9}$ torr, the heating should be discontinued until the pressure recovers to $< 5x10^{-10}$ torr. Cooling the TSP (titanium sublimation pump) cold-plate in the base of the chamber with liquid nitrogen (without using the TSP) can increase total pumping speed during the anneal and help to maintain a low pressure; contaminants trapped on the plate desorb slowly upon warming when the sample is cool and the ion pumps can handle the load. The mass spectrometer (and ion gauge) should be turned off before the sample cools below 800° C on the final flash to avoid hydrogen contamination.

Sample Approach

To establish tunneling, the sample is first moved near the tip under manual control of the translator from the computer keyboard with the aid of a long-range microscope looking through the chamber viewport. The approach is then completed automatically under computer control. The UHV operating

environment allows a rapid alternative approach method based on field emission. The Z-DAC is used to apply a high voltage (~-180 V) to the tip. The translator is moved rapidly forward under computer control until the field-emission current is greater than the setpoint. The STM is then returned to the normal configuration, and the auto-approach sequence is engaged. This procedure works well with very sharp tips.

Performance

Base Pressure

The base-pressure with the new head in the STM chamber has been ~3-4x10^{-10} torr and may be limited by Torr-Seal outgassing or the effectiveness of the seal at the wheeler flange. The instrument's suitability for surface science studies was demonstrated through imaging the Si(111) 7x7 reconstruction. Its ability to non-destructively image weakly bound adsorbates was assessed with vapor-deposited clusters on graphite. Reproducible lateral translation, desirable for searching for macromolecules at low coverage, was demonstrated using rough silicon surfaces.

Imaging Si (111) 7x7

Silicon samples were 6.1 mm squares cut from an .005-.02 Ω-cm *n*-type Sb doped 76x0.38 mm (111) wafer with one side polished. The vicinal miscut of the wafer was determined from Laue diffraction to be 4°. If the slope were accommodated solely by biatomic steps (the 3.13 Å single-step height of the 7x7 reconstructed surface), the average terrace width would be 45 Å. The samples were cleaned either by sonicating ~5 minutes successively in

trichloroethylene, acetone, ethanol, and water or by soaking in stirred hot concentrated nitric acid ~1 hr and rinsing in running 18 MW water for ~15 minutes. Immediately before mounting on the sample stub and introducing into the UHV system load-lock, the sample was rubbed on an acetone-soaked continuous filament polyester cloth[10] until no scattering from small particulates could be seen under bright light illumination. In a typical session, samples were outgassed several hours at ~600° C and annealed by cycling between <600 and >1100° C until the pressure could be kept below $2x10^{-9}$ torr for more than 10 seconds at the high temperature. The temperature was always increased rapidly, taking <10 seconds to reach the peak temperature. After 10 seconds at >1050° C and $<2x10^{-9}$ torr, the temperature was reduced rapidly to ~900° C, gauges were turned off, and the temperature was reduced through the 7x7 phase transition to 800° C at ~2°/s. The heating current was reduced to zero over the next ~5 minutes.

Figure 2.6 shows a 4250 x 3430 Å image of the highly stepped Si (111) surface. The 7x7 reconstruction can be seen in higher resolution images. Figure 2.7 shows a 850 x 685 Å image. Straight-edged step bunches go through the corner holes of the 26.9 Å short diagonal of the (7x7) unit cell in the $[1\bar{1}0]$ direction. The other major step bunches form higher energy high-index facets between the (111) terraces but are necessary to accommodate the inherent 4° miscut which is somewhat skewed from the $[1\bar{1}0]$ direction. Zooming in on one of the terraces, the atomic arrangement of the 7x7 reconstruction is clearly resolved as shown in Figure 2.8.

Imaging Weakly Bound Adsorbates

A 6 x 6 x 1 mm square of ZYA grade highly-oriented pyrolytic graphite (HOPG)[11] was soldered to a sample stub with indium by heating the stub topped with a small piece of indium wire and the graphite crystal to ~160° C on a hot plate. The HOPG was cleaved with adhesive tape immediately before introduction to the UHV system load-lock. The sample was placed near the silicon heater assembly in the UHV chamber while a silicon sample was annealed. STM images of large areas showed a low coverage of 10 Å clusters. Figure 2.9 shows an atomic resolution image with a weakly bound particle, probably an SiO_2 cluster. The adsorbate was swept away by the tip during a subsequent image while the lattice underneath showed no discontinuity, thus affirming its physisorbed nature.

It is interesting to note that contaminant clusters on both the silicon and graphite surfaces often appear amorphous, even though the atomic lattice of the underlying substrate is clearly resolved. This demonstrates the essential operating principle of the instrument. In its constant current mode, the STM profiles a constant local density of electronic states rather than atomic positions; only when states are localized over atoms (rather than distributed over clusters) are "atoms" imaged.

Low-Temperature Tunneling Microscopes

Background

Scanning tunneling microscopy can be performed at low temperature to investigate low-temperature phenomena such as superconductivity, to

make spectroscopic measurements which require tunneling electrons to have a well-defined energy range, or to image systems that are not stable at higher temperature. "Low temperature" is typically the boiling point of liquid nitrogen (77 K) or liquid helium (4.2 K); immersion of an instrument in one of these liquids is one of the simplest ways to perform a low-temperature experiment. More complex setups have sometimes been used in order to cool STMs to temperatures as low as 0.4 K together with the application of a strong magnetic field or to maintain continuously variable temperatures all the way up to room temperature in ultrahigh vacuum.[12] A number of ultrastable UHV low-temperature instruments have been constructed with stability in the 0.001Å range.[13]

The instruments here were designed for immersion in a cryogenic liquid. The primary design criterion was that they fit through the necks of standard 30L liquid helium transport Dewärs (28 - 32 mm) so that a custom Dewär would not be necessary and to avoid liquid He loss during cryogen transfer operations. Immersion-cooling has the advantage of fast turn-around with minimal time required for tip or sample changes before return to low-temperature operation. The only fundamental change in an instrument on going to low temperature is reduced response in the piezoelectric elements; the behavior of several different materials has been characterized at low temperature.[14] The piezoelectric materials used for the instruments described here, PZT-4, PZT-5A, and PZT-5H, have 5K/300K response ratios of approximately 0.33, 0.26 and 0.18, respectively.[1]

The STM heads were mounted at the end of a thin-walled (0.5 mm) stainless steel tube which served both as a low-thermal-conductivity dip-stick and as a shield for leads to the instrument. The dip-stick was supported by a split rubber collet fit into the Dewär opening. A preamplifier was mounted at the top of the tube. Low-triboelectric noise microcoaxial cable leads or twisted wire pairs were threaded through nylon guides or mounted on fiberglass perf-board inside the tube to connect the head to the preamplifier and connectors at the top of the dip-stick. (Regular coax lines were extremely sensitive to vibration at low temperature because of either triboelectric effects or capacitance and were unsuitable for the high-impedance line between the gap and preamplifier). The heads were designed with low thermal mass to avoid excessive helium boil-off on immersion.

The instruments were intended primarily for low-temperature spectroscopy; instruments not meeting the stringent low-noise requirements or ease of use thought necessary for the envisioned experiments were replaced in an evolutionary development process. Each of the instruments here was shown to be capable of atomic resolution imaging of highly oriented pyrolytic graphite (HOPG) both in air and liquid nitrogen or helium, but as was demonstrated in early air STM experiments, such imaging is not necessarily indicative of low-noise operation (or even tunneling).[15] Performance was judged qualitatively from the noise on the tunneling current at high gap resistance and reproducibility and character of I vs. V curves with interrupted feedback.

Vibration Isolation for the Low-T STMs

The initial design philosophy was to make the STM assembly sufficiently compact and rigid that no additional vibration isolation would be necessary on the STM dip-stick. Analysis of the laboratory floor motion together with reasonable estimates of achievable STM structural resonances suggested that sufficient vibration immunity could be attained through vibrational isolation of the liquid helium transport Dewär supporting the STM.

A Ranger seismometer was used to characterize the laboratory floor motion. The quietest position in the laboratory suitable for instrument operation was found to have dominant peaks at 30 Hz, 5000 Å p-p, 20 Hz, 2000 Å, and 6 Hz, 2000 Å. An STM head placed on the floor would require a lowest resonance greater than 21 kHz for 0.01 Å gap stability, an appropriate goal for a high-performance microscope head.

A vibration isolation rack was constructed to isolate the Dewär from floor vibrations. A plywood box 0.6 x 0.6 x 0.15 m was filled with 50 kg sand and supported at the corners with eight 10 mm diameter shock cords (self-damping bundles of 1 mm rubber strands in a woven nylon sheath), two at each corner. Each cord was routed through a pulley and linked by a cable to a winch used to raise and lower the platform for ease of Dewär placement. With a 50 kg Dewär in place the total extension of the cords was approximately 1 m (in a nonlinear behavior regime); vertical, torsional and pendulum resonances were at 2, 1, and 0.5 Hz. The Ranger seismometer placed on the platform and allowed to stabilize for 5 minutes measured 2 Hz

vertical oscillation amplitude of 0.9 μm; no higher peaks were detected at 100 Å sensitivity.

The effect of the isolation platform on STM head performance can be calculated using equation (2). Without isolation from the floor, the 5000 Å driving oscillation at 30 Hz would require that the first resonance of the microscope be at least 21 kHz for 0.01 Å gap stability. With the isolation platform, a 1 μm driving oscillation at 2 Hz would allow a lowest resonance of 2 kHz for the same gap stability.

In practice, it was found that acoustic coupling posed a far greater limitation on performance than floor motion. Even with the instruments described below, the ultra-rigid compact STM and the Micro Pulse Systems (MPS) based instrument incorporating intra-Dewär vibration isolation, acoustic coupling was problematic. Low noise experiments probably require that an immersed instrument and its vibration isolation platform be enclosed in an acoustic isolation chamber. The boiling of liquid nitrogen and helium was never found to be the limiting noise source, although this probably should be taken into consideration if the external acoustic coupling can be sufficiently reduced. Enclosure of the instrument in a tube pumped to moderate vacuum and back-filled with <1 torr He exchange gas could alleviate noise transfer from boiling.

Preamplifier and Feedback Control

The low-temperature instruments shared a common current amplifier configuration. It consisted of a current-to-voltage converting metal-film

resistor (1 or 10 MΩ) at the low-temperature end of the dip-stick (taking advantage of reduced Johnson noise at low temperature), a non-inverting operational amplifier (Burr-Brown OPA111BM) at the top of the stick with gain ~20, and an instrumentation amplifier (Analog Devices AD524) at the input of the feedback circuit with switch-selectable gain of 1, 10, 100, or 1000 for total gain of up to 20 V/nA. At the highest gain using a 1 MΩ drop resistor, a 10 mV bias, and 100 MΩ gap impedance, the output voltage is 2 V. This is an appropriate value for superconducting energy gap spectroscopy requiring voltage biases between ±50 mV. The small error due to the gap plus drop-resistor voltage divider can be corrected in post-processing of spectroscopy data. The current-amplifier bandwidth is ~25 kHz at the highest gain and ~100 kHz at the lower gain settings. Johnson noise and op-amp voltage noise were shown to dominate the amplifier characteristics at 300 and 4 K, respectively. The OPA111BM was measured to be the lowest noise readily available commercial op-amp when used in this configuration.

An integral feedback circuit was used to maintain either constant resistance or current depending on whether the tip-voltage or a constant dc voltage was input as a reference. Constant resistance feedback is important for voltage spectroscopy measurements conducted under feedback because it maintains a more constant tip-sample separation than constant current feedback.[16] A 25 kΩ audio taper provided nearly linear control of the gap resistance over several orders of magnitude (1 - 1000 M). A TTL controlled bipolar analog switch (Intersil IH5042) was used to interrupt feedback for gated spectroscopy experiments by switching the integrator input between the error signal and ground. It should be noted that a proportional-integral

feedback circuit provides better feedback characteristics as discussed in Appendix E. A logarithmic amplifier is necessary to linearize the tunneling error signal in UHV instruments, but linear feedback circuits seem to work reasonably well in non-UHV environments, probably because of lower effective barrier heights.

Kaiser/LeDuc Design-Based STMs

The first low-temperature instruments described here were modeled after an instrument designed by W. J. Kaiser and H. G. LeDuc which was in turn based on a design previously used for room temperature work.[17] The first iteration used an alumina base with threaded feedthroughs; it had too many parts prone to loosening on thermal cycling and wobbly coarse approach screws. The second iteration switched to a 303 stainless steel base with 21 fewer parts and added set screws for the coarse approach legs. The difference in thermal expansion between the base and the x-y piezo caused piezo failure. Finally, the instrument shown on the top in Figure 2.10 was constructed with a kovar base; kovar, an Fe alloy with 29% Ni and 17% Co, has a coefficient of expansion similar to that of the x-y piezo material which alleviates the problem.

The X-Y actuator is a 6 mm wide L-shaped piece of PZT-4 ceramic cut from a 38 mm diameter disk 1.3 mm thick. The active electrode length is 19 mm. The calculated responses at 300 K and 4 K are 18 Å/V and 6 Å/V, respectively. The Z actuator is a PZT-5H bimorph 0.5 mm thick, 6 mm wide, and 10 mm long. One end is cemented to the vertex of the L; a small spring-clip tip clamp is mounted on the other end. The calculated Z responses at 300

K and 4K are 1800 Å/V and 350 Å/V. This extreme sensitivity facilitates the tip-sample approach but places stringent requirements on the electrical noise of the piezo driver; 0.01 Å stability requires less than 30 μV p-p fluctuation when operating at 4K.

The approach mechanism used is a differential lever. The sample is mounted on a quartz-glass plate over a 2 mm diameter hole above the tip. Three screws support the plate such that two form a fulcrum 1 mm from the hole beneath the sample (and above the tip) and the third contacts the plate 44 mm from the fulcrum for a displacement ratio of 44:1 at the third screw compared to the sample. The coarse approach is made by adjusting the front screws and then locking them in place with nylon-tipped set screws from the side to prevent wobble. The fine approach is made by turning the back screw which is coupled to a knob at the top of the Dewär through two beveled gears with a factor of two reduction. The control shaft/gear assembly can be raised slightly to decouple it from the head in order to reduce transmission of vibrational noise. Each 1° turn of the fine approach knob moves the sample 100 Å toward the tip. The total sample displacement range is approximately 0.14 mm, 40 turns of the fine-approach knob. A 30 volt range servo driver is used on the Z piezo giving a total range of 1 μm at 4K, or about 0.25 turns of the fine approach knob.

For operation at low temperature, the approach is first made at room temperature, and the coarse and fine approach screws are adjusted so that the fine approach screw is near the center of its range during tunneling. The sample is fully retracted by the fine-approach screw and the instrument is

slowly lowered into the liquid helium Dewär over the course of about 10 minutes. At low temperature, the fine approach screw is turned slowly (~1 turn/5 seconds) until a tunneling current is sensed and the feedback circuit takes over. Unfortunately, thermal contractions cause inconsistent shape changes in the head which often crashed the tip into the sample or moved the sample out of the fine-approach range.

The x-y piezo resonance was measured at 7.5 kHz using a phase-shift detection method. The Z-piezo bimorph produces approximately 50 μV/Å deflection and can be used to detect directly the vertical resonances of the actuator assembly. Spectrum analysis of the Z-output voltage with ambient acoustic noise as the driving force showed considerable structure below 5 kHz with peaks at 1500 and 2500 Hz. (The ambient noise was essentially white without pronounced peaks at those frequencies). If the driving oscillation of the isolation platform (1 μm at 2 Hz) were the only source of noise, the gap instability could still be as good as 0.02 Å, but acoustic coupling was dominant during STM operation at 4K.

The acoustic sensitivity, low resonant frequency, and difficulty of successful approach at low temperature provided impetus for designing a more rigid, easier to use instrument.

Compact Tube-Based STM

A compact instrument based on a piezoelectric tube scanner[18] with a quadranted outer electrode was designed such that the lowest mechanical resonance would be that of the scanner. It is shown on the bottom in

Figure 2.10. Its measured resonance frequency was 15 kHz; the calculated resonance of the tube was 18 kHz. The instrument was capable of imaging HOPG while sitting on the lab bench. (On the floor with 0.5 μm driving oscillation at 30 Hz, the gap noise would be 0.02Å.)

The tube-scanner (EBL #1 length 12.7 mm, diameter 6.4 mm and thickness 0.5 mm) is encased in a 19 mm diameter stainless steel thimble. Its calculated response is approximately 60 Å/V at 300 K and 20 Å/V at 4 K in X, Y, and Z. The instrument uses a differential lever approach. Three 0-80 socket-cap screws function as coarse and fine approach as described above with a lever reduction of 15. The sample is mounted over a hole in a Macor disk mounted kinematically on the rounded ends of the approach screws. The disk is held in place by three coil springs. A spring-steel retainer clip presses against the three approach screws at the center of the thimble to prevent any wobble or backlash. The instrument is loosely coupled to the dip-stick; it rests atop three small coil springs. Both the coarse and fine approach screws are accessible from outside the Dewär with retractable Allen keys welded to 1.5 mm diameter stainless steel rods, so there is no danger of thermal distortion keeping the sample out of tunneling range.

Each 1° turn of the fine approach screw moves the sample 600 Å toward the tip. With a low-temperature sensitivity of 20 Å/V, the full Z-range with a 300 V driver is 6000 Å, or a 10° turn of the fine approach screw. Even with a large diameter wheel on the fine-approach control rod, a "crashless" manual approach proved extremely difficult. In retrospect, a finer pitched screw and/or a small DC motor connected to the control rod with a

rubber drive belt would probably have been an ideal solution; a computer interface would stop the motor and retract the tip when a tunneling current was detected allowing crashless approach and removal of the fine-approach control rod. Instead, the dip-stick was dismantled and its parts used for yet another STM based on new translator technology.

Micro Pulse Systems Based STM

Design criteria for the third low-temperature microscope were computer-controlled approach, diameter < 25 mm for passage through the necks of all standard liquid helium transport Dewärs, intra-Dewär vibration isolation to reduce acoustic coupling, and tip-sample junction accessible to an optical microscope for rapid initial approach. A new device patented by Charles Staufenberg of Micro Pulse Systems, Inc., Santa Barbara was selected for the approach mechanism. The Micro Pulse actuator and its operating principal are illustrated in Figure 2.2. The actuator consists of two small piezoelectric blocks, an alumina wedge, and a frame. When one of the piezo blocks is driven at resonance (~120 kHz), momentum is transferred to a piston pressed against the wedge with components both normal and parallel to the wedge face; a restoring force presses the object against the wedge, but the piston is free to travel laterally. It can be moved continuously or in small steps depending on whether the block is energized continuously or in pulses. The drive circuit is a standard 555 timer based oscillator with a tuned inductor producing a high voltage output.

The STM head is shown in Figure 2.11. The head and actuator frames are kovar; its thermal expansion coefficient is matched to hard glass and

approximates that of the piezoelectric ceramic elements. The sample approach mechanism comprises four Micro Pulse actuators in a V-groove arrangement moving a 6.4 x 50 mm alumina rod held rigidly against the actuator wedges by a rare-earth magnet and a magnetic retaining ring which also serves as a limit stop. The sample is mounted on a spring-clip at the end of the rod. A piezoelectric tube scanner (EBL #1 12.7 x 6.4 x 0.5 mm) and tip are mounted coaxially with the rod. The tip is held by friction in a stainless-steel tube which was cut from a hypodermic needle and cemented into a Macor holder on the end of the scanner tube.

At room temperature, the translator can move the sample continuously as fast as 10 mm/s or, with pulses as short as 50 μs, in reproducible steps smaller than 100 Å. The step size depends strongly on the frequency of the driver and amplitude of the driving signal (which scales with the supply voltage for the driver circuit). At low temperature, the Q of the piezo blocks appears to be significantly higher, so careful tuning of the drive frequency with the head at low-temperature is essential. This is done by adjusting the frequency and then the inductor for maximum translation rate while the instrument is immersed in cryogenic liquid. Use of a wide mouth Dewär with liquid nitrogen and helium gas cross-flow to limit boiling facilitates observation of the piston. The inductor can also be fine-tuned with the aid of an oscilloscope to achieve maximum power and a symmetric waveform. The shape of the waveform can be monitored on the STM sample lead; the sample clip acts as an antenna.

For the approach, a magnifying lens is used to position the sample within 0.2 mm of the tip. Then, under computer control, feedback is disabled, the tip is fully retracted, a pulse of the resonant drive frequency on the actuators moves the sample approximately half the Z-range toward the tip, and feedback is re-enabled. If the sample is out of tunneling range, the process is repeated. After tunneling is established, smaller pulses are used to center the sample in the Z-range. The sample displacement as a function of pulse length can be determined by moving a sample within the Z-range of the scanner and used as a guide for setting parameters for subsequent approaches. The extension of the tube during tunneling is recorded before and after a pulse to measure the displacement; the tip is retracted during the pulse.

At room temperature, an appropriately selected pulse length (one resulting in sample displacement of about one half the piezo Z-range) brings the sample into tunneling range in less than 10 minutes; a 0.2 mm displacement requires 400 0.5 μm pulses. The pulse rate is determined by the feedback parameters, and is typically ~1 Hz. By using an optical microscope one can easily bring the sample within a few tens of microns of the tip under manual control, but attempts at manually decreasing the separation to a few μm before the auto-approach tend to be counterproductive. The apex of the tip is often difficult to see, and a tip crash necessitates its replacement.

For operation at low temperature, tunneling is first established at room temperature. Then the sample is retracted a few microns, and the instrument is slowly lowered into the helium or nitrogen Dewär. It is essential that the

piston and alumina support blocks be clean and dry. If water or other contamination is present, the actuator eventually freezes in place. As mentioned above, precise tuning of the drive frequency is also important, as the Q of the piezo-drivers increases with decreasing temperature. On returning to room temperature, the instrument may be warmed with a hot-air gun, but it should be kept cooler than 100° C to prevent debonding of actuator epoxy and indium-soldered wires and to avoid depoling of the piezoelectric ceramics and magnet.

Since no mechanical linkage to the STM head is required for the approach, a vibration isolation stage can be incorporated into the dip-stick. The head is suspended on a spring from with an extension of ~150 mm for a 1.3 Hz vertical resonance frequency. Small flexible copper leads with ~20 mm excess length connect the head to leads attached to a perf-board support.

Although the instrument functions reasonably well, it is not as stable as the ultra-compact tube-based instrument. The head was designed to have its first resonance normal to the sample surface at ~10 kHz. The STM block, however, has a much lower lateral resonance at ~3 kHz; lateral vibration of the block is coupled to the tunneling gap by the piezo-tube support.

The spring suspension helps to isolate the head from acoustic noise as predicted by equation (4), but it reduces the head performance at low frequencies near the spring resonance. The spring has a resonance at 1.3 Hz and has a low damping ratio. The amplitude transfer function of the spring given by equation (3), is >1 at the 1.3 Hz. With $\nu_h \approx 10$ kHz, the oscillation amplitude of the suspended head must be less than 0.05 mm to maintain gap

stability better than 0.1 Å. If the lower resonance frequency dominates (~2.5 kHz), the requirement could be as low as 4 μm. Oscillation at this frequency is well within the feedback bandwidth and the actual gap fluctuation will be much smaller (such that low-noise spectroscopy measurements would be possible during feedback-controlled tunneling). The measured oscillation at 1.3 Hz is typically <1 Å.

An atomic resolution image of highly oriented pyrolytic graphite obtained with this instrument immersed in liquid nitrogen (T = 77 K) is shown in Figure 2.12.

Tips and Tip Effects

Unless otherwise noted, the tips used for this work were electrochemically etched tungsten. The standard preparation method in the Baldeschwieler laboratory was a self-terminating 6 V ac etch in 2M KOH; several mm of 0.5 or 0.25 mm tungsten were immersed in the electrolyte and etched until the meniscus pulled away from the apex. The typical tip produced by this procedure was cone-shaped with a radius of curvature at the apex of several hundred angstroms. An example is shown in Figure 2.13. Although such tips are known to be covered with a ~50Å thick oxide,[19] they were fairly reliable for atomic-resolution imaging of HOPG. However, later work directed at imaging highly stepped silicon in UHV showed that such tips are generally poor for imaging non-atomically flat surfaces; before (and often after) *in-situ* modification by voltage pulsing or contact with the surface, the *tips* were often imaged by the *surface* as in Figure 2.14. A method for producing sharper tips without a thick electrochemical oxide was developed

and is detailed in Figure 2.15. The wire is first thinned rapidly with an ac etch and then dc electropolished until the lower part of the wire drops away; the lower part is used as the tip. Tips with radii of curvature <200 Å were produced as shown in Figure 2.16. While the tips are much sharper than the ac etched tips, they are also more prone to 'tip-changes' during imaging, probably because they are less robust in collisions with impurities.

Field Emission Microscope

A simple field emission microscope was constructed in the vacuum system for analysis and modification of tips. It is shown in operation in Figure 2.17. A phosphor screen[20] is held at high positive voltage (typically 0.5-3 kV); electrons emitted from the tip ~25 mm away form a magnified image of the electron-emitting surface of the tip. Field emission current can be measured with an electrometer connected to the tip. Alternatively, the tip can be held at electrical ground or resistively heated while the current is measured on the high voltage side using an isolation amplifier circuit. A feedback circuit was designed to protect the tip from destructive surges in emission current as it sharpens under the influence of heat and the electric field. Sharp tips form a visible spot on the screen with as little as a nanoamp of current and 600 V; particularly sharp tips have emitted 5 nA at 600 V. Blunter tips require higher voltage to establish the same current and more current to make a visible (more diffuse) spot. The 30 μm thick ZnS:Ag type 1320 (P22, blue-emitting) high luminosity phosphor can withstand current densities up to 0.25 W/mm^2 and can be used with field emission currents up to several microamps for *in situ* tip sharpening. The quality of the tip can be judged both from the image and from the current-voltage behavior.[21]

Summary

An ultrahigh vacuum (UHV) scanning tunneling microscope (STM) incorporating two-dimensional sample translation under computer control and *in vacuo* tip and sample exchange was developed. A low-hysteresis quadranted-electrode piezoelectric tube scanner was coupled with an inherently rigid 2-D translation stage to make a reliable and stable instrument. It was designed to replace directly an STM of the IBM "pocket-type" design thus utilizing existing UHV equipment with internal eddy-current damped spring vibration isolation stages. The maximum image window size with two quadrants driven is ≈ 1.5 x 1.5 μm. Its performance was documented through atomic-resolution imaging of Si(111) 7x7 reconstructed surfaces and of highly oriented pyrolytic graphite (HOPG) surfaces with 12 Å physisorbed clusters.

Several STM heads were developed for low-temperature imaging and spectroscopy. All were designed for immersion in cryogenic liquids and are suitable for use at 4.2 K inside standard liquid helium transport Dewärs. Two designs require manual sample approach via a screw turned from outside the Dewär. The first is based on a piezoelectric bimorph while the second is an extremely rigid device housing a piezoelectric tube scanner. A third design is based on a 1-D piezoelectric ceramic driven translator which allows automated approach under computer control and STM head vibration isolation via suspension from a spring inside the Dewär.

A method for making sharp tips was developed, and a simple field emission microscope was implemented for tip characterization and modification.

For additional information on instrumentation used and developed for this thesis, the reader is referred to Appendices B through E. Appendix B describes substantial enhancements for instrument control and data acquisition which were added to the STM system originally implemented by John Kramar, Michael Weimer, and Chunli Bai. In the last years of this work, the Baldeschwieler laboratory converted to a digital signal processor/video graphics array (DSP/VGA) based operating system. To complement the new microscope heads, a set of high performance digital control electronics for scanning tunneling microscopy was built in collaboration with Steve Clark. Software for advanced STM applications with the digital control electronics was developed based on a scanned probe microscope (SPM) operating system software written by David Baselt. Appendix C describes several aspects not addressed in Clark's and Baselt's theses,[22,23] and Appendices D and E present manuscripts prepared in collaboration with Clark and Baselt documenting the electronics performance and describing software principles for DSP based operating systems.

Figures -- Chapter 2

Figure 2.1. Photograph of Micro Pulse Systems based ultrahigh vacuum scanning tunneling microscope (MPS UHV STM) with *in vacuo* tip and sample exchange and lateral sample translation. The sample is mounted on a 2-dimensional translation stage driven by Micro Pulse actuators as described in Figure 2.2. The stage is used for both moving the sample into the Z-piezo range and for lateral translation of the sample for imaging of different areas. The sample position in both directions can be changed in increments as small as 100 Å. The tip is mounted atop a piezo electric tube for ease of manipulation with a wobble-stick. Because the translation stage is held rigidly against the STM structure by strong permanent magnets, stability is improved over louse or bearing-supported platform designs.

Figure 2.1

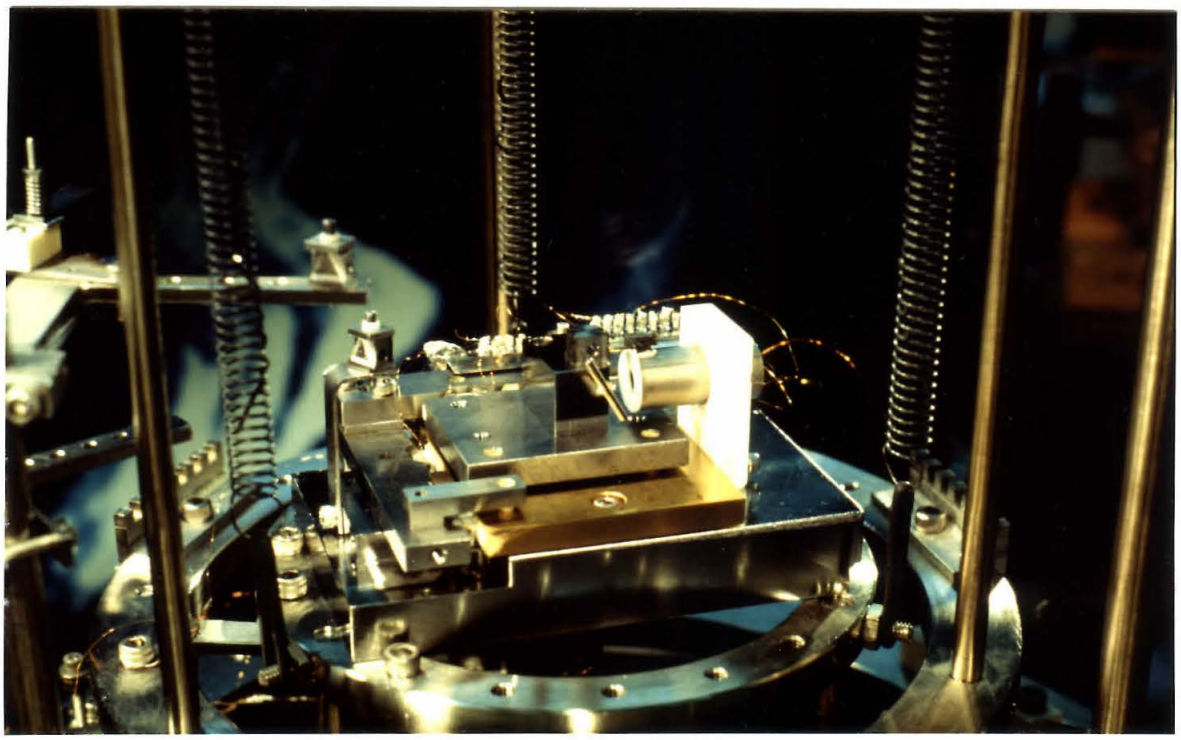

Figure 2.2. Schematic views of the Micro Pulse Systems (MPS) actuator and drive circuit. When one pair of the piezo blocks is driven with an ac signal at a resonant frequency (~120 kHz), momentum is transferred to a piston (or plate) pressed against the alumina spacers with a component parallel to the spacer faces; a restoring force presses the piston against the spacers, but the piston is free to travel laterally. It can be moved continuously or in steps as small as 100 Å, depending on whether the block is energized continuously or in pulses. The drive circuit is a gated 555 timer-based oscillator with a tuned tank circuit which produces a high voltage output.

Figure 2.2

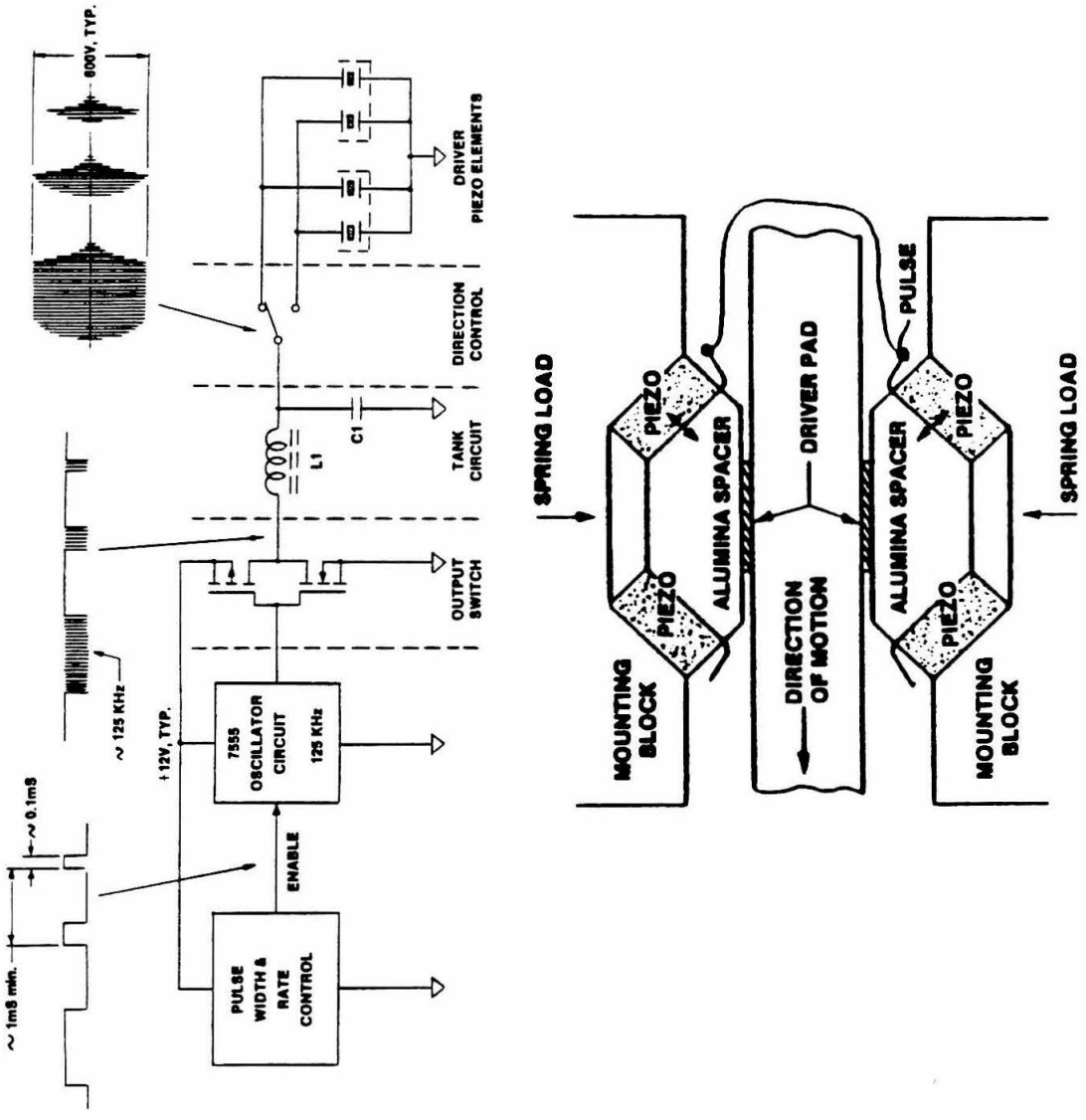
~ 1mS min.
~ 0.1mS
PULSE WIDTH & RATE CONTROL
ENABLE
7555 OSCILLATOR CIRCUIT 125 KHz
+12V, TYP.
~ 125 KHz
OUTPUT SWITCH
L1
C1
TANK CIRCUIT
DIRECTION CONTROL
DRIVER PIEZO ELEMENTS
600V, TYP.
SPRING LOAD
MOUNTING BLOCK
PIEZO
ALUMINA SPACER
DRIVER PAD
DIRECTION OF MOTION
PULSE

Figure 2.3. Schematic representation of tips and the tip mounting procedure for the MPS UHV STM. The tips are shaped from 0.25 mm wire as shown at the lower left. Wobble-stick manipulations in the vacuum system require the loop at the top. The tip material must be sufficiently elastic to be mounted in a three-pin clip like the one shown at upper left. The mounting procedure is illustrated at the right. First, the shaft of the tip is rested against the longer of the two pins at left and slid into the space between. Next, the loop end is bent downward until the loop opening is in front of the pin at right. The loop is then moved against the mounting block and allowed to relax against the bottom of the pin. Finally, the wobble-stick is pulled out of the loop. The curvature is exaggerated for illustrative purposes. Ideally, the tip is nearly normal to the sample surface. A slight curvature of the tip shaft as shown makes mounting simpler. Mechanical tip resonances are reduced if the tip is bent such that the loop presses against the mounting block when the tip is mounted and excess length is minimized.

Figure 2.3

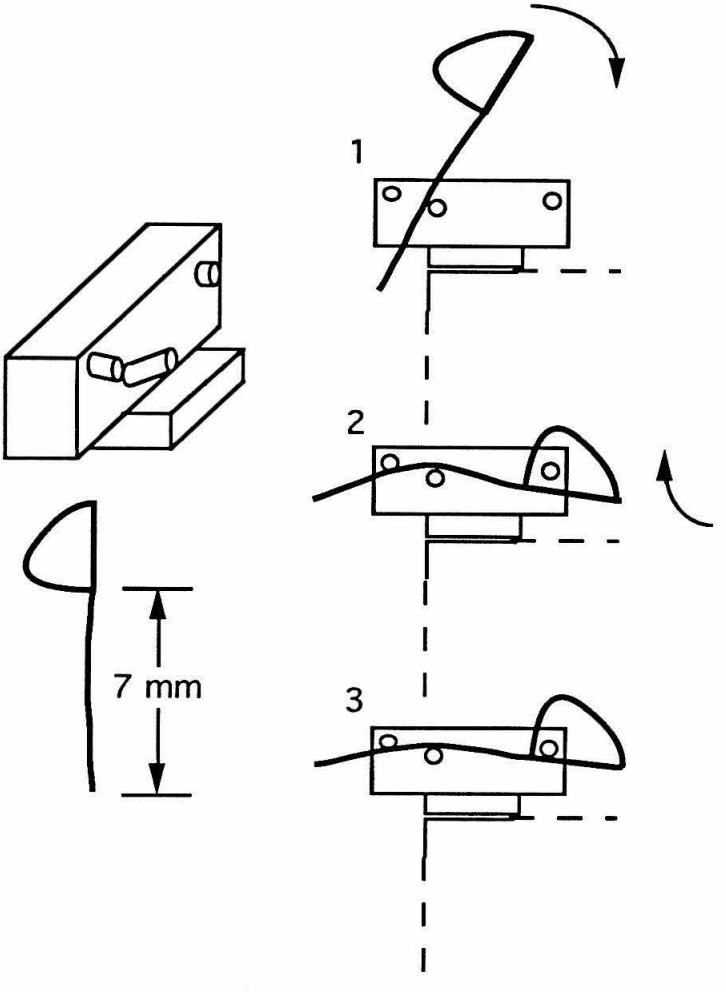

Figure 2.4. Schematic representation of sample stubs for silicon studies. The stub assembly used for the silicon work presented in this chapter is shown in (a). A 0.24 inch square, 5, cut from a silicon wafer is held by opposite edges between two electrically isolated molybdenum parts, 4 and 6. A tantalum 0-80 screw, 1, holds the assembly together via a steel compression spring, 2, pressing against a Macor insulator, 3. The stub can accommodate two samples, but because of low sample resistance and contact non-uniformity the second sample was usually replaced by a triangular quartz-glass spacer, 7, which allowed more uniform contact of 4 and 6 with the edges of the Si. An improved stub design is shown in (b). A sapphire sphere, 8, resting between conical holes in 4 and 6 makes a more stable structure. For compatibility with the sample mounting block in the STM, the pin at the bottom of the stub should be 0.090 inches in diameter and have a 45° groove 0.070 inches below the base of the stub. The sample face should be about 0.125 inches from the center of the pin.

Figure 2.4

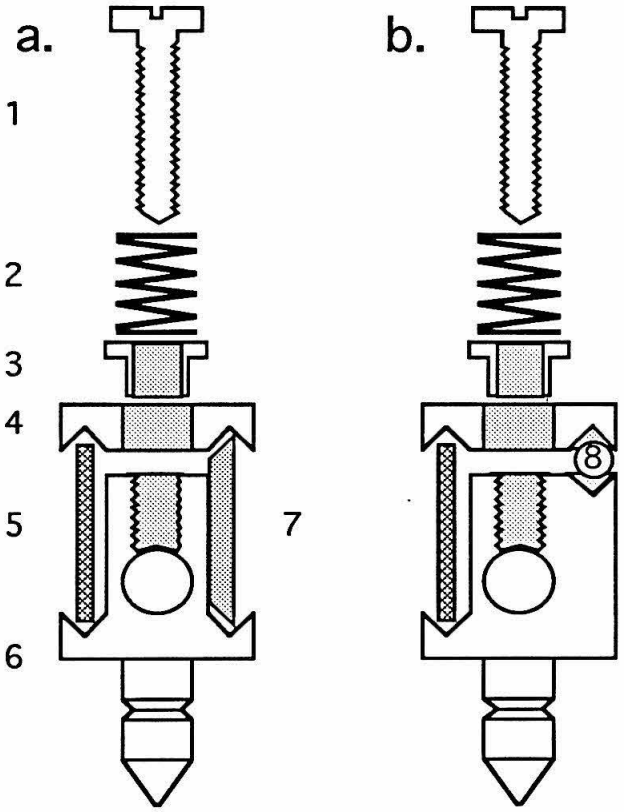

Figure 2.5. Schematic representation of the heater assembly for ohmic heating of silicon. A silicon sample is mounted in a stub as shown in Figure 2.7. The tantalum bar at the top of the heater assembly is rotated out of the sample mounting path, and the stub is inserted into a 0.093 hole in the tantalum base plate. The bar is then moved into contact with the back edge of the sample stub. The bar is pushed downward at the other end by a spring and supported by an electrical lead atop a Macor block. The Si sample functions as a resistor in the electrical circuit and is ohmically heated when current flows.

Figure 2.5

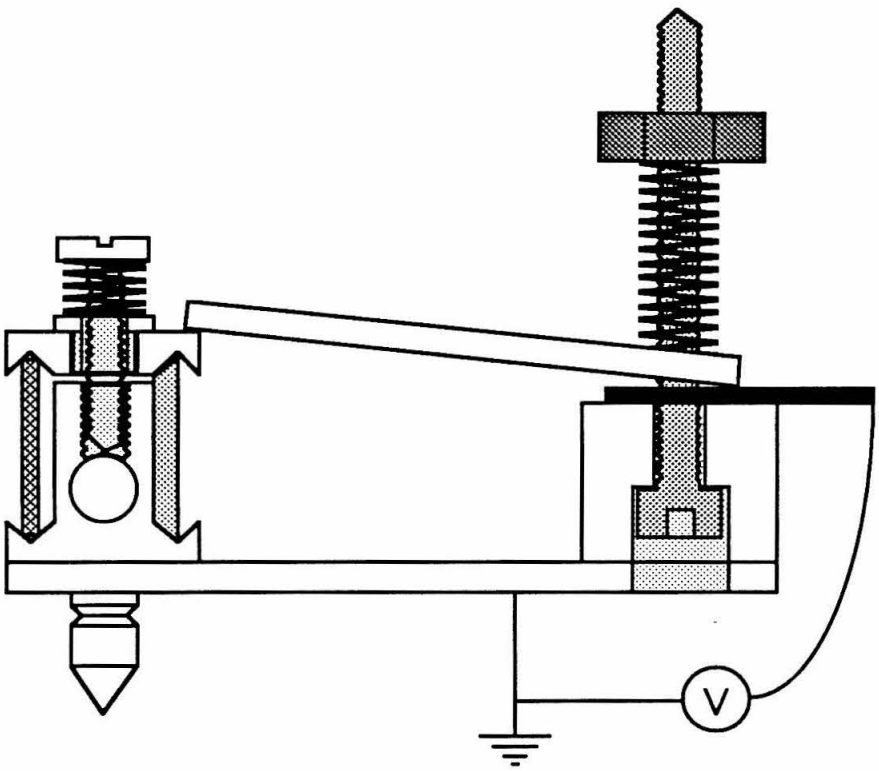

Figure 2.6. Large area image of a silicon surface cut 4° off the (111) plane. This sample was annealed with a dc current flowing in the down-slope direction which resulted in narrow terraces and ununiform step heights ranging from 3 to 60 Å. Electromigration and diffusion cause either step-bunching or step-spreading in dc annealed samples, depending on the direction of the current and the temperature of the anneal.[24] The brightness is slope-keyed such that steps downward from the top of the image appear dark. (4250 x 3430 Å, 250 x 250 pixels, 8500 Å/s, UHV, ac-etched W tip, 2.0 V sample bias, 1 nA constant current.)

Figure 2.6

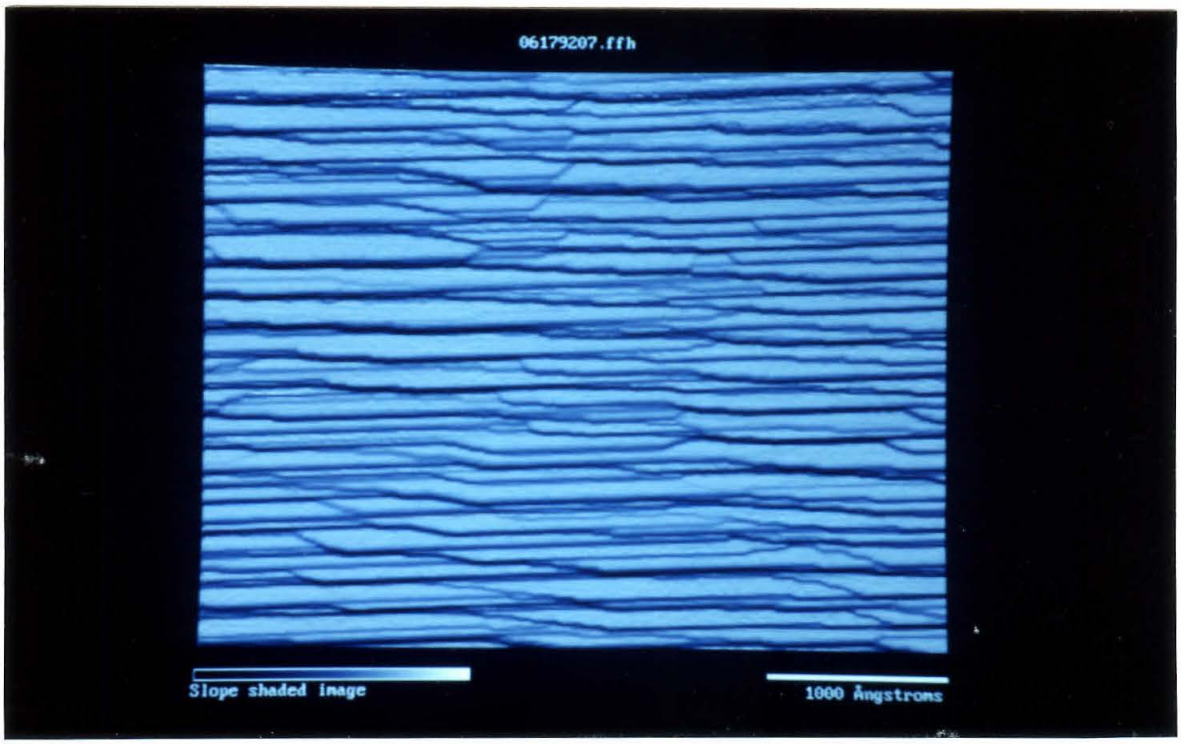

Figure 2.7. Si(111) 7x7 reconstructed terraces in an increased magnification image of Figure 2.6. The reconstruction is visible on the terraces. Note that the straight step edges cut through the corner holes of the 7x7 unit cell along the short diagonal. The structured steps at 12° to the straight steps indicate the rotation of the overall slope of the sample from a crystalline lattice direction. The bright spots are displaced adatoms and contamination, probably resulting from hydrocarbon cracking at the surface during the anneal. Brightness in this image is keyed to local relative height; the data have been processed by statistical differencing over a 10x10 pixel window in order to reduce the prominence of the steps relative to the atomic corrugation.[25] (850 x 685 Å, 500 x 500 pixels, 5200 Å/s, UHV, ac etched W tip, 2.0 V sample bias, 1 nA constant current.)

Figure 2.7

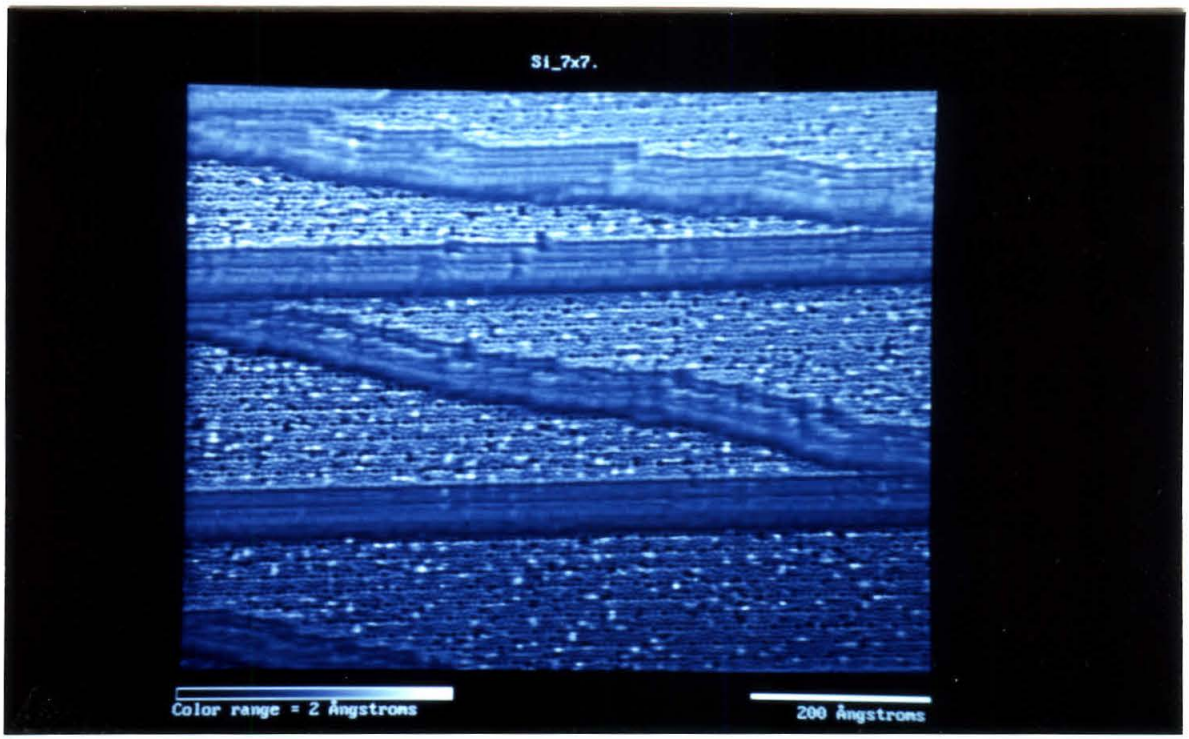

Figure 2.8. Si(111) 7x7 reconstruction in an increased magnification image of a terrace in Figure 2.7. Several adatom vacancies are visible. The amorphous 'clouds' are contamination, probably cracked hydrocarbons. At the bright region along the top, the side of the tip is sensing the nearby step edge. Brightness is proportional to height. (140 x 110 Å, 250 x 250 pixels, UHV, ac etched W tip, 2.0 V sample bias, 1 nA constant current.)

Figure 2.8

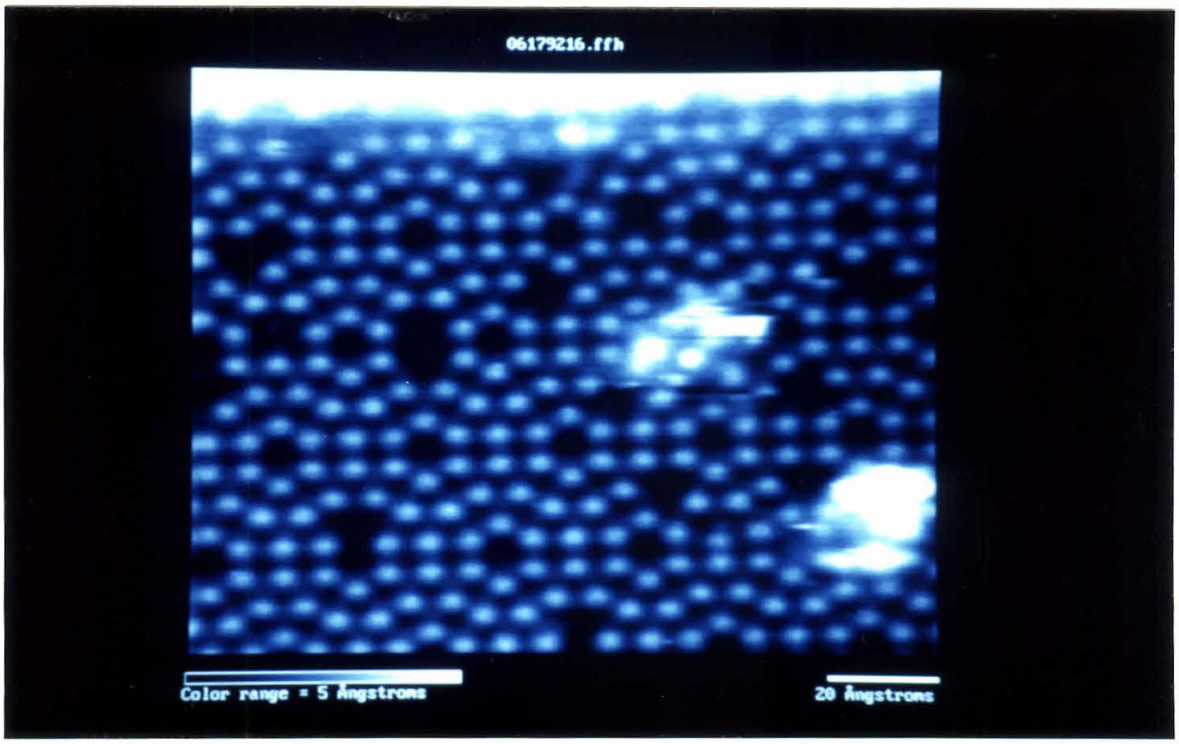

Figure 2.9. Physisorbed cluster on HOPG. The atomic lattice of the inert graphite basal plane is clearly resolved while no atomic structure is apparent in the cluster. The amorphous appearance of the adsorbate indicates that electronic states are not strongly localized at its constituent atoms; the STM images a constant local density of electronic states surface. The weakly-bound particle was swept away by the tip during a subsequent scan revealing a defect-free graphite substrate. Brightness is proportional both to topographic height and upward slope from the left. (40 x 36 Å, 250 x 250 pixels, 40 Å/s, UHV, ac etched W tip, -0.1 V sample bias, 1 nA constant current.)

Figure 2.9

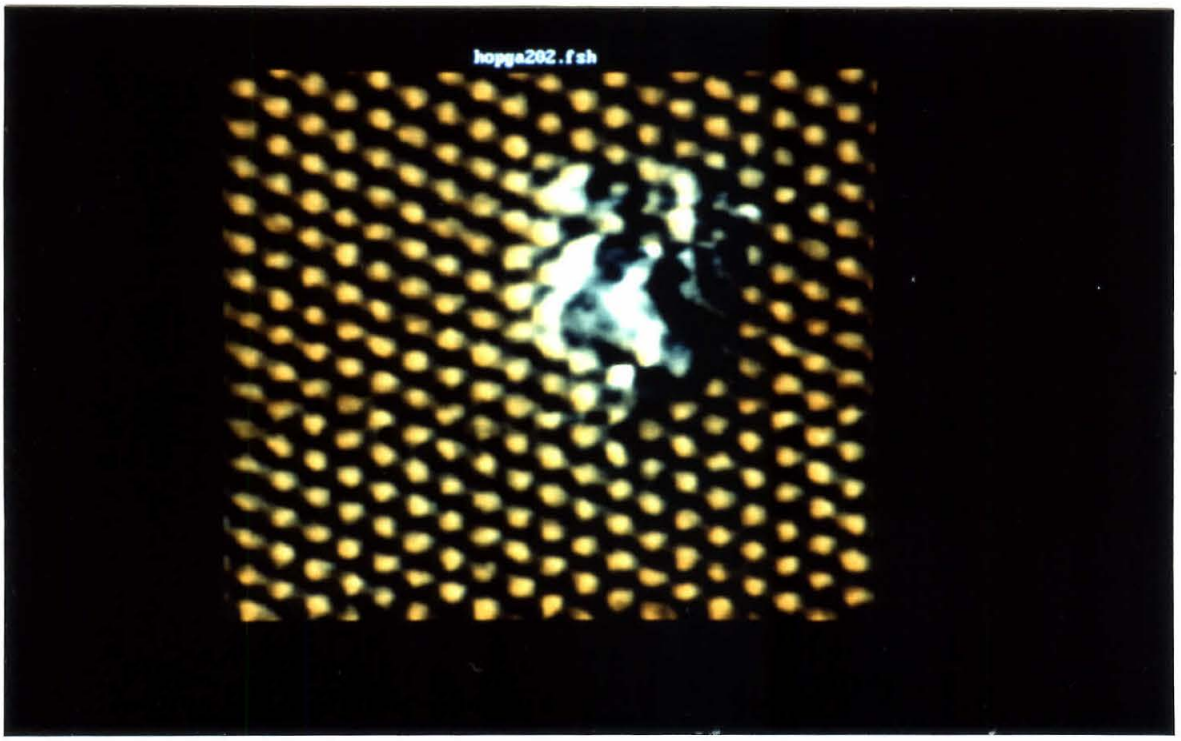

Figure 2.10. Photograph of two low-temperature scanning tunneling microscopes. The instruments are designed for immersion in cryogenic liquids and fit through the necks of standard liquid helium transport Dewärs. Both instruments rely on a screw-driven sample approach with lever-reduction. The instrument at the top incorporates a piezoelectric bimorph for Z and an L-shaped piezo plate for X and Y displacements of the tip. The instrument at the bottom is designed around a piezoelectric tube scanner. Its compact size and rigidity give it a very high lowest resonance frequency of 15 kHz, making it relatively immune from gap fluctuations caused by low-frequency vibration.

Figure 2.10

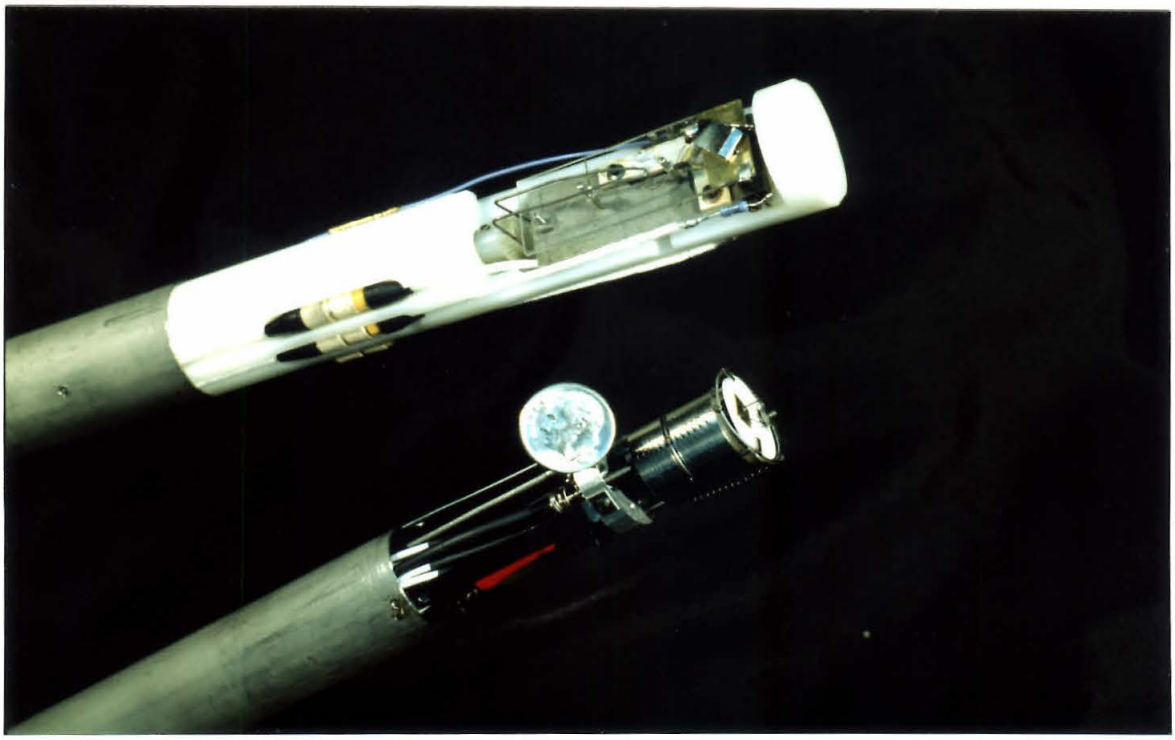

Figure 2.11. Photograph of a low-temperature scanning tunneling microscope based on Micro Pulse Systems actuators (MPS LT STM). The sample is mounted at the end of an alumina rod held against four MPS actuators in a V-groove arrangement by a rare-earth magnet. The tip is mounted coaxially at the end of a piezoelectric tube which is itself coaxial with the alumina rod. The approach is made by moving the alumina rod in small steps with short pulses of resonant ac voltage applied to the MPS actuators. Before each step the tip is retracted, and after each step the constant-current feedback servo is activated to move the tip toward the surface. If the sample remains out of the Z-piezo range, stepping continues. The optimum step size is about 0.5 μm, half the Z-piezo range. The stepping rate is typically about 1/s. Once tunneling is established, smaller steps are used to center the sample in the Z-piezo range.

Figure 2.11

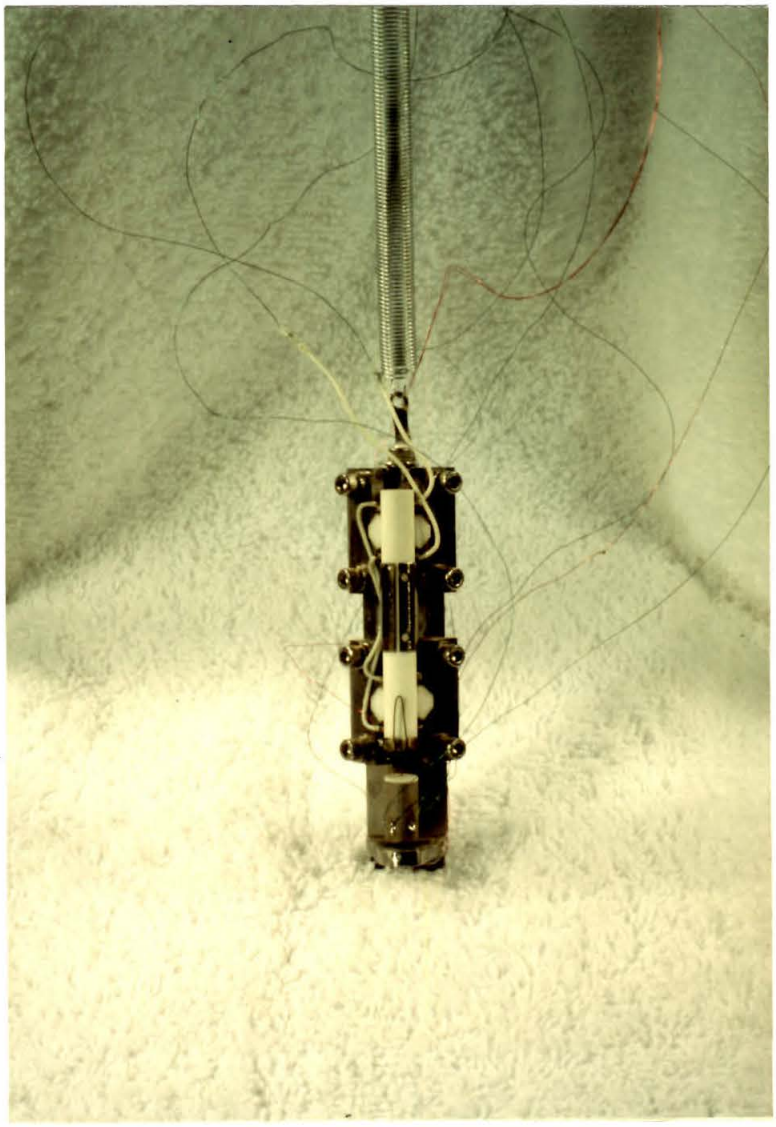

Figure 2.12. Image of HOPG obtained with the MPS LT STM (shown in Figure 2.11) operating at 77 K, immersed in liquid nitrogen. Topographic maxima are white. The hexagonal array of HOPG unit cells is readily apparent. The slight distortion is probably due to an asymmetric imaging tip. (ac W tip, 17 x 23 Å, 250 x 250 pixels, 0.1 V sample bias, 1 nA constant current.)

Figure 2.12

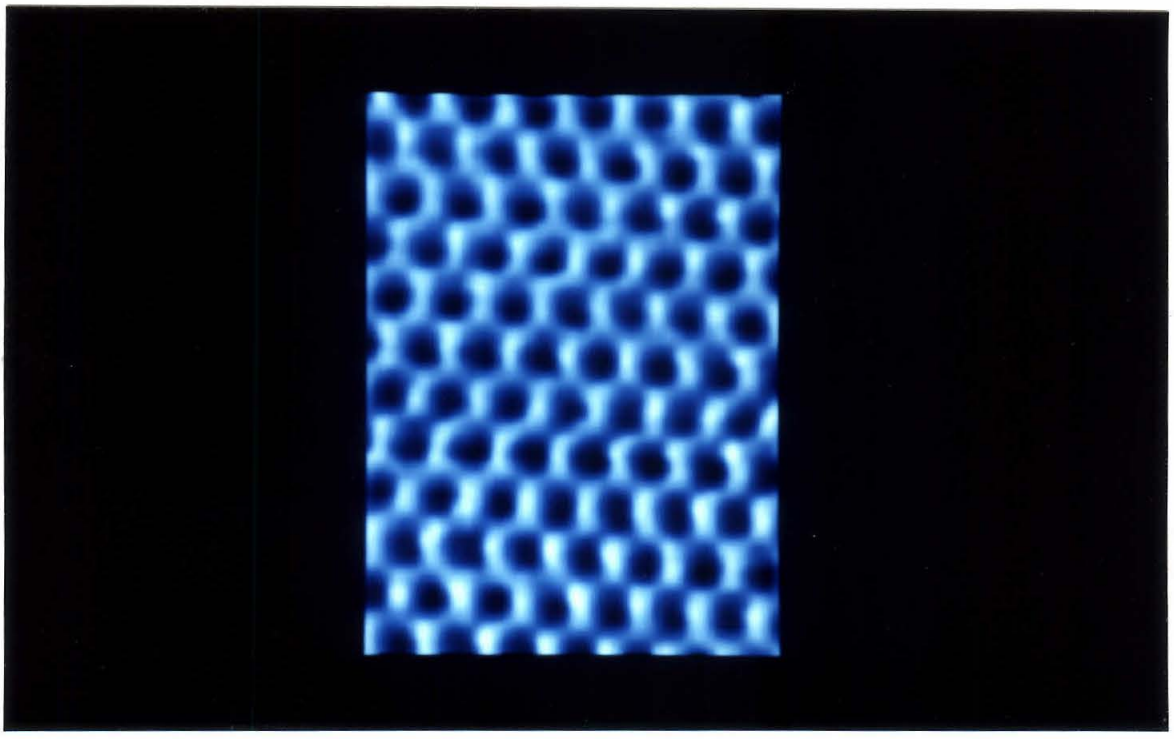

Figure 2.13. SEM micrographs of an ac etched W tip.

Figure 2.13

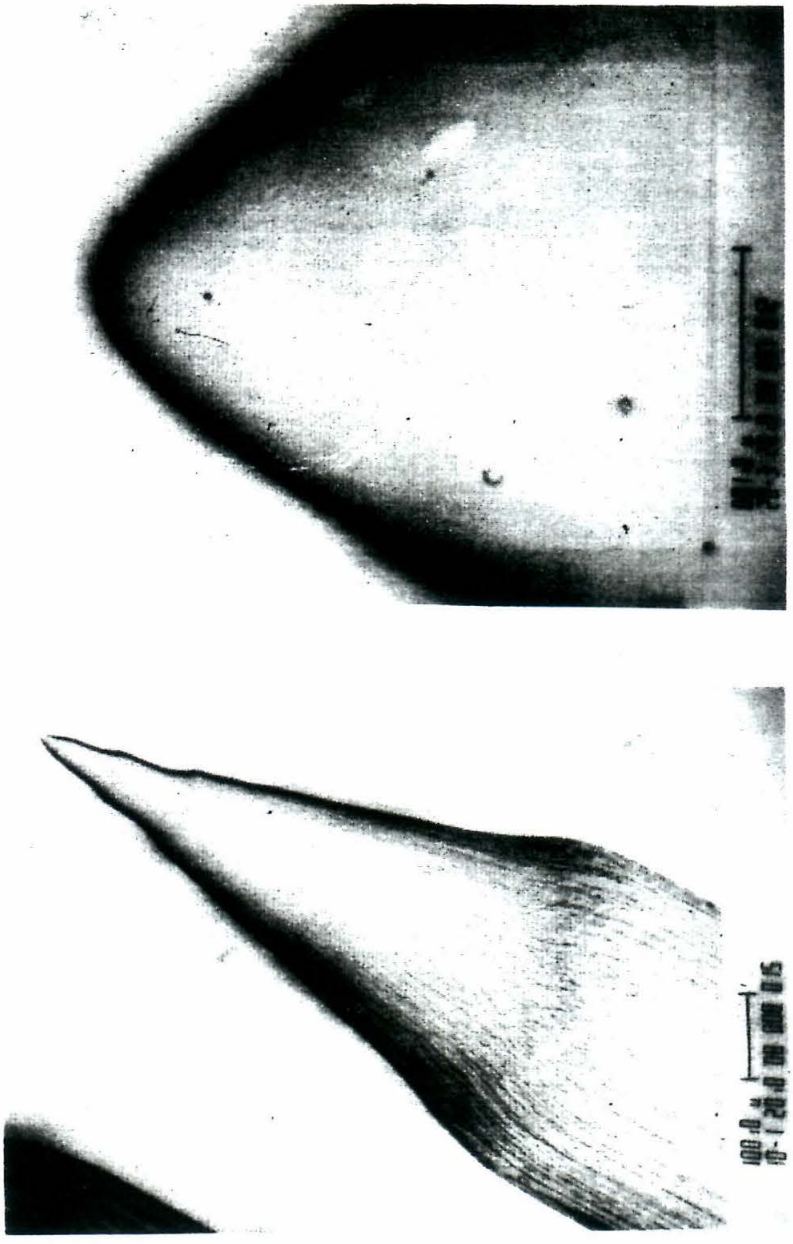

Figure 2.14. Artifactual tip imaging by a structured surface. A series of images of a stepped silicon surface with SiC nodules illustrates the imaging of tip shape by a surface. After the first image, taken with a bluntly curved tip, a 150 ms 10 V pulse is applied to change the tip shape. During the first 2/3 of the subsequent scan, the surface is imaged at much higher resolution, but horizontal bands of slightly different height indicate that the tip has an unstable mechanical structure. 2/3 through the scan, the tip shape changes dramatically, first becoming longer (the bright lines across the image indicating that the tip has been raised to maintain constant current) and then shorter, with a horseshoe-shaped apex which is imaged by bumps on the surface. The new structure is quite stable, as shown in the third image. After the 3rd image, the tip was moved to the corner of the image and voltage pulses are applied repeatedly until a change in tip height occurred. This time the tip shape changed to a relatively sharp and stable configuration allowing the step structure of the surface to be imaged. A surface site common to all four images is indicated in each image by a '!' symbol. Brightness is proportional to height. (4250 x 3430 Å, 250 x 250 pixels, 8000 Å/s, UHV, ac etched W tip, 2.0 V sample, 1 nA constant current).

Figure 2.14

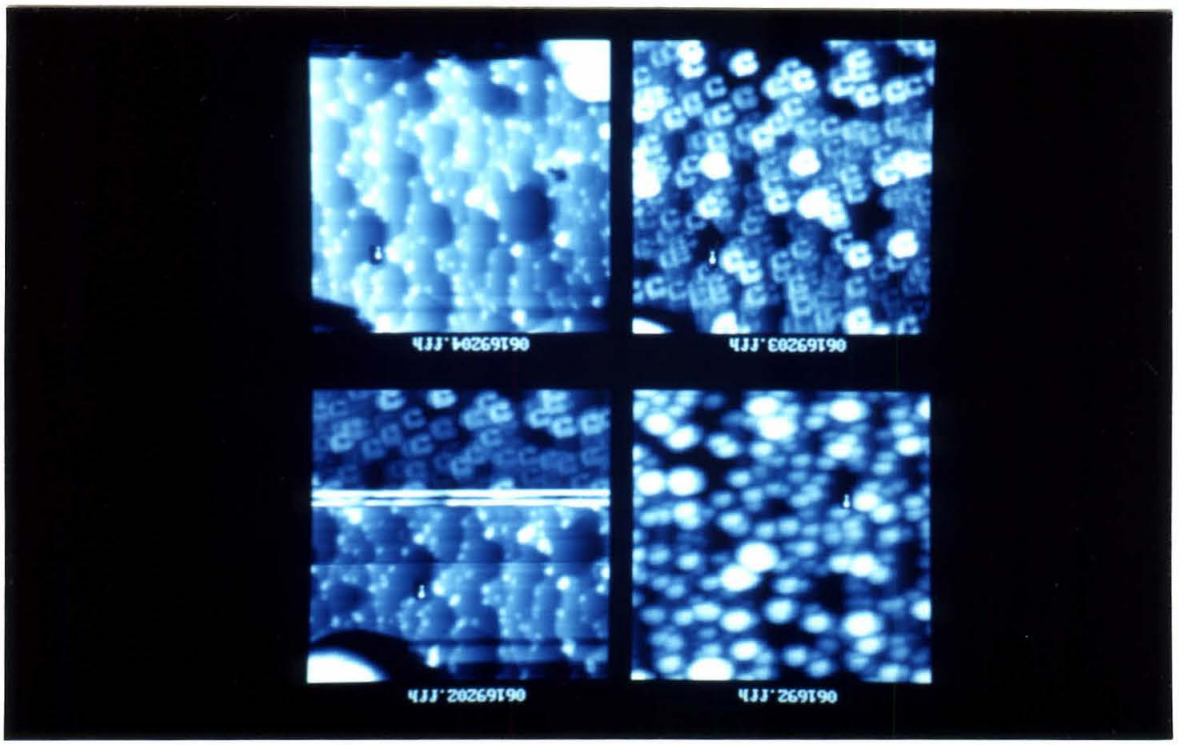

Figure 2.15. Schematic presentation of an ac-dc etch method for making sharp tips. A thin layer of electrolyte, 1 M KOH, is floated on a freon surface. A platinum wire loop counterelectrode is centered in the aqueous layer. A tungsten wire with a 'wobble-stick loop' bent at the end is lowered through the platinum counterelectrode ring and immersed 7 mm beyond the wobble-stick loop into the freon. The part of the wire in the electrolyte layer is rapidly thinned by passing a 6 V alternating current through it. Before the wire breaks, the current is stopped. The wire is then raised so that the lower cone meeting the thinned portion is at the air-water interface. The tip is then connected to +3 V dc, and the wire surface is electropolished away until the weight of the hanging portion causes it to break. The hanging part falls into a stainless steel basket immersed in the freon layer and is the completed STM tip. It is pulled from the freon and rinsed with water, acetone, and ethanol. Since it is immediately disconnected from the voltage source when it breaks away, the tip is not dulled by further etching, and no electrochemical oxide forms. The resulting tip shape is similar to that from a 'dc etch' in which an electronic circuit interrupts the current at the instant the bottom falls away and the top portion becomes the tip, but this method is simpler to use.[26] It is important to move the cone to the air-water interface before the dc polishing step or the tip becomes too long and thin to be stable. Without this step the procedure is identical to that described by Lemke *et al.*[27]

Figure 2.15

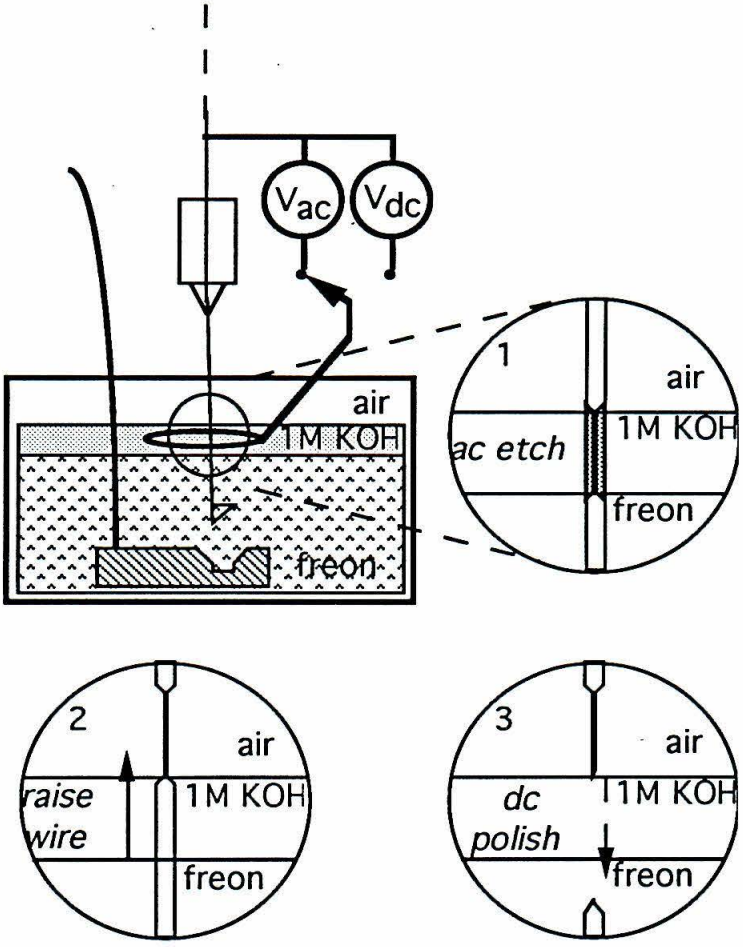
Vac
Vdc
air
1M KOH
freon
1
air
ac etch
1M KOH
freon
2
air
raise
wire
1M KOH
freon
3
air
dc
polish
1M KOH
freon

Figure 2.16. SEM micrographs of an ac-dc etched tip.

Figure 2.16

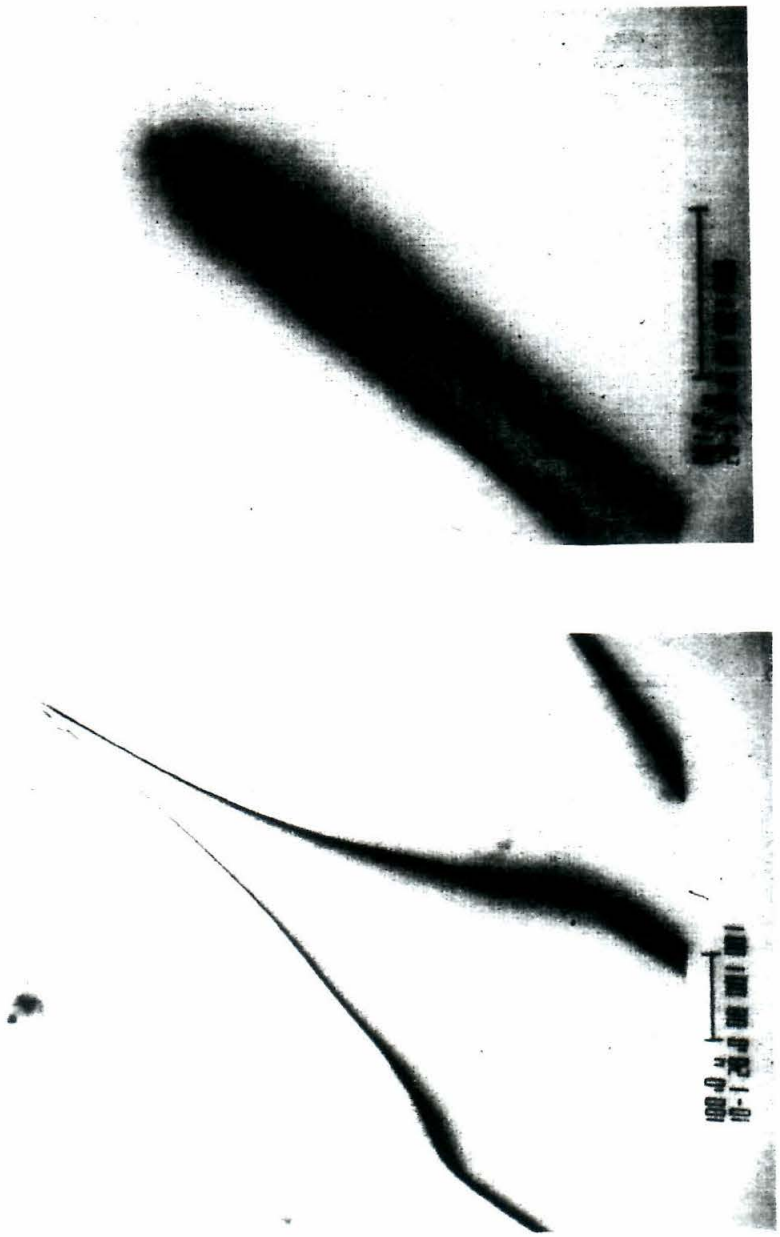

Figure 2.17. Photographs of a simple field emission microscope (FEM) for STM tip characterization in operation. In the top image, a small bright spot forms on the phosphor screen at relatively low voltage and current (600 V, 1 nA), indicative of a small radius of curvature at the tip apex. In the bottom image, a 4-lobed pattern forms on the screen. It arises from preferential emission from high index planes which have lower work functions than the point of the tip, probably a {110} plane. Even though a micro-crystal terminates the tip, it probably has broadly rounded surface rather than a sharp corner at its apex; a relatively high voltage is required to establish a 1 nA field emission current, and the pattern is visible only with several hundred nanoamps.

Figure 2.17

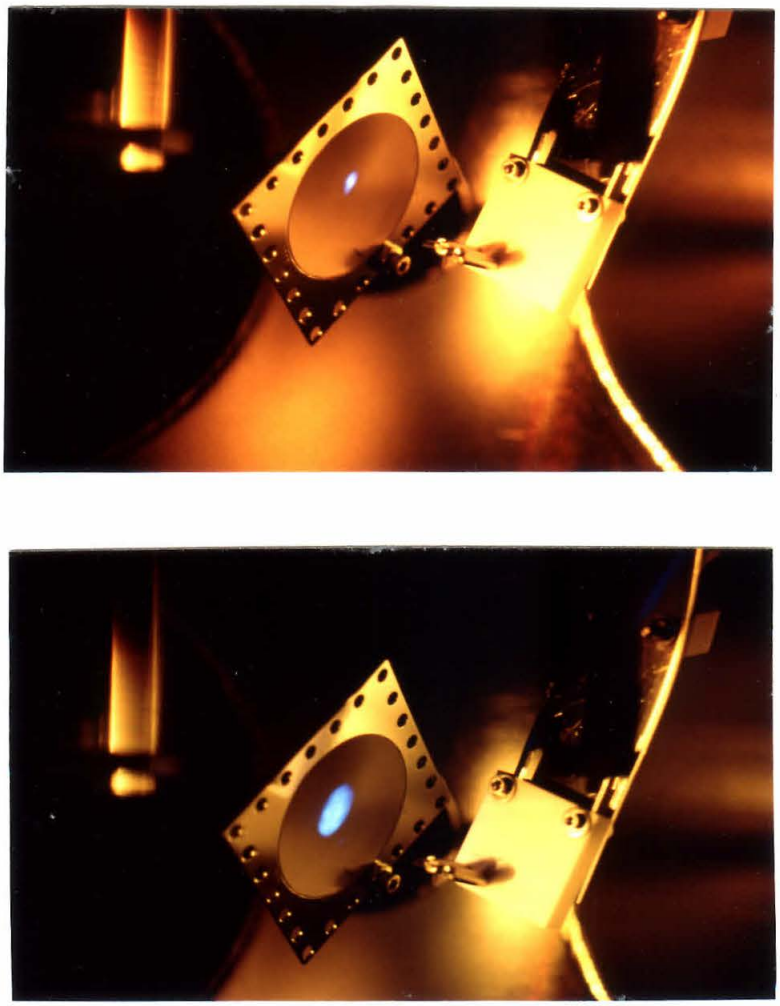

References

1. Piezoelectric Technology Data for Designers, Vernitron Piezoelectric Division, 232 Forbes Rd., Bedford, OH 44146. 216-232-8600.
2. EBL product line, Stavely Sensors Inc., 91 Prestige Park Circle, East Hartford, CT 06108. 203-289-5428.
3. P. K. Hansma, *IBM J. Res. Dev.* **30,** 396 (1986).
   G. Binnig and H. Rohrer, *IBM J. Res. Dev.* **30,** 355 (1986).
4. Y. Kuk and P. J. Silverman, *Rev. Sci. Instrum.* **60,** 165-180 (1989).
5. P-202X Sample Positioner, Micro Pulse Systems, Inc., 3950 Carol Avenue, Santa Barbara, CA 93110.
6. Z sensitivity is calculated; X and Y are measured against the Si (111) 7x7 unit cell.
7. R. G. Carr, *J. Microsc.* **152,** 803 (1988).
8. John A. Kramar, "Scanning tunneling microscopy and spectroscopy of molybdenum disulfide," Ph.D. thesis, California Institute of Technology (1990).
9. B. S. Swarzentruber, Y.-W. Mo, M. B. Webb, and M. G. Lagally, *J. Vac. Sci. Technol.* A **7,** 2901-2905 (1989).
10. Alpha-10™ TX1010 class 100 clean room wipes, Texwipe, P. O. Box 308, Upper Saddle River, NJ 07458.
11. Cut from a 12 x 12 x 2 mm x-ray monochromator, Union Carbide, P. O. Box 94924, Cleveland, OH 44101.
12. A. P. Fein, J. R. Kirtley, and R. M. Feenstra, *Rev. Sci. Instrum.* **58,** 1806 (1987).
13. D. Eigler, *Bull. Am. Phys. Soc.* **32,** 542 (1987); D. M. Eigler, E. K. Schweizer, *Nature* **344,** 524-526 (1990). Similar instruments have been constructed by P. S. Weiss and E. K. Schweizer.
14. B. Yurke, P. G. Kaminsky, and D. M. Eigler, *Cryogenics* **26,** 435 (1986).
    A. M. Simpson and W. Wolfs, *Rev. Sci. Instrum.* **58,** 2193 (1987).
    S. Vieira, M. A. Ramos, and R. Villar, *Jap. J. Appl. Phys.* **26,** Supplement 26-3, 1711 (1987).

15. R. J. Colton, S. M. Baker, R. J. Driscoll, M. G. Youngquist, J. D. Baldeschwieler, and W. J. Kaiser, *J. Vac. Sci. Technol. A* **6,** 349-353 (1988).
16. W. J. Kaiser and R. C. Jaklevic, *IBM J. Res. Develop.* **30,** 411-416 (1986).
17. W. J. Kaiser and R. C. Jaklevic, *Rev. Sci. Instrum.* **59,** 537 (1988).
18. C. P. Germano, *IRE Trans.* **7,** 13 (1959).
G. Binnig and D. P. E. Smith, *Rev. Sci. Instrum.* **57,** 1688 (1986).
19. M. J. Vasile, D. Grigg, J. E. Griffith, E. Fitzgerald, and P. E. Russel, *J. Vac. Sci. Technol. B* **9,** 601-608 (1990).
20. PHOS-UP22SS-C7x7-R1500, Kimball Physics Inc., Wilton, NH 03086-9742.
21. J. R. Meyer, S. J. Stranick, J. B. Wang, and P. S. Weiss, *Ultramicrosc.* **42,** 1538-1541 (1992).
22. Steven M. Clark, "Advances in scanning force microscopy of biological structures," Ph.D. thesis, California Institute of Technology, Pasadena, CA (1992).
23. David R. Baselt, Ph.D. thesis, California Institute of Technology, Pasadena, CA (in preparation).
24. Y. Homma, R. J. McClelland, and H. Hibino, *Jap. J. Appl. Phys.* **29,** L2254 (1990).
25. Wayne Niblack, *An Introduction to Digital Image Processing,* Prentice/Hall International, 45-86 (1986).
26. R. J. Driscoll and M. B. Weimer, unpublished results, and J. P. Ibe, P. P. Bey, S. L. Brandow, R. A. Brizzolara, N. A. Burnham, D. P. Dilella, K. P. Lee, C. R. K. Marrian, and R. J. Colton, *J. Vac. Sci. Technol.* A **8,** 3570-3575 (1990).
27. H. Lemke, T. Goddenhenrich, H. P. Bochem, U. Hartmann, and C. Heiden, Rev. Sci. Instrum. 61, 2538-2541 (1990).

Chapter 3: Tunneling Spectroscopy with a Cryogenic STM

Introduction

Before the scanning tunneling microscope was invented, tunneling spectroscopy of metal-insulator-metal (MIM) sandwich junctions was already well established both as an informative probe of the superconducting state and as a sensitive vibrational spectroscopy for organic molecules.[1,2] With the advent of the scanning tunneling microscope (STM) came the possibility of performing analogous measurements with atomic-scale spatial resolution in the absence of potentially perturbing insulating oxide barriers. This chapter assesses the possibility of using the STM for unimolecular vibrational spectroscopy and presents data obtained using a low-temperature STM to measure I vs. V (tunneling current vs. voltage) and dI/dV vs. V curves for the tunnel junction consisting of a gold STM tip and a superconducting lead thin film. Detection of lead phonons with the STM is a first step toward unimolecular vibrational spectroscopy.

Feasibility of Vibrational Spectroscopy with the STM

Motivation

In the investigation of molecules at surfaces, one of the most informative probes is vibrational spectroscopy.[3] At its most basic level, vibrational spectroscopy can be used to identify adsorbed species through their vibrational "fingerprint." The vibrational states of molecules, unlike their electronic states, are relatively unperturbed by adsorption; consequently, the vast data base already available from the spectroscopy of free molecules can be used to interpret adsorbate vibrational spectra. On a

more advanced level, vibrational spectroscopy can be used to characterize the local environments of adsorbed molecules and the nature of their bonding to the surface. The changes that occur in absorption intensity and vibrational frequency are a direct probe of the interaction between adsorbed molecules and the surface. The enormous potential of surface vibrational spectroscopy has spurred its rapid development, but the improvement of established techniques and the introduction of complimentary methods remains a crucial research area.

The techniques currently available can be used to obtain the vibrational spectra of as little as 0.1% of a monolayer. Nevertheless, all are providing spectra from billions of molecules averaged over an area which is extremely large on the molecular scale. Features due to distinct species on the surface are difficult to separate, since many of the vibrational modes are likely to be at similar frequencies. Furthermore, the spatial averaging makes assessment of effects due to differences in bonding geometry unmanageable. An important example of this limitation is in the investigation of mechanisms in heterogeneous catalysis; only a small fraction of the adsorbates may be at the "active sites," but spectra from those molecules cannot be obtained with specificity. Any means for site-specific vibrational spectroscopy of individual adsorbates would be an important scientific advance and would facilitate the study of chemistry and physics at surfaces. With the scanning tunneling microscope, site-specific vibrational spectroscopy of individual adsorbed molecules together with three-dimensional atomic-scale imaging of their bonding environments may be possible.

The scanning tunneling microscope (STM) has been used with atomic-scale spatial resolution for imaging and electronic spectroscopy of surfaces and has the potential to be used for site-specific vibrational spectroscopy on the same scale. The STM is essentially the non-planar analog of the solid-state planar metal-insulator-metal (MIM) junctions which are used for superconductor spectroscopy and for inelastic electron tunneling spectroscopy (IETS). IETS has been demonstrated to be one of the most sensitive vibrational spectroscopies available, but in the planar MIM junction it is limited by spatial averaging and junction inhomogeneity in the same ways as the other surface vibration probes. Spectroscopic measurements with the STM similar to those made in the planar MIM junction may be possible, but with atomic-scale localization and on a broader range of systems. (Localized STM spectroscopic measurements have already been done on superconductors as will be described later in this chapter). In the MIM junction a metal oxide is the insulating barrier for electron tunneling as well as the adsorption base for molecules in IETS; for study with the STM a molecule can be adsorbed on any sufficiently conducting surface, and the insulating barrier can be vacuum, gas, or even liquid. Combined with the STM's imaging capability, inelastic electron tunneling spectroscopy with the STM would be an extremely powerful surface analysis tool.

IETS

If an inelastic interaction can occur, the electron's tunneling probability is increased due to an additional density of electronic states that is made available at $E-\hbar\omega$. An energy threshold corresponding to a vibrational

mode with frequency ω can then be detected as a step in the differential conductance $G = dI / dV$ of a tunnel junction or a peak in its derivative. Inelastic electron tunneling spectroscopy data for organic molecules in MIM junctions are usually plotted as d^2I / dV^2 versus V and are similar in appearance to infrared or Raman spectra. Conductance changes associated with the inelastic excitation of the most intense molecular vibrational modes in MIM junctions are approximately 1%. Since there is a thermal distribution of electron energies about V, resolution in tunneling spectroscopy is temperature dependent; thermal line broadening in inelastic electron tunneling spectroscopy is approximately $5.4k_bT$ (which would be approximately 1100 cm^{-1} at 300 K, room temperature).[4] For this reason, it is necessary to cool the tunnel junction to near absolute zero (e.g., 4.2 K, the boiling point of liquid helium, where the thermal line broadening would be only 16 cm^{-1}) to obtain sufficient resolution for vibrational spectroscopy. Even at 77 K, the boiling temperature of liquid nitrogen, lines are broadened beyond detection (290 cm^{-1}).

IETS is based on inelastic electron tunneling in which energy from a tunneling electron excites a vibrational transition in a molecule. It was first demonstrated in 1966, when John Lambe and Bob Jaklevic observed voltage dependent structure in the current across lead-aluminum oxide-aluminum tunnel junctions at energies higher than those corresponding to lead phonons.[5] They observed that plots of the second derivative of the current with respect to the voltage as a function of voltage resembled infrared absorption spectra of organic molecules. The peaks occurred at appropriate energies, and further experiments revealed that the vibrational spectra of

molecules present at the metal-metal oxide interface of their junctions could indeed be detected. Spectra of a specific molecule can be obtained by deliberately exposing the oxide to the molecule during junction preparation. In an effort to determine the sensitivity of IETS, R. M. Kroeker and P. K. Hansma used a junction less than 1 mm square and detected a 1% coverage of p-deutero benzoic acid, approximately one deuterium atom/1500 Å^2.[6] The use of IETS is growing but is not widespread, probably because of the limitations imposed by the MIM junction.

Simple Feasibility Analyses

One way of addressing the feasibility of performing IETS with the STM would be to assume that it is directly analogous to the metal-insulator-metal (MIM) experiment. The signal magnitude decreases linearly with increased junction resistance while the noise level goes down as its square root. Since the STM typically operates at 10 Mohm and MIM junctions typically have a resistance on the order of 100 ohms, the signal to noise ratio *for a given ac modulation amplitude* will be roughly 300 times smaller in the STM. However, the signal magnitude is proportional to the modulation amplitude and can thus be increased at the expense of resolution. (As is shown below, it would appear from a Taylor series expansion of the frequency components of a modulated current that the signal is proportional to the square of the modulation amplitude, but the peak amplitude is also dependent on its width which is also proportional to the modulation amplitude). If 50 cm^{-1} is acceptable (which is better than that achieved in most non-IETS surface vibrational spectroscopy and similar to that of HREELS) then the signal can

be enhanced by a factor of about 50 over high resolution MIM measurements. The additional factor of six in signal to noise ratio can be recovered by averaging spectra 40 times longer. The direct analogy to the MIM junction is not perfect, as MIM junctions incorporate an inhomogeneous metal oxide which is not present in the STM. High resistance MIM junctions suffer from increased noise which is probably due to charging and decharging of electron traps in oxide barrier.[7] The highly localized STM measurement will not suffer from this limitation since no oxide barrier is present and the measurement site can be carefully selected to be a "quiet" part of the sample.

Another way to assess the feasibility of doing IETS with the STM is a signal and noise level analysis. Inelastic electron tunneling measurements with the scanning tunneling microscope will be feasible only if the signal to noise ratio can be made sufficiently large with an acceptable acquisition time. Using a simplified analysis which includes the essential features, it is shown here that this should be possible even without geometry-dependent enhancement of the signal. The STM-IETS measurement is modeled using standard modulation techniques to detect directly the second derivative of the current with respect to the voltage. A small sinusoidal voltage is superposed on the bias voltage ($V = V_o + k \sin \omega t$), and the signal detected is the amplitude of the current at the second harmonic of the modulation frequency. A Taylor Series expansion shows that this component of the current is nearly equal to $(k^2/4)d^2I/dV^2$ where k is the amplitude of the modulation voltage. The achievable signal amplitude with acceptable resolution can be determined through a simplified analysis of the signal approximating the shape of the d^2I/dV^2 peak as a Gaussian. The area of the

peak is equal to the change in conductance, $\Delta\sigma$; thus, the amplitude of the peak is given by $2\Delta\sigma(\sqrt{\ln 2})/(W\sqrt{\pi})$ where W is the full width at half maximum. The amplitude of the signal is then obtained by multiplying $k^2/4$ by $2\Delta\sigma(\sqrt{\ln 2})/(W\sqrt{\pi})$. Assuming a 1% relative change in conductance and using a gap resistance of 10 Mohm, which is an acceptable resistance for the STM, gives $\Delta\sigma = 10^{-9}$ A/V. Peak broadening due to the modulation voltage is 1.2 k.[8] With a resolution criterion of 50 cm^{-1} the maximum modulation amplitude is 5 mV. Using these values in the above expression gives a predicted signal amplitude of 1 pA which should be readily detectable.

To complete this analysis, the minimum achievable noise level must be considered. Shot noise, the random current fluctuations present whenever a current flows across a junction, is the limiting factor. The shot noise is given by $I_{sn} = \sqrt{(2qIB)}$ where q is the electron charge, I is the current across the junction, and B is the measurement bandwidth. If the measurement bandwidth is limited to 1 Hz, then the rms shot noise at 2000 cm^{-1} will be 0.1 pA. Using the 1 pA signal predicted above gives a signal to noise ratio at the input of the detecting lock-in amplifier of 10:1. It is clear that, in principle, IETS peaks should be easily detectable. In practice it is unlikely that the STM noise level can be reduced to the shot noise limit. An extremely stable gap resistance would be necessary for the STM noise level to be low enough for IETS.[9] If the noise can be reduced to within a factor of ten of the shot noise limit (which should be possible with a sufficiently rigid instrument and carefully designed and constructed electronics), IETS will still be straight forward with the STM. With a 10 second time constant on the lock-in amplifier used to detect the signal, the output signal to noise ratio would be

approximately 40. This could be further improved by subsequent signal averaging. A complete spectrum from 400-4000 cm^{-1} could be obtained in about an hour.

Theoretical Background

At an inelastic tunneling threshold, the change in conductivity in the STM geometry should be similar to or greater than the change measured in the MIM junction. In the MIM junction the change is usually between .01 and 1% of the total conductance. Persson and Demuth used the dipole approximation for vibrating molecules to calculate the inelastic scattering cross section for electrons tunneling from a metal tip.[10] They predicted a relative change in conductance, $\Delta\sigma/\sigma$, for CO on Cu(100) or Ni(100) of about 1%.[11] Experimental results for CO on Rh-doped alumina in an MIM junction give $\Delta\sigma/\sigma$ of 0.1%. Binnig *et al.*, also using the dipole approximation, showed that $\Delta\sigma/\sigma$ should be enhanced in the STM over the MIM geometry by a factor between ε^2 and $\varepsilon^2/5$ where ε is the relative permittivity of the insulator in the MIM junction. They estimate a factor of three enhancement of the IETS signal in the STM over the MIM junction and suggest that the resulting current changes should be readily detectable with the STM.[12]

In the same paper cited above, Persson and Demuth pointed out that the dipole approximation may not be appropriate for the STM geometry and that resonance and impact scattering might dominate over dipole scattering. Persson and Baratoff calculated that resonant tunneling could give a change (in this case a decrease) in total tunneling conductance of 10% or more, but that this would occur only when certain special conditions were met.[13] Gata,

however, used a different analysis for resonant tunneling through specific orbitals of a molecule adsorbed to an STM tip and a conducting substrate and predicted an increase in conductance larger than that obtainable from dipole coupling processes.[14] He further predicted peaks in the first derivative for resonant states with a sufficiently large lifetime which together with electron-phonon coupling and other related effects may make comparison to gas-phase spectra difficult. Thus, while the IETS signal may be substantially enhanced in the STM junction geometry, its interpretation may be more difficult than with the MIM junction.

Experimental Background

The recent results of Stephen Gregory provide additional encouragement for detection of inelastic tunneling detection of vibrational modes in the scanning tunneling microscope junction geometry.[15] He made a small-area tunnel junction by bending crossed argon-coated current-carrying gold wires into contact under the influence of a magnetic field. Hydrocarbon contamination in the argon layer was detected by a 10% increase in conductivity at the vibrational energy of the C-H stretch.

An early attempt at making a tunneling spectroscopy measurement on molecular adsorbates with a scanning tunneling microscope yielded inconclusive results.[16] A first derivative current spectrum taken with an STM tip positioned over a cluster of sorbic acid molecules on a graphite substrate was assigned to a vibrational spectrum; some of the structure appeared to correlate with peaks observed in the second derivative spectrum obtained by IETS of sorbic acid in an MIM tunnel junction. The signal was four orders of

magnitude greater than predicted and than that seen in the MIM junction geometry. A possible explanation was offered based on a resonant tunneling model developed by Kirtley and Soven.[17] That model, however, predicts on-resonance excitation of the second harmonic of the vibrational frequency with almost the same intensity of the first harmonic. This was not observed in the experiment. While peaks at the same energy in the opposite bias would be expected for inelastic tunneling, the experiment was conducted with only positive bias. Furthermore, the apparent correlation of the peaks with vibrational modes was not verified by isotopic substitution. The results suggest that unforeseen mechanisms may be involved in tunneling with the STM, but additional study is required.

Don Eigler and Paul Weiss measured conductance vs. bias voltage over CO, benzene, and deuterobenzene molecules in an ultrastable UHV STM operating at 4.2 K. They were able to detect conductance changes on the order of 1% in minutes, but found the results were extremely irreproducible. They hypothesized that electronic trapping states or structural instabilities of the tip precluded detection of molecular vibrational levels.[18] The importance of the structure of the tip in superconductor tunneling spectroscopy measurements was demonstrated by Wilkins *et al.* They found that the superconducting density of states of lead was masked when tips with a surface oxide (etched tungsten and stainless steel) were used but easily observable with nonoxidized tips (gold, platinum).[19]

Theoretical analyses coupled with the recent small-area junction observation of IETS by Gregory suggest that IETS with the STM should be

straight forward if an appropriately structured tip is used. Studies aimed at demonstrating IETS with the STM should be directed at the simplest possible systems embodying the essential physics such as hydrogen and deuterium terminated metal surfaces. An ultrastable cryogenic STM operating under UHV should be used to eliminate vibration and contamination mediated interference with the measurements. Inert tip materials such as gold or platinum cleaned *in situ* seem most likely to produce positive results.

Tunneling Spectroscopy of Superconducting Lead Thin Films

Measurement of superconductor current vs. voltage (I vs. V) and conductance vs. voltage (G vs. V) curves with the STM is an important first step toward IETS with the STM. Detection of the superconducting energy gap in I vs. V curves demonstrates that the instrument is capable of high-resolution spectroscopic measurements. Small ~5% changes in conductance associated with phonons in superconducting lead provide an intermediate test signal before detection of the < 1% changes expected for IETS is attempted.

Background

The first STM measurement of the superconducting energy gap was reported in 1984 for Nb_3Sn.[20] The I vs. V curves showed considerable distortion.[21] NbN has been studied with the STM by a number of groups. Marti *et al.* found no indication of an energy gap in their I vs. V spectra.[22] Kirtley *et al.* found both normal and superconducting regions and plotted images of gap variation as a function of tip position; features in their topographic images often correlated with features in their gap images.[23]

LeDuc *et al.* reported that the superconducting energy gap was "always observed" at low tunnel currents.[24] While spectra obtained at high resistance were in good agreement with the BCS (Bardeen-Cooper-Schrieffer) predictions, they saw distortion when tunnel resistance less than 10^7 ohms was used. Similar results were presented for lead and a lead-bismuth alloy. Numerous groups have reported using the STM for spectroscopy of "high T_c" superconductors. The first two reports for measurements on $La_{2-x}Sr_xCuO_{4-y}$ are representative.[25]

Experimental

The data presented here were obtained using a low-temperature scanning tunneling microscope developed at the NASA Jet Propulsion Laboratory by H. G. LeDuc and W. J. Kaiser. The design is similar to the piezo-bimorph STM described in Chapter 2 and was based on one that has been used for room temperature work.[26] Since small changes in the current must be detected, it is important that the instrument be as stable as possible. The instrument was designed to reject vibrational noise through its compact size and rigidity; it can be operated with no external vibration isolation at both room and low temperatures. The instrument is small enough to fit through the neck of a standard liquid helium storage Dewär and is operated while immersed in liquid helium so that the temperature is stable at 4.2 K. For these experiments the Dewär was supported on an air table to assure minimal interference from vibration noise down to 1 hertz.

In order to meet the specialized demands of superconductor energy gap spectroscopy, the operating mode for this work was different from that

used in normal imaging studies. The voltage applied at the tip was a triangle wave or sine wave with a typical frequency between 5 and 500 hertz and a peak-to-peak amplitude between 5 and 50 millivolts. The dynamic tunneling resistance (rather than the tunneling current) was held constant throughout the spectroscopy measurements through feedback control of the tip height. The dynamic resistance was usually chosen to be between 10^7 and 10^9 ohms resulting in current amplitudes ranging from 20 pA to 2 nA. The current as a function of bias voltage was monitored continuously on an x-y oscilloscope for visual analysis of tunneling conditions and ease of STM adjustment. The current through a 10^6 ohm resistor in series with the sample was detected with a low noise liquid helium cooled preamplifier placed in close proximity to the sample.

The spectral data were stored digitally with a Nicolet 370 signal averager, and successive spectra were averaged to give an acceptable signal to noise ratio. The derivative of the tunneling current with respect to the bias voltage, dI/dV, was detected directly using a lock-in amplifier and a ~1 mV sinusoidal modulation superposed on the bias voltage. Noise reduction was accomplished through signal averaging rather than with a large time constant at the lock-in amplifier so that feedback controlled tunneling could be maintained with an alternating tunnel current.

The ~300 nm thick films were prepared by evaporation of 99.999% Pb onto glass or silicon substrates in an oil diffusion-pumped chamber at ~3×10^{-6} torr. In the best circumstances the samples were mounted on the STM immediately after deposition and immersed in liquid helium with less than

ten minutes of air exposure. However, some films gave satisfactory spectra after having been stored for several hours in a desiccator. Mechanically cut gold tips were used for all of the work presented here.

Results

Topographic images of an evaporated lead film sample are shown in Figure 3.1. Both images were scanned with a constant tunneling resistance of approximately 2×10^8 ohms. The bias voltage was a 20 mV p-p triangle wave at 200 Hz. The top image shows a 640 x 900 Å region with roughness on the scale of 75-150 Å. The bottom image is a 270 x 320 Å subarea scanned at higher magnification. The z-scale was not calibrated. The 'hillock' morphology was typical of all of the evaporated films imaged.

While symmetric I vs. V spectra were obtained with ac bias frequencies ranging from 10 to 500 hertz, considerable distortion occurred in dI/dV vs. V spectra obtained with frequencies greater than about 15 hertz. A typical I vs. V curve is shown in Figure 3.2. This 40 mV p-p spectrum was obtained at 20 hertz with a 2×10^8 ohm tunnel resistance; both directions of the voltage sweep are shown. The hysteresis is due to the parasitic capacitance inevitably present in the system. The shape is that expected for a normal metal-insulator-superconductor tunnel (NIS) junction. Fitting to the BCS density of states[27] gives $\Delta = 1.28$ meV. Using the fit at 4.2 K together with the normalized temperature dependence of the energy gap measured by Adler[28] gives the zero temperature gap parameter $\Delta_0 = 1.36$ meV which is within the range observed for lead.[29] The theoretical curve is shown in the figure

displaced for clarity. Similar spectra have been reproducibly obtained at a variety of gap resistances from 10^7 - 10^9 ohms.

On several occasions, I vs. V curves like the one shown in Figure 3.3 were observed. The gap is wider and flatter than that in Figure 3.2. Its character is suggestive of superconductor-insulator-superconductor (SIS) tunneling. The "flat gap" spectra were most often observed immediately after manual tip-sample approach or periods of instability. Tip-sample contact may occur under these conditions with concomitant transfer of lead from the surface to the probe tip.

An STM conductance spectrum (dI/dV vs. V) is shown in Figure 3.4. The structure in these spectra is qualitatively similar to that observed in MIM junctions and is assigned to the effective phonon spectrum of lead. The conductance spectrum of a lead-alumina-aluminum planar tunnel junction at 4.2 K is included for comparison (courtesy of R. C. Jaklevic). The correlation of the features is readily apparent. The lead phonon energies are 4.5 and 8.5 millivolts measured from the gap edge; the tunneling density of states (and hence the conductance) is reduced at phonon energies . This data represents the first detection of superconductor phonons with an STM and is one of the most sensitive tunneling spectroscopy measurements made with an STM to date. The change in conductance associated with the lead phonons is approximately five percent.

Successful detection of the phonon effects in the superconductor tunneling density of states of lead is a first step in investigating the feasibility of using an STM for inelastic electron tunneling spectroscopy (IETS). The

conductance changes due to the largest inelastic tunneling peaks in IETS are on the order of one percent in the MIM junction and, as will be discussed below, are predicted to be of the same order in the scanning tunneling microscope.

Figures -- Chapter 3

Figure 3.1. STM images of evaporated lead films obtained at 4.2 K. (20 mV p-p triangle wave sample bias, 200 Hz, $2x10^8$ ohms constant resistance.)

Figure 3.1

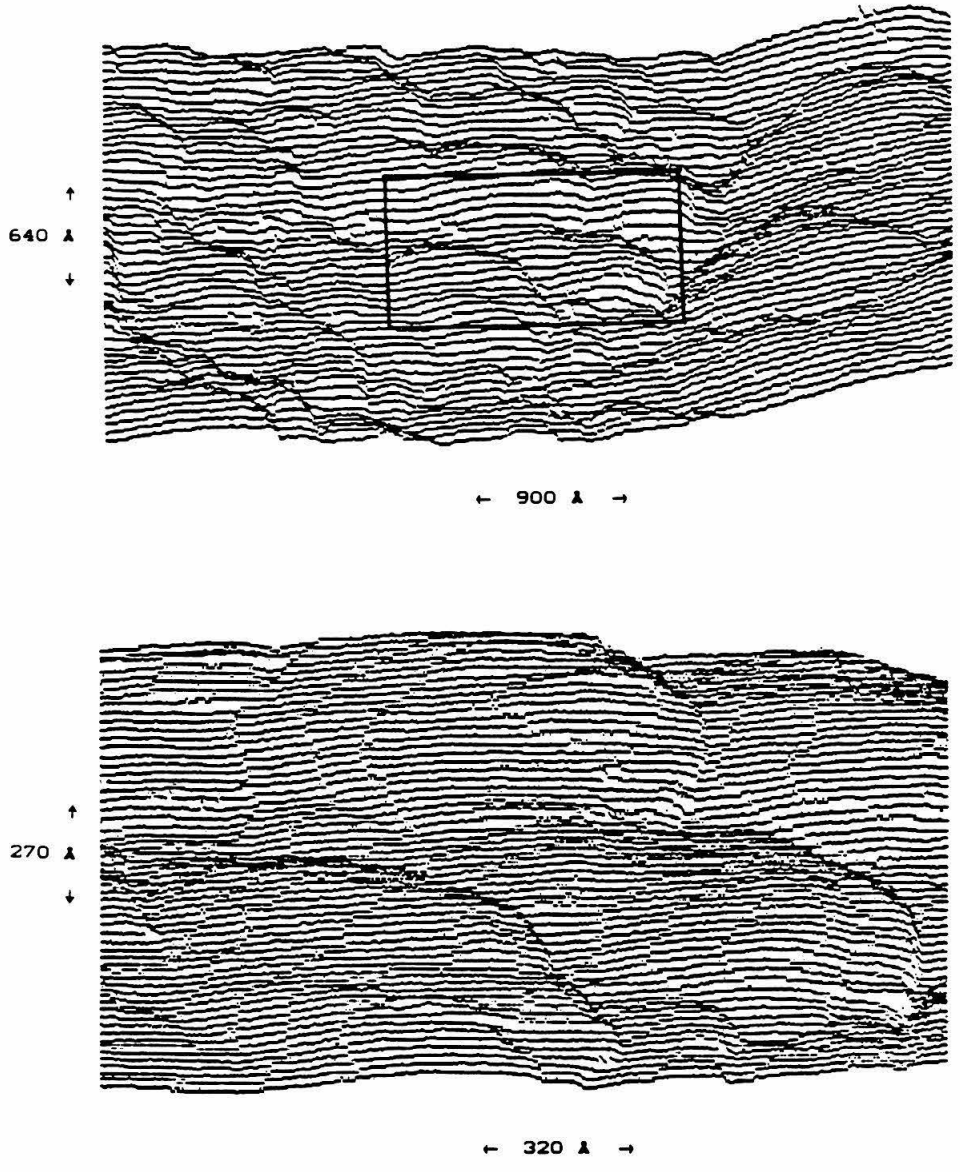

Figure 3.2. Energy gap tunneling spectrum of lead obtained at 4.2 K with an STM at $>10^8$ ohms. The best fit using BCS theory is shown displaced for clarity.

Figure 3.2

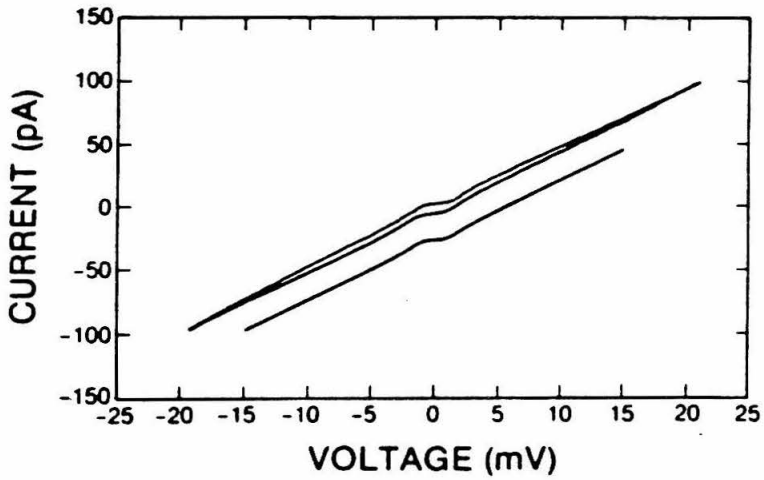
150
100
50
0
-50
-100
-150
CURRENT (pA)
-25 -20 -15 -10 -5 0 5 10 15 20 25
VOLTAGE (mV)

Figure 3.3. Double-gap tunneling spectrum of lead obtained at 4.2 K with an STM at 4×10^7 ohms.

Figure 3.3

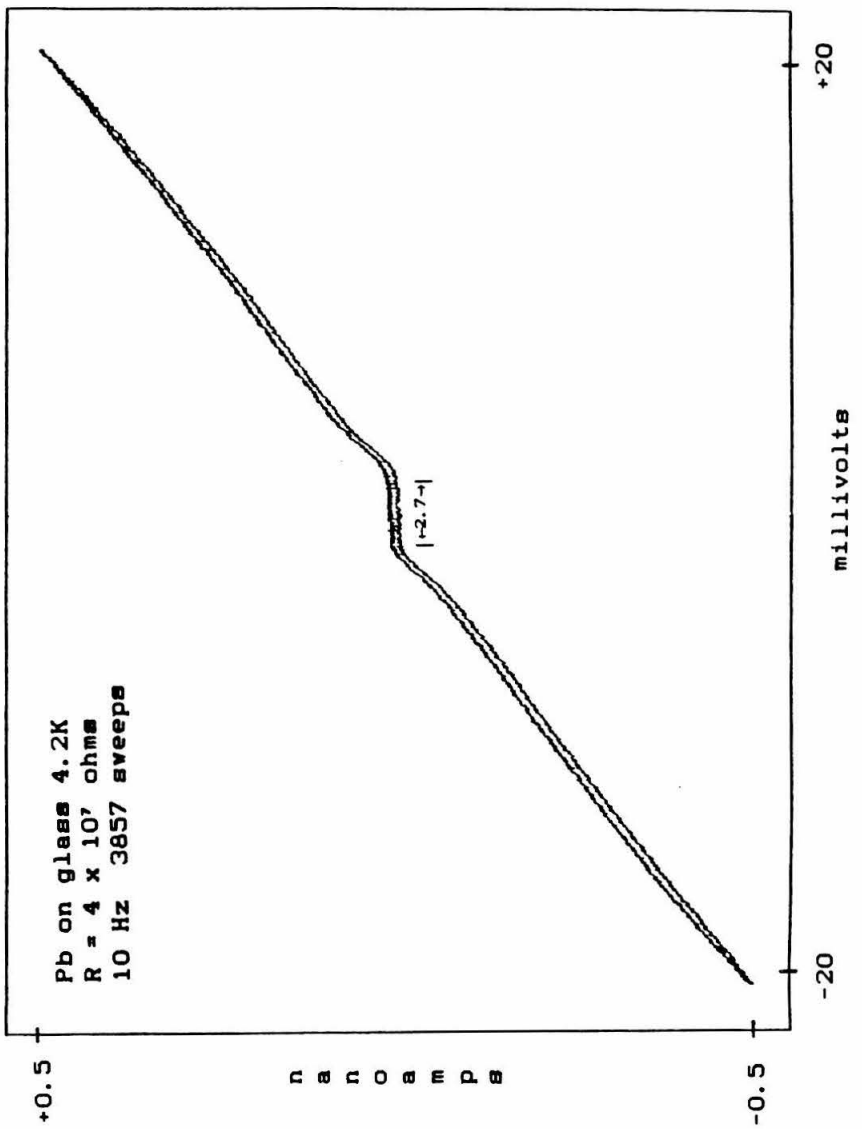
Pb on glass 4.2K
R = 4 x 10' ohms
10 Hz 3857 sweeps
|-2.7-|
+0.5
nanoamps
-0.5
-20
millivolts
+20

Figure 3.4. Phonon spectra of lead obtained at 4.2 K with at 10^8 ohm with an STM (upper curve) and with an aluminum-aluminum oxide-lead (MIM) junction (lower curve). The arrows indicate features associated with the transverse (left arrow) and longitudinal (right arrow) peaks in the phonon density of states which appear as inflections in the slope of the conductance curve.

Figure 3.4

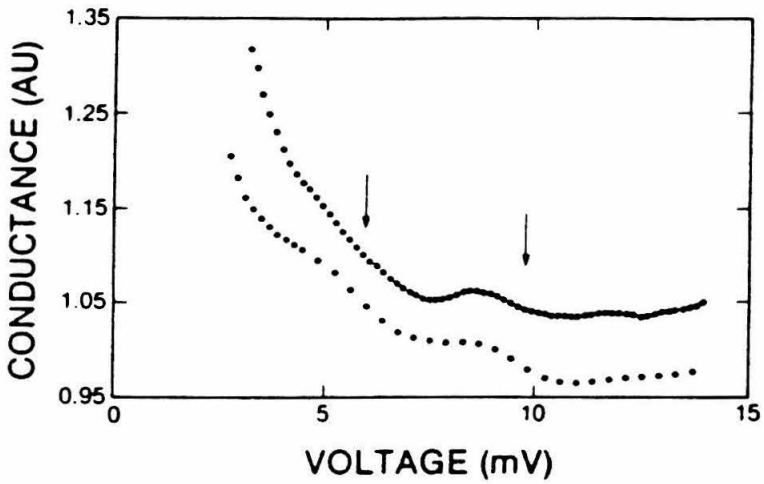

References

1. E. L. Wolf, Principles of Electron Tunneling Spectroscopy, Oxford University Press, New York 1985.
2. Tunneling Spectroscopy, P. K. Hansma, ed., Plenum, New York 1982.
3. Vibrational Spectroscopy of Molecules on Surfaces, J. T. Yates and T. E. Madey, eds., Plenum (NY), 1987.
4. J. Lambe and R. C. Jaklevic, *Phys. Rev.* **165,** 821 (1968).
5. R. C. Jaklevic and J. Lambe, *Phys. Rev. Lett.* **17,** 1139 (1966).
6. R. M. Kroeker and P. K. Hansma, *Surf. Sci,* **67,** 362 (1977).
7 R. C. Jaklevic, private communication.
8. J. Klein, A. Leger, M. Belin, D. Deforneau, and M. J. L. Sangster, *Phys. Rev. B* **7,** 2336 (1973).
9. P. K. Hansma, *IBM J. Res. Dev.* **30,** 370 (1986).
10. B. N. J. Persson and J. E. Demuth, *Sol. State Comm.* **57,** 760 (1986).
11. R. Kroeker, W. C. Kaska, and P. K. Hansma, *J. Catal.* **57,** 72 (1979).
12. G. Binnig, N. Garcia, and H. Rohrer, *Phys. Rev. B* **32,** 1336 (1985).
13. B. N. J. Persson and A. Baratoff, *Phys. Rev. Lett.* **59,** 339 (1987).
14. M. A. Gata, "Vibrational spectroscopy of adsorbates in tunneling microscopy," Ph.D. thesis, University of Texas, Austin, (1990).
15. S. Gregory, *Phys. Rev. Lett.* **64** , 689 (1990).
16. D. P. E. Smith, M. D. Kirk, and C. F. Quate, *J. Chem. Phys.* **86,** 6034 (1987).
17. J. Kirtley and P. Soven, *Phys. Rev. B* **19,** 1812 (1979).
18. P. S. Weiss and D. M. Eigler, private communication.
19. R. Wilkins, M. Amman, E. Ben-Jacob, and R. C. Jaklevic, *J. Vac. Sci. Technol. B* **9,** 996-999 (1991).
20. S. A. Elrod, A. L. de Lozanne, and C. F. Quate, *Appl. Phys. Lett.* **45,** 1240 (1984).
21. S. A. Elrod, A. Bryant, A. L. de Lozanne, S. Park, D. Smith, and C. F. Quate, *IBM J. Res. Develop.* **30,** 387 (1986).
22. O. Marti, G. Binnig, H. Rohrer, and H. Salemink, *Surface Sci.* **181,** 230 (1987).

23. J. R. Kirtley, S. I. Raider, R. M. Feenstra, and A. P. Fein, *Appl. Phys. Lett.* **50,** 1607 (1987).
24. H. G. LeDuc, W. J. Kaiser, and J. A. Stern, *Appl. Phys., Lett.* **50,** 1921 (1987).
25. S. Pan, K. W. Ng, A. L. de Lozanne, J. M. Tarascon, and L. H. Greene, *Phys. Rev. B* **35,** 7220 (1987).
J. R. Kirtley, C. C. Tsuei, S. I. Park, C. C. Chi, J. Rozen, and M. W. Shafer, *Phys. Rev. B* **35,** 7216 (1987).
26. W. J. Kaiser and R. C. Jaklevic, *Rev. Sci. Instrum.* **59,** 537 (1988).
27. S. Shapiro, P. H. Smith, J. Nicol, J. L. Miles, and P. F. Strong, *IBM J. Res. Develop.* **6,** 34 (1962).
28. J. G. Adler and T. T. Chen, *Solid State Commun.* **9,** 1961 (1971).
29. W. L. McMillan and J. M. Rowell, *Phys. Rev. Lett.* **14,** 108 (1965).

Chapter 4: Tunneling Microscopy and Spectroscopy of MoS_2: Observation of Negative Differential Resistance

Introduction

Negative Differential Resistance (NDR), the phenomenon of decreasing electron transmission probability with increasing voltage, occurs in a variety of devices and can be caused by vastly different mechanisms. It was first detected in the Esaki tunnel diode in which the electron tunneling probability abruptly decreases as filled states above the forbidden gap in degenerately doped n-type material begin to overlap the forbidden energy gap of degenerate p-type material.[1] In a similar way, tunneling probability can decrease as electron energy increases in double-barrier resonant tunneling or quantum well structures due to interference of electron wave functions.[2] Gunn diodes have NDR because two conduction bands with different carrier mobilities exist; current can decrease as carriers are excited into the upper band which has lower mobility. An analogous conducting phase separation has been suggested for other systems.[3] MS and MIS structures can have NDR as a result of inhomogeneous doping,[4] minority-carrier accumulation,[5] bias-dependent barrier height,[6] or charge trapping defect states.[7] This survey suggests that the occurrence of NDR under certain conditions in the scanning tunneling microscope (STM) should not be surprising.

NDR in current-voltage spectra obtained with a scanning tunneling microscope has already been reported for several systems. NDR in STM I vs. V curves obtained on mildly oxidized silicon has been attributed to charging of electron traps lying well above the Fermi level.[8] Two groups have observed NDR over boron atoms adsorbed on silicon;[9,10] it is thought to arise from localized surface states together with an electronically structured tip

(which has a non-linear density of electronic states as a function of energy) which cause an Esaki diode type tunneling behavior. In a similar way, NDR commonly occurs over adatoms on the clean Si(111) 7x7 surface when the tip becomes electronically structured due to contamination.[11] In all of these systems, the NDR effect has been confined to small areas less than a nanometer in diameter. Here, I vs. V curves obtained with an STM on molybdenum disulfide (*2H* MoS_2) are presented; nonlocalized NDR which may result from a different mechanism than has been previously reported for NDR in STM current-voltage spectra is shown.

Experimental

The scanning tunneling microscope used in this work is described in Appendix B as the "Kramar UHV STM System." It is a tripod-and-louse type instrument similar to the IBM "pocket" STM[12,13] which operates in an ultrahigh vacuum (UHV) chamber attached to a separate sample preparation chamber with a load-lock; tips and samples can be mounted *in vacuo.* The STM is interfaced to an 80286-based personal computer for data acquisition and instrument control. It has proven sufficiently stable to achieve ~0.01 Å vertical resolution on cleaved gallium arsenide surfaces.[14]

The sample studied was a mineralogical crystal of molybdenum disulfide, *2H*-MoS_2.[12] *2H*-MoS_2 is a layered semiconductor. Its structure is shown in Figure 4.1; it was the first X-ray crystal structure solved by Linus Pauling at Caltech in 1923.[15] Six sulfur atoms are associated with each molybdenum atom in a trigonal bipyramidal arrangement. The trigonal

bipyramids form sheets three atom layers thick which are bound to adjacent sheets via weak van der Waals interactions. The basal plane, seen from the STM point of view, has three structurally and electronically distinct translationally related centered hexagonal arrays -- holes extending through the crystal, sulfur atoms in the surface plane, and molybdenum atoms 1.5Å below the surface plane.

The crystal class of other crystals from the same source was verified by X-ray diffraction.[12] The four-probe van der Pauw method gave the overall character of the sample as n-type with a doping level of 8.9×10^{16} cm^{-3}; Metal - n-type current vs. voltage behavior (rectification with current flowing predominantly with the sample negative) would be observed in macroscopic tunnel junctions made from these samples. Because of the sample's mineralogical origin, small area measurements such as those made with the scanning tunneling microscope may be expected to show considerable variation. Indeed, doping inhomogeneity on a micron scale has been inferred from small-spot X-ray photoelectron spectroscopy on a similar sample.[16] For STM, the crystal was mounted on a stainless steel support with indium solder, cleaved with adhesive tape under nitrogen flow in the load-lock of the STM system, and introduced to the STM operating at $\sim 5 \times 10^{-11}$ torr. The tips used were tungsten, electrochemically etched in 2M KOH at 6V ac and rinsed with ethanol.

For each of the images shown, the sample bias was -0.75 V and the current set point was 1.0 nA. Spectroscopy measurements were open-loop; feedback control of the tip height was disabled for <50 ms using a gated

integrator. For a typical spectrum, current was digitized at fifty voltage values in each ramp direction. I vs. V curves were acquired in one of two modes, either signal-averaged or collected singly. The signal-averaged curves typically summed 500 curves into one spectrum. The time required for acquisition of the averaged curves was tens of seconds, so drift of the sample relative to the tip probably caused spatial averaging on the scale of the unit cell. The single I vs. V curves were correlated with image pixels using the Current Imaging Tunneling Spectroscopy (CITS) method of Hamers, Tromp and Demuth.[17] This approach allowed post-acquisition averaging of I vs. V curves from surface sites sharing the same unit cell position.

Results and Discussion

Imaging

Atom-resolved images of the cleavage surface of *2H*-MoS_2 were obtained in three different imaging modes and are shown in Figure 4.2. The 3-D projection in Figure 4.2a shows a ~12 Å square 'constant height' image of current variation (~15% of the 1 nA average) with 125 data pixels in each direction. Acquisition time was 1.5 seconds. The brightness was keyed to -dz/dx for simulated lighting. This image shows two displaced centered hexagonal arrays of maxima *suggesting* that the two chemically distinct surface species, Mo and S, have been resolved. An alternative explanation for a displaced hexagonal array is a multiple tunneling-point tip. Because this same spatial relationship in MoS_2 images is often observed, it seems likely that both atom types are imaged. A less sharp tip would resolve only one

site.[12,18] (If one of the displaced arrays arises from a second tunneling point on the tip, the spatial relationship may be expected to vary from one tip to another).

A constant current topographic image of the z-piezo voltage is shown in Figure 4.2b. It is ~23Å square and has a 0.5Å corrugation. Acquisition time for the 475 x 100 pixel image was longer than 5 minutes, and some distortion due to sample drift is apparent. This image shows only one site, consistent with a comparatively broad tip.

Figure 4.2c is a 'barrier height' image acquired simultaneously with the topographic image shown in Figure 4.2b and shows variations in $d(ln\ i)/ds$, the effective local barrier height. It was acquired by modulating sinusoidally the tip-sample separation 0.2Å p-p at 1 kHz and detecting the component of the logarithmic current at that frequency with a lock-in amplifier.

Images of MoS_2 obtained in the current-variation and topographic imaging modes have been previously shown by others.[19] Images of this surface acquired in the barrier-height imaging mode have not previously been reported. The $d(ln\ i)/ds$ mode is inherently quieter than the topographic mode; the measurement bandwidth is narrowed using a lock-in amplifier, and the frequency can be chosen to be at a relatively quiet part of the tunneling current frequency spectrum. Because the local effective work function is related to the chemical nature of the surface, barrier height images may reveal compositional information complementary to that obtained from density of states variations associated with state-localization and observed at different bias voltages.

Spectroscopy

The initial stage of this work was a systematic survey of the MoS_2 surface in which a standard series of images and signal-averaged I vs. V curves was obtained at ~ 1 micron intervals. Most of the I vs. V series acquired in this survey were self-consistent and showed essentially symmetric non-rectified I vs. V character. Changes in I vs. V character (degree of rectification) did not appear strongly correlated with the surface topography; in most cases the imaged areas were atomically flat. Sarid *et al.* conducted a cursory spectroscopic investigation of MoS_2 with an STM operating in air and obtained similar results.[19] Kramar *et al.* conducted a more extensive UHV STM imaging and spectroscopy study of mineralogical MoS_2 and found great variability in the degree of rectification and character of current-voltage spectra; this was attributed to doping inhomogeneity.[12]

In several of the I vs. V series, some of the curves exhibited a current peak, *i.e.*, negative differential resistance, in the negative sample bias regime. A subset of curves from one such series is shown in Figure 4.3. Two of the curves have broad negative peaks in the current at about -0.6 V sample bias. Spectra with the same parameters obtained later in this series (also shown) did not show the peaks. In other series, early I vs. V curves did not show NDR, but later spectra did. In every case that NDR was observed, it was present when the tip-sample separation was defined by a -1.5 or -0.75 V sample bias at 1 nA but not when the sample bias was -3.0 V or when it was positive.

One possible explanation for the transient nature of the NDR was that during the course of the I vs. V series, the tip may have drifted from one electronically distinct site on the surface to another. To test this hypothesis, CITS was used to obtain images with pixel-correlated I vs. V curves. The sample bias during feedback control to 1 nA was set at -1.5 V, the bias at which the strongest NDR had been observed. Several images were obtained which had I vs. V curves exhibiting NDR. In all but one case, each I vs. V curve throughout the ~25 Å square images showed the effect, indicating that it is not highly localized and that changes in surface site probably do not cause the drastic changes observed in the I vs. V series. In an exceptional case, the character of the image changed from featureless to showing atomic periodicity, a change associated with a change in tip morphology. The I vs. V character changed from NDR to p-type rectified, and the 'knee' at positive bias shifted to a lower energy at the same site. The latter observation suggests that the appearance of NDR is intimately associated with the structure of the tip. Single I vs. V curves from before and after the 'tip change' are shown in Figure 4.4.

None of the CITS images showing NDR had high quality atomic resolution, although some did show sufficient periodicity to define a unit cell. I vs. V curves from similar sites in one such image were averaged in order to assess the degree of correlation between I vs. V character and surface site. Figure 4.5 shows I vs. V curves averaged for topographic maxima (atoms), topographic minima (holes), and the entire image. The I vs. V curves over maxima and minima are nearly identical, while the surface averaged I vs. V

curve has a greater current magnitude than the others above -1.25 V. All show *two* weak NDR peaks.

Possible Mechanisms of NDR

A mechanism is needed which explains the observation of (a) non-localized NDR, (b) occurrence when tunneling from the sample to the tip, and (c) occasional multiple NDR peaks. It should also accommodate the transient appearance of the effect. The two mechanisms already cited in STM may be applicable to this system. In addition, another which might be expected to cause NDR under similar conditions is discussed.

The NDR mechanism invoked by Hamers and Koch[8] requires localized electron trapping states lying well above the Fermi level of, in this case, the tip. As the bias is increased (as the sample is made more negative), the tunneling current also increases until electrons have sufficient energy to occupy the traps. The additional electrostatic potential due to charged traps increases the tunneling barrier, so the tunneling current is reduced until the bias is raised sufficiently to overcome the barrier. Such traps may exist if the tip is oxide (or otherwise) contaminated. Trapping sites at different energies could result in more than one NDR region in the I vs. V curve. Since tip structure would be the sole cause of the effect, no surface-site localization is expected, as is the case here; indeed, similar effects should be observed with other sample systems unless the tip-contamination required is sample-specific.

Lyo and Avouris[10] and Bedrossian *et al.*[9] adopted a mechanism similar to that active in the Esaki diode. It requires peaks in the energy density of states (DOS) of the tip and sample such that tunneling probability increases, decreases, and subsequently increases as the bias is increased. A computer simulation (see Figure 4.6) of current-voltage spectra expected for a given sample and tip DOS showed that spectra very similar to those presented here can occur if DOS maxima exist slightly below and above the Fermi levels of the sample and tip, respectively.[10] This may be possible in the MoS_2 system. Angle resolved photoemission studies have shown that there is a strong peak at the top of the valence band, presumably due to the non-bonding $4dz^2$ orbitals of Mo.[20] The tip electronic structure may, as Lyo and Avouris suggested, be the consequence of a weakly bound tip apex and adsorption induced resonances. Alternatively, it may be caused by contamination. A likely tip contaminant is sulfur; Zabinski and Tatarchuk reported an excess of sulfur at the MoS_2 cleavage surface.[21] In this case, rather than a maximum in the tip density of states, a reduction may occur. Lang has predicted that adsorbed sulfur will reduce the number of metal states available for tunneling near energies corresponding to NDR peaks in the I vs. V spectra shown here.[22] Differences in local sample doping level and the strength of the tip-adsorbate interaction could explain the variability in position and number of NDR regions.

The negative differential resistance observed in STM of MoS_2 can be adequately explained by either of the two mechanisms described above. Nevertheless, another interesting possibility deserves mention. MoS_2 has only weak van der Waals interaction between dichalcogenide layers such that

intra-crystal layer separation is likely to occur. Cleaving damage may result in loose flakes or buckling opening a vacuum gap between layers which may, in conjunction with the tip-sample barrier, give rise to a double-barrier resonant tunneling structure. If this happens, a peak in tunneling probability should occur at each energy corresponding to an allowed state in the intervening quantum well. For the simplest case the well width would be $\lambda/2n$ where λ is the electron wavelength. In the case of a single layer of MoS_2 the well would be ~ 6 Å wide. The De Broglie relation predicts that the first NDR peak would occur at ~ 1 eV, reasonable for observation in an STM experiment and consistent with the data presented here. In practice, the actual energy of the maximum tunneling probability would depend on the shapes and widths of the two tunneling barriers. If these conditions existed in the course of these measurements, they could account for the observation of NDR in only a narrow feedback voltage range, as was seen here; the width of the first barrier (tip-sample separation) is determined by this parameter. The other two mechanisms do not offer an obvious explanation for this aspect of the data. It is suggested that if layer separation occurs, a resonant tunneling condition detectable by STM could exist, but a more thorough analysis is required before this mechanism's merit can be adequately assessed.

Summary

A systematic imaging and spectroscopy study of the MoS_2 surface was conducted using a scanning tunneling microscope operating in ultrahigh vacuum. Atom-resolved images acquired in barrier height, topographic, and current imaging modes, as well as current-voltage spectra showing one or

more negative differential resistance regions were presented. The effect was shown to be non-localized, unlike prior STM observations of NDR. The mechanism causing the NDR cannot be conclusively determined, but the most likely is contamination-induced electronic structure in the tip density of states. The applicability of mechanisms invoked by other authors was assessed, and another mechanism that would lead to NDR in STM of MoS_2, double-barrier resonant tunneling, was proposed.

Figures -- Chapter 4

Figure 4.1. Schematic of the $2H$-MoS_2 crystal structure. The unit cell is indicated by the dotted lines.

Figure 4.1

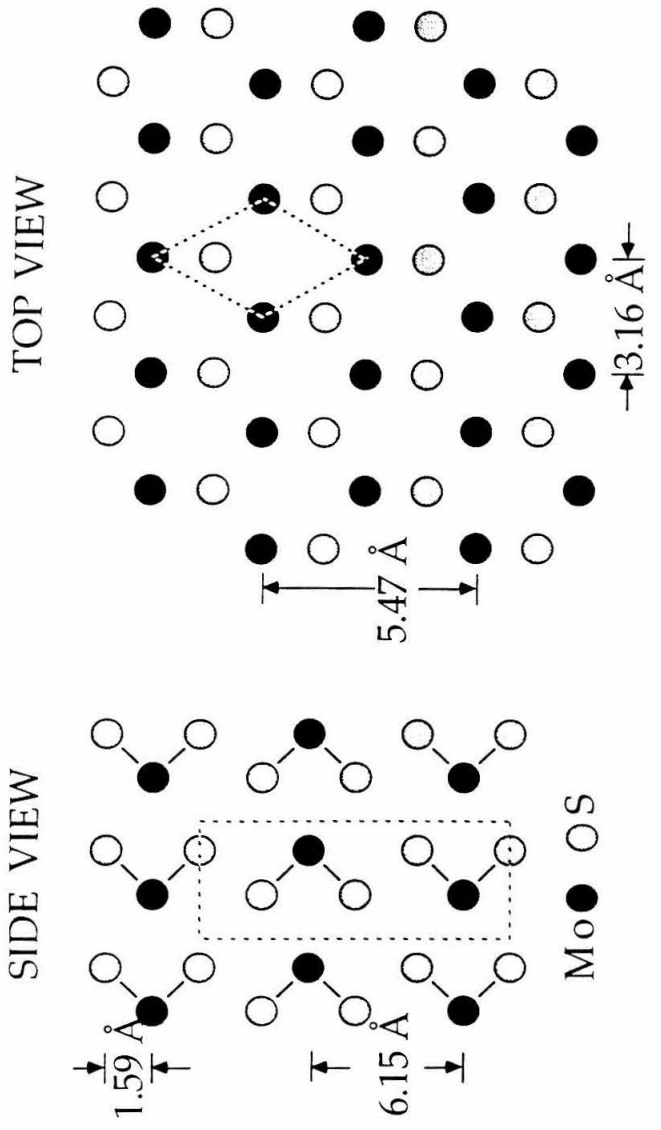

Figure 4.2. STM images of molybdenum disulfide obtained in three contrast modes.

(a) current variation at constant z

(b) z variation at constant current

(c) barrier height variation at constant current

Figure 4.2a

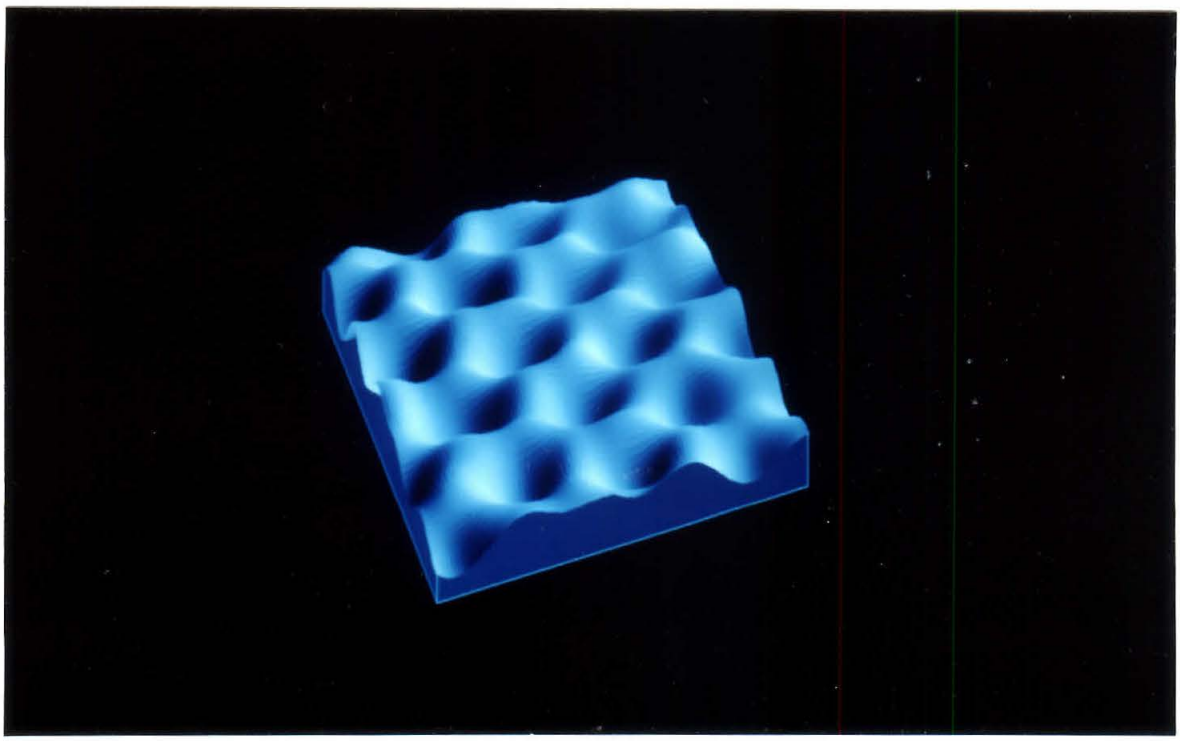

Figure 4.2b

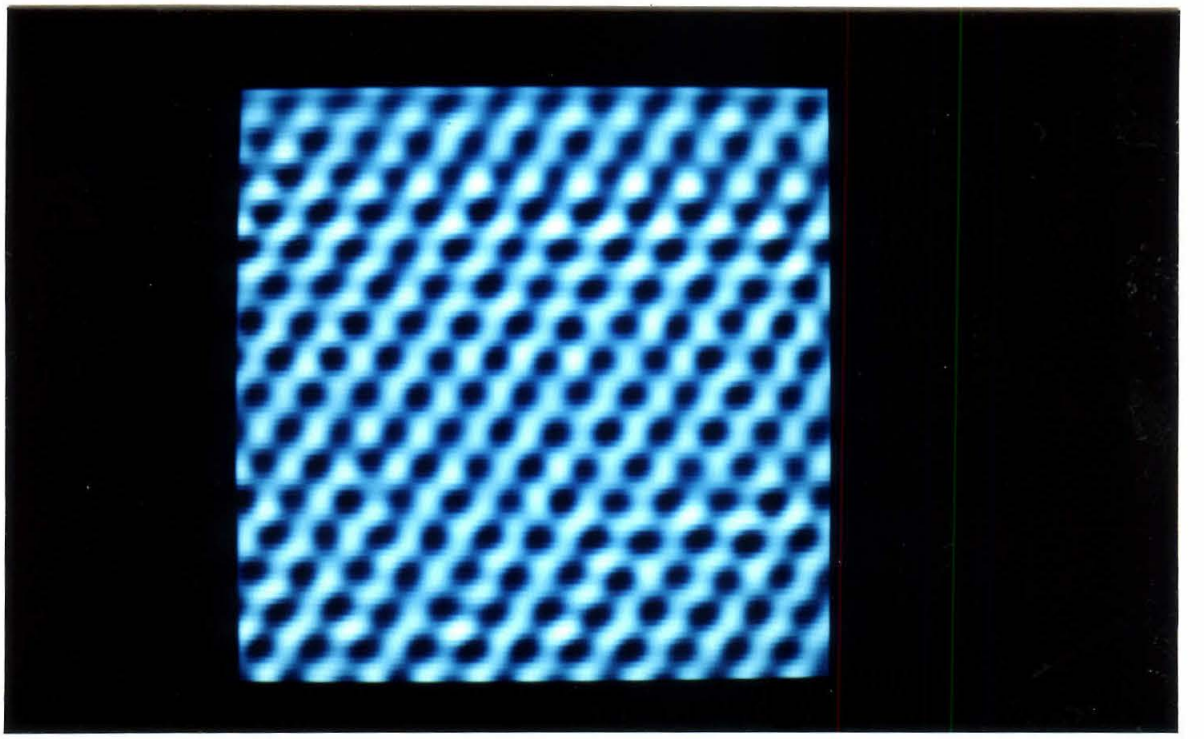

Figure 4.2c

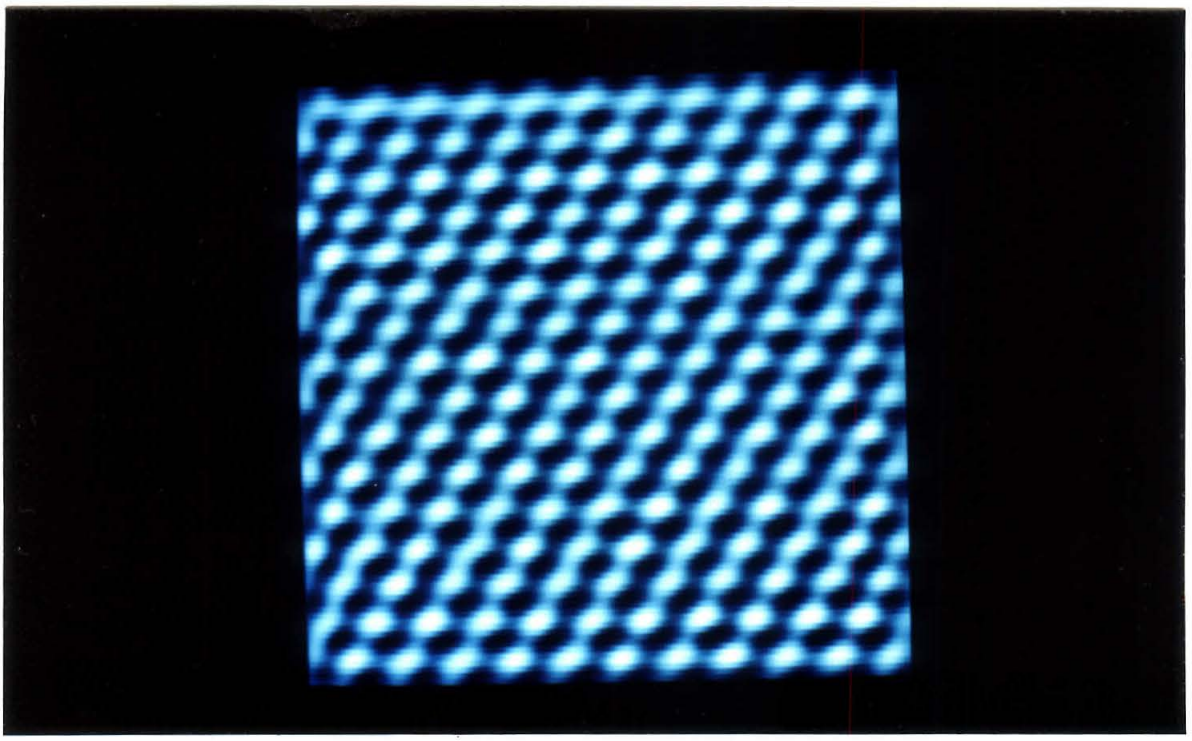

Figure 4.3. I vs. V spectra with and without NDR. Two curves show negative differential resistance, while two others obtained later in the same series with identical parameters do not.

Figure 4.3

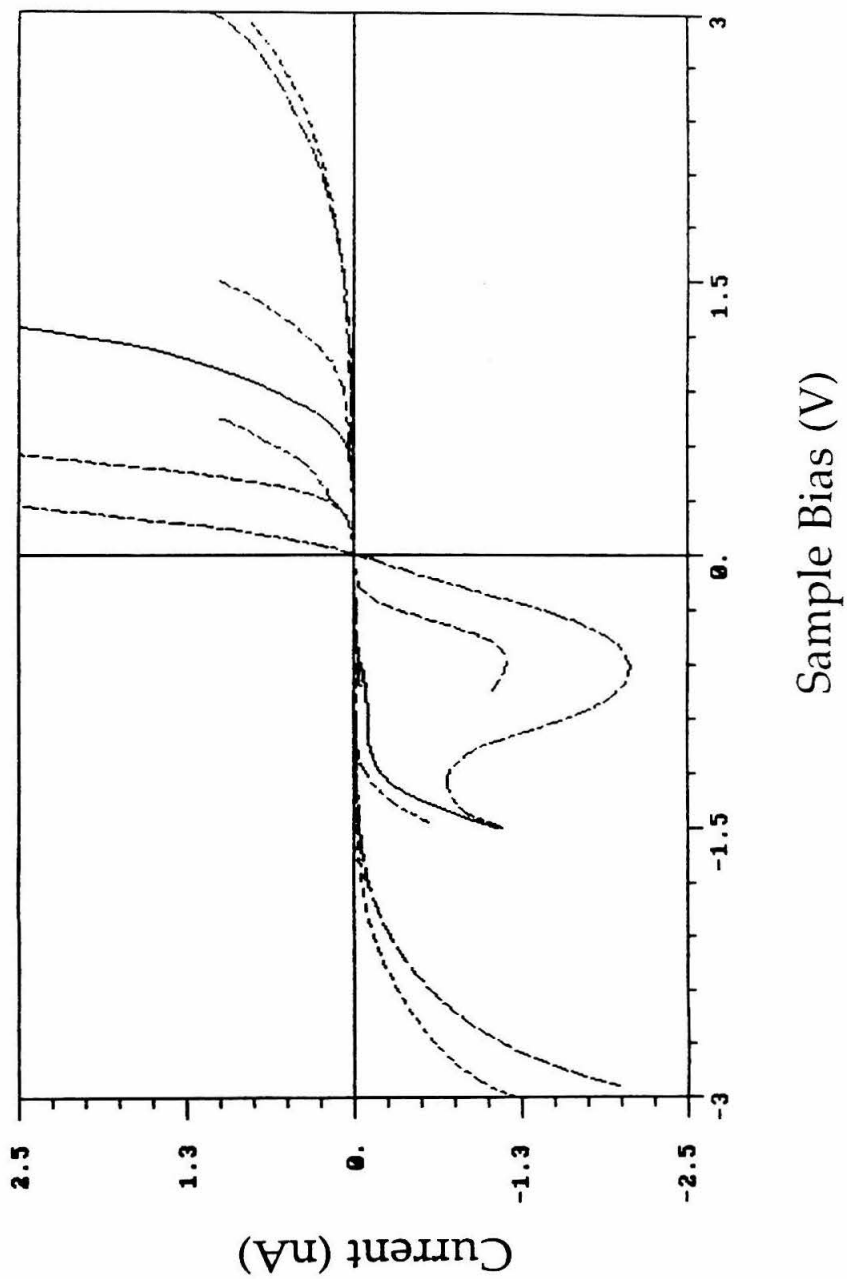

Figure 4.4. I vs. V spectra from a CITS image showing NDR before a change in image character (probably due to a tip change) and not showing NDR after the change.

Figure 4.4

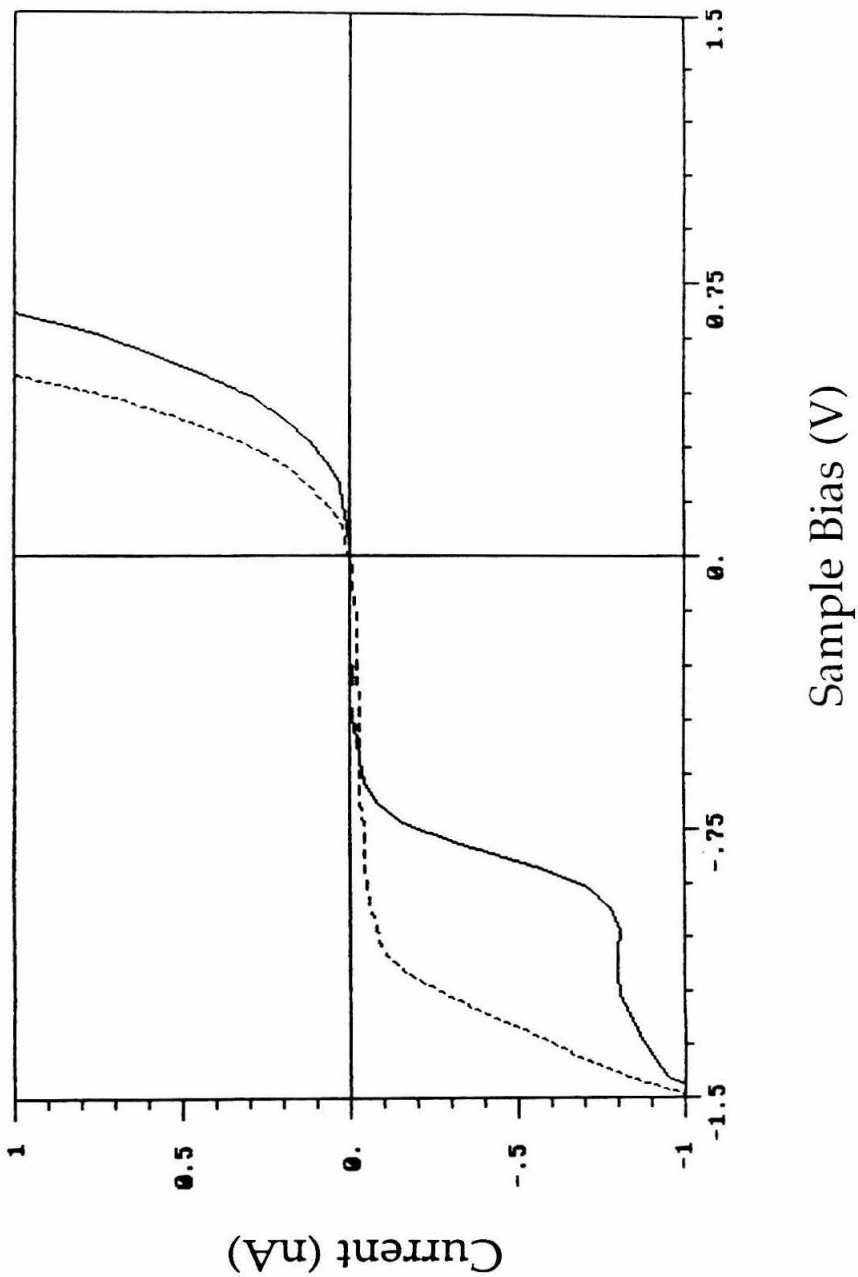

Figure 4.5. Site-averaged I vs. V spectra from a CITS image. Those obtained at topographic maxima are nearly identical to those obtained at topographic minima, while the surface averaged curve has a greater current magnitude. All show two weak NDR regions.

Figure 4.5

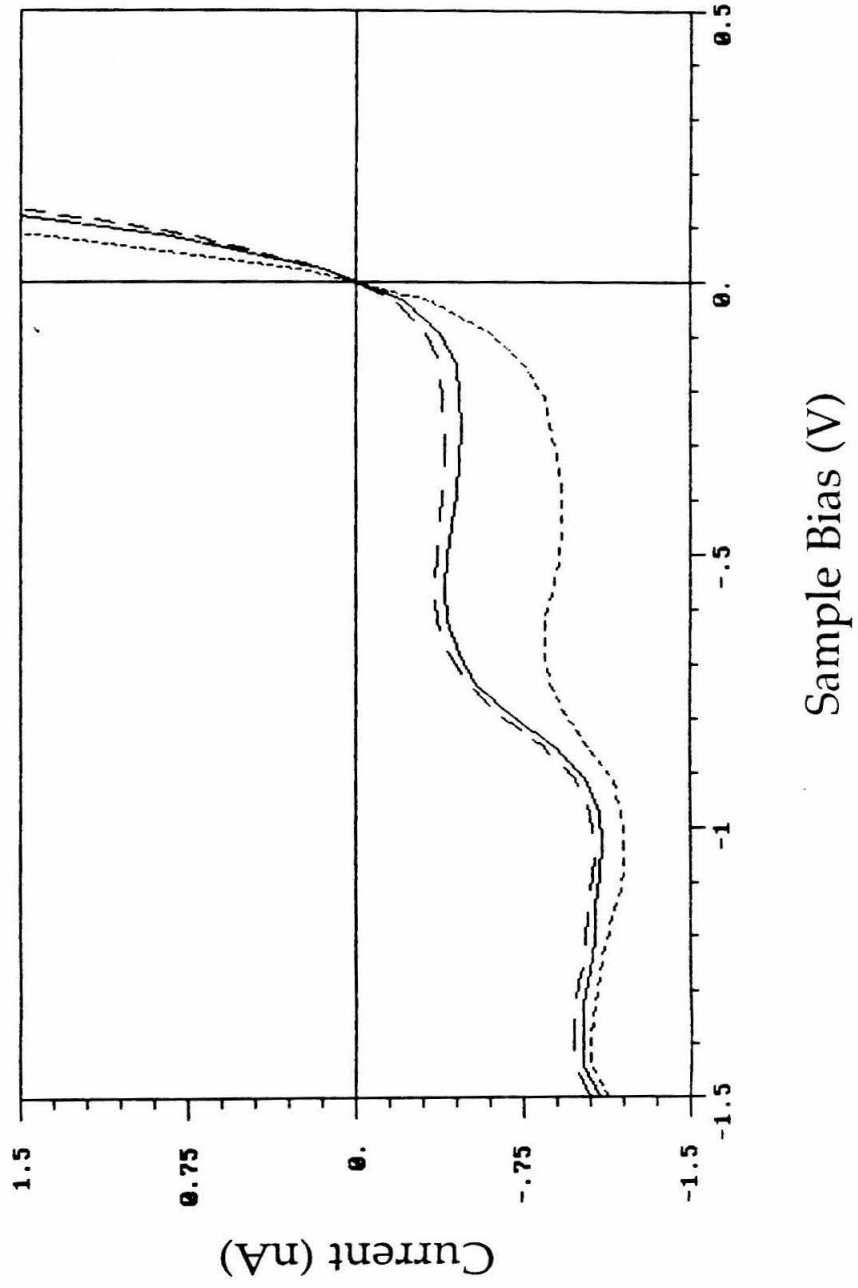

Figure 4.6. Computer simulations of NDR in the STM due to sample and tip electronic structure. The electronic density of states (DOS) for three localized states of sample and tip are shown on the left, and associated I vs. V characteristics are shown on the right. The DOS in (a) gives I vs. V curves much like those obtained in the measurements presented here.[10]

Figure 4.6

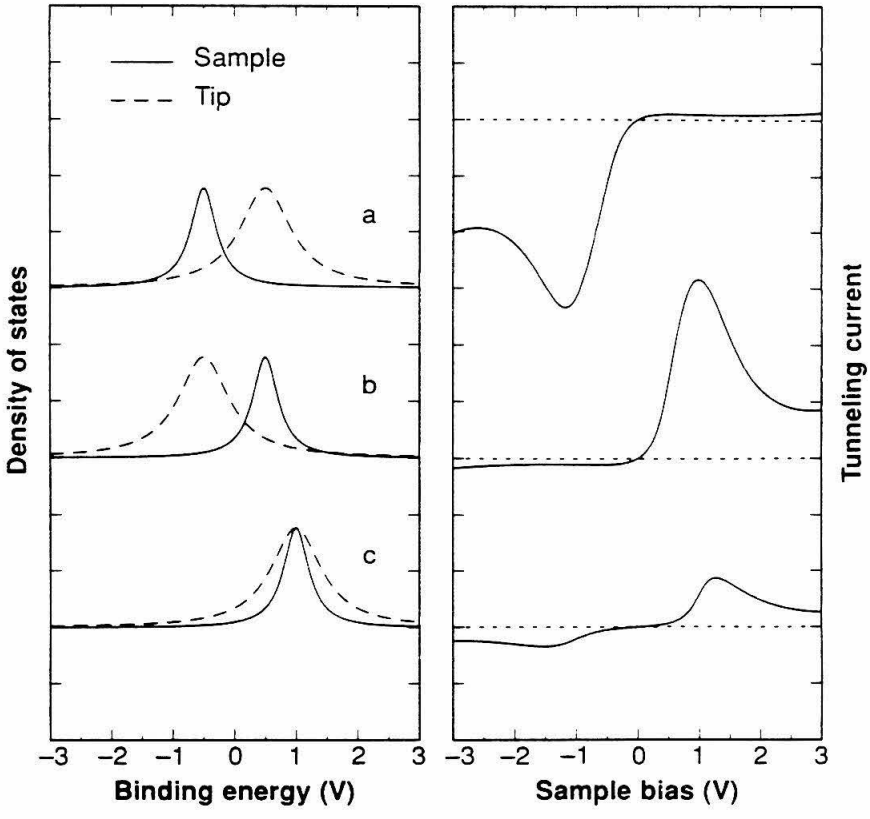
Sample
Tip
a
b
c
Density of states
Tunneling current
−3 −2 −1 0 1 2 3
Binding energy (V)
−3 −2 −1 0 1 2 3
Sample bias (V)

References

1. L. Esaki, *Phys. Rev.* **109,** 603 (1958).
2. L. L. Chang, L. Esaki, and R. Tsu, *Appl. Phys. Lett.* **24,** 593 (1974).
3. J. Peinke, D. B. Schmid, B. Röhricht, and J. Parisi, *Z. Phys. B* **66,** 65 (1987).
4. Yu. G. Gurevich, V. L. Zozulya, and V. B. Yurchenko, *Sov. Phys. Semicond.* **23,** 402 (1989).
5. Y. Yamamoto and H. Miyanaga, *IEEE Trans. Elect. Dev.* **37,** 1364 (1990).
6. L. Esaki and P. J. Stiles, *Phys. Rev. Lett.* **16,** 1108 (1966).
7. R. J. Brown, M. Pepper, H. Ahmed, D. G. Hasko, D. A. Ritchie, J. E. F. Frost, D. C. Peacock, and G. A. C. Jones, *J. Phys: Condens. Matter* **2,** 2105 (1990).
8. R. J. Hamers and R. H. Koch in *The Physics and Chemistry of SiO_2 and the Si-SiO_2 Interface* (eds. C. Helms and B. Deal, Plenum, New York) 201 (1988).
9. P. Bedrossian, D. M. Chen, K. Mortensen, and J. A. Golovchenko, *Nature* **342,** 258 (1989).
10. I-W. Lyo and P. Avouris, *Science* **245,** 1369 (1989).
11. Lyo and Avouris, *op. cit.*, and J. Boland, private communication.
12. J. A. Kramar, "Scanning tunneling microscopy and spectroscopy of molybdenum disulfide," Ph.D. thesis, California Institute of Technology (1990).
13. Ch. Gerber, G. Binnig, H. Fuchs, O. Marti, and H. Rohrer, *Rev. Sci. Instrum.* **57,** 221 (1986).
14. R. J. Driscoll, "Scanning tunneling microscopy and spectroscopy: I. Semimetals and Semiconductors; II. Atom-resolved imaging of DNA," Ph.D. thesis, California Institute of Technology (1992).
15. R. G. Dickinson and L. Pauling, *J. Am. Chem. Soc.* **45,** 1466 (1923).
16. Data provided by J. R. Lince, The Aerospace Corp., El Segundo, CA.
17. R. J. Hamers, R. M. Tromp, and J. E. Demuth, *Phys. Rev. Lett.* **56,** 1972 (1986).

18. T. R. Coley, W. A. Goddard, and J. D. Baldeschwieler, *J. Vac. Sci. Technol. B* **9,** 470-474 (1991).
19. G. W. Stupian and M. S. Leung, *Appl. Phys. Lett.* **51,** 1560 (1987).
D. Sarid, T. D. Henson, N. R. Armstrong, and L. S. Bell, *Appl. Phys. Lett.* **52,** 2252 (1988).
M. Weimer, J. Kramar, C. Bai, J. D. Baldeschwieler, and W. J. Kaiser, *J. Vac. Sci. Technol.* **A 6,** 336 (1988).
M. Weimer, J. Kramar, C. Bai, and J. D. Baldeschwieler, *Phys. Rev. B* **37,** 4292 (1988).
T. D. Henson, D. Sarid, and L. S. Bell, *J. Microsc.* **152,** Pt 2, 467 (1988).
T. Ichinokawa, T. Ichinose, M Tohyama, and H. Itoh, *J. Vac. Sci. Technol.* **A 8,** 500 (1990).
20. R. Mamy, A. Boufelja, and B. Carricaburu, *Phys. Stat. Sol.* **B 141,** 467 (1987).
21. J. S. Zabinski and B. J. Tatarchuk, *Mat. Res. Soc. Symp. Proc.* **140,** 239 (1989).
22. N. D. Lang, *Phys. Rev. Lett.* **58,** 45 (1987).

Chapter 5: STM of DNA in UHV

Introduction

Atomic-resolution imaging of large molecules with the scanning tunneling microscope (STM) has been of great interest but an elusive goal. Such imaging would be useful both for the study of complex molecules and for the investigation of imaging mechanisms in the scanning tunneling microscope. Real-space atom-resolved images of double-helical DNA are presented in this chapter. This result demonstrates the potential of the scanning tunneling microscope (STM) for characterization of biomolecular structures while at the same time placing tighter constraints on mechanisms which may be proposed to explain STM imaging of such materials.

The DNA double-helix has been a popular target in scanning tunneling microscopy. The first STM image of DNA was obtained by Binnig and Rohrer in 1984.[1] DNA was deposited on a silver-coated silicon crystal and imaged under ultrahigh vacuum. Long features approximately 30 angstroms wide but hundreds of angstroms deep were observed. They were interpreted as DNA molecules which appeared as depressions because of DNA's insulating character; as the tip moved over a molecule, it blocked the tunneling current, and a reduction in the tip-substrate separation was required in order to maintain a constant current. Although the piezoelectric actuator moved several hundred Å, the actual change in tip-sample separation was thought to be much less because of elastic deformations of the tip and sample due to the considerable force present in the tunnel junction.[2] No submolecular structure was resolved. In other early work, Amrein *et al.* used metal shadowing to make freeze-dried DNA samples conducting for

imaging with the STM and were able to image DNA molecules and DNA-protein complexes. Large-scale molecular structure was resolved on the protein, but the metal overlayer precluded submolecular resolution on the DNA.[3]

Later studies showed that the STM can image naked DNA molecules with *positive* contrast under a variety of conditions. Cricenti *et al.* deposited DNA on gold along with an organic molecule intended to bind the DNA to the surface. Imaging in air in the barrier-height mode,[4] they observed a pattern of sharp features which they suggested were portions of the base pairs and the phosphate-sugar backbone of the double-helix, but interpretation of the images was not straight-forward.[5] Beebe and coworkers, also working in air, imaged DNA adsorbed on highly oriented pyrolytic graphite (HOPG) and showed a structure approximately 60 Å wide twisted into a loop. They interpreted the loop as a supercoil of DNA and the substructure in the image as the major and minor grooves of the double-helix.[6] Lindsay pioneered imaging DNA on gold electrode surfaces under water, achieving molecular resolution.[7] Arscott *et al.* adsorbed Z-DNA on HOPG and immersed it in mineral oil.[8] They showed clear images of the major and minor grooves. In the work presented here, DNA adsorbed on HOPG was imaged under ultrahigh vacuum.

The experiment was intended to test the capability of the STM for atomic-scale imaging of DNA and to provide data leading to the elucidation of the image-contrast mechanism for weakly-bound, presumably non-conducting adsorbates. Ultrahigh vacuum conditions were employed to

remove hydration layers and excess volatile salt (NH_4OAc) codeposited with the DNA and to maintain sample cleanliness through long periods (hours-days) of searching for isolated molecules. Images were obtained which demonstrate that, under certain conditions, the STM can resolve the physical shape of the molecule on the *atomic* scale.

Experimental

The sample was a ~550-base-pair fragment of mouse B-cell V-region DNA.[9] A 2 µl drop of 10 mM aqueous ammonium acetate solution containing 10 ng DNA/µl was deposited onto freshly cleaved HOPG (Union Carbide ZYA grade) under nitrogen-flow at the opening of the vacuum-chamber load-lock. The sample was immediately sealed into the nitrogen-filled load lock, and the valve to the roughing line was opened slightly to allow a slow reduction in pressure. After several minutes, the valve was slowly opened over the course of about 20 minutes, and the load-lock pressure was reduced to 10^{-7} torr in ~3 hours. No visible residue was present after drying and introduction to the UHV chamber.

Imaging was done at ~10^{-10} torr in a UHV-STM system which is similar to the familiar IBM "pocket-size" STM.[10] It is described in Appendix B as "The Kramar System." Tips used were electrochemically etched (6 V ac; 2 M KOH) tungsten. Sample bias for the atom-resolved data was +100 mV with a tunneling current of 1 nA. The z modulation in barrier height measurements was 0.6 Å p-p at 1 kHz.

Results and Discussion

General Observations

With the sample preparation used, large areas of atomically flat graphite were seen with occasional mono- and bi- atomic steps, *i.e.*, clean HOPG was prevalent. These steps can be mistaken for DNA strands in topographical images,[11] especially if insufficient data-pixel resolution is used.[12] Graphite steps are often linear over hundreds of angstroms and accompanied by similar steps at 60° or 120° to each other. Substrate and DNA structures may be distinguishable using barrier height information;[13] barrier height changes in UHV are usually much greater over DNA than steps. The *d(ln i)/ds* values measured using the gap modulation technique are often too low to reflect the true barrier height of the surface;[14] however, such "barrier height" images were an indispensable aid in interpreting topographic images. Barrier heights over DNA structures were usually approximately 100 - 300 meV, but values as high as 1.5 eV were not uncommon. The barrier heights over the bare graphite substrate and steps were almost always lower.

HOPG as a substrate has both advantages and disadvantages. It was chosen because it can be easily cleaved to expose a clean surface atomically flat over hundreds or thousands of angstroms. Its flatness was expected to make identification of adsorbed molecules simple. Unfortunately, as mentioned above, HOPG step structures may have structure similar to that expected for a linear molecule like DNA. Furthermore, the surface is chemically inert, and only at steps or defects are individual molecules likely to be sufficiently bound to the surface to remain undisturbed by the tunneling

tip. Step edges are the most-likely sites for stable adsorption due to the presence of dangling bonds and increased reactivity. The mobility of material adsorbed on HOPG is illustrated in Figure 5.1. The first frame shows a cluster of DNA or a flake of HOPG together with a linear structure, probably a strand of DNA. In the next frame, the DNA strand has been brushed away. In the third frame, a DNA aggregate has appeared next to the cluster. Adsorption and tip-mediated removal of material adsorbed at a step edge is shown in Figure 5.2. In the first frame, material appears to be adsorbed along atomic steps; the edges are textured and the barrier-height high. A few scans later, the steps appear clean and the barrier-height low. (An alternative explanation is a change in the tip structure due to loss or addition of adsorbed material). The (rarely encountered) DNA structures consisted mainly of large aggregates and clumps. Figure 5.3 shows a series of three STM topographical images of a typical DNA aggregate; at increasing magnifications. At the highest magnification, linear portions can be seen with 30Å periodicity, consistent with the helical period of A-DNA. Although there appear to be several parallel strands, it is actually a single strand imaged several times by a relatively blunt tip with several asperities; more substantially displaced shadow images of the cluster due to a broad tip can be identified in the lower magnification images.

DNA structures were imaged using a variety of scan rates and bias voltages. Although the highest resolution images were obtained with very low scan rates (100 Å/s) and +100 mV sample bias, it is not known whether these parameters are critical. The fundamental requirement is that the scan rate be sufficiently low for the feedback system to respond to > 10Å changes

in topography before the tip has moved more than about an angstrom. It is possible that the tip-height-modulation used for barrier-height imaging also contributed to the passage of the tip over the undisturbed molecule in a manner analogous to Jericho's "hopping STM."[15] Images obtained successively with opposite biases were generally indistinguishable and appeared qualitatively the same over the explored range from 50 mV to 1 V. Current imaging tunneling spectroscopy (CITS) may reveal chemical information,[16] but the measurements made in the course of this work showed little structure in current-voltage curves over clumps or individual adsorbed DNA molecules. It must be noted, though, that such measurements were not conducted during the period of highest imaging resolution, and changes in I vs. V character associated with specific molecular features may have been averaged away.

Atom-Resolved Imaging

The DNA double-helix has distinctive structural characteristics on several spatial scales which together can both test the limits of the STM for imaging and serve as a signature of the DNA molecule in STM images. These include the molecular length and width, helix pitch, widths of the major groove, minor groove, and phosphate-sugar backbone, base-pair tilt, and helical symmetry. Under low-humidity conditions all of the secondary and part of the primary hydration shells are removed from the DNA molecule, and its conformation changes from the 'B-form' to the 'A-form;' thus, the A-form is expected to be prevalent in UHV. The conventional A-form of DNA, determined by X-ray crystallography, is characterized by a width of ~ 23 Å,

helical symmetry of 11 base pairs/turn, a +19° base pair tilt to the helix axis, a 28.5 Å pitch, and an axial nucleotide rise of 2.59 Å.[17] Subtracting the van der Waals radii of the backbone phosphate groups, the major groove is narrow and deep (2.7 Å and 13.5 Å, respectively) and the minor groove is wide and shallow (11.0 Å and 2.8 Å).

While the essential conditions for imaging DNA with atomic-scale resolution are not yet known, the data presented in this section demonstrate that such imaging *is* possible. A series of images from a single tip-sample combination will be shown, and data from high-resolution scans will be compared directly to the known DNA structure derived from x-ray crystallography. Figure 5.4 is a 200 Å x 200 Å image of an isolated DNA molecule. The image is neither filtered nor smoothed and shows just over seven turns of the helix. The helix pitch appears somewhat varying but the average pitch is ~ 30 Å and the molecular width is ~ 25 Å. Imaging at this level of resolution may be sufficient to address problems of biomolecular structure. For example, the center of the image shows a probable "kink site" with a single turn at ~ 30° to the helix axis; such kinks are thought to be sequence-related, and studies have been directed at understanding this phenomenon.[18] Recognition of elements of the DNA 'signature' beyond the molecular width and helix pitch requires higher resolution.

The middle portion of Figure 5.4 was scanned with greater pixel density and is shown in Figure 5.5. The image window is approximately 80 Å in x and 120 Å in y and was acquired with a scan rate of ~100 Å/s. Again, no filtering or smoothing has been applied to the image. The kink site from the

previous image is quite evident in this figure and is marked by lines A and B. At this resolution, the double helix and the major-minor groove alternation become apparent, as do parallel features spanning the minor grooves at an ~+18° angle to the helix axis. These may be identified as the base-pairs. The helix symmetry estimated from these bases is approximately 11 base pairs/turn, consistent with A-DNA. The average pitch is ~ 29 Å and the axial nucleotide rise is ~ 2.6 Å, in agreement with the structure of A-DNA. The average width (full width at half maximum) of the molecule is ~ 23 Å, and the average "apparent height" is ~ 12 Å. The image acquired scanning in the opposite direction in x shows similar structure, but the molecule appears slightly narrower (~ 21 Å). This may indicate some elastic interaction between the tip and the molecule.

The dimensions from the STM image and those derived from X-ray crystallography are compared in Table 1. While the match appears quite complete, it should be recognized that dimensional differences may arise from the variability in the structure of A-family polynucleotides, substrate-tip thermal drift, and/or piezo creep. The thermal drift rate in the STM used here is typically between 1 and 10 Å/minute after stabilization, and these images were acquired with extremely low scan rates requiring more than 10 minutes/image; thus, the dimensional measurements may not be particularly accurate, and the correlation with crystallographic data, while excellent in this case, should not be considered essential for convincing data interpretation. Further, it is not clear that DNA dried in vacuum on a substrate *should* have a structure fully consistent with X-ray crystallographic data; the crystals used for diffraction studies have higher salt and water concentrations.

Table 1. Comparison of A-DNA dimensions derived from the STM and X-ray crystallography

	STM	X-ray
Helix pitch	29 Å	28.5 Å
Minor groove width	10 Å	11.0 Å
Major groove width	3 Å	2.7 Å
Molecular width	23 Å	23 Å
Phosphate backbone width	10 Å	11.6 Å
Axial nucleotide rise	2.6 Å	2.59 Å
Base-pair angle	+18°	+19°
Helix symmetry	11	11.0

The imaging technique itself can distort the measured shape of the molecule in more fundamental ways than the nonidealities of drift and creep. The DNA molecule may be expected to appear broadened in STM images because of the size and curvature of the tip which may be on the scale of DNA; the edge of the tip will probably sense the 23 Å high molecule before the apex of the tip is over the molecule. An aphysical molecular "height" is likely to result from the dependence of the tunneling probability on both the tip-sample separation and the tunneling barrier. In response to an increased potential barrier over the molecule, the feedback system must reduce tip-sample separation to maintain constant current.

The bottom third of Figure 5.5 is compared in Figure 5.6 with an identical section of the DNA strand from an image taken about 15 minutes earlier. The essentially identical appearance of the two successive images provides evidence of the STM's potential for non-destructive of a large biomolecule like DNA. The same portion of Figure 5.5 is compared to a corresponding section of a van der Waals surface model in Figure 5.7. The y

axis is skewed to facilitate direct comparison with the model. The STM image window is ~ 35 x 55 Å and contrast has been enhanced in Figure 5.7 by histogram equalization; no smoothing has been effected. The similarity between the two is most clearly shown in the profile of the molecule, but close inspection shows that even the base-pair regions are quite similar.

To assess the presence of structure on the atomic scale experimental tip trajectories were directly compared to molecular models. In Figure 5.8, interpolated cross-sections of the STM tip trajectories over the DNA molecule along the lines A and B shown in Figure 5.5 are compared to the atomic contours of A-DNA approximating the cross-sectional regions. These line cuts were chosen to span the minor groove showing the best base pair resolution in both the topograph and the barrier-height data. In each case, the experimental cross-section is placed above the corresponding region of the model. The sugar-phosphate backbone is dark and the base pairs light. The image data used for the cuts were smoothed with a binomially weighted sliding window average corresponding to a 2-D Gaussian of ~ 0.60 Å FWHM (small compared to the van der Waals diameter of 3 Å). In the top half of Figure 5.8, the cut was taken across the base pair planes along the minor groove axis. Starting at the left, line A cuts through the phosphate-sugar backbone on the leading edge and shows the base pair periodicity across the groove. The cross-section in the bottom half of Figure 5.8 shows a similar comparison for line B taken across the minor groove through the two high backbones and an intermediate base pair. The nearly atom-for-atom agreement of the cross-sections to the contours of the surfaces is highly suggestive of *atomic resolution* in this region of the image. The ability to

resolve surface atoms on a 23 Å diameter "insulating" biomolecule is an extremely interesting result which places a new constraint on proposed imaging mechanisms.

Interpolated cross-sections of the topographical and barrier height data from the image in Figure 5.5 are compared in Figure 5.9. Although the barrier height data are shown in arbitrary units (au), measured effective local barrier heights over DNA typically ranged between 0.2 eV and 1.5 eV. The topographical and barrier height features show fair correlation of structure over the backbone atoms. However, the barrier height reveals considerable complementarity (anti-correlation) in the minor groove where atoms of the base pairs are resolved; the barrier height shows a peak where there is a valley in the topographical cross-section and vice versa. This complementarity is quite pronounced over the base pair atoms in Figure 5.9a. The topography in Figure 5.9b shows two high backbones with a concave minor groove of depth 2 to 3 Å and width about 10 Å, again consistent with the van der Waals surface model. The agreement of features over the backbone and complementarity over the bases is also evident in this cross-section. Complementarity is partially a consequence of the barrier-height dependence of the electron tunneling probability; if the barrier-height increases by a factor of n, tunneling probability is reduced by $\sqrt{n}$, and a compensating reduction in separation must occur; the topography and barrier-height may appear similar when the barrier change is small but inverted when the barrier change is large. Barrier height changes are generally associated with electron-density changes and may be due in part to chemical identity differences.

Solid-modeled perspective representations of two high-resolution images of DNA are given in Figures 5.10a and 5.10b. The former shows the bottom three-fourths of Figure 5.5. The latter is of an image obtained about 15 minutes earlier. The data have been smoothed ~ 0.60 Å as described above. Orientation differences in the images presented in this section resulted from adjustment of the raster rotation between scans.

Contrast Mechanism

The atomic lattice, chemical bonds, and electronic energy levels of semiconductors are routinely visualized, as is the topography of metal surfaces. The imaging 'mechanism' in these systems is well understood in terms of the theory developed by J. Tersoff and D. R. Hamann.[19] When adsorbed molecules are present, however, the picture becomes somewhat complicated.

Tersoff and Hamann showed that for small voltage biases the tunneling current is proportional to the surface local density of states (LDOS) at the Fermi level at the position of the tip.[19] Lateral resolution is proportional to the square root of the sum of the tip radius of curvature and the separation between the probe and sample. In a metal at finite temperature the 'Fermi level' is the energy at which electronic states have a 50% probability of being filled, *i.e.*, the chemical potential. The number of states per unit energy at a specific position is called the local density of states or LDOS. Tersoff and Hamann suggest that a constant current STM image shows contours of constant LDOS at the Fermi energy. This theory has been

successfully applied to predict "images" for several metal and semiconductor surfaces.

Unfortunately, an understanding of Tersoff and Hamann STM theory together with some knowledge of biomolecules does little to predict the trajectory of an STM tip as it passes over a biomolecule on a conducting surface. With single atom adsorbates, Lang has shown that the local s and p state density contributions at the Fermi level by the adsorbed atom can be significant compared to the LDOS of the underlying metal.[20] The apparent height of xenon adsorbed on nickel and imaged with an STM has been shown to be consistent with Lang's theoretical treatment. While imaging of large molecules may remain similarly consistent with the Tersoff and Hamann theory, the formalism is much more difficult to apply because of the complex interaction between molecular energy levels, the tip, and the substrate. STM theory is not sufficiently advanced to predict the STM images that are obtained for a large molecular adsorbate on a conducting substrate. Adsorbed biomolecules (and covalent molecules in general) have very little state density at the Fermi level -- molecular orbitals are generally more than an electron volt above or below.[21] This suggests the mechanism for tunneling current modulation is only indirectly related to the physisorbed molecule's states.

Several ideas have been advanced to explain the STM imaging of adsorbates. These include adsorbate-induced barrier height change,[22] simple resonant tunneling,[23] pressure-induced shifting of molecular levels into resonance,[24] long-range electron transfer,[25] and inelastic electron tunneling.[26]

None seem consistent with the imaging of the atomic contour of the *surface* of the DNA molecule as demonstrated here.

T. R. Coley and W. A. Goddard have assisted with the interpretation of the images and have proposed that the contrast mechanism arises from an interaction between the graphite substrate and the adsorbate which serves only to modulate the underlying bulk states. There are two parts to this interaction, both of which can affect the tunneling current and lead to contrast changes near an adsorbate. The first part of the modulation effect arises from the Pauli principle which effectively requires the orbitals for different bond pairs to be orthogonal. Whereas graphite band states would normally decay exponentially into the vacuum, the presence of the adsorbate interferes with this decay. Orthogonalization of the graphite band states to the orbitals of the adsorbate causes the tail of the band orbitals to rapidly oscillate in the region of the adsorbate and then resume exponential fall-off above the adsorbed molecule. This leads to an extension of the substrate band orbitals to larger distances with the total extent depending on the orientation and character of the molecular orbitals of the interfering molecule. Thus, it is plausible that some adsorbate surface features will be imageable with atomic resolution.

The second part of their proposed contrast mechanism arises from changes in the density of surface states induced by the adsorbate. It is well known that an adsorbate interacting with a surface will have the effect of "pushing" states away from certain energy levels characteristic of the interaction. This has the effect of changing the energy density of states near the interaction. Since the tunneling current is an integral of the product of

state-to-state tunneling probabilities and the energy density of states, contrast will appear physically near the adsorbate. This type of modulation will be most pronounced for strongly interacting adsorbates, so the first factor (surface state modulation) is expected to be the dominant contrast mechanism for DNA which is expected to interact only weakly with the substrate.

Coley and Goddard are developing a theoretical model to test this hypothesis. Even without a quantitative understanding of the imaging mechanism, it is clear from the images obtained that a worthwhile contribution can be made using STM to investigate biological molecules.

Tip Considerations

The improved resolution of these data compared to previously published STM images of DNA may be attributable to ultrahigh vacuum, high data-pixel density, slow scan rate, a relatively dilute and extremely clean sample solution, electronic properties of the substrate and/or a fortuitously structured tip. The most likely limiting factor in imaging is the tip. Because of the exponential dependence of tunneling probability on separation, nearly all of the current flows through the atom(s) on the tip nearest to the surface. On macroscopically atomically flat surfaces like highly oriented pyrolytic graphite (HOPG), only a small asperity on a broadly curved tip is necessary for atomic resolution. If, however, a double-helical DNA molecule is present, its 23Å thickness will preclude high resolution imaging if the tip does not have a long sharp protrusion at the apex. The broadly-curved portion of the tip nearest the molecule will dominate the tunneling current even before the tip apex is over the molecule and the resulting image will be a convolution of

the broad tip and comparatively narrow molecule. This is illustrated in Figure 5.11. Unfortunately, the apex atomic arrangement is always a matter of chance, and the probability of its having a long asperity suitable for DNA imaging is still quite low.

Progress in imaging biomolecules will probably depend on optimizing tip structures. Focused ion beam ion milling has recently been demonstrated as a means for making long sharp tips for metrology applications.[27] Cone angles between 12° and 15° are reported with radii of 30-40 Å. The same methodology could be used to tailor the length of the sharp asperity from the bulk of the tip shaft so that it is long enough to avoid contact with the adsorbed molecule by the broad support structure while short enough to be extremely rigid, *e.g.*, ~100 Å. Such a tip profile would be ideal for molecular imaging, but the apex structure may not be. Additional controlled modifications of the apex can be made. The surface of a sharp tip has been shown to become fluid at approximately 1/3 the bulk melting point, and under the influence of the field in a field ionization microscope perfectly shaped atomic pyramidal tips can be produced.[28] The exact atomic structure of the tip and support can be determined and controlled. Atomic-scale shape of the tip has been shown to change easily for high-index faces, but the (111) apex atom can be very stable and may be the most suitable for STM use.[29]

Summary

It was demonstrated that the STM can, under some conditions, image the surface of a large biomolecule, double-helical DNA. The STM imaging of DNA in ultrahigh vacuum was intended to test the capability of the STM for

atomic-scale imaging of DNA and to elucidate the mechanism giving rise to image contrast for weakly-bound adsorbates. Ultrahigh vacuum conditions were employed to remove hydration layers and excess volatile salt (NH_4OAc) and to maintain sample cleanliness through long periods (hours-days) of searching for isolated molecules. Emphasis was placed on image interpretation through comparison of experimental results with the well-known optimized structure of A-DNA derived from X-ray crystallographic data. Seven distinct structural features were presented as a 'DNA signature' for the STM and identified in STM images. While the physical mechanisms which make imaging large molecules with the STM possible are not yet understood, the primary obstacles to routine atomic-scale imaging of molecules like DNA appear to be mostly technical -- attaining spatially uniform deposition of isolated molecules and appropriately structured probe tips.

Figures -- Chapter 5

Figure 5.1. Mobility of material adsorbed on HOPG. Three successive 1750 x 1750 Å images of DNA-dosed HOPG are shown. The first shows a globular cluster and a linear aggregate. In the second image, the cluster has changed shape and moved toward the lower right while the aggregate is no longer in the image window. In the third image, the aggregate has drifted further to the lower right while a new cluster appears below it. The apparent height difference at the curved line extending from lower left to upper right is an instrumental artifact, but is somewhat useful here in that its position is constant in X and Y for the full STM window and would reveal any change in image window offset from one scan to the next.

Figure 5.1

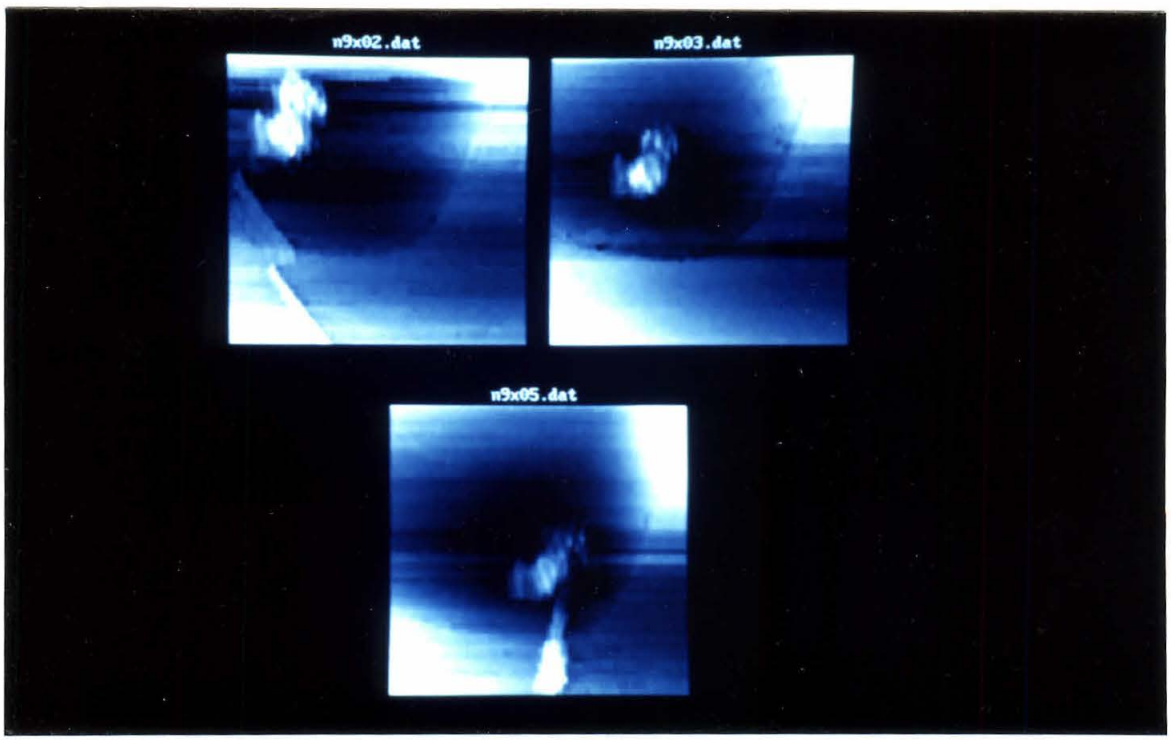

Figure 5.2. Tip-mediated removal of material from a step. Two 1200 x 400 Å images of the same area of a DNA-dosed graphite surface are shown. In the top image, material appears to be adsorbed at a step. In the bottom image, the step looks clean. Between the two images, the area was scanned with parameters which caused unstable tunneling, possibly leading to increased interaction between the surface and the tip. (An alternative explanation of the change in image character is a change in tip structure).

Figure 5.2

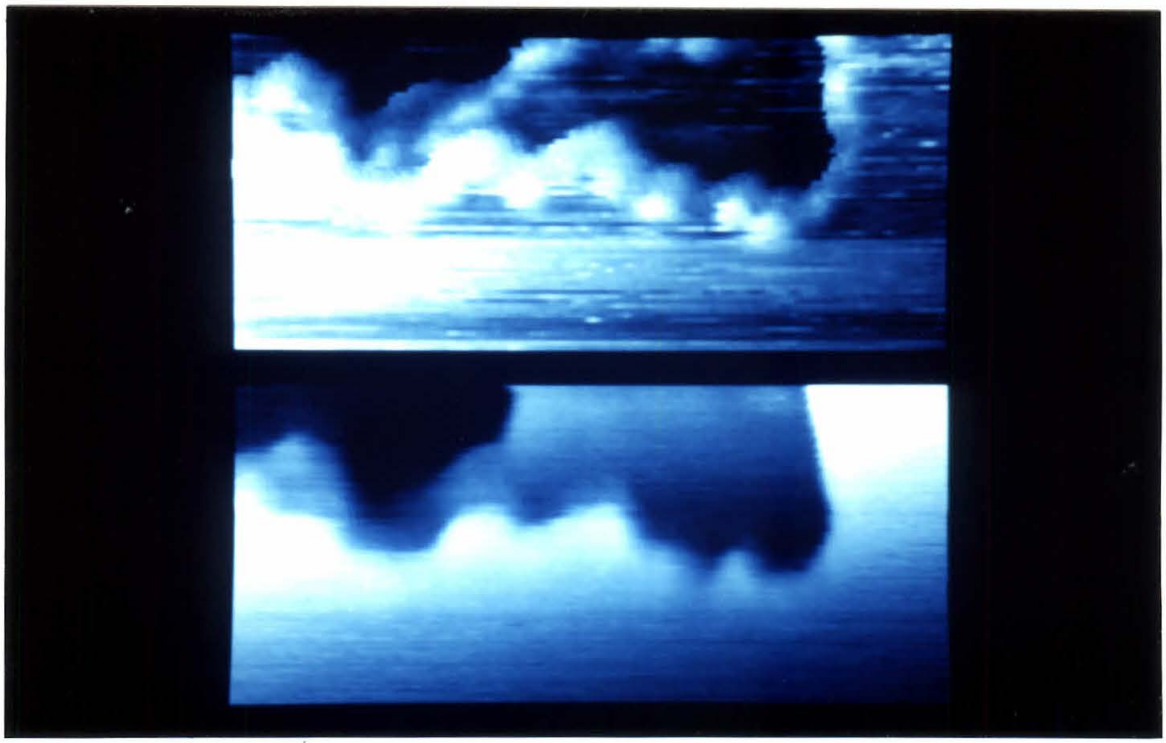

Figure 5.3. STM images of DNA aggregates. A series of three topographical images of a stadium-shaped DNA aggregate is shown at successively higher magnification clockwise from top left. Raw data are shown; white corresponds to topographic maxima. The image areas are approximately (3000 Å)^2, (1500 Å)^2 and (750 Å)^2 respectively. The lower right region of the highest magnification image shows several vertical closely packed side-by-side DNA strands with pitch repeats of ~ 30 Å. (0.20 V sample, 1 nA constat current.)

Figure 5.3

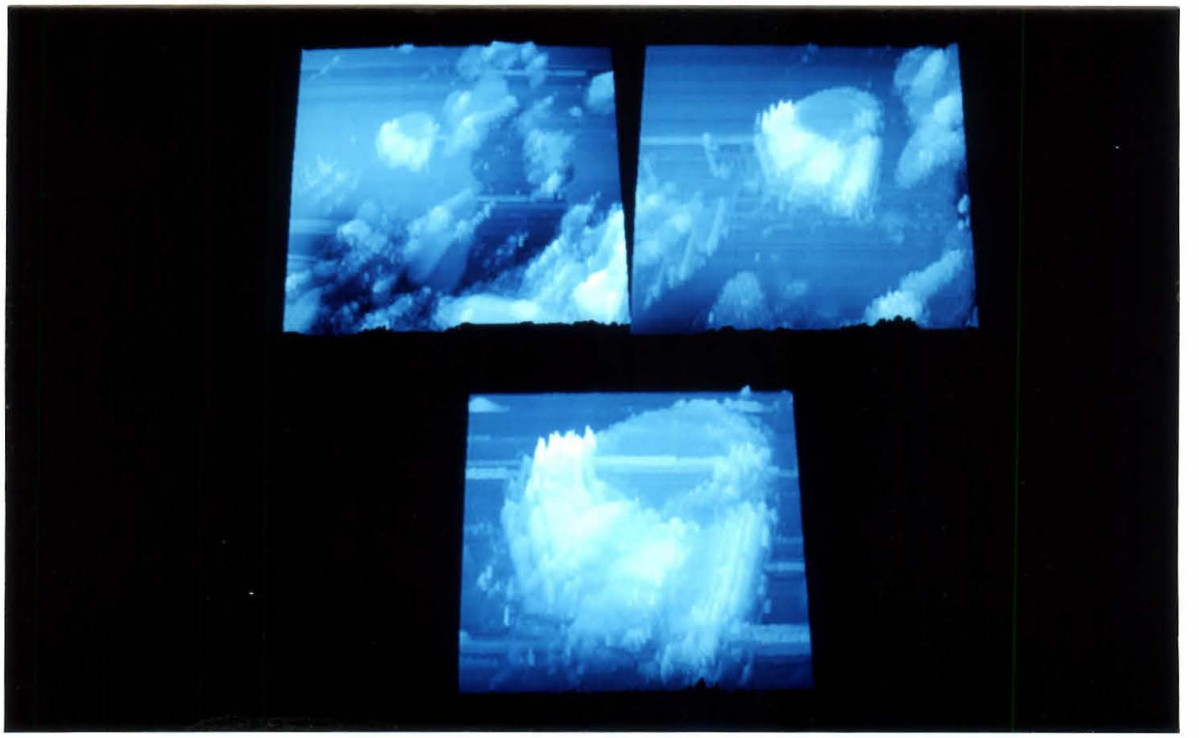

Figure 5.4. Medium-resolution STM image of an isolated DNA molecule. The unsmoothed, unfiltered plane-subtracted constant-current image shows a ~200 x 200 Å (500 x 100 data pixels) region crossed by an isolated DNA molecule. Nearly eight turns of the helix are shown. The average helix pitch is 30 Å and molecular width 25 Å. A "kink site" with a relative angle of 30° is seen in the middle of the image. (0.10 V sample, 1 nA constant current.)

Figure 5.4

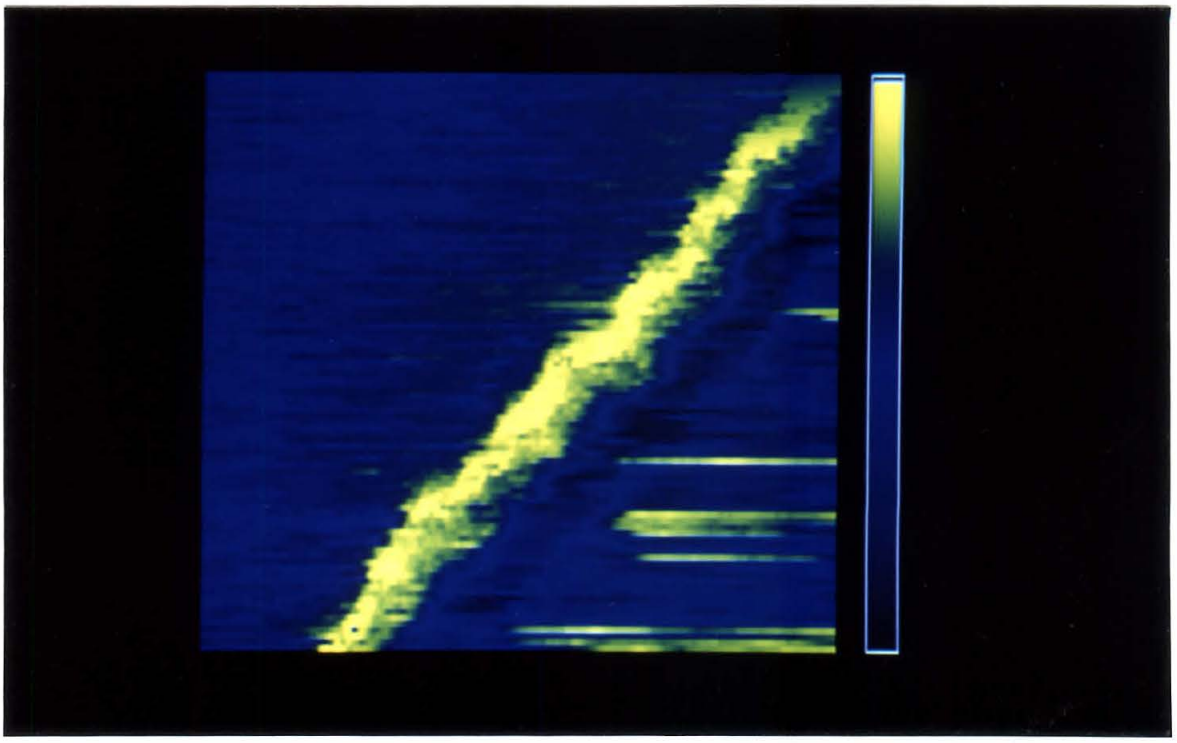

Figure 5.5. High-resolution STM image of DNA. The plane-subtracted atom-resolved image shows with no filtering or smoothing a DNA molecule crossing an ~ 80 x 120 Å (400 x 250 data pixels) area. The parallel bands bridging the minor grooves are base pairs at 18° ± 3° to the helix axis. The central arrow points to a tip instability. (0.10 V sample, 1 nA constant current 1 nA.)

Figure 5.5

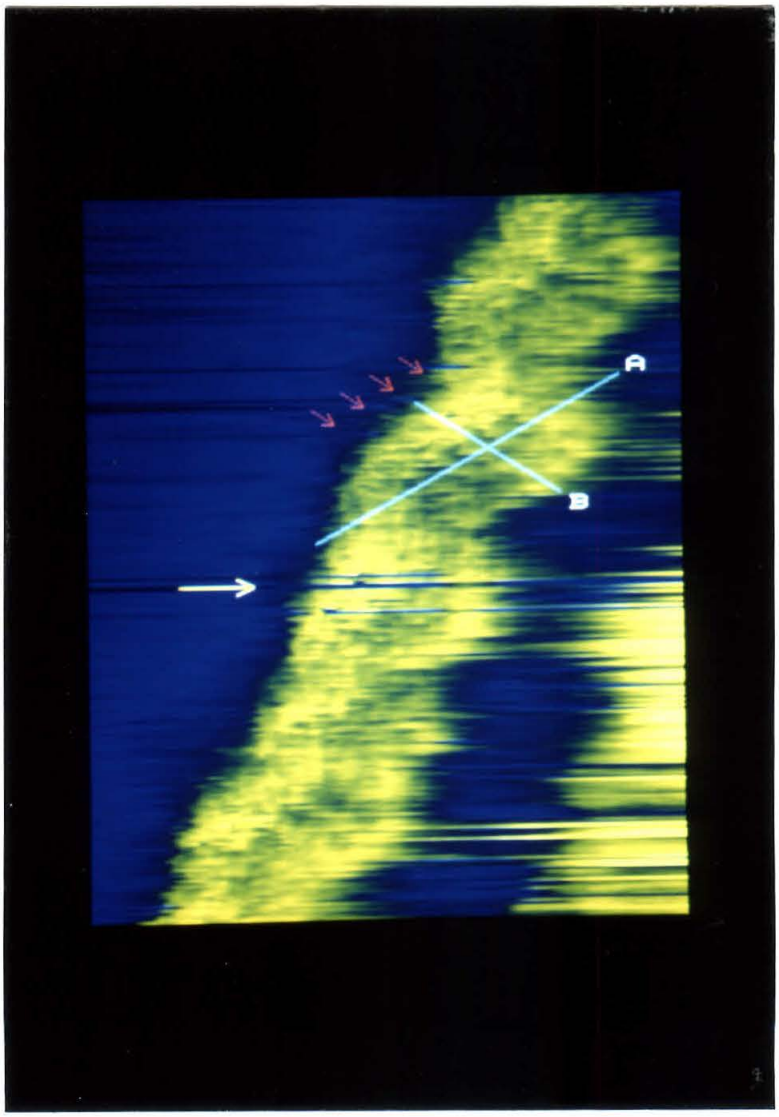

Figure 5.6. Comparison of subsequent STM images of DNA. The bottom portion of the STM image of Figure 5.5 is shown at the left, and an STM image of the identical section of the DNA strand obtained ~ 15 minutes earlier is shown on the right. The two images are essentially identical, providing evidence of the non-destructive imaging capabilities of STM. The images are not histogram equalized.

Figure 5.6

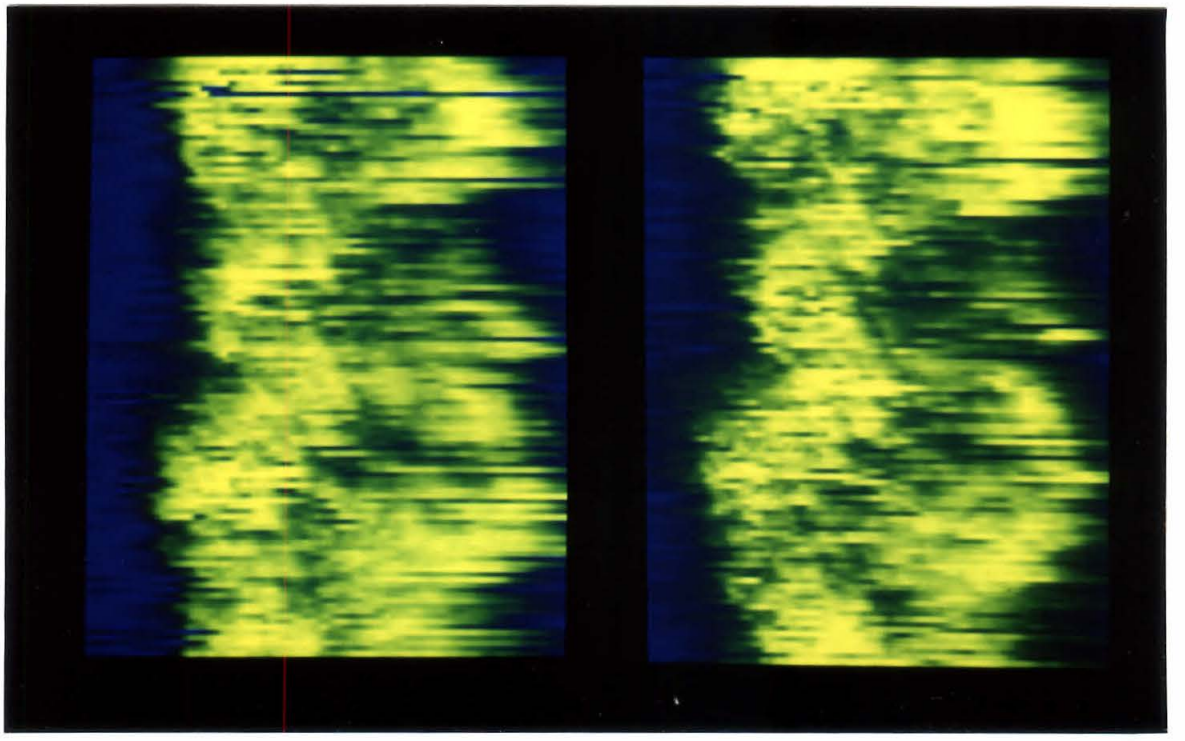

Figure 5.7. Comparison of an STM image of DNA to a van der Waals surface model. The bottom portion of Figure 5.5 is shown with a corresponding section of a van der Waals surface model of A-DNA. The STM data are plane-subtracted and unsmoothed, but contrast has been enhanced by histogram equalization. Hydrogen atoms are omitted from the model for clarity. Model constructed using Biodesign Biograf™ software.

Figure 5.7

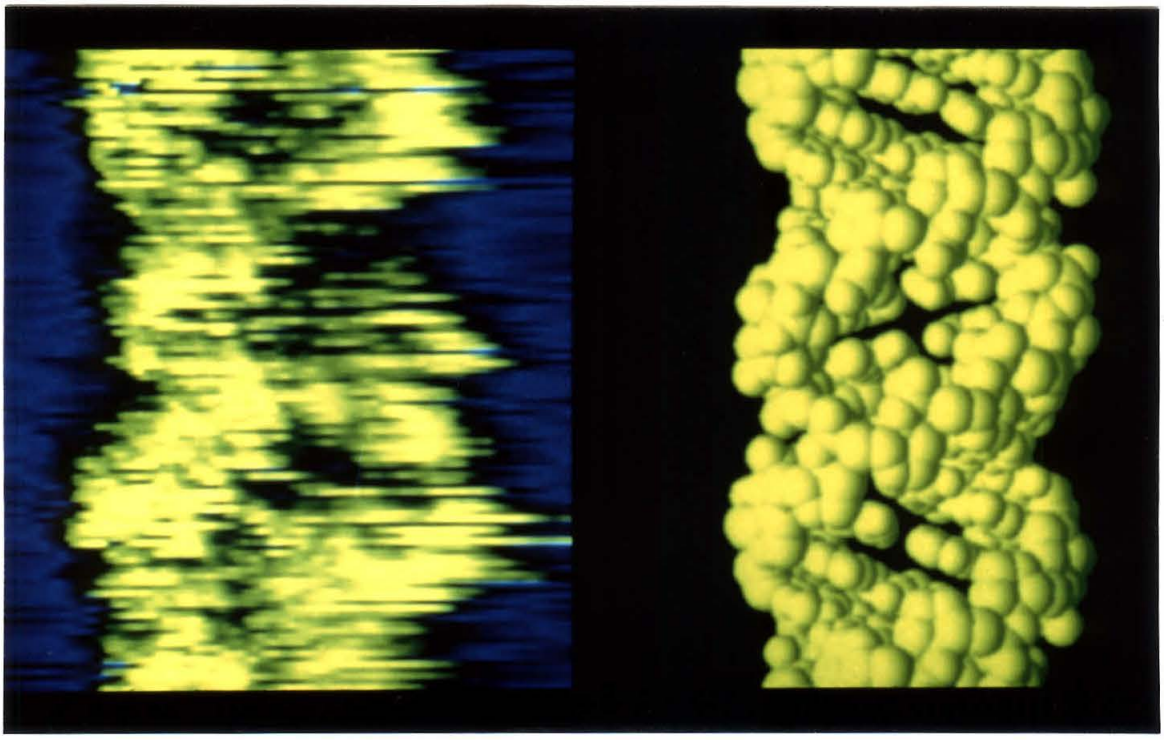

Figure 5.8. Correspondence of experimental STM tip trajectories with DNA atomic contours. Interpolated experimental STM tip trajectories following lines marked A and B in Figure 5.5 are compared with corresponding atomic contours of an A-DNA van der Waals model. The data for line A are shown on top; line B data are on the bottom. Height and length are on the same scale. The data have been smoothed ~ 0.60 Å. Hydrogen atoms are omitted from the model for clarity.

Figure 5.8

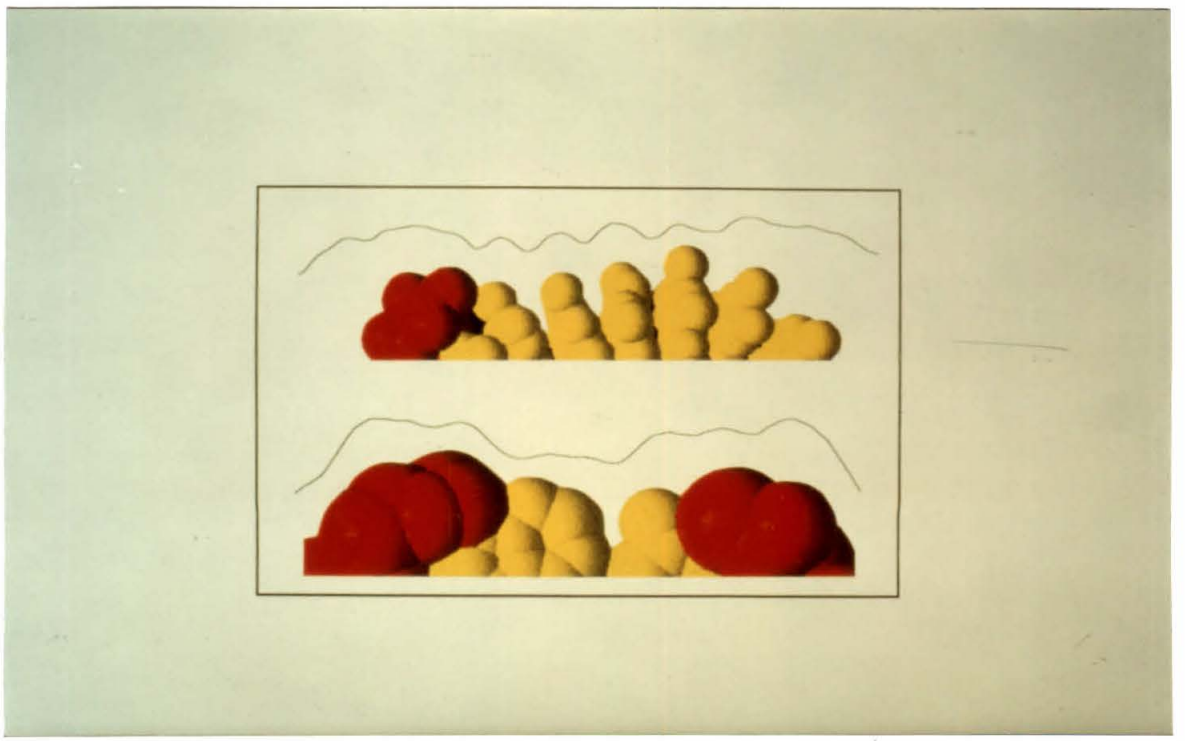

Figure 5.9. Interpolated cross-sections from the topographical and barrier-height data of Figure 5.5. Solid lines in (a) and (b) are tip trajectories following lines 'a' and 'b' shown in Figure 5.8, and dashed lines are corresponding data from a simultaneously acquired gap-modulated barrier height image. Barrier-height axes are in arbitrary units. The effective local barrier height was measured using the standard method of sinusoidally modulating the tip-sample separation (0.67 Å p-p at 1 kHz) and detecting d(ln *i*)/ds, the derivative of the natural logarithm of the tunneling current (*i*) with respect to the tip-sample separation, with a lock-in amplifier.

Figure 5.9

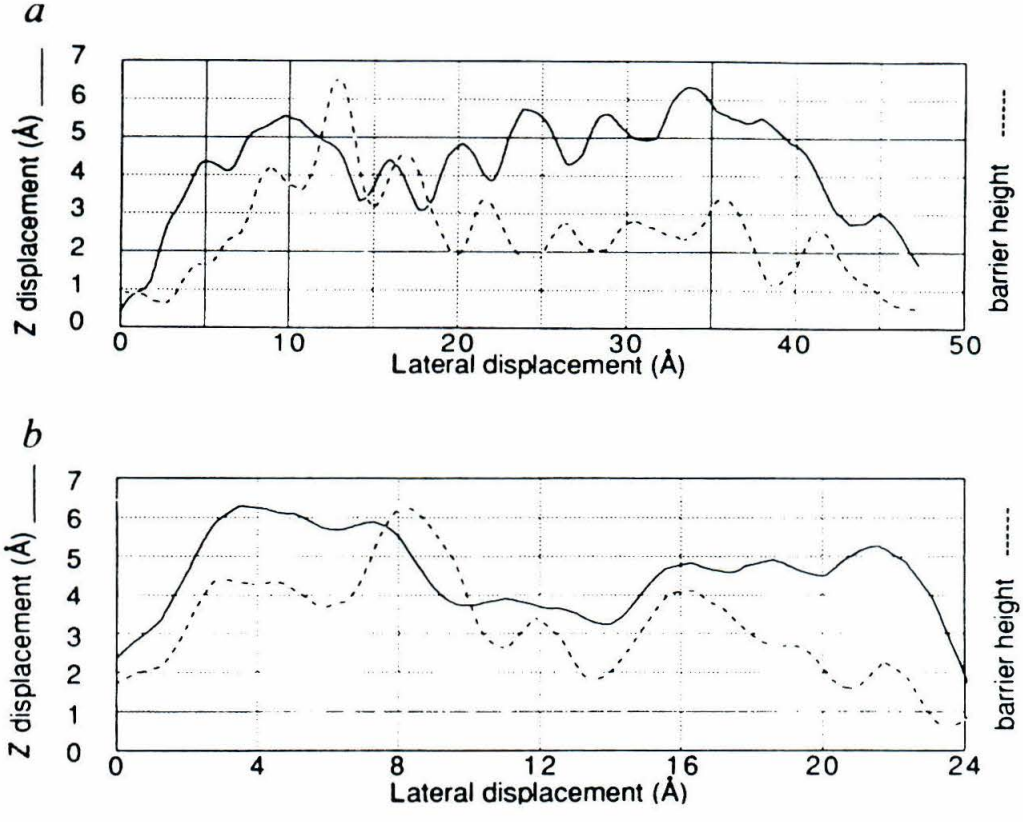
a
Z displacement (Å) ——
barrier height -----
0
1
2
3
4
5
6
7
0
10
20
30
40
50
Lateral displacement (Å)
b
Z displacement (Å) ——
barrier height -----
0
1
2
3
4
5
6
7
0
4
8
12
16
20
24
Lateral displacement (Å)

Figure 5.10. Solid-modeled perspective views of subsequent DNA images. In (a), the bottom three-fourths of the DNA molecule shown in Figure 5.5 is shown. The ~ 50 x 100 Å image has been smoothed ~ 0.60 Å. In (b), a similar presentation of data obtained 15 minutes earlier is shown. Between the two images, the raster rotation and offset were adjusted to center the molecule in the scan window.

Figure 5.10a

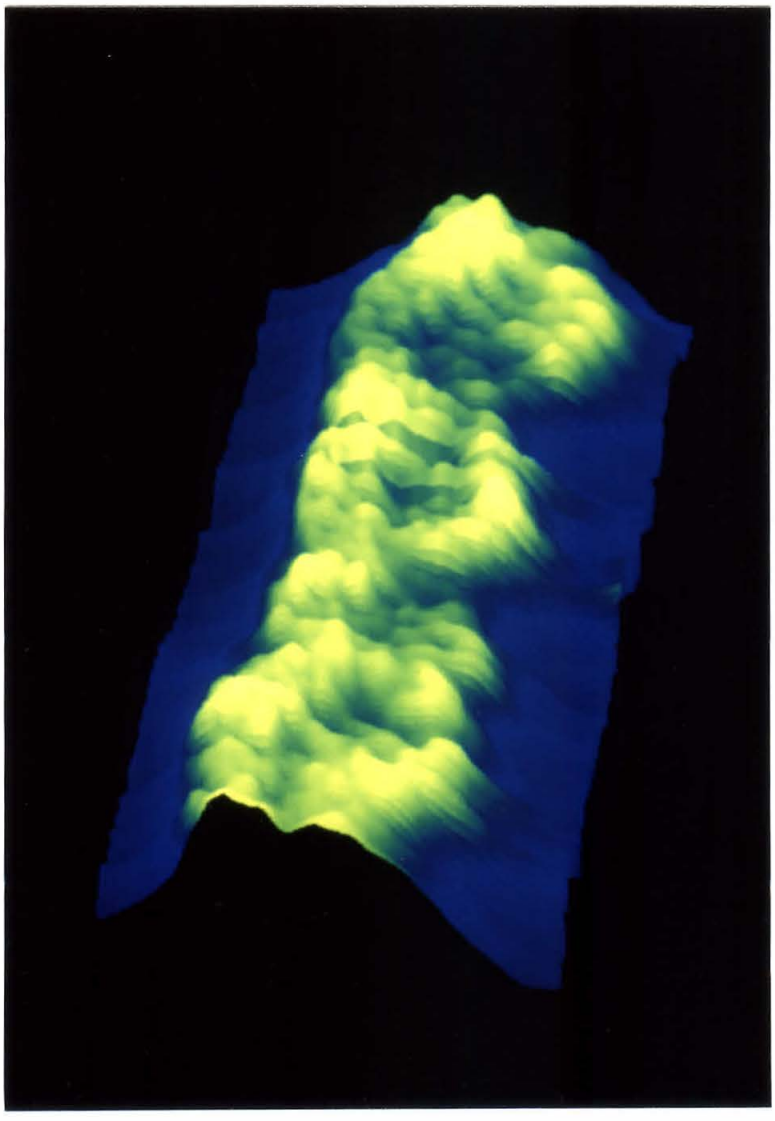

Figure 5.10b

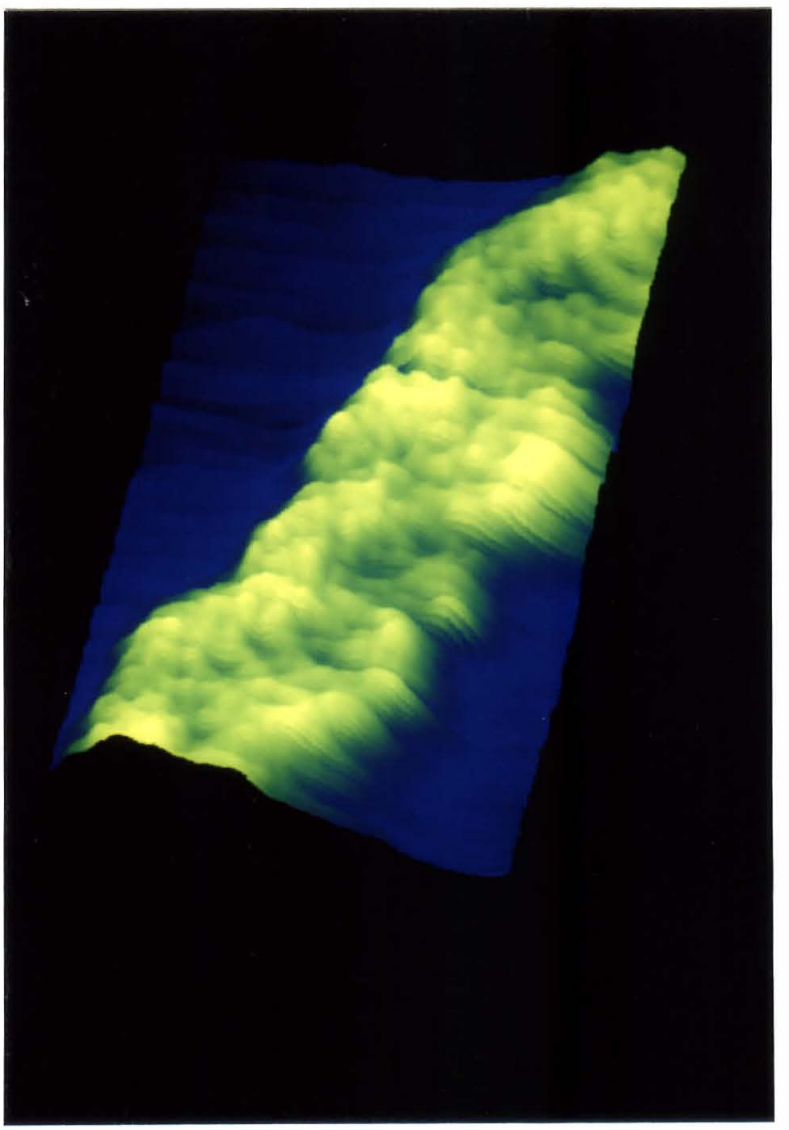

Figure 5.11. Graphical depiction of the convolution of tip and molecule shapes in STM imaging. The apparent shape of a surface or an adsorbate, as measured by the scanning tunneling microscope, is partially dependent on the shape of the tip.

Figure 5.11

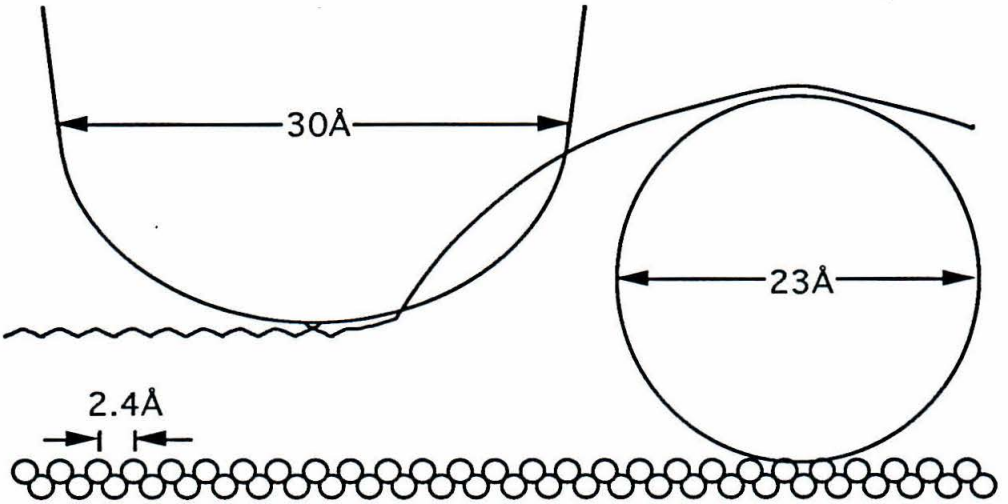

References

1. G. Binnig and H. Rohrer, in *Trends in Physics Vol 1*, Eds. J. Janta and J. Pantoflicek (European Physical Society, The Hague), 38-46 (1984); G. Binnig, *Ultramicroscopy* **42-44,** 7-15 (1992).
2. U Dürig, J. K. Gimzewski and D. W. Pohl, *Phys. Rev. Lett.* **57,** 2403 (1986).
3. M. Amrein, A. Stasiak, H. Gross, E. Stoll and G. Travaglini, *Science* **240,** 514 (1988).
4. J. S. Villarrubia and J. J. Boland, *Phys. Rev. Lett.* **63,** 306-9 (1989).
5. A. Cricenti, S. Selci, A. C. Felici, R. Generosi, E. Gori, W. Djaczenko and G. Chiarotti, *Science* **245,** 1226 (1989).
6. T. P. Beebe, Jr., T. E. Wilson, D. F. Ogletree, J. E. Katz, R. Balhorn, M.B. Salmeron and W. J. Siekhaus, *Science* **243,** 370 (1989).
7. S. M. Lindsay, T. Thundat, L. Nagahara, U. Knipping and R. L. Rill, *Science* **244,** 1063 (1989).
8. P. G. Arscott, G. Lee, V. A. Bloomfield and D. F. Evans, *Nature* **339,** 484 (1989).; **346,** 706 (1990).
9. Ava II fragment of the V_{13} region, from pBV13L cloned by Jerry Siu in Dr. Leroy Hood's research group, Caltech Biology division. Solution prepared by Joseph Meier.
10. Ch. Gerber, G. Binnig, H. Fuchs, O. Marti and H. Rohrer, *Rev Sci. Instrum.* **57,** 221 (1986).
11. M. Salmeron, T. Beebe, J. Odriozola, T. Wilson, D. F. Ogletree and W. Siekhaus, *J. Vac. Sci. Technol.* A **8,** 635 (1990).
12. For an example of insufficient pixel density and possible mistaken step-imaging see C. Bendixen, F. Besenbacher, E. Laegsgaard, I. Stengaard, B. Thomsen and O. Westergaard, *J. Vac. Sci. Technol. A* **8,** 703-705 (1990).
13. S. M. Lindsay, *EMSA Bull.* **19,** 60 (1989).
14. J. Gómez-Herrero, J. M. Gómez-Rodrìquez, R. Garcìa and A. M. Baró, *J. Vac. Sci. Technol.* **A 8,** 445 (1990).
15. M. H. Jericho, B. L. Blackford, and D. C. Dahn, *J. Appl. Phys.* **65,** 5237-5239 (1989).

16. R. M. Tromp, R. J. Hamers, and J. E. Demuth, *Science* **234,** 304-309 (1986).
17. W. Saenger, *Principles of Nucleic Acid Structure* (Springer-Verlag, New York, 1984).
18. S. M. Lindsay, L. A. Nagahara, T. Thundat, and P. Oden, *J. Bio. Struc.* **7,** 289-299 (1989).
19. J. Tersoff and D. R. Hamann, "Theory and application for the scanning tunneling microscope," *Phys. Rev. Lett.* **50(25),** 1998-2001 (1983); "Theory of the scanning tunneling microscope," *Phys. Rev. B* **32(2),** 805-813 (1985).
20. N. D. Lang, "Theory of single-atom imaging in the scanning tunneling microscope," *Phys. Rev. Lett.* **56,** 1164 (1986); "Apparent size of an atom in the scanning tunneling microscope as a function of bias," *Phys. Rev. Lett.* **58(1),** 45-48 (1987).
21. P. Yannoulis, K.-H. Frank and E.-E. Koch, "Electronic structure and orientation of anthracene on Ag(111)," *Surf. Sci.* **241,** 325-334 (1991).
22. J. K. Spong, H. A. Mizes, L. J. LaComb, Jr., M. M. Dovek, J. E. Frommer, and J. S. Foster, "Contrast mechanism for resolving organic-molecules with tunnelling microscopy," *Nature* **338,** 137-139 (1989).
23. W. Mizutani, M. Shigeno, M. Ono, and K. Kajimura, "Voltage-dependent scanning tunneling microscopy of liquid crystals on graphite," *Appl. Phys. Lett.* **56(20),** 1974-1976 (1990).
24. S. M. Lindsay, O. F. Sankey, Y. Li, C. Herbst, and A. Rupprecht, "Pressure and resonance effects in scanning tunneling microscopy of molecular adsorbates," *J. Phys. Chem.* **94(11),** 4655-4660 (1990).
25. D. P. E. Smith, A. Bryant, C. F. Quate, J. P. Rabe, Ch. Gerber, and J. D. Swalen, "Images of lipid bilayer at molecular resolution by scanning tunneling microscopy," *Proc. Natl. Acad. Sci. USA* **84,** 969-972 (1987).
26. K. Sakamaki, K. Itoh, A. Fujishima, and Y. Gohshi, "Surface density of states of TiO_2 (110) single crystal and adsorbed molecular observation by scanning tunneling microscopy and tunneling spectroscopy," *J. Vac. Sci. Technol. A* **8(1),** 614-617.

27. M. J. Vasile, D. Grigg, J. E. Griffith, E. Fitzgerald and P. E. Russell, "Scanning probe tip geometry optimized for metrology by focused ion beam ion milling," *J. Vac. Sci. Technol. B* **9**, 3569-3572 (1991).
28. V. T. Binh, "Atomic metallic ion emission, field surface melting and scanning tunneling microscopy tips," *J. de Physique* I **1**,605-612 (1991).
29. T. Hashizume, K. Motai and T. Sakurai, "Correlation between the STM resolution and atomic geometry of the tip," Abstracts, International Conference on Scanning Tunneling Microscopy, Interlaken, 192 (1991).

Appendices

Appendix A presents images of silicon and gold surfaces showing the interaction of steps with impurities.

Appendices B through E provide additional information on the instrumentation used in this thesis. Appendix B describes substantial enhancements for instrument control and data acquisition which were added to the STM system originally implemented by John Kramar, Michael Weimer, and Chunli Bai. In the last years of this work, the Baldeschwieler laboratory converted to a digital signal processor/video graphics array (DSP/VGA) based operating system. To complement the new microscope heads, a set of high performance digital control electronics for scanning tunneling microscopy was built in collaboration with Steve Clark. Software for advanced STM applications with the digital control electronics was developed based on a scanned probe microscope (SPM) operating system software written by David Baselt. Appendix C describes several aspects not addressed in Clark's and Baselt's theses,[1,2] and Appendices D and E present manuscripts prepared in collaboration with Clark and Baselt documenting the electronics performance and describing software principles for DSP based operating systems.

1. Steven M. Clark, "Advances in scanning force microscopy of biological structures," Ph.D. thesis, California Institute of Technology, Pasadena, CA (1992).
2. David R. Baselt, Ph.D. thesis, California Institute of Technology, Pasadena, CA (in preparation).

Appendix A: Step Pinning on Silicon and Gold Surfaces

STM images of impurity-pinned atomic steps on silicon and gold surfaces are presented. Highly sloped surfaces of gold spheres made by melting gold wire in a propadiene stabilized methylacetylene gas flame and quenching in air have bunches of atomic steps separated by atomically flat terraces where the step motion was impeded by an impurity. (See Figures A.1-A.4.) Glide dislocations are also observed on some gold samples. (See Figure A.4.) The pinned steps on the gold surface curve smoothly around the impurities with only short linear coherence lengths along crystalline lattice directions as would be expected on a material with long-range electronic interaction (like gold.) Step loops around the impurities may be present as indicated by the terrace structure of the protrusions. The shapes are similar to those observed when bulk dislocations move past refractory impurities by the Orowan mechanism. (See Figure A.5.) Vicinal Si(111) surfaces were prepared in high vacuum with impurity-pinned steps, but step loops were not observed. (See Figures A.6 and A.7.) The edge shape of Si steps moving past impurities seems closely associated with the degree of order in the surface reconstruction. On ordered (7x7 reconstructed) surfaces, $[2\bar{1}\,\bar{1}]$ ledges minimize the surface energy and lead to the observed facetting. However, on disordered surfaces, the importance of short-range interaction is reduced; the ledge is unable to significantly lower surface stress, and curved step edges are observed.[1]

Figures -- Appendix A

Figure A.1. Gold steps pinned at an impurity. Brightness is proportional to dZ/dX; positive slope from left is bright. (0.57 x 0.57 μm, 250 x 250 pixels, 2.9 μm/s, -0.25 V sample, 0.05 nA constant current.)

Figure A.1

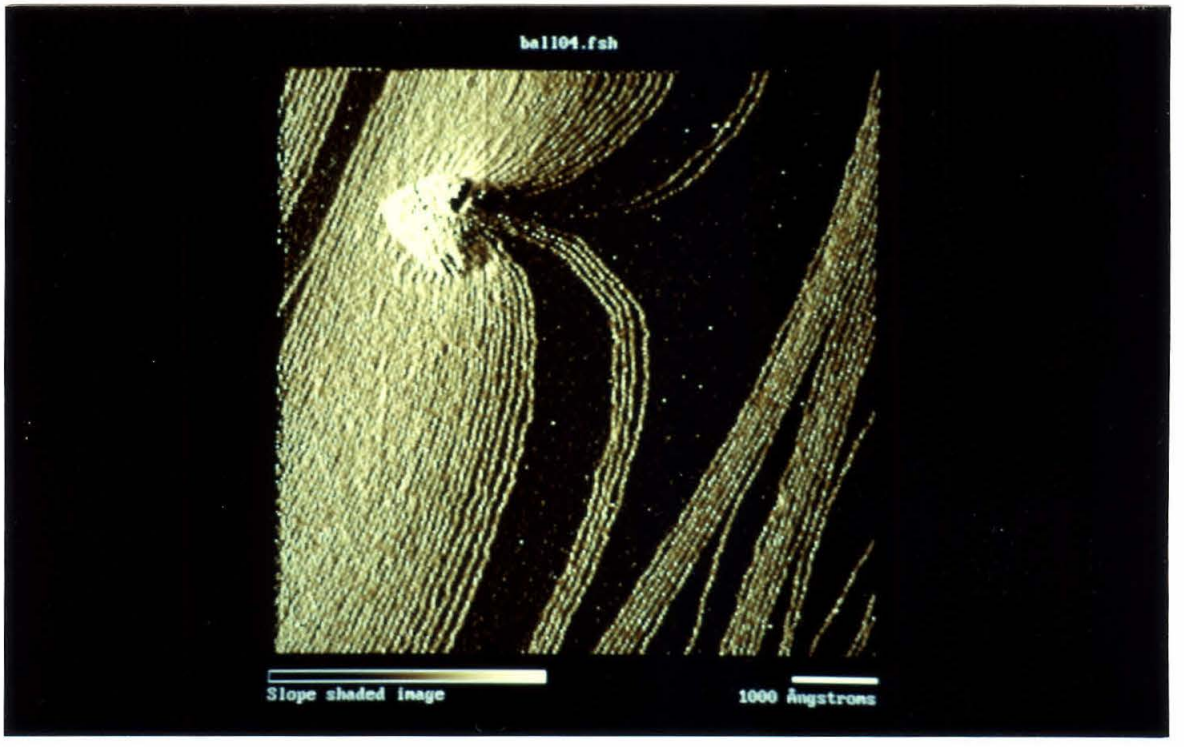

Figure A.2. Gold steps pinned at two impurities 0.25 μm apart. (0.57 x 0.57 μm, 350 x 350 pixels, 2.3 μm/s, -0.25 V sample, 0.05 nA constant current.)

Figure A.2

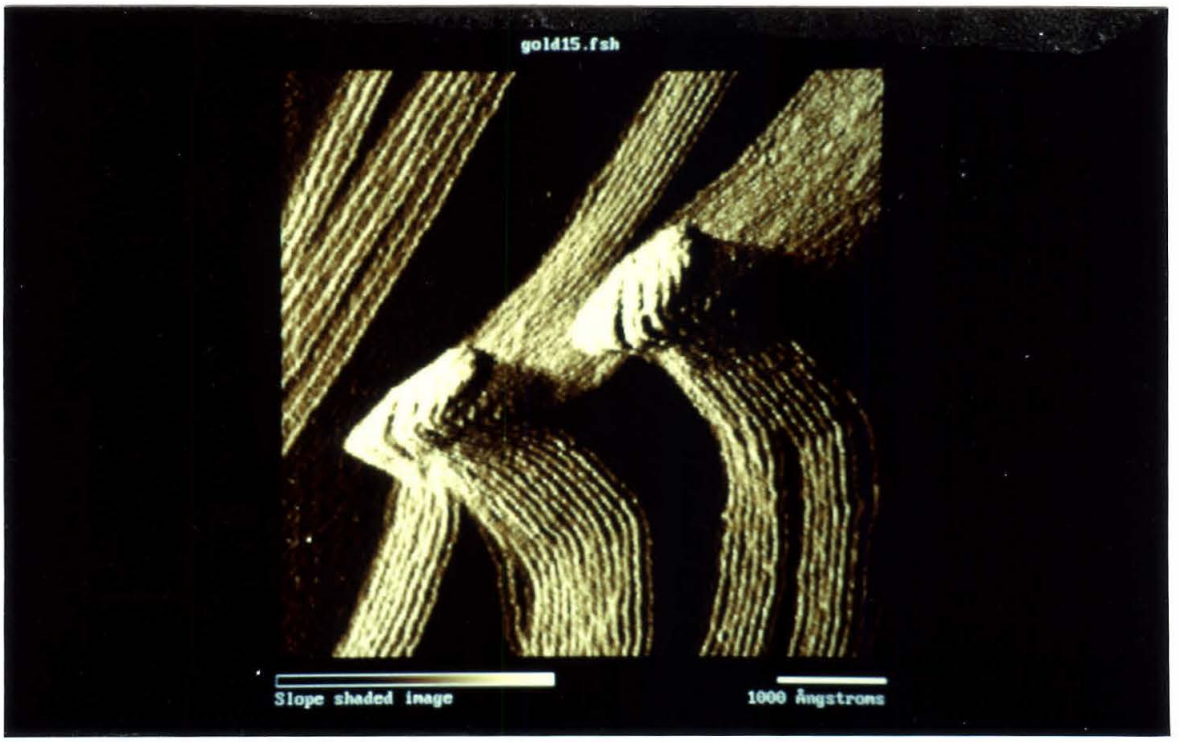

Figure A.3. Reduced magnification image of Figure A.2 and surrounding area. Brightness proportional to dZ/dX. (1.68 x 1.68 μm,

Figure A.3

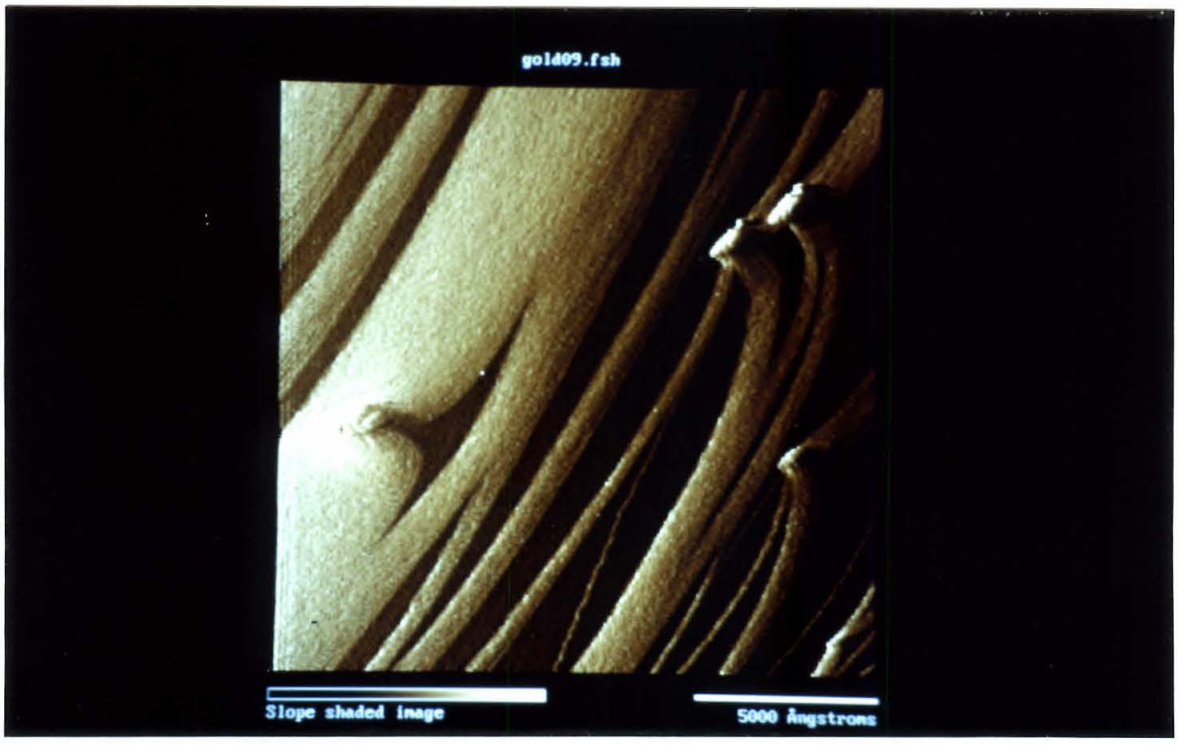

Figure A.4. Glide dislocations and pinned steps at a gold surface. Brightness is proportional to dZ/dX; positive slope from left is bright. (1.68 x 1.68 μm, 6.7 μm/s, -0.25 V sample, 0.05 nA constant current.)

Figure A.4

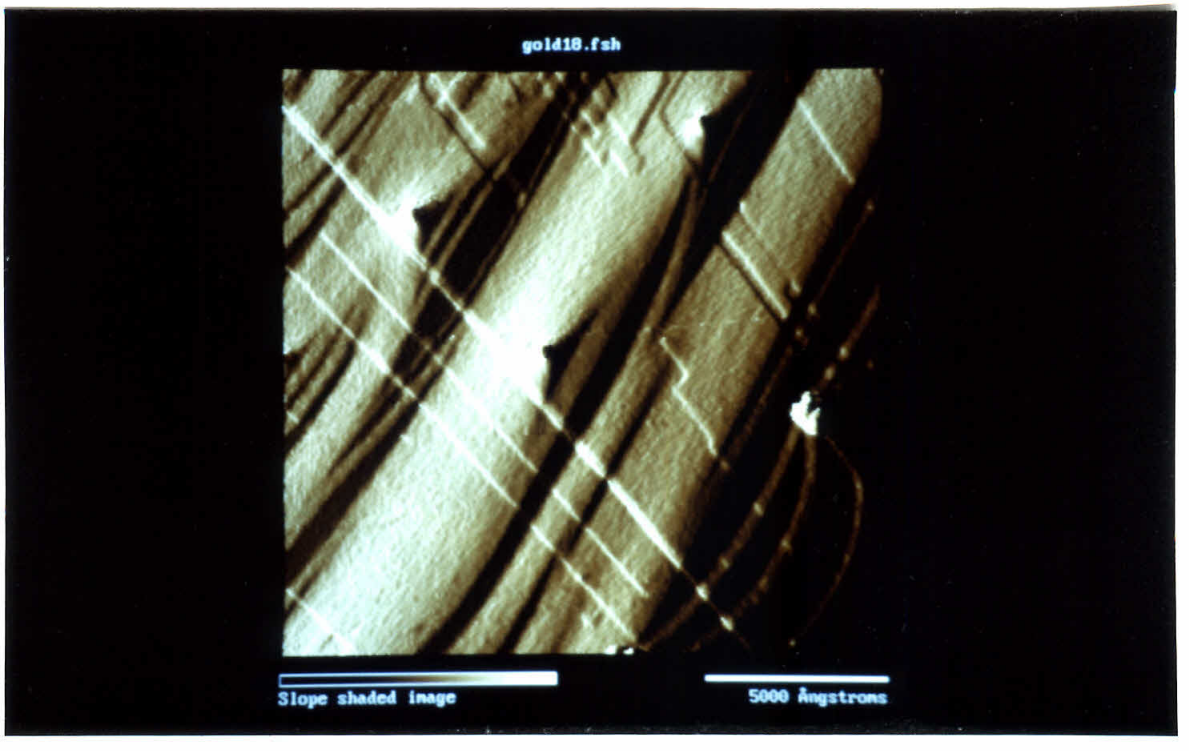

Figure A.5. The Orowan mechanism. Figure from M. Mundschau, E. Baur, and W. Telieps, *Surf. Sci.* **223,** 413-423 (1989).

Figure A.5

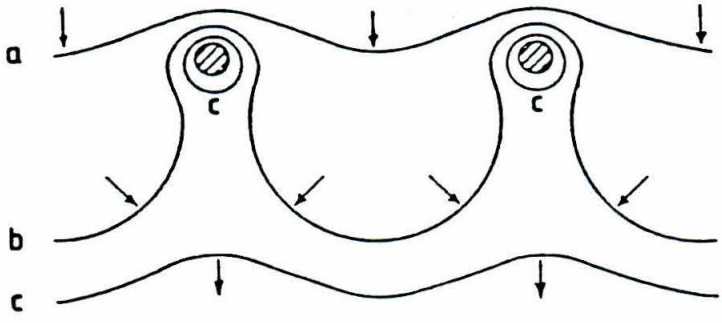

Figure A.6. Si steps pinned at impurities on a disordered (111) surface. Brightness is proportional to height. (0.40 x 0.40 μm, 500 x 100 pixels, 1 nA constant current.)

Figure A.6

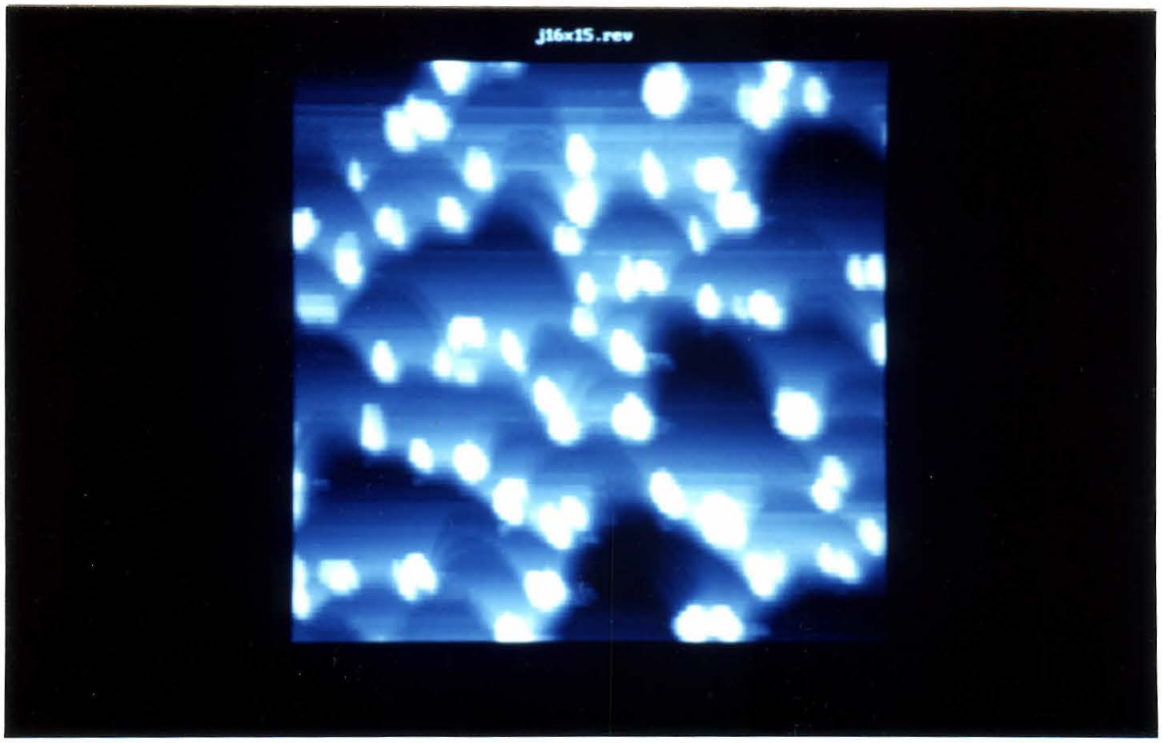

Figure A.7. Si steps pinned at impurities on a 7x7 reconstructed surface. Brightness is proportional to dZ/dX; upward slope from the left is bright. (0,425 x 0,343 μm, 250 x 250 pixels, 0.8 μm/s, 2 V sample bias, 1 nA constant current.)

Figure A.7

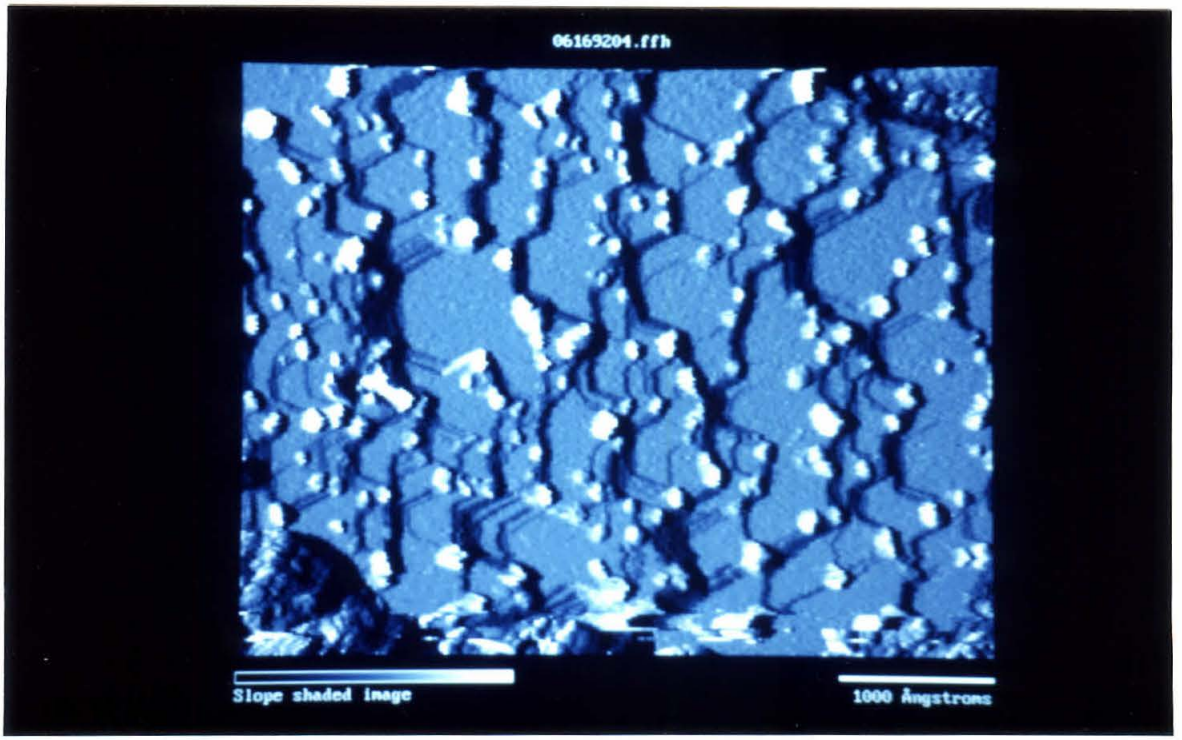

References

1. W. A. Tiller, Materials Science and Engineering 201A class notes, Fall 1988, Stanford University.

Appendix B: Enhancements of the Kramar UHV STM

Overview of the Kramar UHV STM System

The starting point for the work presented in Chapters 4 and 5 was the UHV STM system developed by John Kramar, Michael Weimer, and Chunli Bai.[1] It served as the foundation for the enhancements described below. The "IBM-pocket-type" head[2] has an XYZ piezoelectric-tripod-mounted tip and a piezoelectric "louse" sample positioner. The primary vibration isolation is a two-stage spring suspension with magnetic eddy current damping; the inner and outer stage first resonances are ≤1 Hz and 3-20 Hz in all six fundamental modes, respectively. A diagram of the ion-pumped UHV system is shown in Figure B.1. Integral-type analog feedback and computer-controlled rastering/data acquisition are used. Block diagrams of the feedback loop and digital control system are shown in Figures B.2 and B.3.

Each high voltage amplifier (X, Y, and Z) is equipped with x1 and x15 summing inputs. In the original configuration, the integrator output was connected to Zx15. Zx1 was used for ac modulation input during barrier-height imaging or digital tip-height ramping during approach. The scan area

was selected by attaching raster DACs to either X and Y x1 or x15 inputs. Six additional ADC channels were available.

Rudimentary FORTRAN/Assembly software routines for control, data acquisition, and display were available. "Walk," and "Approach" programs controlled the louse. Serial-prompt programs controlled "slow scan," "fast scan," and "I vs. V curve" data acquisition. A basic menu-driven "Plot" program allowed image display in xy-recorder-type y+z line-plots and top-view gray scale as well as cursor-controlled distance measurements in "DAC units," the fundamental digital step size.

Hardware Enhancements

Imaging, Spectroscopy, and Data Archiving

Several changes and additions were made to the basic hardware configuration of the system. Two additional DACs were dedicated to the raster generation eliminating the necessity of moving wires between x1 and x15 inputs to change scan range. An analog raster rotator[3] with DAC controllable rotation was added to the low-voltage raster loop. An instrumentation amplifier was added between the electrometer[4] and tunneling-current ADC for the Chapter 4 spectroscopy measurements. A switching and scaling module was added between the lockin-amplifier modulation output and x1 Z input for more convenient barrier-height imaging control. The Zx1 input was used exclusively for modulation; its use during automated approach was unnecessary. Additional ADCs were dedicated to barrier-height and conductance spectroscopy signals from lock-

in amplifiers. A 40 MByte tape drive was added to the system for data archiving. Support for an optical read-write drive with 128 MByte cartridges was also added, although the drive is usually dedicated to another system.

Tracking Tunneling Microscopy (TTM)

A tracking-tunneling microscopy (TTM) module was designed after Pohl *et al.*[5] In TTM, the tip is moved in a small circular path by a sinusoidal modulation added to the x and y piezo voltages; the modulation on the y-piezo is phase-shifted 90° relative to the x modulation. A lock-in amplifier detects in quadrature the component of the tunneling current at the modulation frequency. The output signals for the 0° and 90° components are input into integrator circuits, the outputs of which are summed into the x and y piezo voltages. The lock-in amplifier measures the local slope of the surface, and the integrators move the tip up (or down) the slope. Eventually, the tip is effectively locked onto and tracks a surface minimum or maximum (depending on the reference phase of the lock-in amplifier), as may be desirable for spectroscopy experiments. The x and y piezo voltages can be monitored to measure the sample drift. Schematic diagrams of the module panel and circuitry are shown in Figure B.4.

Software Enhancements

Data Acquisition / Instrument Control

FORTRAN data acquisition and instrument control routines were integrated into a flexible menu-driven program with many new features. The main menu is shown in Figure B.5. Submenus are available for spectroscopy.

One of the most useful additions is offset x-y scanning. The x15 DACs are used to center the high-resolution imaging window in any part of the full image window, and the x1 DACs are used to raster the tip for imaging. This allows scanning the full window at low resolution and selecting any feature for imaging at increased resolution. Another enhancement is the addition of pixel-correlated current-voltage spectroscopy. The scan can be interrupted at any time for acquisition of an I vs. V curve by pressing 'p' during scanning, or spectra can be obtained at each nth pixel for current imaging tunneling spectroscopy (CITS -- see below and Figure B.9).[6] Work function and tunneling spectroscopy options toggle storage of additional ADC channels as image files. A 'pulse' option sends a variable length and height voltage pulse to the tip for tip or sample modification. A new delay function is incorporated for timed operations, replacing the original one which had only millisecond resolution. Header files are expanded to include more detailed parameter and options information. New automated approach and translation routines are incorporated to control the Micro Pulse translation stages.

A stand-alone spectrum analyzer program "Specalyze" was written in the C programming language. It uses a 12 bit ADC (Data Translation 2821DF) and a Tall Tree Systems 2 MB memory expansion card to store up to 2^{15} samples at any sampling rate up to 50 kHz for frequency analysis of bandwidth-limited signals up to 25 kHz. The data are Fourier transformed with linear or frequency-dependent averaging for display in a standard plotting program. This program is useful for troubleshooting and for laboratory vibration analyses. Time and frequency data for a test signal (G4

on a b-flat trumpet) are shown in Figure B.6 which demonstrate a high quality spectrum analysis.

Image Processing

The FORTRAN-based "Plot" program was expanded into a powerful image display program. It was used for presentation of nearly all of the figures in R. J. Driscoll's and S. M. Baker's theses[7,8] and for those in chapters 4 and 5 of this work. The main menu is shown in Figure B.7.

3-d Presentation, Cropping, Skewing, Scaling, and Stereo Viewing

The most significant addition is three-dimensional projection of data files with simulated perspective. The submenu (option 'L') for three-dimensional data handling is shown in Figure B.8. Wire frame and space-filling presentation formats are available as is the more rapid recorder-plot Y+Z line presentation. Other options on this menu include image cropping, flexible display-screen placement (for assembling Mosaic images and images too large to fit into the computer memory), simulated light shading (brightness proportional to slope, dx/dz), non-orthogonal plot axes (for thermal-drift compensation) and floating-point image scaling (*e.g.*, for plotting 1.5:1 X:Y size ratios rather than integer ratios as was previously required). Another display option is stereo viewing.

Color Lookup Tables

After the 3-D data-presentation, the most noticeable change is the addition of color. New color lookup tables can be selected at several different

menu levels. The lookup tables, themselves, are created and edited by a stand-alone program written in C.

CITS Data Processing

CITS images can be plotted as a function of voltage. An example using the Si (111) 7x7 reconstruction is shown in Figure B.9. Current-voltage curves associated with any pixel in the topographic image are displayed interactively; as a cursor is moved across the image, corresponding spectra are shown. The cursor can be "scanned" to show new I vs. V curves at approximately 5/second. Spectra can be grouped and averaged by specific image area or for specific Z-ranges. The latter feature is useful for averaging I vs. V curves obtained exclusively over atoms or holes.

Cursor Menu Options

The cursor menu is shown in Figure B.10. On-screen display of interpolated line-cuts and drawing features (colored lines and areas) are added as are distance measurements in Å units. The menu also includes the option of subtracting a user-defined plane from the Z-data file and the CITS I vs. V curve averaging options.

Other Options

Edge enhancement, image-color histogram display, internal access to DOS, and weighted three-point averaging features were also added. Stand-alone programs were written in C for histogram equalization, 1-D and 2-D

Fourier transform image filtering (low-pass, high-pass, and notch), and statistical glitch removal.

Figures -- Appendix B

Figure B.1. Schematic representation of the Kramar UHV system, including the STM chamber, sample preparation chamber, and vacuum load lock with long stroke translator. (Drawn by John Kramar).

Figure B.1

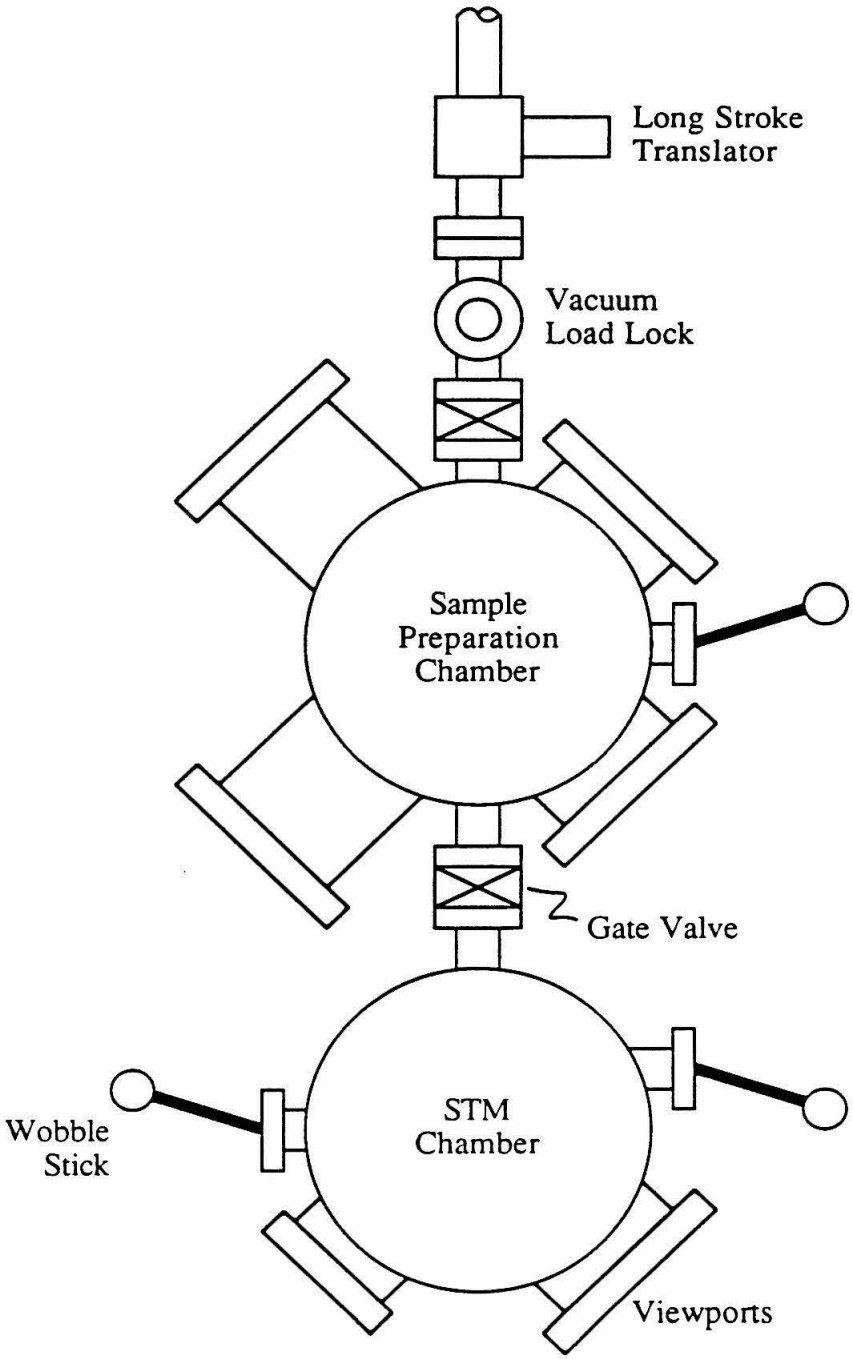
Long Stroke
Translator
Vacuum
Load Lock
Sample
Preparation
Chamber
Gate Valve
STM
Chamber
Wobble
Stick
Viewports

Figure B.2. Block diagram of the Kramar STM feedback control electronics. (Drawn by John Kramar).

Figure B.2

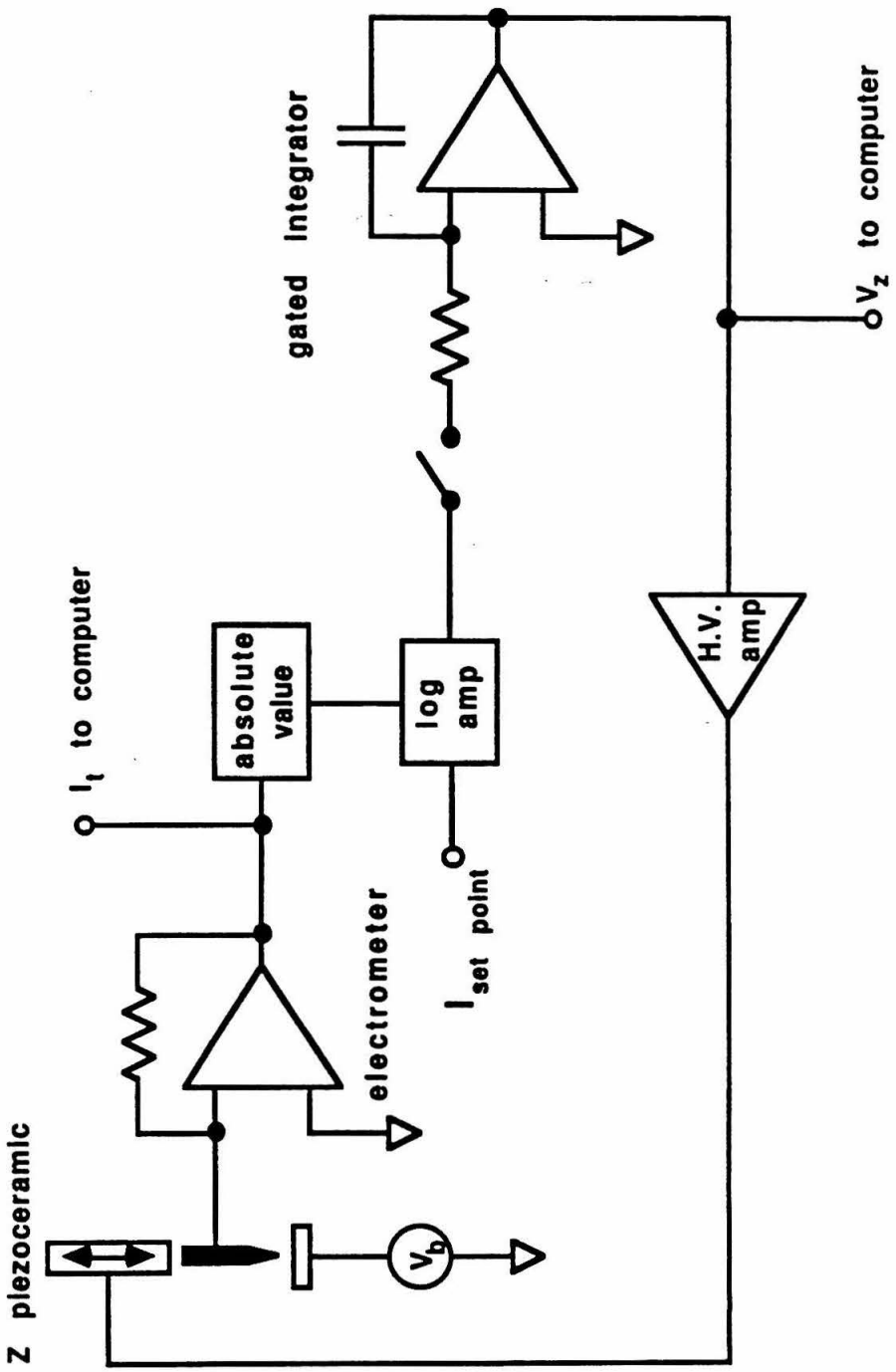
gated integrator
V_z to computer
H.V. amp
absolute value
log amp
I_t to computer
$I_{set\ point}$
electrometer
Z plezoceramic
V_b

Figure B.3. Block diagram of the microprocessor-based control system for the Kramar UHV STM system. (drawn by Michael Weimer).

Figure B.3

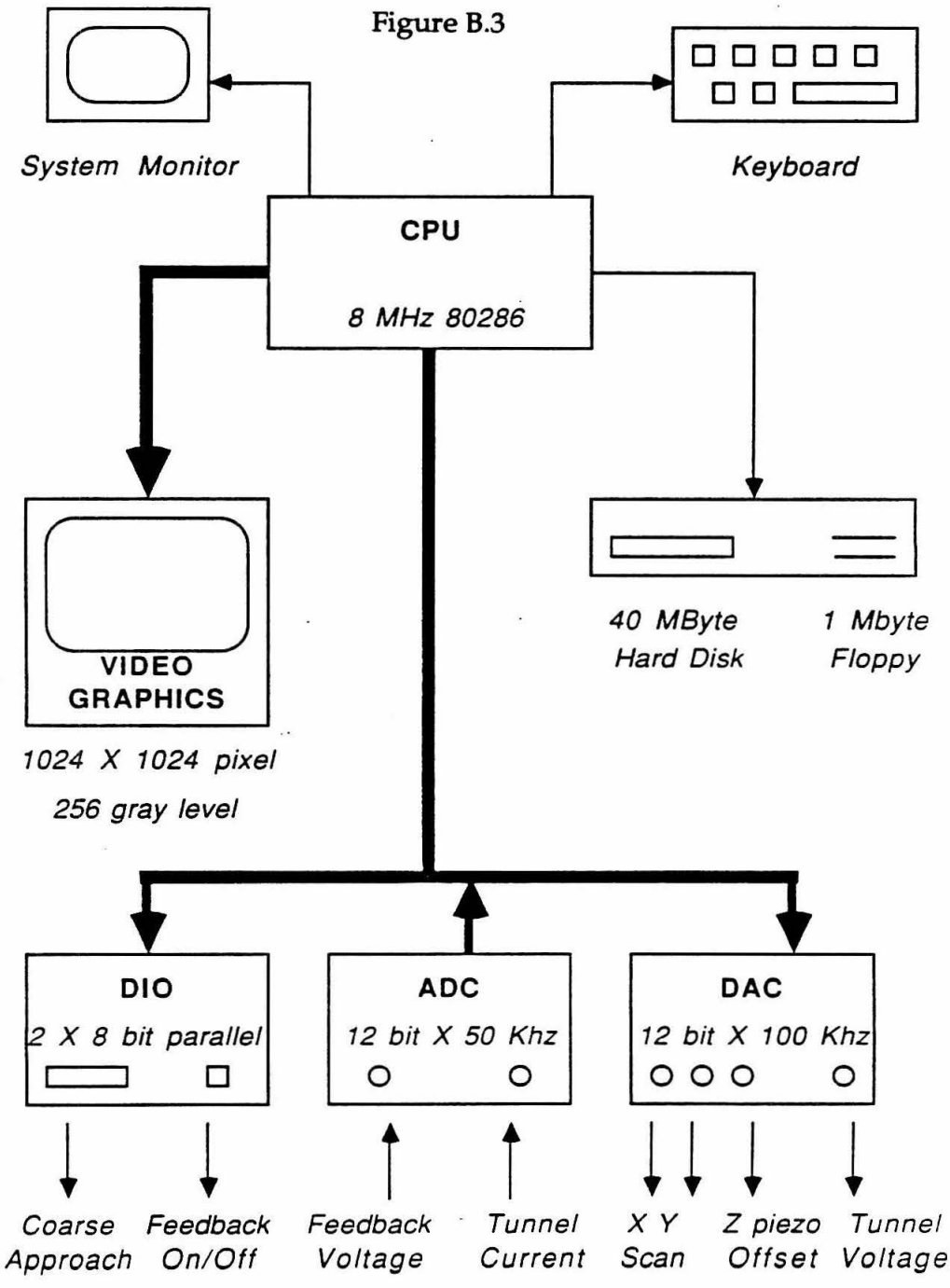

(figure from Michael Weimer)

Figure B.4. Tracking tunneling microscopy module panel and circuit schematic diagram.

Figure B.4a

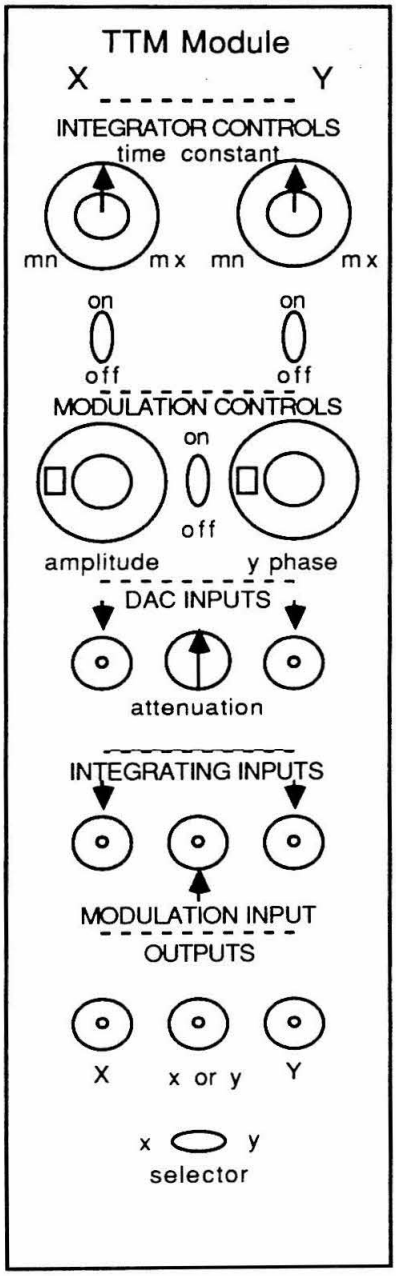
TTM Module
X
Y
INTEGRATOR CONTROLS
time constant
mn
mx
mn
mx
on
off
on
off
MODULATION CONTROLS
on
off
amplitude
y phase
DAC INPUTS
attenuation
INTEGRATING INPUTS
MODULATION INPUT
OUTPUTS
X
x or y
Y
x
y
selector

Figure B.4b

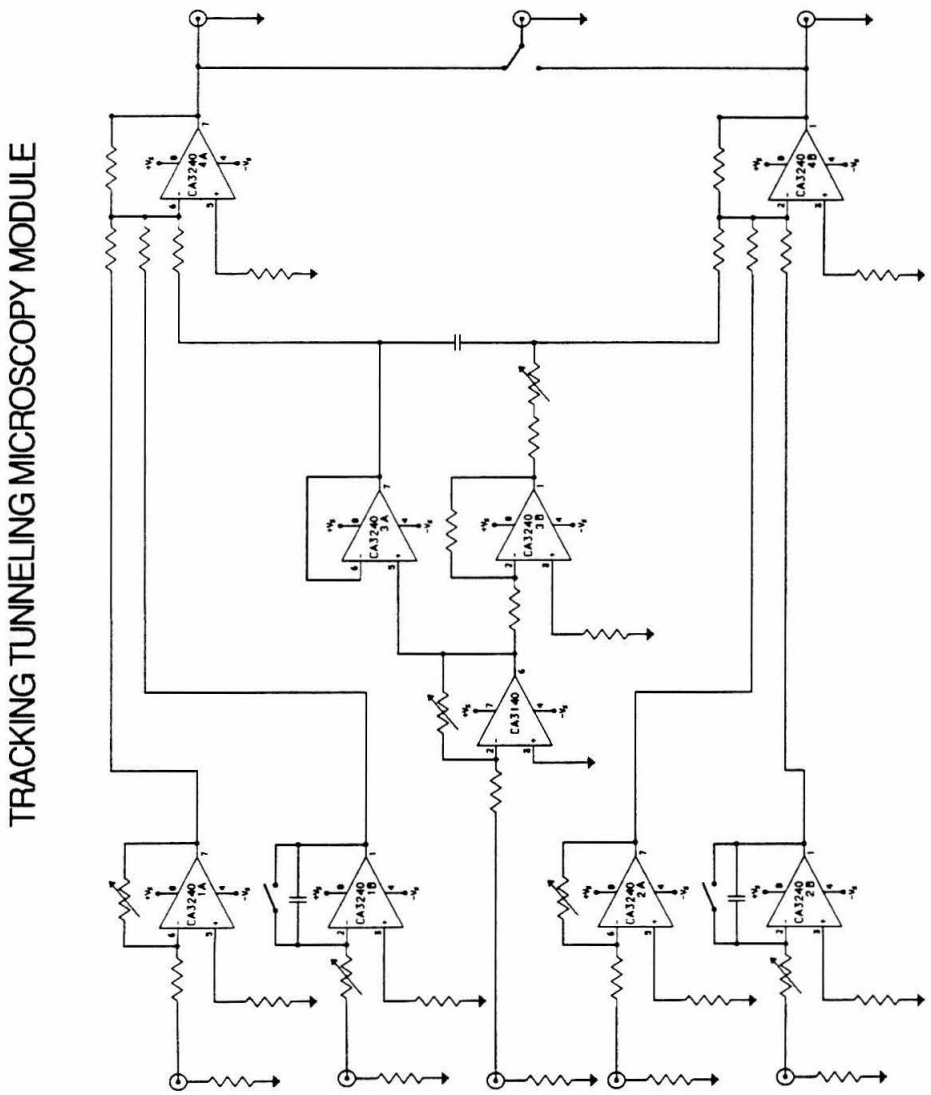
TRACKING TUNNELING MICROSCOPY MODULE
CA3240 4A
CA3240 4B
CA3240 3A
CA3240 3B
CA3140
CA3240 1A
CA3240 1B
CA3240 2A
CA3240 2B

Figure B.5. Menus from 'SCAN.EXE,' an STM data acquisition program. The main menu and the current-voltage spectroscopy submenu accessed by *p*ausing during a scan (pressing 'p') are shown.

Figure B.5

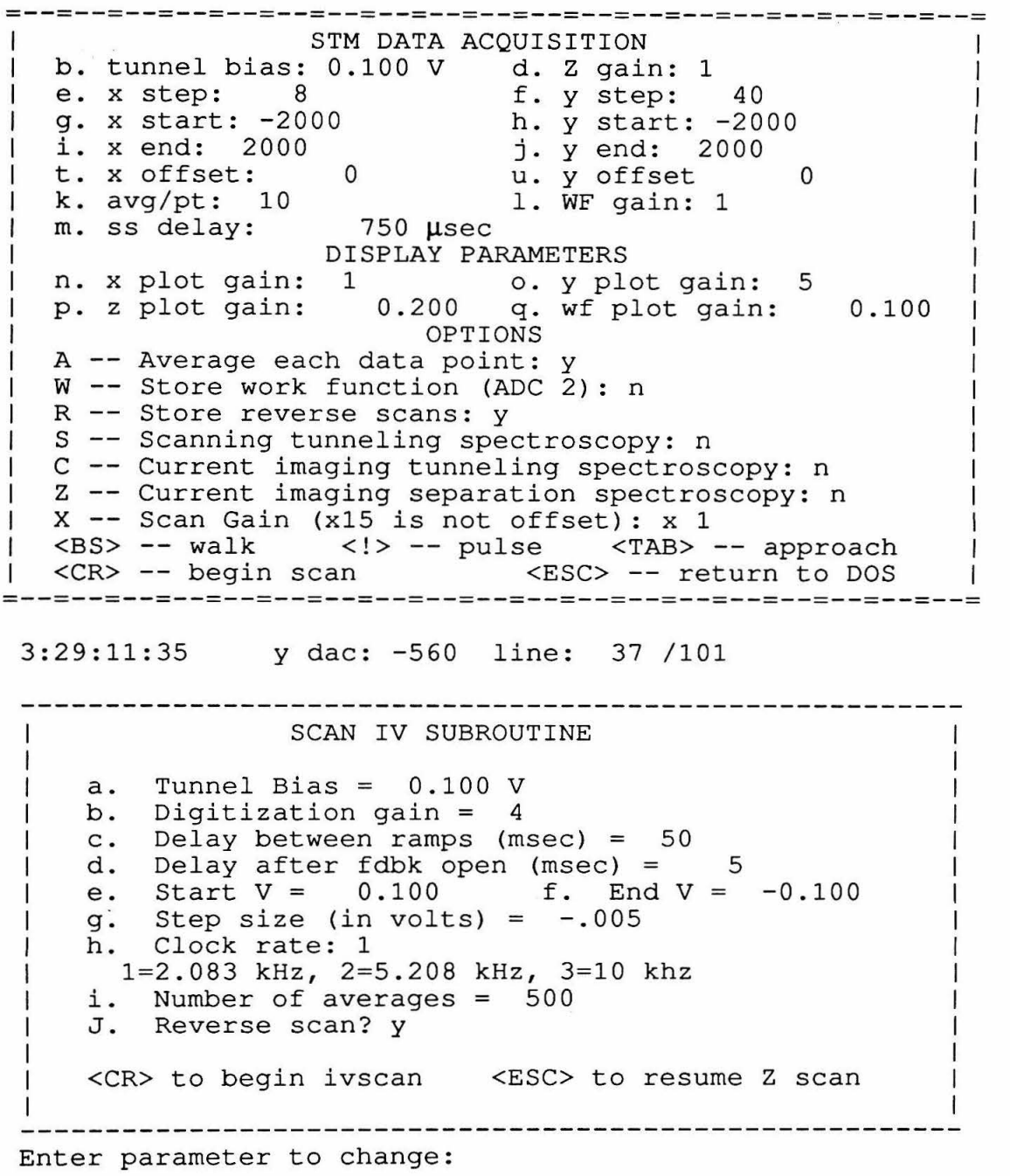
STM DATA ACQUISITION
b. tunnel bias: 0.100 V
d. Z gain: 1
e. x step: 8
f. y step: 40
g. x start: -2000
h. y start: -2000
i. x end: 2000
j. y end: 2000
t. x offset: 0
u. y offset 0
k. avg/pt: 10
l. WF gain: 1
m. ss delay: 750 µsec
DISPLAY PARAMETERS
n. x plot gain: 1
o. y plot gain: 5
p. z plot gain: 0.200
q. wf plot gain: 0.100
OPTIONS
A -- Average each data point: y
W -- Store work function (ADC 2): n
R -- Store reverse scans: y
S -- Scanning tunneling spectroscopy: n
C -- Current imaging tunneling spectroscopy: n
Z -- Current imaging separation spectroscopy: n
X -- Scan Gain (x15 is not offset): x 1
<BS> -- walk
<!> -- pulse
<TAB> -- approach
<CR> -- begin scan
<ESC> -- return to DOS
3:29:11:35
y dac: -560
line: 37 /101
SCAN IV SUBROUTINE
a. Tunnel Bias = 0.100 V
b. Digitization gain = 4
c. Delay between ramps (msec) = 50
d. Delay after fdbk open (msec) = 5
e. Start V = 0.100
f. End V = -0.100
g. Step size (in volts) = -.005
h. Clock rate: 1
1=2.083 kHz, 2=5.208 kHz, 3=10 khz
i. Number of averages = 500
J. Reverse scan? y
<CR> to begin ivscan
<ESC> to resume Z scan
Enter parameter to change:

Figure B.6. Output from the spectrum analysis program 'SPECALYZ.EXE' showing a note from a trumpet sampled at 50 kHz for 20 ms (1024 points). (Only part of the time record is shown). The program can acquire up to 32767 points at any sampling rate up to 50 kHz for frequency analysis of bandwidth-limited signals from dc up to 25 kHz. Data averaging options are available which allow nonlinear frequency resolution and reduce the output file size.

B flat trumpet G4 time spectrum

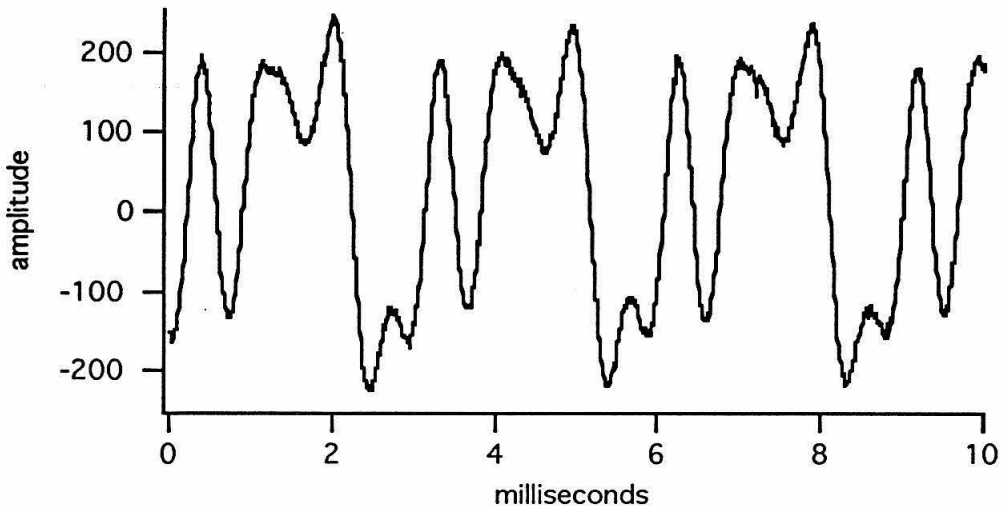

B flat trumpet G4 frequency spectrum

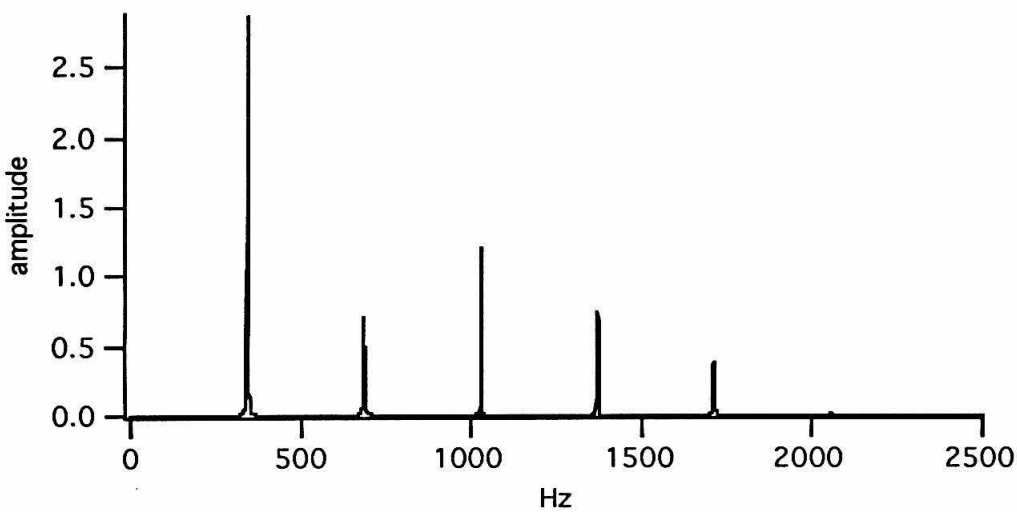

Figure B.7. Main menu of the image processing and presentation program 'PLOT.EXE.'

Figure B.7

```
------------------------MENU-------------------------
|                                                    |
|          A --    Print ASCII file                  |
|          B --    Print BINARY file                 |
|          C --    Go to CURSOR menu                 |
|          D --    Enter new data file               |
|          E --    Edge Enhancement                  |
|          F --    Print cropped BINARY file         |
|          G --    Draw grayscale image              |
|          H --    Print histogram                   |
|          I --    Build current image (CITS)        |
|          L --    Draw line plot image              |
|          M --    Move plot center                  |
|          N --    New color lookup table            |
|          O --    Out to secondary DOS              |
|          P --    Planar background subtraction     |
|          R --    Rewrite header file               |
|          S --    Sliding window average            |
|          T --    Print standard deviation file     |
|          W --    Weighted 3 point average          |
|          Q --    Return to DOS                     |
----------------------------------------------------

Enter MENU selection:
```

Figure B.8. 'Line Plot' submenu of the image processing and presentation program 'PLOT.EXE.' Three dimensional projections, slope-keyed coloration, cropping, and nonorthogonal plot axes are selected in this menu.

Figure B.8

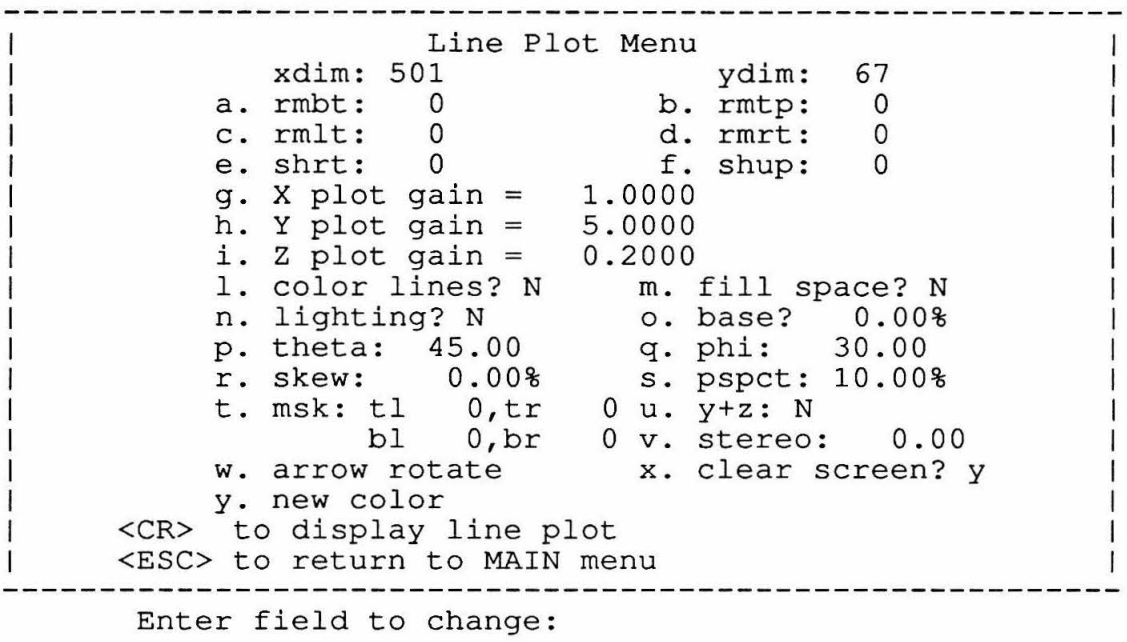
Line Plot Menu
xdim: 501
ydim: 67
a. rmbt: 0
b. rmtp: 0
c. rmlt: 0
d. rmrt: 0
e. shrt: 0
f. shup: 0
g. X plot gain = 1.0000
h. Y plot gain = 5.0000
i. Z plot gain = 0.2000
l. color lines? N
m. fill space? N
n. lighting? N
o. base? 0.00%
p. theta: 45.00
q. phi: 30.00
r. skew: 0.00%
s. pspct: 10.00%
t. msk: tl 0,tr 0
u. y+z: N
bl 0,br 0
v. stereo: 0.00
w. arrow rotate
x. clear screen? y
y. new color
<CR> to display line plot
<ESC> to return to MAIN menu
Enter field to change:

Figure B.9. Example of Current Imaging Tunneling Spectroscopy. A double-height step edge on a Si(111) 7x7 reconstructed surface was imaged at constant current with +2.0 V sample bias. At every 5th pixel of the 500 x 100 pixel image, a current vs. voltage spectrum was stored with 50 points from -2.0 V to + 2.0 V sample bias. A 100 x 100 pixel current image can be constructed for any voltage in the I vs. V spectra. Clockwise from upper left, Z-data, current at +2.0 V, current at -2.0 V, and current at +1.0 V are shown. At positive sample bias, unfilled electronic states are imaged, while at negative bias, the filled are probed. The faulted and unfaulted halves of the unit cell appear markedly different in the negative sample bias image; the left-pointing subunits are the unfaulted halves.

Figure B.9

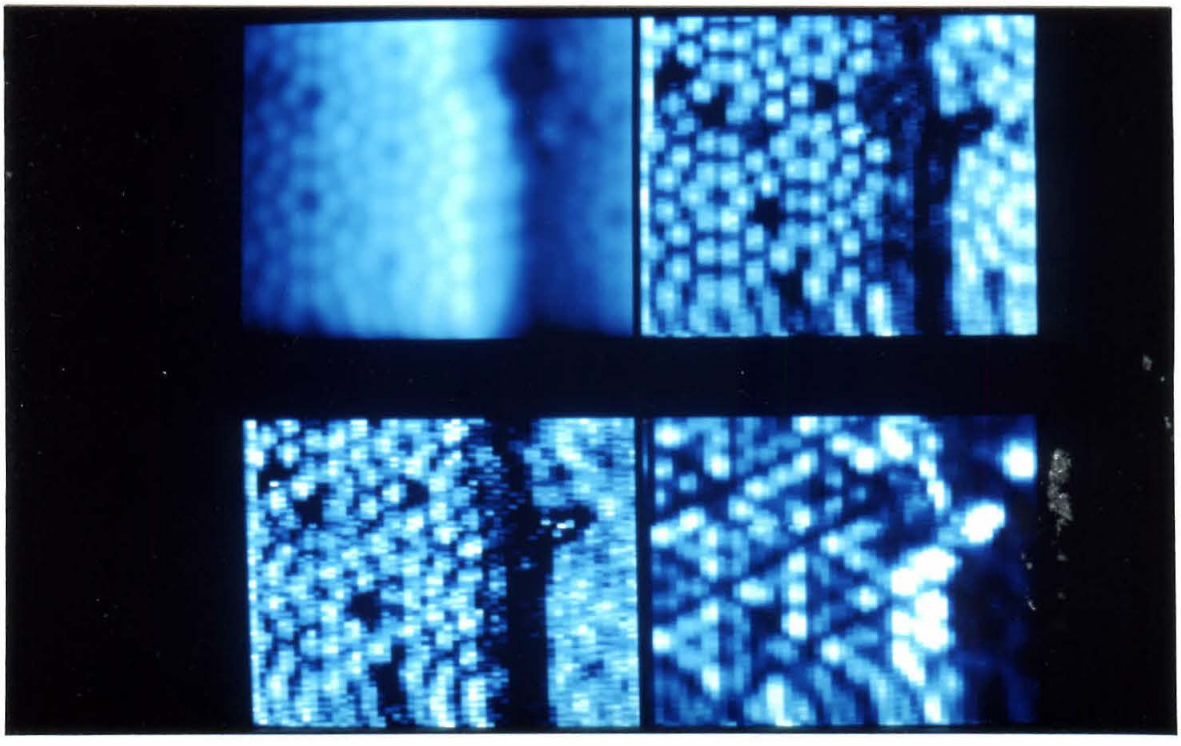

Figure B.10. 'Cursor' submenu of the image processing and presentation program 'PLOT.EXE.' Distance measurements, interpolated tip trajectories, and CITS I vs. V curve display and averaging options are controlled from this menu.

Figure B.10

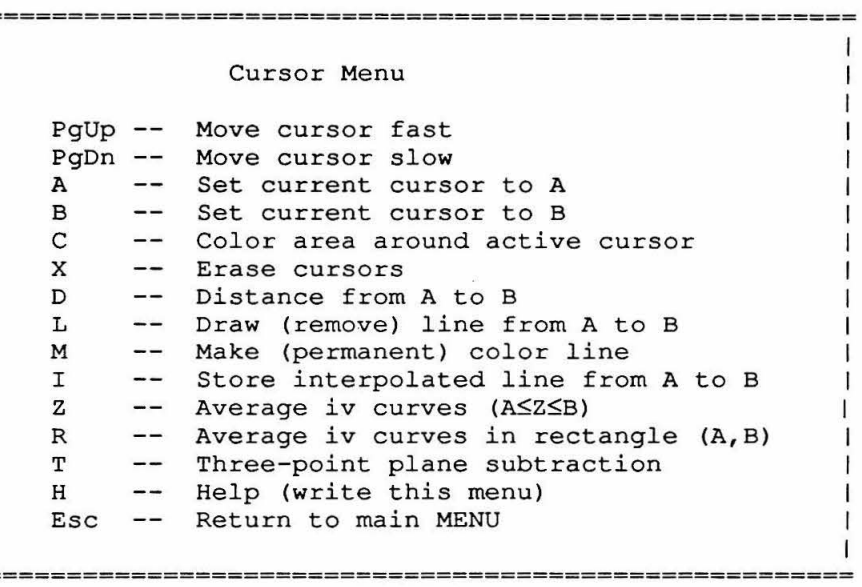


```
A: X = 1760 DAC units; Y = 1320 DAC units; Z =    0.19 Å (13.1 Å/V)
B: X = 2320 DAC units; Y = 1320 DAC units; Z =    0.13 Å (13.1 Å/V)
   XY =  560.00 DAC units        Z =    1.00 ADC units  = <z> *  1.00
   XY =  40.742 Å   (14.9 Å/V)   Z =   0.064 Å   (13.1 Å/V)
```

References

1. John A. Kramar, "Scanning tunneling microscopy and spectroscopy of molybdenum disulfide," Ph.D. thesis, California Institute of Technology (1990).
2. Ch. Gerber, G. Binnig, H. Fuchs, O. Marti, and H. Rohrer, *Rev. Sci. Instrum.* **57,** 221-4 (1986).
3. Model 6125A, Optical Electronics, Inc., Tucson AZ.
4. 427 Current Amplifier, Keithley Instruments, Inc. Cleveland, OH.
5. D. W. Pohl and R. Moller, *Rev. Sci. Instrum.* **59,** 840 (1988).
6. R. J. Hamers, R. M. Tromp, and J. E. Demuth, *Phys. Rev. Lett.* **56,** 1972 (1986).
7. Robert J. Driscoll, "Scanning tunneling microscopy and spectroscopy: I. Semimetals and semiconductors, II. Atom-resolved imaging of DNA," Ph.D. thesis, California Institute of Technology, Pasadena, CA (1993).
8. Shenda M. Baker, "Scanning tunneling microscopy and spectroscopy of silicon and carbon surfaces," Ph.D. Thesis, California Institute of Technology (1992).

Appendix C: Implementation of a Digital Control System

As part of this work, a high-performance digital scanned probe microscope control system was built and debugged. The work contributed to the development of the electronics which were designed by Steve Clark, and readers are referred to his thesis for a detailed description.[1] A block diagram is shown in Figure C.1, and its performance is documented in Appendix C. SPM operating system software for the control system was designed by David Baselt, and the reader is referred to his thesis and Appendix E for details. STM-specific parts, performance and software modifications are described below.

STM Version of Clark's SPM Electronics

Z / Tip Voltage Module

A DAC module for Z and tip voltages was based on the "Z-Axis/Approach Motor Drive Board.[2]" The PA01 motor-driver was replaced with an OP27 operational amplifier to function as the STM tip voltage source. Summing inputs were added to both the Z and tip output amplifiers for use in modulation experiments. A relay-switch with TTL-compatible control

voltage was added to the Z high voltage amplifier for remote selection of full (±188 V) and 1/4 (±47 V) range. Schematic diagrams of the Z-Axis/Tip voltage board circuitry are shown in Figure C.2.

Micro Pulse Control Module

The Micro Pulse Systems E-111 drive circuit for the MPS-LTSTM was interfaced to the digital control system thorough mounting in a modified single-width-NIM module equipped with the Clark-standard address decoder and dataline buffers. The oscillator is toggled on and off by writing any value to address 0x800015. The direction is set and the oscillator disabled by writing an integer 0-15 to address 0x800014; the four data bits select the actuators energized (up, down, left, and right). The TTL levels are converted to ECL levels for compatibility with the MPS interface. A schematic diagram of the interface circuitry is shown in Figure C.3. A cable from the module connects to the E-109 drive circuit for operation of the MPS-UHV-STM head.

Performance Limitations

Differential Nonlinearity

As in any digital-to-analog converter (DAC) system, differential nonlinearities exist in this system. The 18-bit DAC used is based on 18 current sources, one for each bit, which are summed to produce any of 2^{18} output currents. When a new current source is switched in or out (as happens, for example, at all four bits when digital code 0111 is incremented to 1000), any error in the accuracy of the current source appears as a "differential nonlinearity" in the analog output. Analog voltage error can be as large as

two LSBs. These nonlinearities can appear as artifactual lines (actually contours of constant digital Z-value, X-value, or Y-value) in images of extremely flat surfaces. An image showing the differential nonlinearity artifact is shown in Figure C.4. In order to reduce these effects on high-resolution images and to improve imaging capabilities for low-corrugation surfaces, a divide-by-four option was added at the output stage of the Z-DAC.

Digital Modulation

An attractive aspect of a digital control system is the possibility of generating complex waveforms for compensation of scanner nonlinearities or adding sinusoidal modulations to control signals (*e.g.*, Z or V) for derivative spectroscopies. (See Appendix E.) However, because of differential nonlinearities, small-amplitude modulations of changing outputs (*e.g.*, Z modulation in barrier height imaging) should not be effected at the control signal DAC. The analog modulation amplitude can change with the base signal (even though the digital amplitude is constant) introducing systematic error into the measurement. The proper way to add modulation digitally is to use a separate DAC to generate the modulation and sum the modulation and control signals at the analog output stage.

Lock-in Amplifier Emulation

Along with digital modulation, the digital signal processor based system offers the option of lock-in amplifier emulation. Algorithms are given in Appendix E. Digitally detected first and second derivatives of a structured

voltage test signal were obtained with a digitally superposed sinusoidal modulation, f = 1 kHz. The ramp was digitized using the system's 16 bit ADC. The first and second derivatives were extracted by autocorrelation of the signal with sinusoids at f and 2f. The derivatives measured using digital lock-in detection appeared the same as those obtained numerically. Further testing, however, showed that the digital lock-in detection did not work as expected. The measured noise level on derivative spectra should be inversely proportional to the square-root of the number of cycles over which the signal is averaged. Such does not occur in this system. The problem probably originates in a programming error or ADC phase jitter. Until the problem is corrected, derivative spectroscopy experiments requiring bandwidth limiting should be conducted using an external lock-in amplifier.

Adaptation of Baselt's SPM Operating System

The SPM operating system developed by David Baselt is optimized for scanning force microscopy. It supports standard imaging modes for scanning tunneling microscopy, but does not include pixel-correlated spectroscopy options. As part of this work the code was modified for operation of the Low T and UHV Micro Pulse Systems-based STMs. Translation and automated approach routines and macros were developed for the Micro Pulse stages. Four-dimensional data handling capabilities were woven into the PC code for pixel-correlated spectroscopies like CITS. The DSP code was rewritten support several new operating modes. It now calls different interrupt handling routines for feedback with different modulation options (none, V, Z, X, V & Z). This allows optimization of sampling rate for each spectroscopy

option. First and second derivative spectroscopy features were added. An option for writing data files in floating point format was added to preserve precision greater than 16 bits achieved through signal averaging. (This is especially important in STM imaging of very flat surfaces). Improved digital oscilloscope features were added. Although the Baselt operating system and STM operating system were initially fully compatible, they have diverged. The Baselt Operating System now includes many features which would be useful in the STM code, while the STM code contains many STM-specific options which are unlikely to be useful additions to the Baselt code. The Baselt Operating system is also fully documented and has a detailed users manual. A new user on the UHV STM should dissect and understand the STM code and then update it to incorporate the new features of the Baselt Operating System. The parameters of many commands are different. They should be made consistent with the Baselt manual where possible, and a manual supplement for the UHV-STM operating system should be written. The interrupt service routines and a portion of the DSP-resident code listing are included below after the figures. The complete DSP-resident and PC-resident code listings are available in the laboratory.

Figures -- Appendix C

Figure C.1. Block diagram of the scanned probe microscope control system. (Drawn by S. M. Clark).

Figure C.1

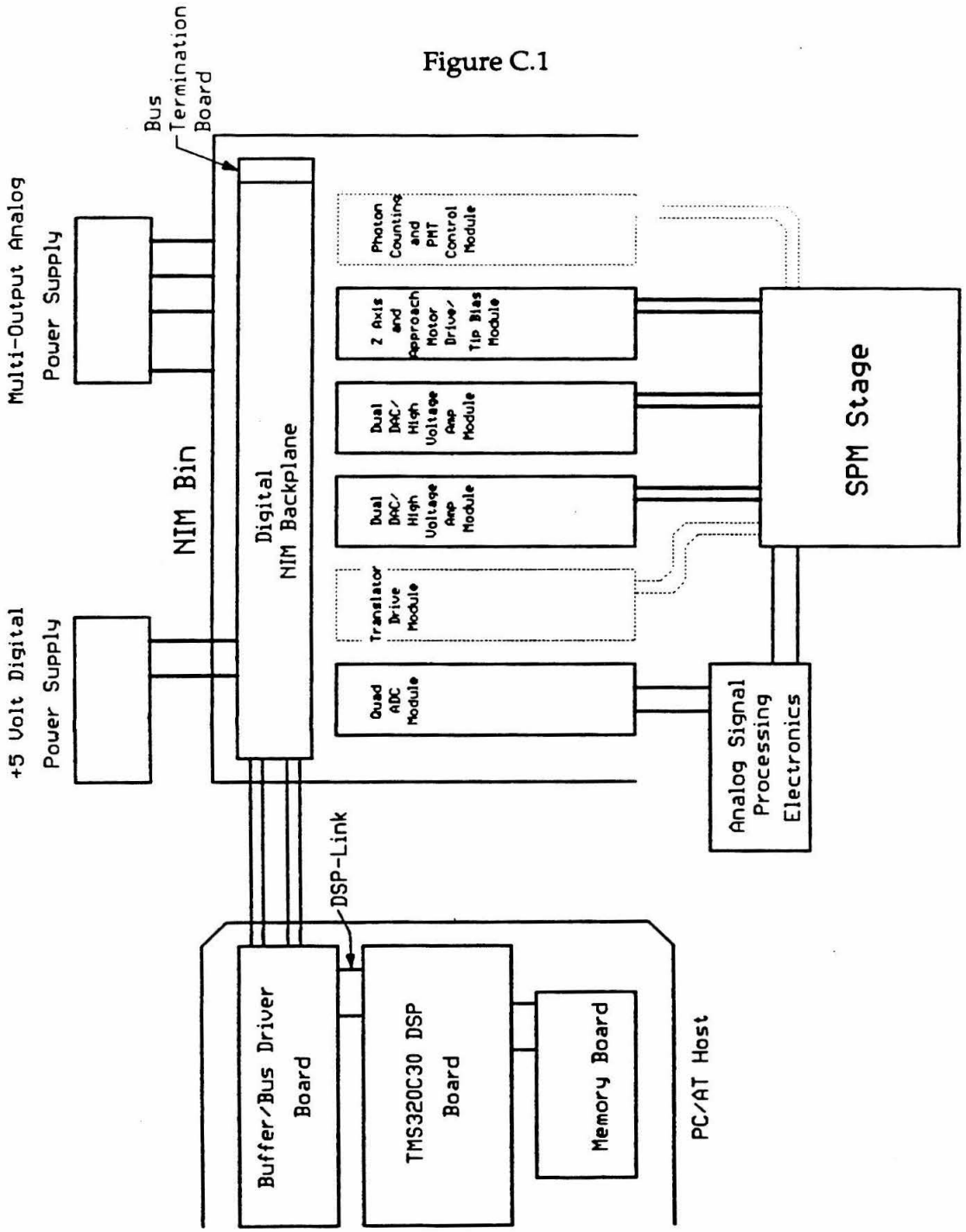
Bus Termination Board
Multi-Output Analog Power Supply
+5 Volt Digital Power Supply
NIM Bin
Digital NIM Backplane
Photon Counting and PMT Control Module
Z Axis and Approach Motor Drive/ Tip Bias Module
Dual DAC/ High Voltage Amp Module
Dual DAC/ High Voltage Amp Module
Translator Drive Module
Quad ADC Module
SPM Stage
Analog Signal Processing Electronics
DSP-Link
Buffer/Bus Driver Board
TMS320C30 DSP Board
Memory Board
PC/AT Host

Figure C.2. Schematic diagram of the Z-piezo and tip voltage circuitry.

Figure C.2

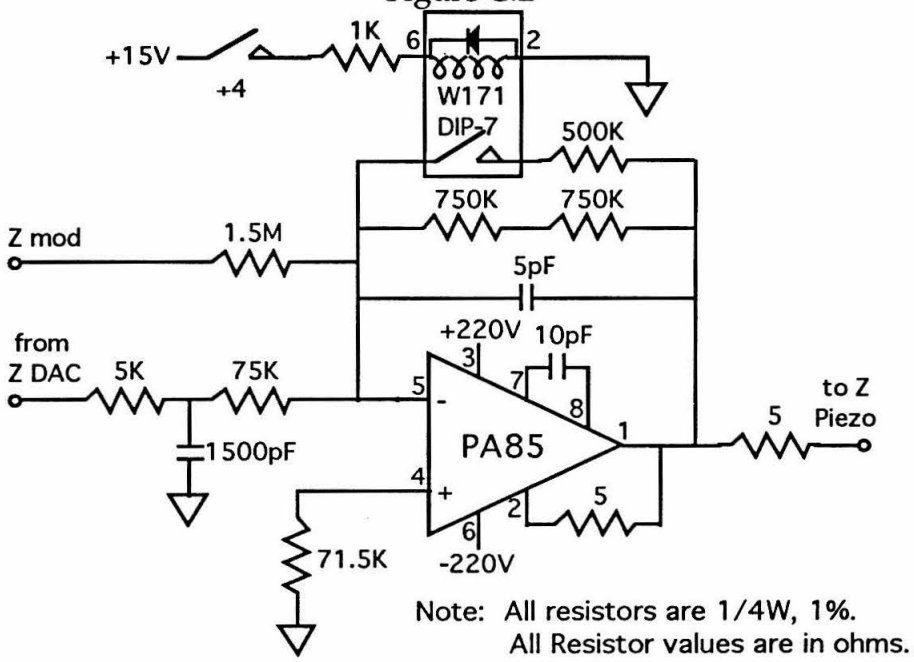
+15V
+4
1K
6
2
W171
DIP-7
500K
750K
750K
Z mod
1.5M
5pF
+220V
10pF
from
Z DAC
5K
75K
3
5
7
8
1
to Z
Piezo
5
1500pF
PA85
4
+
2
5
6
71.5K
-220V
Note: All resistors are 1/4W, 1%.
All Resistor values are in ohms.

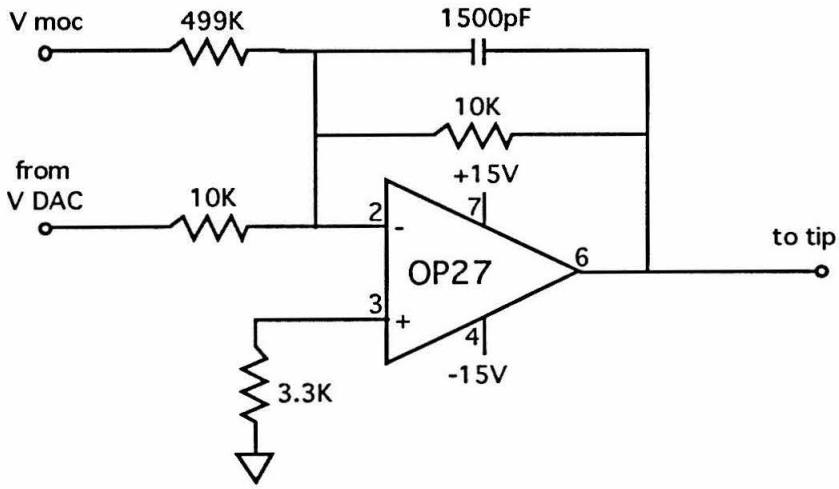
V moc
499K
1500pF
10K
from
V DAC
10K
+15V
2
7
to tip
OP27
6
3
+
4
-15V
3.3K

Figure C.3. Schematic diagram of the SPM control system / MPS driver interface.

Figure C.3

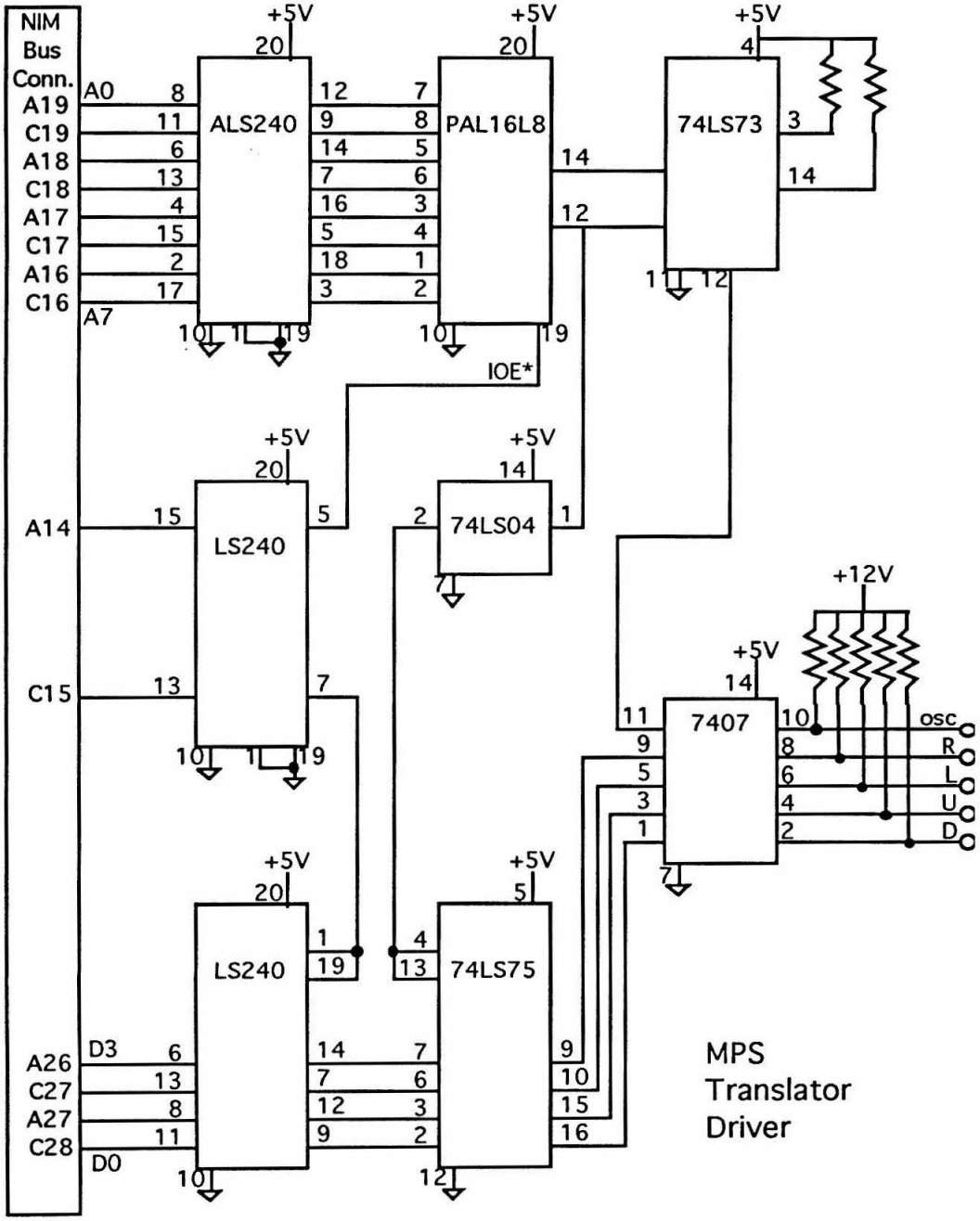
NIM
Bus
Conn.
A19
C19
A18
C18
A17
C17
A16
C16
A0
A7
ALS240
PAL16L8
74LS73
IOE*
A14
C15
LS240
74LS04
+12V
7407
osc
R
L
U
D
LS240
74LS75
A26
C27
A27
C28
D3
D0
MPS
Translator
Driver

Figure C.4. STM image showing DAC differential nonlinearity artifacts. A graphite sample was mounted with a substantial slope (from the X-Y plane) and imaged at 1 nA constant current with a dull tip such that atomic corrugation is not resolved. The most prominent diagonal lines result from differential nonlinearity at the 14th bit (bit 0 = MSB) in the Z DAC. The vertical lines result from differential nonlinearity in the X DAC.

Figure C.4

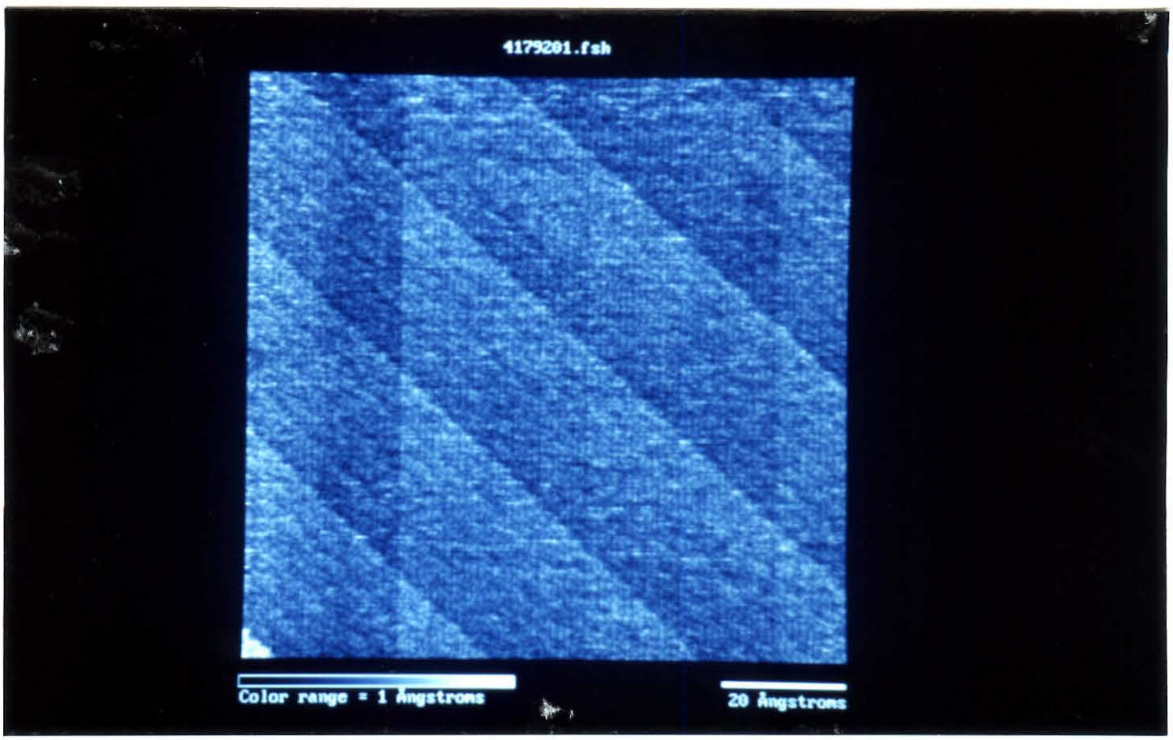

Code Listings

Interrupt Routines: INT.ASM

```
; INT.ASM:  FEEDBACK/LOCK-IN ROUTINES FOR CIT ELECTRONICS
; rotated ADC_channels up one so current is ADC_B.  changes indicated with @@
; 66 instructions (for feedback with dv if in range)          62 for no mod
;  +  10 I/O * 1 extra each                                   12 for no mod
;  +  1? pipeline conflict * 2 steps
;  +  21 access conflicts (for code in external RAM) * 1 step  16 for no mod
;  =  98 instruction cycles
;  +   7 extra for calling (4) and returning (3) -> 105 instruction cycles
;
; Register usage:
; R0-3:    Not used
; R4:      interrupt_completed
; R5:      General purpose
; R6:      E[1]*mod_90 or z
; R7:      E[1]*mod
; AR0-5:   Not used
; AR6:     General purpose
; AR7:     cosine_wave_pointer
; IR0:     90 degree offset into 1f
; IR1:     90 degree offset into 2f

       .globl  _V
       .globl  _X
       .globl  _Y
       .globl  _Z
       .globl  _F_0
       .globl  _F_90
       .globl  _RESPONSE
       .globl  _E
       .globl  _tint1
       .globl  _c_int01
       .globl  _fb_with_no_modulation
       .globl  _fb_with_V_modulation
       .globl  _fb_with_Z_modulation
       .globl  _fb_with_X_modulation
*******************************************************
* FUNCTION DEF : _fb_with_no_modulation
*******************************************************
_c_int01:                              ; expected by TMS320C30 boot routine
_fb_with_no_modulation:
       PUSH    ST                      ; The program won't work without this!

       LDF     @_Z,R6                  ; z = Z
       LDF     @_RESPONSE+2,R5         ; z += RESPONSE[2]*E[2]
       MPYF    @_E+2,R5
       ADDF    R5,R6
       LDF     @_E+1,R5                ; E[2] = E[1]
       STF     R5,@_E+2
       LDI     @CONST+0,AR6            ;                          AR6 = 800021h ADC_A
       MPYF    @_RESPONSE+1,R5         ; z += R[1]*E[1]
       ADDF    R5,R6
       LDI     *AR6++,R5               ; E[1] = (float)(ADC_A>>16) - SETPOINT
       LSH     -16,R5                  ;                          AR6 = 800022h ADC_B
       FLOAT   R5
       SUBF    @_RESPONSE+3,R5
```

```
        STF     R5,@_E+1
        MPYF    @_RESPONSE,R5       ; z += RESPONSE[0]*E[1]
        ADDF    R5,R6
        STF     R6,@_Z              ; Z = z

        CMPF    @CONST+1,R6         ; if z < DAC_MAX
        BLED    NL1                 ;   goto NL1 after next 3 steps
        NOP
        ADDI    1,R4                ; interrupt_completed++
        LDI     *AR6++,R5           ; R5 = ADC_B        AR6 = 0x800023h ADC_C

        LDF     @CONST+1,R6         ;   z = DAC_MAX - AMPLITUDE
        SUBF    @_RESPONSE+4,R6
        STF     R6,@_Z              ;   Z = z
NL1:
        CMPF    @CONST+2,R6         ; if z > DAC_MIN
        BGED    NL2                 ;   goto NL2 after next 3 steps
        LSH     -16,R5              ; E[0] = (float)(ADC_B>>16)
        FLOAT   R5
        STF     R5,@_E
                                ; if z < DAC_MIN:
        LDF     @CONST+2,R6         ;   z = DAC_MIN + AMPLITUDE
        ADDF    @_RESPONSE+4,R6
        STF     R6,@_Z              ;   Z = z
NL2:
        ; LDI     *AR6++,R5           ; R5 = ADC_C        AR6 = 0x800024h ADC_D
        LDI     *AR6--(3),R5        ; @@ R5 = ADC_D AR6 = 0x80021h ADC_A
        LSH     -16,R5              ; E[3] = (float)(ADC_C>>16)
        FLOAT   R5
        STF     R5,@_E+3
        ; LDI     *AR6--(4),R5        ; R5 = ADC_D      AR6 = 0x800020h Convert
        LDI     *AR6--,R5           ; @@ R5 = ADC_A AR6 = 0x800020h Convert
        LSH     -16,R5              ; E[4] = (float)(ADC_D>>16)
        FLOAT   R5
        STF     R5,@_E+4
        STI     R1,*AR6--(22)       ; CONVERT    AR6 = 0x80000ah 18 bit Z_DAC
        MPYF     4,R6
        FIX     R6,R5               ;  18 bit Z
        LDI     R5,R6
        LSH     22,R5
        STI     R5,*AR6++
        LSH     14,R6
        STI     R6,*AR6--(10)       ;                    AR6 = 800001h XP_DAC

        LDF     @_X,R5              ; X
        FIX     R5
        LSH     16,R5
        STI     R5,*AR6++(2)        ;                    AR6 = 800003h XN_DAC
        NOT     R5
        STI     R5,*AR6++(2)        ;                    AR6 = 800005h YP_DAC

        LDF     @_Y,R5              ; Y
        FIX     R5
        LSH     16,R5
        STI     R5,*AR6++(2)        ;                    AR6 = 800007h YN_DAC
        NOT     R5
        STI     R5,*AR6++(2)        ;                   AR6 = 800009h TIP_DAC

        LDF     @_V,R5              ; V
        FIX     R5
        LSH     16,R5
```

```
        STI     R5,*AR6

NEPI0_1:
        POP     ST
        RETI

*******************************************************
* FUNCTION DEF : _fb_with_V_modulation
*******************************************************
_fb_with_V_modulation:
        PUSH    ST                      ; The program won't work without this!

        LDF     @_Z,R6                  ; z = Z
        LDF     @_RESPONSE+2,R5         ; z += RESPONSE[2]*E[2]
        MPYF    @_E+2,R5
        ADDF    R5,R6
        LDF     @_E+1,R5                ; E[2] = E[1]
        STF     R5,@_E+2
        LDI     @CONST+0,AR6            ;                       AR6 = 800021h ADC_A
        MPYF    @_RESPONSE+1,R5         ; z += R[1]*E[1]
        ADDF    R5,R6
        LDI     *AR6++,R5               ; E[1] = (float)(ADC_A>>16) - SETPOINT
        LSH     -16,R5                  ;                       AR6 = 800022h ADC_B
        FLOAT   R5
        SUBF    @_RESPONSE+3,R5
        STF     R5,@_E+1
        MPYF    @_RESPONSE,R5           ; z += RESPONSE[0]*E[1]
        ADDF    R5,R6
        STF     R6,@_Z                  ; Z = z

        CMPF    @CONST+1,R6             ; if z < DAC_MAX
        BLED    VL1                     ;   goto VL1 after next 3 steps
        NOP
        ADDI    1,R4                    ; interrupt_completed++
        ; LDI     *AR6--(2),R5          ;  ; R5 = ADC_B      AR6 = 0x800020h CONVERT
        LDI     *AR6--(3),R5            ; @@ R5 = ADC_C    AR6 = 0x800020h CONVERT

                                ; if z > DAC_MAX:
        LDF     @CONST+1,R6             ;   z = DAC_MAX - AMPLITUDE
        SUBF    @_RESPONSE+4,R6
        STF     R6,@_Z                  ;   Z = z
VL1:
        STI     R1,*AR6--(22)           ; CONVERT    AR6 = 0x80000ah 18 bit Z_DAC
        CMPF    @CONST+2,R6             ; if z > DAC_MIN
        BGED    VL2                     ;   goto VL2 after next 3 steps
        LSH     -16,R5                  ; E[0] = (float)(ADC_B>>16)
        FLOAT   R5
        STF     R5,@_E

                                ; if z < DAC_MIN:
        LDF     @CONST+2,R6             ;   z = DAC_MIN + AMPLITUDE
        ADDF    @_RESPONSE+4,R6
        STF     R6,@_Z                  ;   Z = z
VL2:
        MPYF     4,R6
        FIX     R6,R5                   ; 18 bit Z
        LDI     R5,R6
        LSH     22,R5
        STI     R5,*AR6++
        LSH     14,R6
        STI     R6,*AR6--(10)           ;                       AR6 = 800001h XP_DAC
```

```
        LDF     @_X,R5              ; X
        FIX     R5
        LSH     16,R5
        STI     R5,*AR6++(2)        ;                       AR6 = 800003h XN_DAC
        NOT     R5
        STI     R5,*AR6++(2)        ;                       AR6 = 800005h YP_DAC

        LDF     @_Y,R5              ; Y
        FIX     R5
        LSH     16,R5
        STI     R5,*AR6++(2)        ;                       AR6 = 800007h YN_DAC
        NOT     R5
        STI     R5,*AR6++(2)        ;                      AR6 = 800009h TIP_DAC

        LDF     @_V,R6              ; V
        LDF     *AR7++%,R7          ; Derivative mode:  fetch 1f v_mod
        LDF     @_RESPONSE+4, R5    ; Derivative mode:  fetch amplitude
        MPYF    R7,R5               ; Derivative mode:  v_mod *= amplitude
        ADDF    R5,R6               ; Derivative mode:  v + v_mod
        FIX     R6
        LSH     16,R6
        STI     R6,*AR6             ; Output modulated V
        MPYF    @_E+1,R7            ; Derivative mode:  1f v_mod *= E[1]
        STF     R7,@_F_0
        LDF     *+AR7(IR0),R6       ; Derivative mode:  fetch 1f v_mod(90)
        MPYF    @_E+1,R6            ; Derivative mode:  v_mod(90) *= E[1]
        STF     R6,@_F_90
        LDF     *AR7++%,R7          ; Derivative mode:  fetch 2f v_mod
        MPYF    @_E+1,R7            ; Derivative mode:  2f v_mod *= E[1]
        LDF     *+AR7(IR1),R6       ; Derivative mode:  fetch 2f v_mod(90)
        MPYF    @_E+1,R6            ; Derivative mode:  2f v_mod(90) *= E[1]

VEPI0_1:
        POP     ST
        RETI
*****************************************************
* FUNCTION DEF : _fb_with_Z_modulation
*****************************************************
_fb_with_Z_modulation:
        PUSH    ST                  ; The program won't work without this!

        LDF     @_Z,R6              ; z = Z
        LDF     @_RESPONSE+2,R5     ; z += RESPONSE[2]*E[2]
        MPYF    @_E+2,R5
        ADDF    R5,R6
        LDF     @_E+1,R5            ; E[2] = E[1]
        STF     R5,@_E+2
        LDI     @CONST+0,AR6        ;                        AR6 = 800021h ADC_A
        MPYF    @_RESPONSE+1,R5     ; z += R[1]*E[1]
        ADDF    R5,R6
        LDI     *AR6++,R5           ; E[1] = (float)(ADC_A>>16) - SETPOINT
        LSH     -16,R5              ;                          AR6 = 800022h ADC_B
        FLOAT   R5
        SUBF    @_RESPONSE+3,R5
        STF     R5,@_E+1
        MPYF    @_RESPONSE,R5       ; z += RESPONSE[0]*E[1]
        ADDF    R5,R6
        LDF     *AR7++%,R7          ; Derivative mode:  fetch 1f z_mod
        LDF     @_RESPONSE+4, R5    ; Derivative mode:  fetch amplitude
        MPYF    R7,R5               ; Derivative mode:  z_mod *= amplitude
```

```
        STF     R6,@_Z                  ; Z = z
        ADDF    R5,R6                   ; Derivative mode:  z + z_mod

        CMPF    @CONST+1,R6             ; if z < DAC_MAX
        BLED    ZL1                     ;   goto ZL1 after next 3 steps
        NOP
        ADDI    1,R4                    ; interrupt_completed++
        ; LDI     *AR6--(2),R5            ; R5 = ADC_B      AR6 = 0x800020h CONVERT
        LDI     *AR6--(3),R5            ;@@
                                ; BRANCH if z < DAC_MAX
                                ; if z > DAC_MAX:
        LDF     @CONST+1,R6             ;   z = DAC_MAX - AMPLITUDE
        SUBF    @_RESPONSE+4,R6
        STF     R6,@_Z                  ;   Z = z
ZL1:
        STI     R1,*AR6--(22)           ; CONVERT    AR6 = 0x80000ah 18 bit Z_DAC
        CMPF    @CONST+2,R6             ; if z > DAC_MIN
        BGED    ZL2                     ;   goto ZL2 after next 3 steps
        LSH     -16,R5                  ; E[0] = (float)(ADC_B>>16)
        FLOAT   R5
        STF     R5,@_E
                                ; BRANCH if z > DAC_MIN
                                ; if z < DAC_MIN:
        LDF     @CONST+2,R6             ;   z = DAC_MIN + AMPLITUDE
        ADDF    @_RESPONSE+4,R6
        STF     R6,@_Z                  ;   Z = z
ZL2:
        MPYF     4,R6
        FIX     R6,R5                   ; 18 bit Z
        LDI     R5,R6
        LSH     22,R5
        STI     R5,*AR6++
        LSH     14,R6
        STI     R6,*AR6--(10)           ;                       AR6 = 800001h XP_DAC
        MPYF    @_E+1,R7                ; Derivative mode:  1f z_mod *= E[1]
        LDF     *+AR7(IR0),R6           ; Derivative mode:  fetch 1f z_mod(90)
        MPYF    @_E+1,R6                ; Derivative mode:  z_mod(90) *= E[1]
        NOP     *AR7++%                 ; circular increment AR7 to point to 1F wave

        LDF     @_X,R5                   ; X
        FIX     R5
        LSH     16,R5
        STI     R5,*AR6++(2)             ;                       AR6 = 800003h XN_DAC
        NOT     R5
        STI     R5,*AR6++(2)             ;                       AR6 = 800005h YP_DAC

        LDF     @_Y,R5                  ; Y
        FIX     R5
        LSH     16,R5
        STI     R5,*AR6++(2)            ;                       AR6 = 800007h YN_DAC
        NOT     R5
        STI     R5,*AR6                 ;


ZEPI0_1:
        POP     ST
        RETI
*****************************************************
* FUNCTION DEF : _fb_with_X_modulation
*****************************************************
_fb_with_X_modulation:
```

```
        PUSH    ST                  ; The program won't work without this!

        LDF     @_Z,R6              ; z = Z
        LDF     @_RESPONSE+2,R5     ; z += RESPONSE[2]*E[2]
        MPYF    @_E+2,R5
        ADDF    R5,R6
        LDF     @_E+1,R5            ; E[2] = E[1]
        STF     R5,@_E+2
        LDI     @CONST+0,AR6        ;                       AR6 = 800021h ADC_A
        MPYF    @_RESPONSE+1,R5     ; z += R[1]*E[1]
        ADDF    R5,R6
        LDI     *AR6++,R5           ; E[1] = (float)(ADC_A>>16) - SETPOINT
        LSH     -16,R5              ;                       AR6 = 800022h ADC_B
        FLOAT   R5
        SUBF    @_RESPONSE+3,R5
        STF     R5,@_E+1
        MPYF    @_RESPONSE,R5       ; z += RESPONSE[0]*E[1]
        ADDF    R5,R6
        STF     R6,@_Z              ; Z = z

        CMPF    @CONST+1,R6         ; if z < DAC_MAX
        BLED    XL1                 ;   goto XL1 after next 3 steps
        NOP
        ADDI    1,R4                ; interrupt_completed++
        ; LDI     *AR6--(2),R5      ;  R5 = ADC_B      AR6 = 0x800020h CONVERT
        LDI     *AR6--(3),R5        ;@@

                                ; if z > DAC_MAX:
        LDF     @CONST+1,R6         ;   z = DAC_MAX - AMPLITUDE
        SUBF    @_RESPONSE+4,R6
        STF     R6,@_Z              ;   Z = z
XL1:
        STI     R1,*AR6--(22)       ; CONVERT    AR6 = 0x80000ah 18 bit Z_DAC
        CMPF    @CONST+2,R6         ; if z > DAC_MIN
        BGED    XL2                 ;   goto XL2 after next 3 steps
        LSH     -16,R5              ; E[0] = (float)(ADC_B>>16)
        FLOAT   R5
        STF     R5,@_E

                                ; if z < DAC_MIN:
        LDF     @CONST+2,R6         ;   z = DAC_MIN + AMPLITUDE
        ADDF    @_RESPONSE+4,R6
        STF     R6,@_Z              ;   Z = z
XL2:
        MPYF     4,R6
        FIX     R6,R5               ; 18 bit Z
        LDI     R5,R6
        LSH     22,R5
        STI     R5,*AR6++
        LSH     14,R6
        STI     R6,*AR6--(11)       ;             AR6 = 18 bit 800000h XP_DAC

        LDF     @_X,R6              ; X
        LDF     *AR7++%,R7          ; Derivative mode:  fetch 1f x_mod
        LDF     @_RESPONSE+4, R5    ; Derivative mode:  fetch amplitude
        MPYF    R7,R5               ; Derivative mode:  x_mod *= amplitude
        ADDF    R5,R6               ; Derivative mode:  x + x_mod
        MPYF     4,R6
        FIX     R6,R5               ; 18 bit X w/ modulation
        LDI     R5,R6
        LSH     22,R5
```

```
        STI     R5,*AR6++
        LSH     14,R6
        STI     R6,*AR6++           ; Output modulated X AR6 = 800003h XN_DAC
        NOT     R5
        STI     R5,*AR6++
        NOT     R6
        STI     R6,*AR6++(2)        ;                      AR6 = 800005h YP_DAC
        MPYF    @_E+1,R7            ; Derivative mode:  1f x_mod *= E[1]
        LDF     *+AR7(IR0),R6       ; Derivative mode:  fetch 1f x_mod(90)
        MPYF    @_E+1,R6            ; Derivative mode:  x_mod(90) *= E[1]
        NOP     *AR7++%             ; circular increment AR7 to point to 1F wave

        LDF     @_Y,R5              ; Y
        FIX     R5
        LSH     16,R5
        STI     R5,*AR6++(2)        ;                      AR6 = 800007h YN_DAC
        NOT     R5
        STI     R5,*AR6++(2)        ;                     AR6 = 800009h TIP_DAC


XEPI0_1:
        POP     ST
        RETI
*******************************************************
* DEFINE CONSTANTS                                    *
*******************************************************
        .bss    CONST,3
        .sect   ".cinit"
        .word   3,CONST
        ;.word   800021h          ;0   ADC_A (CURRENT)
        .word   800022h          ;0   ADC_B (CURRENT) @@
        .float  6.5535e4         ;1   Z_DAC_MAX
        .float  0.0000e1         ;2   Z_DAC_MIN
        .end
```

DSP Code Header File: STM_DSP.H

```
/* DSP OPERATING SYSTEM HEADER STM_DSP.H */


/* MISCELLANEOUS */
#define DAC_TYPE unsigned int
#define ADC_TYPE unsigned int

#define XY_DAC_MAX    65535.0f
#define XY_DAC_ZERO   32768.0f
#define XY_DAC_MIN        0.0f

#define  Z_DAC_MAX    65535.0f
#define  Z_DAC_ZERO   32768.0f
#define  Z_DAC_MIN        0.0f

#define LOCAL_SETPOINT  RESPONSE[3]
#define LOCAL_AMPLITUDE RESPONSE[4]

/* VARIABLES */
#define TEST                    *((float *)0x030000)
```

```
#define ALPHA                   *((float *)0x030001)
#define BETA                    *((float *)0x030002)
#define GAMMA                   *((float *)0x030003)
#define SETPOINT                *((float *)0x030004)
#define WMIN                    *((float *)0x030024)
#define XMIN                    *((float *)0x030005)
#define YMIN                    *((float *)0x030006)
#define WSIZE                   *((float *)0x03002e)
#define XSIZE                   *((float *)0x030007)
#define YSIZE                   *((float *)0x030008)
#define WRES                    *((float *)0x03002f)
#define XRES                    *((float *)0x030009)
#define YRES                    *((float *)0x03000a)
#define SCAN_RATE               *((float *)0x03000b)
#define COS_ROTATION            *((float *)0x03000c)
#define SIN_ROTATION            *((float *)0x03000d)
/*#define                       *((float *)0x03000e)*//* not used */
#define AMPLITUDE               *((float *)0x03000f)
#define LEVELING_FACTOR         *((float *)0x030010)
#define X_TARGET                *((float *)0x030011)
#define Y_TARGET                *((float *)0x030012)
#define Z_TARGET                *((float *)0x030013)
#define STEP_HEIGHT             *((float *)0x030014)
#define DATA_TYPE_DATA_SUBSET    *((int *)0x030015)
#define TIP_VOLTAGE             *((float *)0x030016)
#define OFFSET_A                *((float *)0x030017)
#define RELAY_SETTINGS  *((unsigned int *)0x030018)
#define WALKER_DIRECTION         *((int *)0x030019)
#define WALKER_STEP_SIZE         *((int *)0x03001a)
#define PULSE_HEIGHT            *((float *)0x03001b)
#define PULSE_LENGTH            *((float *)0x03001c)
#define LASER_STATUS            *((float *)0x03001d)
#define SCOPE_CHANNEL           *((float *)0x03001d)
#define PERIOD                   *((int *)0x03001e)
#define INT_PERIOD              *((float *)0x03001f)
#define DATA_TYPE    DATA_TYPE_DATA_SUBSET & 0x0FFF
#define DATA_SUBSET     DATA_TYPE_DATA_SUBSET >> 12

#define HEIGHT_DATA      0
#define CURRENT_DATA     1
#define B_DATA           2
#define DZ_DATA          3
#define DV_DATA          4
#define DX_DATA          5
#define IV_DATA          6
#define C_DATA           7
#define F_1_0                       0
#define F_1_90                      1
#define F_2_0                       2
#define F_2_90                      3

/* MESSAGES TO DSP */
#define INSTRUCTION              *((int *)0x030020)
       #define READY              0
       #define TERMINATE          1
       #define SCAN               2
       #define COARSE_APPROACH    6
       #define RAMP               7
       #define MOVE_TO_X_TARGET   8
       #define MOVE_TO_Y_TARGET   9
       #define MOVE_TO_XY_TARGET 10
```

```
        #define MOVE_TO_Z_TARGET    11
        #define PULSE               13
        #define SAMPLE              14
        #define LOAD_PERIOD         15
        #define TRANSFER_DATA       16
        #define LOAD_VARIABLES      17
        #define FEEDBACK_ON         18
        #define FEEDBACK_OFF        19
        #define TRANSLATE           20

/* MESSAGES FROM DSP */
#define ERROR                       *((int *)0x030021)
#define RESPONSE_ADDRESS *((unsigned int *)0x030022)
#define FEEDBACK                    *((int *)0x030023)
        #define OFF 0
        #define ON  1
                            /* wmin         0024 */
#define VZ                      *((float *)0x030025)
#define SIGNALA                 *((float *)0x030026)
#define SIGNALB                 *((float *)0x030027)
#define SIGNALC                 *((float *)0x030028)
#define SIGNALD                 *((float *)0x030029)
#define FORWARD_WRITE_COUNT       *((int *)0x03002a)
#define REVERSE_WRITE_COUNT       *((int *)0x03002b)
#define VX                      *((float *)0x03002c)
#define VY                      *((float *)0x03002d)
                            /* wsize        002e */
                            /* wres         002f */
#define VT                      *((float *)0x030030)
#define WALKER_STEPS            *((float *)0x030031)
#define ENCODER_READING         *((float *)0x030032)

/* TOGGLES */
#define MODE                     *((int *)0x030043)
#define HOLD_ROTATION            *((int *)0x030044)
#define DIRECTION                *((int *)0x030045)
#define BUFFER_NUMBER            *((int *)0x030046)

/* DATA */
#define FORWARD_DATA                       0x030050
#define REVERSE_DATA                       0x030450

/* EXTERNAL ANALOG INTERFACE for LTSTM */
#define XP_LSB          *((unsigned int *)0x800000)
#define XP_DAC              *((DAC_TYPE *)0x800001)
#define XN_LSB          *((unsigned int *)0x800002)
#define XN_DAC              *((DAC_TYPE *)0x800003)
#define YP_LSB          *((unsigned int *)0x800004)
#define YP_DAC              *((DAC_TYPE *)0x800005)
#define YN_LSB          *((unsigned int *)0x800006)
#define YN_DAC              *((DAC_TYPE *)0x800007)
#define TIP_LSB         *((unsigned int *)0x800008)
#define TIP_DAC             *((DAC_TYPE *)0x800009)
#define CEN_LSB         *((unsigned int *)0x80000a)
#define CEN_DAC             *((DAC_TYPE *)0x80000b)
/* #define ?_LSB        *((unsigned int *)0x80000c)*//* not used */
/* #define ?_DAC            *((DAC_TYPE *)0x80000d)*//* not used */
#define MPS_DIR_RES     *((unsigned int *)0x800014)
#define MPS_OSC_TOGGLE  *((unsigned int *)0x800015)

#define CONVERT                 *((float *)0x800020)
```

```
#define CURRENT_ADC          *((ADC_TYPE *)0x800021)
#define ADC_B                *((ADC_TYPE *)0x800022)
#define ADC_C                *((ADC_TYPE *)0x800023)
#define ADC_D                *((ADC_TYPE *)0x800024)
```

DSP Resident Code for STM: STM_DSP.C

A subsection of the DSP resident code is presented below which includes a function listing, the main routine, and the instruction parser.

```
/* FUNCTIONS */

void instruction_parser(void);
  /* The main menu. */

void scan(void);
void scan_dv_iv(void);
  /* Generate the WXY raster and store the requested types of data. */
void ramp_v(void);
  /* Generate a voltage ramp and store the requested types of data. */
  /* For dI/dV (V) measurements with external lockin amplifier.     */

void coarse_approach(void);
  /* Moves the stage until the input current crosses the setpoint. The input
     current is recorded in a circular buffer so that a graph of the current
     for 2.5 ms before and 7.5 ms after engaging can be plotted. */

void move_to_xy_target(void);
  /* Ramps the XY outputs to the given targets at half the scan rate. */

void move_to_z_target(void);
  /* Ramps Z to the given target in 10,000 steps.  The current is recorded
     once every 10 steps so that IZ curves can be plotted. */

void pulse(void);
  /* For STM only, pulse the tip voltage. */

void transfer_data(void);
  /* For slowplot() and write_datafile(), puts the requested data line by
     line into dual port memory. */

void timer_period(float microseconds);
  /* Set the period of the interrupt timer and thus the frequency of the
     feedback loop. */

void step_response(void);
  /* For sample(), change the setpoint to create a step and record the
     resulting input current step response curve for 1024 points (interrupts).
     Also used to sample the input current by setting the step size
     to zero.  SCOPE_CHANNEL determines which ADC data is sampled.*/

void translate(void);
  /* move the sample translator. */

void set_period(void);
```

```
  /* Sets the modulation period for derivative imaging */

extern void fb_with_no_modulation(void);
extern void fb_with_V_modulation(void);
extern void fb_with_Z_modulation(void);
extern void fb_with_X_modulation(void);
extern void c_int01(void);

void main(void)
{
  int i, reps;
  float derivative1, derivative1_90, scan_rate;
  float derivative2, derivative2_90, inverted_scan_rate;
  float z_average, current_average, b_average, c_average;
  register int interrupt_completed;/* R4 */
  register float mod_90, mod_0;/* R6, R7 */

  /* Set outputs to zero */
  X = Y = XY_DAC_ZERO;
  Z = Z_TARGET;

  RESPONSE_ADDRESS = (unsigned int)RESPONSE;
  FORWARD_WRITE_COUNT = REVERSE_WRITE_COUNT = 10000;
  XCEN = XMIN + (XSIZE*0.5f);
  YCEN = YMIN + (YSIZE*0.5f);
  FEEDBACK = OFF;

  /*TEST = 0.1f;*/
  for (i=0; i<25; i++) SEGMENTS_USED[i] = 0;
  for (i=0; i<1024; i++) Z_CIRCULAR_BUFFER[i] = C_CIRCULAR_BUFFER[i] = 0.0f;
  set_period();
  timer_period(INT_PERIOD);
  asm("\tOR\t3000h, ST\t;global interrupt enable");
  INSTRUCTION = TERMINATE;
  while(1) {
       /*TEST = 1.1f;*/ /* don't use 1.0f -- appears when register is emptied */
       DZ_ON=(MODE & 0x08);  DV_ON = (MODE & 0x40);  DX_ON = (MODE & 0x80);
       IV_ON=(MODE & 0x100); RAMP_ON=(MODE & 0x400); CONST_R=(MODE & 0x800);
       LOG_AMP=(MODE & 0x1000);
       if (DZ_ON) TINT1 = (int)fb_with_Z_modulation;
       else if (DV_ON) TINT1 = (int)fb_with_V_modulation;
       else if (DX_ON) TINT1 = (int)fb_with_X_modulation;
       else TINT1 = (int)fb_with_no_modulation;
       WAIT;
       asm("\tLDI\t@_TINT1,R5; pointer to correct feedback routine");
       asm("\tLDI\t0Ah,AR6   ; pointer to interrupt vector address");
       asm("\tSTI\tR5,*AR6   ; interrupt vector = feedback routine");
       z_average = current_average = b_average = c_average = 0.0f;
       derivative1 = derivative1_90 = derivative2 = derivative2_90 = 0.0f;
       if (scan_rate != SCAN_RATE){
         scan_rate = SCAN_RATE;
         inverted_scan_rate = 1.0f/scan_rate;
         }
       VT = V = TIP_VOLTAGE;
       reps = 0;
       while (reps++ < scan_rate) {
         WAIT;
         z_average += Z;
         current_average += E[1];
         b_average += E[0];
         c_average += E[3];
```

```
        derivative1    += mod_0;
        derivative1_90 += mod_90;
        derivative2    += F_0;
        derivative2_90 += F_90;
        }
      VX = X; VY = Y; VZ = z_average*inverted_scan_rate;
      SIGNALA = current_average*inverted_scan_rate + LOCAL_SETPOINT;
      SIGNALB = b_average*inverted_scan_rate;
      if (MODE & 0x200) SIGNALC = c_average*inverted_scan_rate;
      else if (DV_ON && DATA_SUBSET < 2)
        SIGNALC = derivative2*derivative2 + derivative2_90*derivative2_90;
      else SIGNALC = derivative1*derivative1 + derivative1_90*derivative1_90;
      if (INSTRUCTION) {
        ERROR = 0;
        instruction_parser();
        INSTRUCTION = READY;
        }
    }
}


void instruction_parser(void)
{
  register int interrupt_completed;/* R4 */

  TEST = 2.0f;
       if (INSTRUCTION == SCAN && (IV_ON||DV_ON) && WRES > 1) scan_dv_iv();
  else if (INSTRUCTION == SCAN && RAMP_ON) ramp_v();
  else if (INSTRUCTION == SCAN) scan();
  else if (INSTRUCTION == COARSE_APPROACH) coarse_approach();
  else if (INSTRUCTION == MOVE_TO_X_TARGET) {
       if (!HOLD_ROTATION) {
         XCEN = XMIN + (XSIZE*0.5f);
         YCEN = YMIN + (YSIZE*0.5f);
         }
       Y_TARGET = -(X-XCEN)*SIN_ROTATION + (Y-YCEN)*COS_ROTATION + YCEN;
       move_to_xy_target();
       }
  else if (INSTRUCTION == MOVE_TO_Y_TARGET) {
       if (!HOLD_ROTATION) {
         XCEN = XMIN + (XSIZE*0.5f);
         YCEN = YMIN + (YSIZE*0.5f);
         }
       X_TARGET = (X-XCEN)*COS_ROTATION + (Y-YCEN)*SIN_ROTATION + XCEN;
       move_to_xy_target();
       }
  else if (INSTRUCTION == MOVE_TO_XY_TARGET) {
       if (!HOLD_ROTATION) {
         XCEN = XMIN + (XSIZE*0.5f);
         YCEN = YMIN + (YSIZE*0.5f);
         }
       move_to_xy_target();
       }
  else if (INSTRUCTION == MOVE_TO_Z_TARGET) move_to_z_target();
  else if (INSTRUCTION == PULSE) pulse();
  else if (INSTRUCTION == TRANSFER_DATA) transfer_data();
  else if (INSTRUCTION == LOAD_VARIABLES) {
       LOCAL_SETPOINT = SETPOINT;
       LOCAL_AMPLITUDE = AMPLITUDE;
       TIP_DAC = (unsigned int)(TIP_VOLTAGE) << 16;
```

```
        timer_period(INT_PERIOD);
        }
    else if (INSTRUCTION == FEEDBACK_ON) {
        WAIT;                              /* make sure interrupt doesn't come */
                                           /* while feedback parameters are    */
                                           /* being changed */
        RESPONSE[0] = ALPHA;
        RESPONSE[1] = BETA;
        RESPONSE[2] = GAMMA;
        FEEDBACK = ON;
        }
    else if (INSTRUCTION == FEEDBACK_OFF) {
        RESPONSE[0] = RESPONSE[1] = RESPONSE[2] = 0.0f;
        FEEDBACK = OFF;
        }
    else if (INSTRUCTION == TRANSLATE) translate();
    else if (INSTRUCTION == SAMPLE) step_response();
    else if (INSTRUCTION == LOAD_PERIOD) set_period();
    /* TEST = 0.0f; */
}
```

References

1. S. M. Clark, "Advances in scanning force microscopy of biological structures," Ph.D. thesis, California Institute of Technology (1992).
2. S. M. Clark, *ibid.*, p. 117.

Appendix D: Hardware for Digitally Controlled Scanned Probe Microscopes

This paper documents the performance of the digital control electronics. The reader is referred to Steven M. Clark's thesis for design details.

Hardware for digitally controlled scanned probe microscopes

S. M. Clark
Division of Biology, California Institute of Technology, Pasadena, California 91125

D. R. Baselt
A. A. Noyes Laboratory of Chemical Physics, Division of Chemistry, California Institute of Technology, Pasadena, California 91125

C. F. Spence
Division of Biology, California Institute of Technology, Pasadena, California 91125

M. G. Youngquist and J. D. Baldeschwieler
A. A. Noyes Laboratory of Chemical Physics, Division of Chemistry, California Institute of Technology, Pasadena, California 91125

(Received 18 March 1992; accepted for publication 23 June 1992)

The design and implementation of a flexible and modular digital control and data acquisition system for scanned probe microscopes (SPMs) is presented. The measured performance of the system shows it to be capable of 14-bit data acquisition at a 100-kHz rate and a full 18-bit output resolution resulting in less than 0.02-Å rms position noise while maintaining a scan range in excess of 1 μm in both the X and Y dimensions. This level of performance achieves the goal of making the noise of the microscope control system an insignificant factor for most experiments. The adaptation of the system to various types of SPM experiments is discussed. Advances in audio electronics and digital signal processors have made the construction of such high performance systems possible at low cost.

I. INTRODUCTION

Among the most promising applications of scanning probe microcopies (SPM) are those concerned with the study of biomaterials. Although progress has been made in this arena,[1-3] the routine imaging of biomolecules and biological tissues at nanometer-scale resolution has remained a challenge.

We believe there are at least two barriers to increased resolution during scanning force microscopy (SFM) on biological samples. The first barrier is the limitation on resolution imposed by the shape of the cantilever tip (stylus).[4] A rounded stylus tends to reduce lateral resolution and to limit tip excursions on highly sloped sample features. The second barrier is the pressure of the stylus on the sample which may degrade image quality by inducing or exacerbating sample motion and deformation. The force exerted on a sample depends not only on the physical forces involved in tip-sample interaction, but is also influenced by the system noise of the SFM. It is only possible to fully exploit tip-sample interactions and other factors which alter microscope resolution if the system noise of the microscope can be made an insignificant factor. The use of sharper styluses to increase resolution may also demand lower system noise to avoid sample distortion and damage, especially when imaging relatively soft samples. We believe that the use of low noise control systems, such as we describe here, is an important step toward realizing the potential of SFM for biology.

The qualities that we feel are most important for scanned probe microscopes to possess are high resolution, low noise, and flexibility. Although several commercial SPMs are available, few are able to achieve the resolution and noise performance that we require for our planned experiments. They can also be difficult to adapt to new approaches (e.g., concurrent optical fluorescence microscopy on biological samples, etc.). We have designed and constructed a high performance digital control and data acquisition system for SPMs in order to increase the resolution of SFM data on biological samples. In this system the output noise may be considered negligible for most experiments and should be adequate for SFM of biomaterials. Due to the modular approach taken, the system is highly flexible and is able to support a wide variety of experiments. With a minimal addition of electronics the system is capable of supporting scanning tunneling microscopy (STM), near field scanning optical microscopy[5] (NSOM), scanning ion conductance microscopy[6] (SICM), and scanning electrochemical microscopy[7] (SECM) experiments. This system may be of interest to others due to its inherent flexibility, low cost, and improved performance.

We will first discuss the ideas behind the use of a digital control system for SPM as well as some of the factors governing ultimate SPM sensitivity and their impact on the design goals for a high-resolution SPM. We then present our instrument as one example of the implementation of a digital control system, concentrating on the design of the analog signal I/O section and performance verification of the circuitry as well as demonstrating the system's flexibility using its adaptation to NSOM as an example.

II. DIGITAL CONTROL FOR SCANNED PROBE MICROSCOPY

The minimal set of tasks to be handled by an SPM control system are coarse approach to the sample, the control of a probe micropositioner (usually a piezoelectric ce-

 0034-6748/92/104296-12$02.00

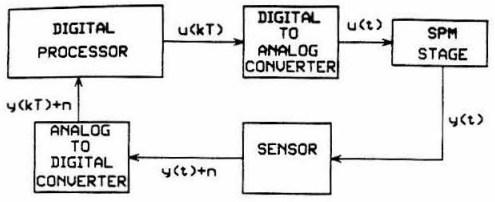

FIG. 1. A block diagram of a digital control system for scanned probe microscopy. Two distinct types of signals occur in a digital control system: (i) those which are time and amplitude continuous (analog signals) denoted $f(t)$; and (ii) those which are quantized in time and amplitude (digital signals) denoted g (kT). In a digital control system both the conversion resolution and the sampling rate effect the degree to which the digital control system approximates an analog control system (Ref. 25). Specialized mathematical techniques which address the digital nature of the signals are used to effectively analyze digital control systems and to insure their performance. In this figure noise is denoted by n regardless of its source.

ramic transducer, hereafter referred to simply as a piezo), and the measurement of a signal which can be used to control the proximity of the probe to the sample. In addition to these elementary functions, the ability to control auxiliary devices and to synchronously acquire multiple types of data is highly desirable.

Discussions of several implementations of control systems for SPMs are available in the literature.[8–12] Our goals in the design of the present system were to increase performance by avoiding some of the compromises which had been made in other systems and increase system flexibility through a modular design approach using a digital signal processor (DSP). Despite the availability of DSPs in commercial SPMs, we are unaware of any detailed discussion of DSP based control systems as applied to SPMs. Hence, we will review some of the principles involved below.

In a digital control system for SPM (see Fig. 1) the proximity signal (tunneling current in STM, cantilever deflection in SFM, etc.) is measured by a sensor using analog signal processing electronics and digitized by an analog to digital converter (ADC). The digital value representing the signal is compared against a digital setpoint to obtain an error signal. This error signal is used to calculate a digital value representing the ideal voltage to be applied to the Z axis of the micropositioner. The algorithm used for this calculation comprises the Z feedback loop. This new Z value is converted into the actual Z voltage by a digital to analog converter (DAC) and amplified by a high voltage amplifier to provide the output voltage necessary to drive the micropositioner. Although it is possible to correct for nonlinearities inherent in the piezoelectric actuators through position feedback,[13] typically the voltages used to drive the micropositioner in the X and Y dimensions are generated in an open loop fashion (that is, they are calculated and sent to the X and Y DACs without measuring a control signal for them).

The major advantages offered by a DSP-based control system are flexibility, improved performance (decreased scan times, increased noise immunity, etc.), and the possibility of easily using sophisticated techniques such as phase sensitive detection, optimal filtering, active damping, evolutionary feedback parameter optimization, and so forth. The tremendous flexibility of a DSP-based system arises from the generic nature of the analog I/O electronics combined with the ability to modify the control software. This allows the implementation of novel imaging modes or the adaptation of the system to control different devices with a minimum of hardware development thus saving both time and expense. Another advantage lies in the capabilities of the DSP itself. Because DSPs typically contain features such as single machine cycle multiplication and matrix manipulation facilities, they are particularly well suited to real-time computation and signal processing. They are much faster for these tasks than microcontrollers or other dedicated microprocessors. The last barrier to the use of DSPs for SPM control systems was removed with the advent of low cost, high performance DACs and ADCs for application in the audio frequency range.

Another key to system flexibility is to use a modular design approach. By breaking the system into generic components which can be controlled through a standard interface it is possible not only to simplify component design, but also to update easily the system configuration as requirements change. For more elaborate experiments, modules can simply be added which follow the standard communication protocol and which perform specialized functions.

As an illustration of the potential engendered by modular design, we show, in Fig. 2, a block diagram of a multiprocessor architecture. This type of architecture allows task sharing between the central DSP and other embedded processors. In this system, "smart" DACs could serve to relieve the DSP of raster generation and other peripheral control tasks, these tasks being handled by embedded microprocessors (either DSPs or microcontrollers). Through the use of such "smart" DACs the system could be tailored to particular piezos and real time hysteresis and creep correction could be done. One way in which this might be achieved is by implementing the real time optical scan correction system of Barrett and Quate[13] using a digital servo loop. In such a design the optical beam displacement sensors would provide a measurement of the piezo displacement and the desired X-Y raster pattern becomes a two-dimensional, time-dependent reference input to the servo. The implementation of various types of control loops such as proportional-integral-differential (PID) control, optimal control, or feedforward control could be easily done in the control software. A particularly attractive microcontroller for this application might be the Motorola MC68332[14] due to its hardware interpolation feature which would allow rapid generation of smooth raster signals. The field programmable gate array (FPGA) shown in the diagram allows complex timing and logic functions to be handled easily and facilitates the interface between the processors. The "smart" module concept can be extended to more interesting applications such as microprocessor controlled scanning bipotentiostats for scanning electrochemical microscopy and so forth.

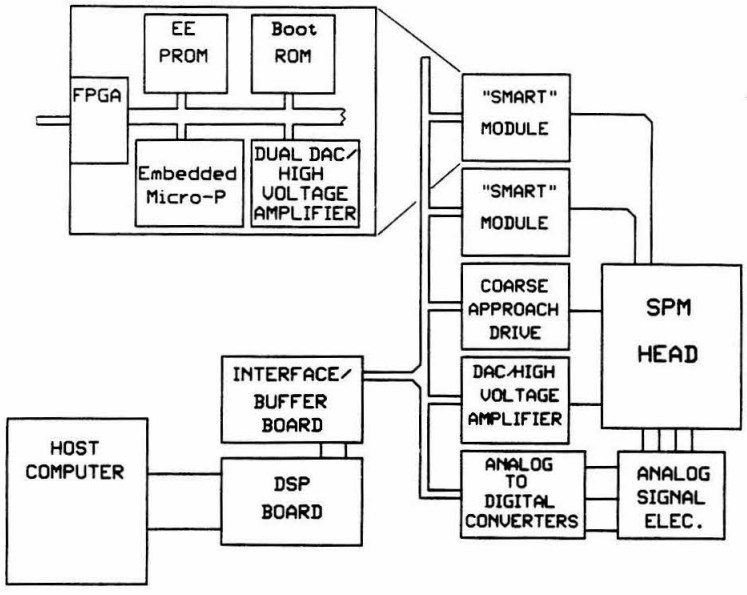

FIG. 2. A block diagram of a multiprocessor control and data acquisition system for scanned probe microscopy. This architecture allows task sharing between the central DSP and other embedded processors. In one version of such a system the central DSP would be used to execute the Z feedback loop and store image data, while the other processors could be used for raster generation, digital rotation, control of auxiliary equipment (e.g., a scanning bipotentiostat, hybrid photomultiplier detectors, etc.).

III. NOISE IN SPM

The noise level of a SPM control system is a significant factor in its ability to meet experimental demands. To understand how noise influences SPM experiments, and to provide a framework for minimizing noise, one can divide noise sources into two categories, output noise and input noise. Output noise originates in the piezo drive electronics and can be minimized by the use of special low noise design techniques. Input noise is inherent in SPM measurements and cannot be reduced beyond a certain minimal level. We discuss both noise categories below.

Reduction of piezo drive output noise was one of our major design goals. Because the force applied by a cantilever is proportional to its deflection, noise on the Z axis output lying outside the servo bandwidth introduces uncontrollable force fluctuations which are undesirable (within the servo bandwidth the noise will be reduced by the feedback gain). Our specific design goal for the SFM was that the system noise contribution from the piezo drive electronics be slightly less than the mechanical noise contribution from the microscope stage and head; from calculation we expect the mechanical noise from thermal stage vibration to be $\approx$0.1-Å rms amplitude. We frequently use tubular piezos and a response of $\approx$50 Å/V, hence our system can tolerate an output noise of 2-mV rms over a 100-kHz bandwidth while maintaining a 1-μm scan range.

Resolution is another key consideration; ideally the cantilever could be positioned at any arbitrary deflection. The average incremental force applied by the stylus depends on the DAC output step size, with smaller steps providing finer control of the applied force. Typically, higher resolution DACs also exhibit lower output noise, so high-resolution DAC circuitry provides a real advantage in terms of controlling forces for SPMs. Large zoom ratios are another feature gained by using high resolution DACs. The ability to zoom in on rare features initially found by scanning large areas can be crucial in systems without sample translators and greatly simplifies the use of any *SPM*.

In almost every experimental measurement, weak input signal detectability is limited by noise. In many cases interfering signals generated externally to the experiment may be excluded from the measurement by proper shielding and grounding, however, noise can be reduced only to a finite limit. This ultimate noise floor is the result of the thermal motion of charge carriers (Johnson noise) and the quantization of charge (shot noise). The voltage noise (rms) due to Johnson noise of a resistance R is given by[15]

$$V_n=(4kTRB)^{1/2}.$$

In this equation, T is the absolute temperature (K), B is the measurement bandwidth (Hz), and k is Boltzmann's constant (1.380662×10^{-23} J K^{-1}).

Just as Johnson noise from a source resistance presents a fundamental limit for voltage measurements, shot noise presents a fundamental limit in the experimental measure-

ment of currents. The shot noise (rms) for a current of average value $\langle I \rangle$ is[15]

$$i_n = \{2q\langle I \rangle B\}^{1/2},$$

where again, B is the bandwidth of the measurement (Hz) and q is the electron charge (1.602189×10^{-19} C). The best measurements one can make are limited by noise at these levels. Only Johnson noise can be decreased by lowering the temperature of an experiment; however, both shot noise and Johnson noise can be reduced by limiting the detection bandwidth. By using techniques such as lock-in detection, bandwidths of a few Hertz can be readily obtained.

When one considers the effect of shot noise on STM experiments one finds that for a tunneling current of 100 pA and a 10-kHz bandwidth the shot noise is 0.4 pA. Thus, the maximum signal-to-noise ratio for these conditions is ≈ 250. Similarly, for a 1-pA tunneling current, in the same 10-kHz bandwidth, the best signal-to-noise ratio is less than 20. Often the effects of shot noise are not obvious in topography data from STM; this is due to the fact that high impedance amplifiers typically used as STM preamplifiers tend to have a limited frequency response, effectively limiting the bandwidth to ≈ 1 kHz or less. One might expect, however, that shot noise would play a more significant role in experiments done at high gap resistances, over large bandwidths, or in tunneling spectroscopy.

Shot noise also limits optical beam deflection sensitivity for SFM. For a photodiode, $\langle I \rangle$ is given by $\langle I \rangle = P\varnothing$, where P is the optical power incident on the photodiode and $\varnothing$ is the spectral responsivity at the wavelength of interest. Under typical operating conditions in our SFM, $\langle I \rangle$ is ≈ 15 μA/quadrant and i_n is ≈ 690 pA/quadrant assuming a 100-kHz measurement bandwidth. Thus, in our SFM as presently used, current fluctuations of amplitude $2i_n$ give rise to signals of ≈ 280 μV which roughly corresponds to a change of one ADC unit (± 10 V full scale and 16-bit resolution). In the sense that our instrument can detect changes in photocurrent of amplitude $2i_n$, we can say that it is shot noise limited. Further increasing the gain of the difference amplifier, whose output is the deflection signal, provides larger signal amplitude, but does not increase signal-to-noise ratio.

To increase sensitivity further requires increasing the laser power on the photodiode, increasing the optical lever gain (i.e., the ratio of beam deflection distance to cantilever tip motion) or decreasing the measurement bandwidth. The laser power can easily be increased; however, as the light intensity on the cantilever increases so does the momentum transferred to the cantilever. The force exerted on the cantilever by photon pressure is given by

$$F = 2P/c,$$

where P is the laser power incident on the cantilever and c is the speed of light. Thus, for a helium-neon laser with 10% intensity noise, to keep laser noise induced force fluctuations below 10^{-11} N one is limited to less than ≈ 20 mW. On the other hand, the optical lever gain can be increased without compromising other aspects of the instrument's performance. However, optical lever gain is limited in practice by the mechanical design of the instrument both in terms of mechanical noise and ease of use.

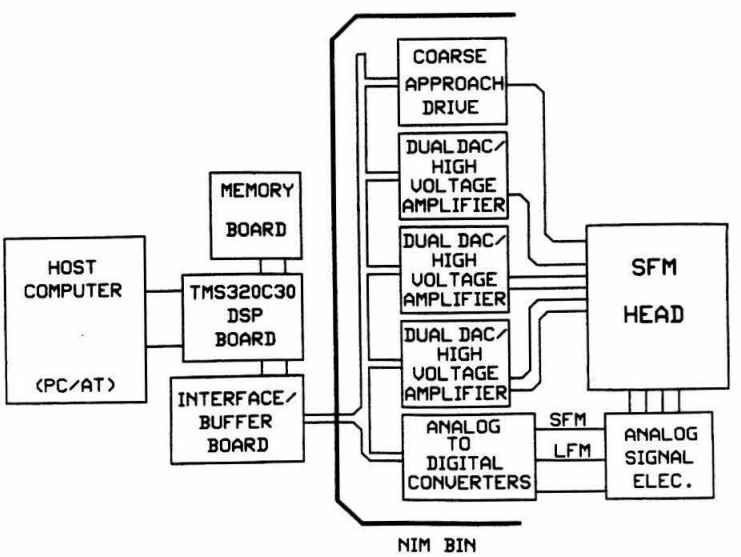

FIG. 3. A block diagram of the scanned probe microscope control and data acquisition system. The NIM (nuclear instrumentation module) bin is indicated only schematically and all power supplies have been omitted for diagram clarity. Other host systems and alternative packaging could clearly be used (e.g., workstations and VXI bus).

To interpret the shot noise limit in terms of position sensitivity for an optical lever based SFM requires knowledge of the diameter of the reflected beam at the photodiode face and the optical lever gain. For the SFM head presently used, the beam diameter at the photodiode is ≈ 10 mm and the optical lever gain is ≈ 2500 when using a 100-μm cantilever. Although the beam on the face of the photodiode has a Gaussian intensity profile, a worst case shot noise sensitivity value may be calculated by assuming a uniform intensity distribution. Using this approximation, with a 20-mW incident on the photodiode the shot noise limit corresponds to a position sensitivity of ≈ 0.05 Å.

IV. SYSTEM OVERVIEW

The system which we have designed and are presently using for experiments is based on a single DSP. We opted to purchase a board level DSP and to focus effort on developing the algorithms and software for SPM control as well as the analog *I/O* described in this paper. As can be seen in Fig. 3, the major components of the digital control and data acquisition system are the DSP, the piezo drivers, the analog signal processing section, and the ADCs. Because the analog signal processing electronics are instrument specific they will not be discussed in detail here.

For our system we chose the Spectrum TMS320C30 DSP board[16] which uses a personal computer (PC) as the host. The PC also serves for software development and image processing and display tasks. Due to the noise level introduced onto the DSP board by the PC, we found the on-board analog *I/O* to be inadequate for our needs, hence our custom designed analog *I/O* uses the external interface bus (DSP-Link).

For our laboratory the most cost effective method of packaging the analog *I/O* was to modify nuclear instrumentation module (NIM) bins by adding a digital backplane and to use commercially available NIM enclosures to house individual printed circuit boards. Using the NIM format forces design modularity and facilitates the exchange of modules between microscopes. We have buffered the DSP-Link signals and used these to drive directly the terminated digital backplane. This implementation of a generic high-speed digital bus allows zero wait state communication between the NIM modules and the DSP; in fact, by using high-speed bus drivers the present hardware could easily accommodate bus bandwidths in excess of 50 Mbytes/s. Other NIM bin modifications include the addition of an independent +5-V linear power supply for powering the digital circuitry and the addition of high voltage power supplies.

V. SYSTEM COMPONENTS

A. Digital signal processors

For most users the selection of a DSP for application in a SPM system will entail the selection of a board level component for a particular computational platform (personal computer, workstation, etc.). The major issues involved in the selection of a DSP board, such as floating point or integer operation, memory addressing capability, and the quality of on-board *I/O* functions are discussed in Ref. 17. Although the electronics described in this paper will function with any DSP board having an external bus, processor speed is an important factor if fast scan rates are required. Processors that have fast clock rates allow either more operations to be performed in the feedback loop or faster sampling intervals. At the time this work was begun, a TMS320C30 DSP(Texas Instruments[18]) based board from Spectrum Signal Processing was chosen due to its ready availability and reasonable price. This board has a 33-MHz DSP clock rate which allows 150 instructions to be executed in the interrupt interval used in our system (10 μs). We find that the 100-kHz sampling rate easily permits a feedback servo bandwidth of 20 kHz and that 150 instructions are adequate for the implementation of the *Z* feedback loop and the scan raster generation. Since the time of our purchase, board level products suitable for SPM control based on several different DSPs have come onto the market providing a variety of sophisticated products to choose from.

If the capabilities of board level DSP products prove to be inadequate for a particular microscope design, one may be forced to design a DSP board from scratch. This is obviously not a trivial undertaking and should only be done as a last resort; however, some points merit consideration.

The first point is that the performance of the *Z* feedback loop and its complexity are constrained by the speed of the DSP. Second, because the feedback loop is a real-time process, only minimal time delay can be tolerated without compromising scan rate. There are two potential areas in which to gain performance: (i) DSP speed, (ii) relieving the DSP of tasks easily handled by less sophisticated processors. Other advantages gained by the design of a SPM specific DSP board are the ability to place substantial amounts of fast memory and/or dual port memory on the board as well as the ability to use the serial data ports and external buses of the DSP to interface directly with the DACs and ADCs.

B. Piezoelectric ceramic drive electronics

Because we require high-resolution digital to analog converter (DAC) outputs we considered two ways to achieve high resolution: (i) by using a single high-resolution DAC; and (ii) by scaling the outputs of two or more lower resolution DACs and summing their outputs. Previously one would have been forced to implement the latter alternative, however, recently, tremendous progress has been made in the performance of low cost audio frequency DACs. With the availability of these components, the single DAC alternative becomes more attractive due to its simplicity.

Several manufacturers produce DACs which offer greater than 16-bit resolution with total harmonic distortion plus noise of less than -96 dB. Typical of this class of DAC is the PCM58P-K from Burr–Brown[19] which we have used in our SPM system. This is an 18-bit serial-input, current-output DAC with an idle channel signal to noise ratio of +126 dB at bipolar zero. This DAC per-

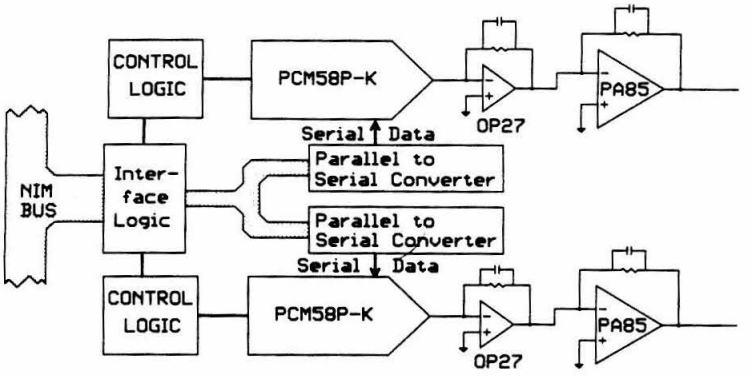

FIG. 4. A diagram of the piezoelectric ceramic electronics. The piezodrive electronics are composed of dual DACs and high voltage amplifiers. The interface logic consists of data and address buffers and address decoders. The address decoders are implemented in programmable array logic (PAL) devices. The control logic is also implemented in PALs and functions to provide the required clock and control signals for the DACs and the parallel to serial converters (shift registers).

forms suitably in SPM applications in our laboratory; however, even higher performance DACs such as the PCM63P (Burr–Brown) have recently come on the market. The PCM63P offers 20-bit resolution with low noise and for new designs this type of DAC should also be considered.

For our system the selection of high voltage amplifiers to drive the piezos was uncomplicated due to the narrow field of parts to choose from. Component level high voltage operational amplifiers suitable for SPM applications are available from primarily two companies, Apex Microtechnology[20] and Burr–Brown. The major considerations in judging a high voltage amplifier for use with piezoceramic scanners in SPM are (i) total output voltage swing, (ii) output noise, and (iii) current drive capacity. The current capability required of an amplifier is an important consideration because of the capacitance presented by the piezoceramic to the output of the amplifier. The output currents required of the amplifier to achieve a given output voltage slew rate may be found from $i=C\,dV/dt$. We used the PA85 from Apex because at the time it offered the greatest output voltage range at a suitable current capability.

C. Piezoelectric ceramic drive performance

A schematic diagram of a piezodrive module is shown in Fig. 4. The piezodrive electronics are composed of dual DACs and high voltage amplifiers. The interface logic consists of data and address buffers and address decoders. The address decoders are implemented in programmable array logic (PAL) devices. The control logic is also implemented in PALs and functions to provide the required clock and control signals for the DACs and the parallel to serial converters (shift registers).

The assembly is physically composed of two printed circuit boards mounted in a double width NIM module; one board contains the dual DAC circuitry and the other board contains the high voltage amplifiers. This division of the circuitry allows the use of the DAC section alone for low voltage applications (e.g., tip-sample bias generation) without having to fabricate special boards.

A theoretical analysis of the DAC/HV amplifier circuitry would predict that with a 420-V output range, the output noise of this section should be ≈ 100-μV rms in a 100-kHz bandwidth (discounting $1/f$ noise below about 10 Hz). Figures 5 and 6 present data to document the time

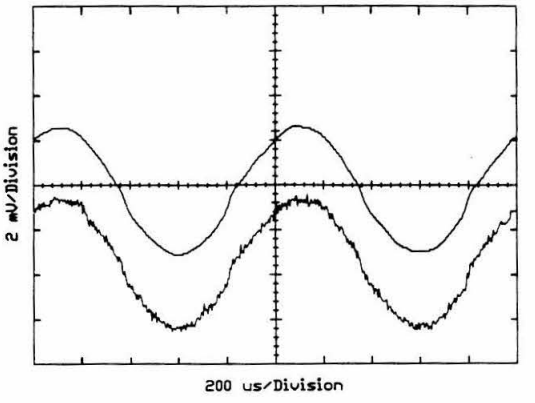

FIG. 5. Measured time domain characteristics of the 420-V range piezodrive electronics. The upper trace presents the average of 256 time traces taken by a digital storage oscilloscope (Tektronix 2440). The waveform amplitude is ≈ 5 mV (-98 dB) and its frequency is ≈ 1 kHz. This representation eliminates random noise (as it averages to zero) while maintaining any systematic features of the signal. The structure seen in the waveform is due to oscilloscope digitization and not individual DAC steps. The lower trace presents a single time trace of the same amplitude and frequency so that noise contribution may be seen. At this signal level the output consists of only three DAC steps but they are not visible due to the output low pass filters.

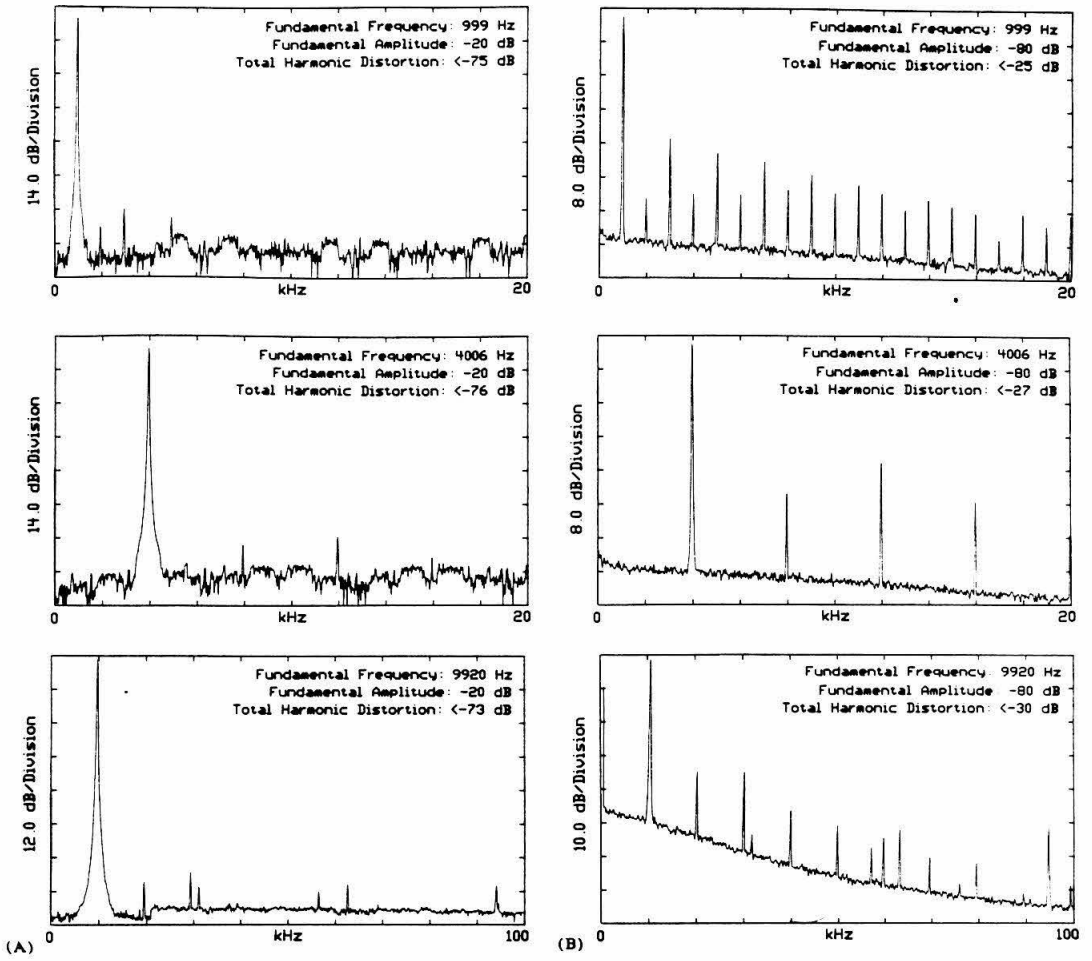

FIG. 6. Measured frequency domain characteristics of the 420-V range piezo drive electronics. Power spectra of the piezo drive electronics taken to assess the total harmonic distortion at various frequencies and signal amplitudes. The spectra were taken using a Hewlett-Packard 3563A Control Systems Analyzer. A resistor divider was used to scale the signal to avoid overloading the analyzer input circuitry. For all of the spectra, the analyzer was set to 50 time record averages. Note that the total dynamic range (maximum output signal/noise level of the output) of the piezo drive is ≈ 118 dB. (A) -20-dB signal level spectra. The total harmonic distortion is < -75 dB. (B) -80-dB signal level spectra. The total harmonic distortion is < -25 dB.

domain and frequency domain performance of the DAC/HV amplifier section. As can be seen in the time domain traces of Fig. 5, the broadband output noise of this section (without feedback) is 450-μV peak to peak (320-μV rms, or 0.016-Å rms for a microscope using a 50-Å/V piezo). This gives a measured dynamic range (maximum output signal/noise level of the output) of ≈ 118 dB.

In Fig. 6 we show power spectra measured to judge if the harmonic distortion of the DSP/HV amplifier section would present a problem. To perform this test of the circuitry, digital representations of the sine waves of various amplitudes and frequencies were generated and output via the piezo drive circuitry. The power spectra were measured using a Hewlett-Packard 3563A Control Systems Analyzer. An ideal spectrum would have a singie peak (strictly speaking, a delta function) located at the frequency of the sine wave with no other features. Two aspects of these spectra are of particular interest; the broadband noise can again be seen to be negligible (the baseline of the spectra match the recording instrument noise floor) and the spectral purity of the output signals eliminates concerns that nonlinearity in the drive electronics might give rise to noise in the Z feedback loop or excite undesired resonances in the piezotube.

When examined together, the data of Figs. 5 and 6 document a level of output performance which compares very favorably with completely analog SPM control systems and was previously unattainable with low cost digital systems. The outstanding performance of this circuitry strongly suggests that this section should function adequately for most SPM applications. In the event that this level of performance is inadequate, further reductions in the output noise level and signal purity may be obtained by using better high voltage power supplies in conjunction with better electrical shielding.

D. Analog to digital converters

In the area of analog to digital converters (ADCs), again striking progress has been made both in cost and performance. Recently several companies have introduced parts which offer 16 bit and greater resolution. Two architectures dominate the field: (i) the delta/sigma type and (ii) the successive approximation type.[21] We have found that the conversion time, defined as the time interval between the sampling of a signal at the start of the conversion process and the end of the conversion at which time the digital value is available for the servo loop to act on, typical of commercially available delta/sigma converters (on the order of 1 ms) would severely limit feedback loop bandwidth. Thus we have chosen the PCM78P from Burr–Brown, a 16-bit successive approximation converter which offers a 5-μs conversion time with better than -80-dB signal-to-noise ratio. Although the PCM78P claims 16-bit resolution, it is specified as having only 14-bit linearity and no missing codes at 14-bit resolution.

The other components which determine the performance of the ADC section are the anti-aliasing filter and the track and hold amplifier. The practical criterion which must be met by the anti-aliasing filter is that signals in the frequency region above half the ADC sampling frequency must be attenuated to less than one least significant bit. We have found the APQ-25 series of passive filters from Toko America[22] to be more than suitable in this role. The particular part used in our system is a seven pole low pass filter with a constant $\approx$35-μs group delay (the time taken for a signal to pass through the filter) throughout the passband and a nominal cutoff frequency of $\approx$30 kHz. Passive filters are preferred for low noise applications because passive components add a minimum of noise to the processed signal.

The track and hold amplifier used in conjunction with the ADC must be compatible with the desired system performance (i.e., a 12-bit track and hold will degrade the performance of a 16-bit ADC). As specified by Analog Devices,[23] the AD1154BW track and hold amplifier is compatible with our design goals. The AD1154BW is a true 16 bit, low cost track and hold amplifier with a 2-μs settling time. It performs well in our SPM.

E. ADC section performance

Figure 7 presents a schematic of a single ADC section. The four ADC sections contained on a single ADC board

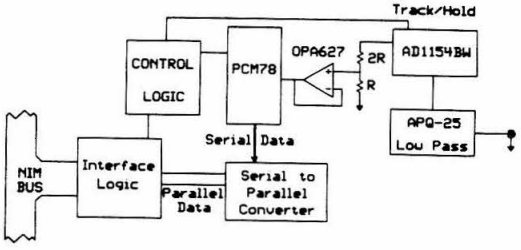

FIG. 7. A diagram of a single-channel analog to digital converter for the scanned probe microscope control and data acquisition system. The resistor divider is included to correctly scale the input to the ADC and the operational amplifier (OPA627) serves to buffer the divider voltage from the dynamic 1.5-kΩ input impedance of the ADC. In the prototype system there are four such channels on the ADC board. The interface logic consists of data and address buffers and address decoders. The address decoders are implemented in programmable array logic (PAL) devices. The control logic is also implemented in PALs and functions to provide the required clock and control signals for the ADCs and the serial to parallel converters (shift registers).

are housed in a double width NIM module. One convert command triggers the conversion start for all of the ADCs, thus avoiding any question concerning the phase relations of the individual ADCs. For SFM we use three of the ADCs; one for vertical cantilever deflection, one for torsional cantilever motion, and one for total light intensity on the quadrant photodiode. An alternative scheme for SFM is to directly digitize all four photodiode quadrant signals. This approach has the advantage that an almost perfect common mode signal rejection ratio can be obtained. In order to do the digital signal processing required by digitizing all of the quadrant signals the sampling interval would have to be lengthened and this might limit the Z feedback servo bandwidth. In our system we might have to increase the sampling interval from 10 to 15 μs to provide the required computational time.

The design goal for the ADC section was to achieve full 16-bit measurement capability with a $\pm$10-V input range at a sampling rate in excess of 100 kHz. This would give four times oversampling of the highest frequency signals of interest, thus meeting the requirements of the Z feedback loop and allowing high scan rates. The ADC section achieves a maximum conversion time of $\approx$6 μs allowing a sampling rate in excess of 150 kHz. At this sampling rate the ADC section yields 14 bit performance which is limited by ADC noise of 2 bits (4 ADC units or 1.2 mV referred to the ADC section input).

We have done a more detailed evaluation of the ADC circuitry for missing codes (at 12–16 bit resolution levels) and differential linearity[21] which is shown in Fig. 8. To do the evaluation we use a low-frequency linear bipolar ramp as the input waveform to the ADC. By using this waveform and acquiring data over many cycles of the ramp we should accumulate a significant number of samples at each of the ADC output codes. We then construct a histogram which has each of the output codes along the abscissa and the number of samples at each output code as the ordinate.

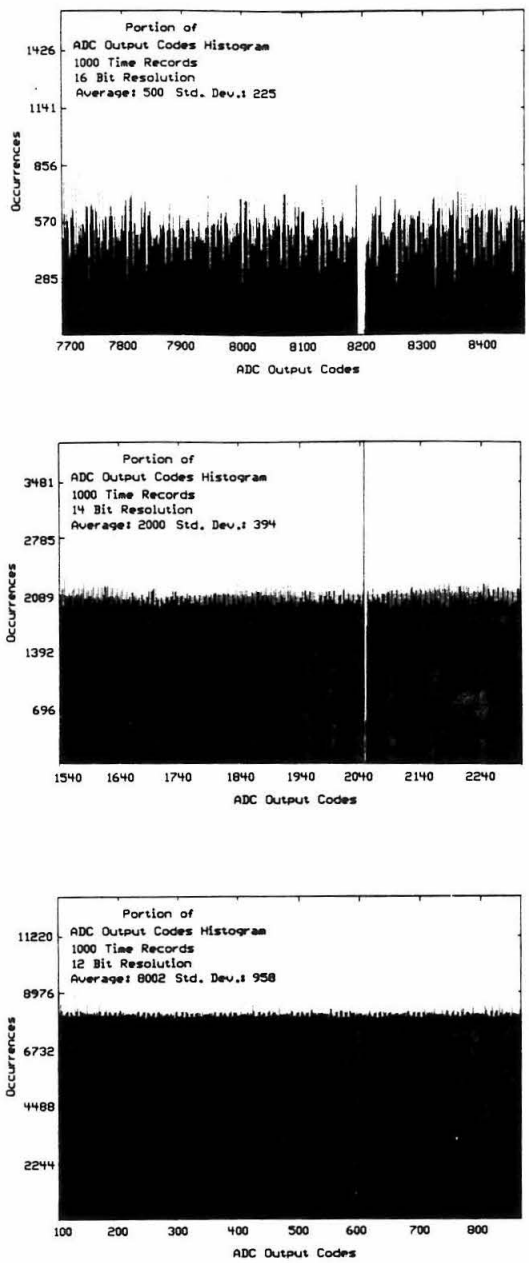

FIG. 8. Measured performance of the analog to digital converter section. A typical section of ADC output code histogram at three resolution levels. The same area of missing codes is presented in each of the histograms at a different resolution level so that the effects of rebinning would be clear. The sections of histograms shown were selected because they are illustrative of clusters of missing codes found in the ADC output. All of the histograms are derived from a data set consisting of 1000 time records.

For an ideal ADC this histogram would have an average number of samples in each of the bins with the expected deviation from this being given by the square root of the number of samples expected in the bin. If the ADC has missing codes one would expect that there would be no samples falling within the bin for the missing code. Differential linearity may also be coarsely judged by this technique; bins which show deviation from the expected value of samples in the bin by more than the standard deviation can be judged to have a linearity problem. In Fig. 8, two aspects of the histogram structure are noteworthy. First, we find that there are indeed bins with no samples and that if we reduce the effective ADC resolution by rebinning (i.e., to bin at 15-bit resolution we combine adjacent bins from the 16-bit histogram, etc.) it is only when we reach the 12-bit resolution level that there are no missing codes. Second, the histograms show significant deviations from ideal behavior in both periodic structure and deviation from the value expected in the bins.

One can view the number of counts in a bin as representative of the width of a bin (i.e., the voltage range resulting in a count being added to a particular bin). Adopting this view, one finds from Fig. 8, that bins corresponding to missing codes often have very wide bins adjacent to them. Thus, if one regards the ADC output code histogram as constituting a type of transfer function for the ADC, one could increase ADC performance by post-processing data to normalize bin width (reduce differential linearity error to zero).

In order to summarize the differential linearity measurement we have constructed a second type of histogram, shown in Fig. 9, called the count distribution histogram. In this histogram we display the number of counts in a bin (bin value) as the abscissa and the number of bins which contain that bin value as the ordinate. Again, if the ADC performance were ideal, this should produce a distribution with a single mode located at the average number of samples in a bin. The area of the histogram equals the total number of samples and the standard deviation of the distribution would be found from Poisson statistics to be the square root of the average number of samples expected in a bin. As can be seen in Fig. 9, the stringency of this test technique varies with the number of samples. In the small sample cases, 10 and 100 time records, the distribution does not show significant departure from ideal behavior (i.e., the distributions show one mode and Poisson character). However, in the large sample cases there is a clear deviation from ideal. The appearance of multiple maxima in the distribution indicates that ADC bin widths are not uniform, but rather, their widths occur in clusters. The clustering of bin widths at values distinct from the mean necessarily implies differential nonlinearity. Although these test data indicate that the differential linearity of PCM78P leaves a great deal to be desired, we find in practice, that the signal-to-noise ratios of our SPM system are sufficiently large that missing codes and nonlinearities in the ADC circuitry do not seriously degrade instrument performance (e.g., four consecutive ADC codes for ± 10-V input range at 16-bit resolution corresponds to a "dead

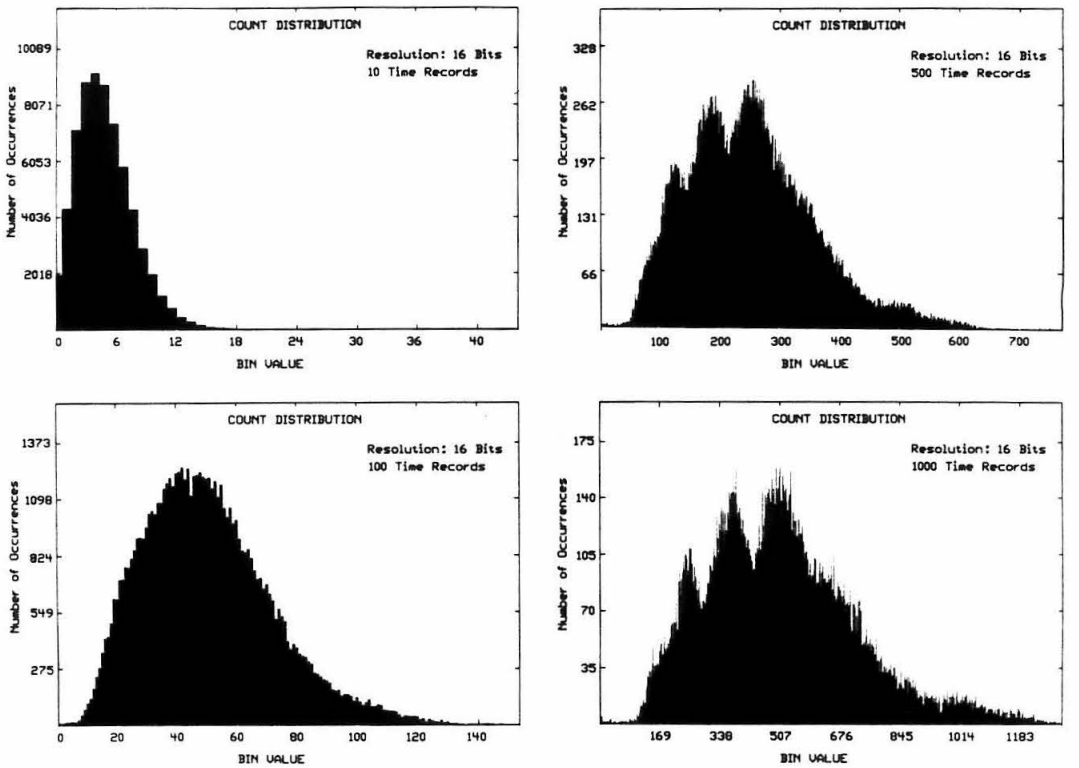

FIG. 9. Evolution of the count distribution histogram with sample size. These histograms demonstrate the general Poisson character of the count distribution histogram. The construction of the histograms from the binned data of Fig. 9 is described in the text. In the histograms with larger numbers of samples one can see not only significant deviation from an ideal Poisson distribution, but also the multimodal character of the histogram. These data are indicative of the poor differential linearity of the PCM78P.

band" of ≈ 1.2 mV). For systems in which this is not the case, we believe that the diagnostic tests outline above may prove useful in the selection of ADCs.

Although we are not able to achieve 16-bit performance, we would point out that a 14-bit performance level is tolerable for most SPMs, and that systems which offer performance superior to ours are much more expensive (by factors of 5–10). Also, as mentioned previously, the adaptation of the system to accommodate higher performance ADCs as they are required is quite straightforward. One should also note that, for some SPM designs, high-speed true 12-bit ADCs may be an optimal ADC choice.

VI. SYSTEM PERFORMANCE

To evaluate the ability of the system to control a SPM we have used the system in conjunction with several different types of microscope available in our laboratory. Perhaps the instrument which best illustrates the capability of the control system is the ultrahigh vacuum scanning tunneling microscope (UHVSTM). We have recently constructed a new scanner and sample translator assembly for the UHVSTM. The new scanner is capable of motions six times larger along the Z axis (2 μm) and ten times larger in the X and Y dimensions (3 μm) than our previous scanner. The new scanner was limited by the electronic noise of the control electronics which were previously used and could only achieve atomic resolution with the servo control voltage was limited to a 30-V range. When using the control system described in this paper, atomic resolution was achieved with a full 380-V control range; the imaging capability was limited in this case by the mechanical stability of the scanner assembly, rather than by the control electronics. Additionally, the modular design of the system and its standard communication interface allowed simple integration of control electronics for the sample translator.

The use of data from the UHVSTM to illustrate the system performance avoids some of the questions raised of STM in air, and tip sharpness can be evaluated by field ion microscopy in this microscope thus avoiding concerns common to SFM. In Fig. 10 we show an image of highly oriented pyrolytic graphite (HOPG) taken with the UHVSTM controlled by the digital control system. The

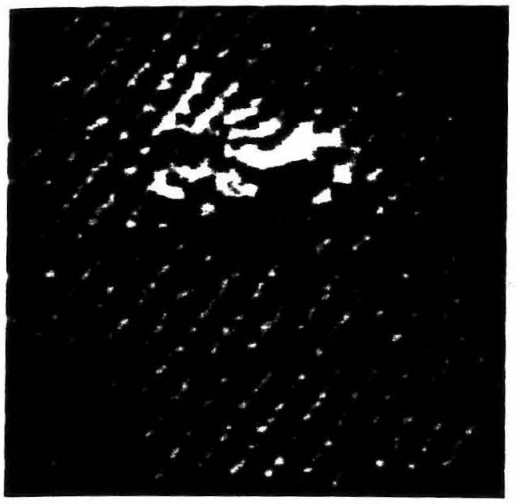

FIG. 10. An image of highly oriented pyrolytic graphite (HOPG) taken using the SPM control electronics presented in this article to control an ultrahigh vacuum (UHV) scanning tunneling microscope. A physisorbed contaminant is seen on the inert graphite basal plane. The image is approximately 50×50 Å with 250×250 pixels acquired at 250 pixels/s. It is a constant current image (tunneling current ≈1 nA) at a sample bias of −0.1 V. The brightness in the image is proportional to both topographic height and slope. For details of image processing see the text.

data show atomic resolution as well as a physisorbed contaminant on the inert graphite basal plane. (During a subsequent scan, the contaminent was swept away midscan, thus affirming that it was weakly bound through physisorption rather than chemisorption.) The image is approximately 50×50 Å with 250×250 pixels acquired at 250 pixels/second. It is a constant current image acquired at a tunneling current of 1 nA with a −0.1-V sample bias. The image is displayed with brightness proportional to both topographic height and slope. Tilt was removed by plane subtraction, and noise reduction was done through median filtering followed by smoothing with a binomially weighted sliding window 1-Å square (full width at half maximum) which is small compared to the 2.4 Å unit cell of HOPG.

VII. ADAPTATION OF THE SPM CONTROL AND DATA ACQUISITION SYSTEM TO NEAR FIELD SCANNING OPTICAL MICROSCOPY

Finally, as an example of the flexibility afforded by modular design we consider the adaptation of the system to near field scanning optical microscopy (NSOM). NSOM holds great potential for imaging biomaterials because it provides all of the advantages of optical microscopy with subwavelength resolution. As a field of microscopy, NSOM is still evolving rapidly. With the need to implement quickly various imaging modes and feedback schemes, the flexibility provided by a modular SPM control system could be a tremendous advantage.

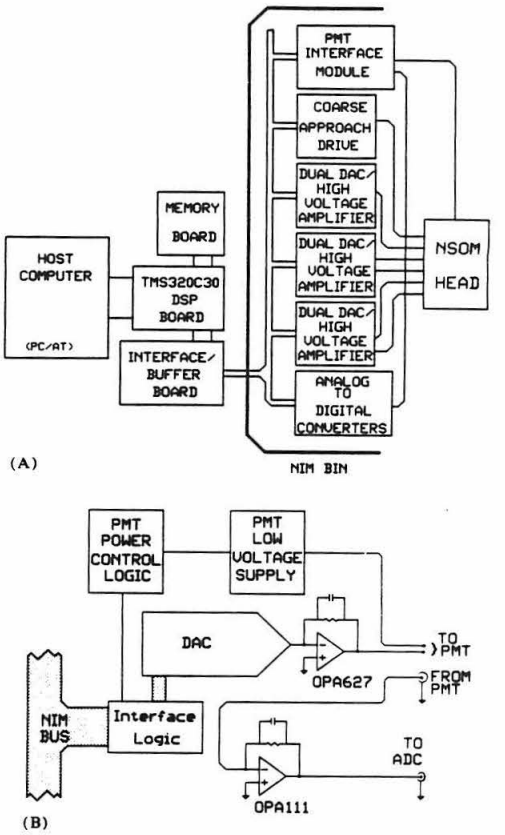

FIG. 11. A block diagram of the SPM control and data acquisition system as it might be adapted for near field scanning optical microscopy. The major addition needed to perform NSOM experiments is the photomultiplier tube (PMT) control and data acquisition module. (A) A diagram showing how the PMT module interfaces with the rest of the SPM system. (B) A more detailed diagram of the PMT module itself showing conceptually how such a module might be implemented.

The adaptation of the SPM control and data acquisition system to do NSOM is quite simple. In terms of the software, only minor reconfiguration is required. As for the hardware, the only additional requirement is that the instrument be able to detect very weak intensity light signals; thus there is a need for the ability to control and acquire data from photomultiplier tubes (PMTs). In Figs. 11(a) and 11(b) we present a diagram of how the control of and data acquisition from a PMT might be done. Figure 11(a) shows a diagram of how a PMT control module could be added to the system. In Fig. 11(b) we show a more detailed diagram of the contents of the PMT control module.

The relevant parameters for PMTS are the magnitude of the high voltage applied to the tube during use and the photocurrent that is generated. Currently, at least one manufacturer[24] supplies a hybrid photodetector which con-

sists of a PMT, a PMT socket, and a miniaturized switching mode power supply to provide the high voltage. The high voltage applied to the PMT may be varied by adjusting a low voltage control line via a DAC and the supply may be turned on and off by turning off the low voltage power to the detector. We have found these self-contained units to have excellent performance as well as being quite compact and convenient.

When photon counting is not required, acquisition of data from the PMT is easily done by using the standard current to voltage conversion circuit with a high input impedance amplifier. When using this type of circuit it is important to note that electrometer amplifiers tend to have significant output impedances and may require some buffering before the ADC input.

The adaptation of the SPM control system for NSOM is as simple as the construction and installation of a module to interface with PMTs. With this type of module both integrated light intensity and light modulation detection could easily be done.

ACKNOWLEDGMENTS

The authors would like to thank Jean-Paul Revel for a critical reading of the manuscript. Financial support for this work was provided by Abbott Laboratories, Inc., the National Institutes of Health Training Grant GM07617 (S.M.C.), the Ford Motor Company, and a National Science Foundation Fellowship (D.R.B.). The authors will gladly supply more detailed documentation to interested readers.

[1] J. H. Hoh, R. Lal, S. A. John, J.-P. Revel, and M. F. Arnsdorf, Science **253**, 1405 (1991).
[2] H. G. Hansma *et al.* Science (in press).
[3] A. Engel, Annu. Rev. Biophys. Biophys. Chem. **20**, 79 (1991).
[4] C. Bustamante, J. Vesenka, C. Tang, W. Rees, M. Guthold, and R. Keller, Biochemistry **31**, 22 (1992).
[5] A. Lewis and K. Lieberman, Anal. Chem. **63**, 625 A (1991) and references therein.
[6] C. Prater, P. Hansma, M. Tortonese, and C. Quate, Rev. Sci. Instrum. **62**, 2634 (1991).
[7] A. Bard, F. Fan, D. Pierce, P. Unwin, D. Wipf, and F. Zhou, Science **254**, 68 (1991).
[8] O. Marti, S. Gould, and P. K. Hansma, Rev. Sci. Instrum. **59**, 836 (1988).
[9] A. Brown and R. W. Cline, Rev. Sci. Instrum. **61**, 1484 (1990).
[10] R. S. Robinson, T. H. Kimsey, and R. Kimsey, J. Vac. Sci. Technol. B **9**, 631 (1991).
[11] A. J. Hoeven, E. J. van Loenen, P. J. G. M. van Hooft, and K. Oosterveen, Rev. Sci. Instrum. **61**, 1668 (1990).
[12] R. Piner and R. Reifenberger, Rev. Sci. Instrum. **60**, 3123 (1989).
[13] R. C. Barrett and C. F. Quate, Rev. Sci. Instrum. **62**, 1393 (1991).
[14] Motorola, Inc., P. O. Box 1466, Austin, TX 78767 USA.
[15] A. Ambrozy, *Electronic Noise* (McGraw–Hill, New York, 1982).
[16] Spectrum Signal Processing, Inc., #301 3700 Gilmore Way, Burnaby, B.C. V5G4M1, Canada.
[17] D. Baselt, S. Clark, M. Youngquist, C. Spence, and J. Baldeschwieler, in preparation.
[18] Texas Instruments, Inc., P.O. Box 655012, Dallas, TX 75265 USA.
[19] Burr–Brown Corp., 6730 S. Tucson Blvd., Tucson, AZ 85734 USA.
[20] Apex Microtechnology, Corp., 5980 N. Shannon Rd., Tucson, AZ 85741 USA.
[21] D. Sheingold, ed., *Analog-Digital Handbook* (Prentice–Hall, Englewood Cliffs, NJ, 1986).
[22] Toko America, Inc., 1250 Feehanville Dr., Mount Prospect, IL 60056 USA.
[23] Analog Devices, Inc., One Technology Way, P.O. Box 9106, Norwood, MA 02062 USA.
[24] Hamamatsu Photonics Corp., 360 Foothill Road, P.O. Box 6910, Bridgewater, N.J. 08807 USA.
[25] G. Franklin and J. Powell, *Digital Control of Dynamic Systems* (Addison–Wesley, Menlo Park, CA 1980).

Appendix E: Digital Signal Processor Control of Scanned Probe Microscopes

This appendix is adapted from a manuscript originally submitted to *Review of Scientific Instruments* and is included to allow a more complete understanding of the digital control system implemented with the new microscope heads. The original SPM operating system software from which the STM code was adapted is the work of David Baselt.

Digital Signal Processor Control of Scanned Probe Microscopes

David R. Baselt, Steven M. Clark†, Michael G. Youngquist, Charles F. Spence†
and John D. Baldeschwieler

A. A. Noyes Laboratory of Chemical Physics

Division of Chemistry and Chemical Engineering

and

[†]Division of Biology

California Institute of Technology

Pasadena, CA 91125

Abstract

Software for a digital signal processor based scanned probe microscope (SPM) control system is described. The SPM control system consists of a commercial digital signal processor board interfaced to analog I/O and run by the control system software. All of the SPM control functions are implemented in software allowing unprecedented flexibility without sacrificing performance. The system is capable of supporting a wide variety of SPM experiments including tunneling, force and nearfield optical microscopy. We discuss implementations of feedback, raster generation (including hysteresis correction, compensation for sample tilt and scan rotation), automatic tip-sample approach and a digital lock-in amplifier. We also present an instruction parser architecture which significantly enhances the control system.

Introduction

Since the invention of the scanning tunneling microscope in 1981,[1] a new branch of microscopy has emerged. Scanned probe microscopy (SPM), as it has come to be known, now encompasses more than twenty different modalities of sample imaging via their interaction with a rastered probe.[2] While the physics underlying the microscopies is diverse, they all share basic requirements for microscope control and data acquisition. To perform SPM a probe must be positioned near a sample and (usually) rastered while various signals are measured as functions of probe position, input parameters (e.g., tip-sample bias in STM), and/or time. The primary experimental differences

which must be addressed by an SPM control system are input signal generation and sensor linearity, Z-feedback response rate and the number of data types recorded at each sampling interval.

Digital signal processor (DSP) boards which enable straightforward implementation of digital control systems have recently become available. By using these boards it is possible to assemble an effective and flexible SPM control system. The key advantages of such a system are its inherent flexibility, modularity, improved noise immunity and relatively low cost (10-30% of commercial SPM systems). Additionally, functions which may be too complex or cumbersome to implement using hardware can often be added by modifying the DSP control software. Despite the common use of DSPs for SPM control in commercial instruments, we are unaware of any detailed treatment of DSP based SPM control systems in the literature.[3-13]

In this paper we describe the software for a DSP based SPM control system assembled using board level components. In its most basic form the control system generates the XY raster, performs the Z-feedback and records SPM data. We present algorithms for these functions as well as more advanced features such as digital oscilloscope and lock-in amplifier emulations. To give the context in which the software operates, we begin with an overview of the basic hardware requirements of the system and discuss some of the considerations involved in component selection.

Hardware Overview

In a digital control system for SPM (see Figure C.1) the proximity signal (tunneling current in STM, cantilever deflection in SFM, etc.) is measured by a sensor using analog signal processing electronics and digitized by an analog to digital converter (ADC). This ADC reading of the sensor output (referred to as C) is compared against a digital setpoint to obtain an error signal. The error signal is used to calculate a digital code representing the ideal voltage to be applied to the Z axis of the piezoelectric micropositioner (hereafter referred to as the piezo). The algorithm used for this calculation comprises the Z feedback loop. This new Z code is converted into the actual Z voltage (later referred to as Z), which moves the piezo in a direction perpendicular to the sample surface, by a digital to analog converter (DAC). The DAC output is amplified by a high voltage amplifier to provide the output voltage necessary to drive the piezo. The raster voltages used to drive the piezo in the X and Y dimensions are typically generated in an open loop fashion (that is, they are calculated and sent to the X and Y DACs without measuring a control signal for them); however closed loop XY positioning offers the capability to correct imperfections in the piezo

response.[14] In this paper we have adopted the convention that X refers to the fast raster voltage and Y to the slow raster voltage.

DSPs are particularly well suited for the real-time computation and signal processing tasks necessary for implementing a digital SPM. They typically contain features such as single cycle multiplication, matrix manipulation facilities and clock speeds of 20 MHz and greater. Thus, DSPs are much faster for these tasks than microcontrollers or other dedicated microprocessors. Another point should be made about DSPs; because they are independent processors they can perform operations concurrently with the host processor. In many cases a DSP can be used to accelerate tasks to be performed by a host, but for instrument control it is often more useful to load a program which the DSP runs independently of the host platform. One way to optimally exploit this dual processor architecture is to divide tasks into two sets, instrument control to be run by the DSP and user interface to be run by the host system.

Since board level DSP coprocessor products are now commercially available for a variety of host computer platforms, the ability to use DSPs for controlling SPMs is a practical alternative for those constructing their own SPM. A basic system, illustrated by the scanned probe microscope schematic of Figure E.1, consists of the DSP board, its host computer and the analog I/O circuitry. The two major considerations involved in the selection of processors are whether floating point or integer DSPs are to be used and how much memory should be directly addressable by the DSP. Additionally, the selected DSP board must be compatible with the intended analog I/O and the

host computer. For the system that we have built, a TMS320C30 system board[15] was chosen. This board uses a 80386 IBM PC\AT compatible computer as its host.

The amount of DSP memory required is another matter of programming convenience. Our particular system is capable of generating data at rates of 1.2 Mbytes/sec. Although storing data on the host computer, a PC, at this rate is an inexpensive option, it requires extensive knowledge of PC hardware and 80x86 assembly language programming. Therefore, we chose a DSP board with enough memory for on-board image storage. For on-board image storage a minimum of 250 Kwords is recommended and 2 Mwords is not excessive. The TMS320C30[16] has a 16 Mword directly addressable memory space and not the segmented memory space of the 80x86 processors when run under DOS. The TMS320's straightforward memory structure greatly decreases analysis time and simplifies programming especially for image manipulation routines. While purchasing DSP on-board memory is significantly more expensive, the programming simplicity it provides makes it cost effective.

The last major area that must be addressed during the hardware design phase of the construction of an SPM control system is the type of analog I/O to be used. There are three major alternatives to consider: i) the use of DSP on-board analog I/O, ii) the use of off-board analog I/O, and iii) the construction of custom designed analog I/O.

While the use of DSP on-board analog I/O provides the most convenient alternative, this advantage often comes at the price of resolution

and noise performance. On-board analog I/O sections may be susceptible to noise generated by the host computer and the DSP itself; hence, even if the board contains high resolution parts (e.g., full 16 bit ADCs) the system performance can be compromised to the 10 to 12 bit level. During the initial stages of system construction, we found the use of on-board I/O to be very helpful because it allowed software development to proceed in parallel with custom hardware design. For those who need the flexibility obtainable with a DSP based system, but do not need particularly high final performance the use of on-board analog I/O may be the optimal alternative.

Almost the same degree of convenience of on-board I/O can be achieved through the use of off-board analog I/O. This type of I/O circuitry is available as board level products internal or external to the host from many different manufacturers.[17] We prefer to use boards external to the host computer in order to keep the I/O section out of the noisy host environment and separately powered, while maintaining the ability to directly connect to the DSP board. Internal board level products usually suffer from the same host induced noise as do on-board I/O. However, some properly shielded and carefully powered products are available which can obtain 16-bit performance and boards of this type are strongly recommended if external I/O cannot be used.

One last issue of importance in the selection of any analog I/O product is the type of analog to digital converter used. Board level products containing delta-sigma converters[18] should not be used for control loop applications. While these converters provide high resolution, good noise

immunity and high sample rates, their long group delay (on the order of 1ms) precludes their use in feedback loops. Successive approximation converters[18] and their variants are preferred for high resolution, servo loop applications because their short conversion times and low group delay times do not require a sacrifice in feedback loop bandwidth.

As the final analog I/O alternative, one must also consider custom built I/O. By designing and constructing custom I/O, true state-of-the-art performance can be achieved. The major drawback to this alternative is the cost in terms of development time. The process of custom I/O development from conceptual design through testing and debugging of the final hardware can occupy an experienced engineer for several months. For those seriously considering this choice, some of the issues involved in the design of a custom I/O section are covered in Reference 19.

Software

The major advantage offered by a DSP based instrument control system is flexibility. Because the software is responsible for all instrument control functions, many of the instrument's fundamental features can be tailored and optimized through simple software changes. The dual processor architecture described in this paper naturally lends itself to a division of software tasks in which instrument control functions are handled by the DSP program and the user interface by a separate PC program.

Timing Considerations

Most SPM control functions occur in "real-time" and so they require consistent and predictable timing to function properly. This is true not only of the feedback loop, where a regular sampling interval is crucial to predictable loop performance, but also for raster generation and modulation imaging. Because DSPs are specifically designed for "real-time" signal processing, they often have built-in timers which make it easy to reliably time control functions. These timers are usually programmable and can be used to generate processor interrupts. An interrupt is a signal which stops the execution of the current program the processor is running and starts the execution of another specific program (the interrupt service routine or ISR). For example, by having the ISR perform a function such as read an ADC and return control to a main program one can record data from an ADC at regular intervals.

In our control system we set one of the built-in timers of the DSP to trigger once every 10-15 μs, depending on the experiment in progress. This timer period serves as the fundamental clock by which all the time dependent functions of the SPM operate. Once per timer period, the XY raster is advanced, the ADCs are read, the feedback loop calculations are performed, and image data is updated (see Figure E.2). In our software this set of functions comprises the ISR. After the ISR has been executed, the software calculates the next X and Y positions, sends data to the host for display and waits for the timer to generate the next interrupt. By using this scheme, control functions are timed to the accuracy of the DSP clock.

The total time required for the "once-per-timer-period" tasks must be less than the timer period. It is desirable to keep the timer period as short as possible. Because the system cannot take more than one data point per timer period, a shorter period means that faster scans are possible and that more oversampling can be done on slower scans. Additionally, the optimum response rate of the feedback (i.e., its ability to follow the topography of the sample surface) depends in part on the timer period. However, the period cannot be arbitrarily short since the period cannot be less than the ADC conversion time, typically 5-10 μs for 16 bit ADC's. With our DSP a 10 μs period, which allows 166 instruction cycles, is enough for basic SPM operation. If many time-consuming features (i.e., several types of modulation imaging at once, numerous data channels, etc.) are used simultaneously, up to a 15 μs timer period may be needed.

Feedback

One of the greatest advantages of the DSP-based architecture is that it enables software emulation of analog feedback. Analog feedback is capable of superb servo loop performance in many applications and would be preferred for feedback in an SPM except that hardware implementations of analog servos tend to be difficult to optimize in real time. By using digital feedback it is possible to vary feedback parameters over a wide range from within the software. This allows the feedback loop response to be optimized for each combination of tip and sample which can be cumbersome in exclusively analog systems. Another advantage gained by using digital

feedback is the simplified implementation of more advanced functions such as spectroscopy, digital modulation, and sample tilt compensation.

The fundamental function of the feedback loop is to maintain the sensor output voltage at a constant level (the "setpoint") specified by the user. The loop does this by continually adjusting Z, as determined by the algorithm which composes the loop. The feedback algorithm determines the sign and the magnitude of Z to compensate for any difference between C and the setpoint. If the adjustment to Z is made based on the previous Z values, the loop is a feedback loop. On the other hand, if Z is adjusted in anticipation of what the next value of Z should be (based on some model or other information) the loop is referred to as a feedforward loop. In our software we use a feedback loop to maintain constant C on a local basis, however sample tilt compensation is done using feedforward correction.

Feedback Algorithms

Several different types of feedback loops can be implemented using DSPs, but only a few are appropriate for use as a control loop for SPM. Among the types of feedback we have found most useful are integral and proportional-integral-differential (PID) feedback. Although a feedback loop based on an optimal feedback design approach may provide superior performance for atomic force microscopy (AFM), we were interested in a control loop which is generally applicable to various types of SPM; we have found that PID feedback works well for both STM and AFM. In order to simplify the discussion of feedback algorithms we begin by examining the principles involved in the integral feedback loop.

Integral Feedback

Perhaps the simplest feedback algorithm can be constructed as follows: Measure the sensor output and determine its deviation from the setpoint (the "error"). Assume that changing Z produces a proportional change in the sensor output (i.e., the sensor is linear). To reduce the error, Z should then be changed by an amount proportional to the error. This can be expressed mathematically as:

$$E_{(kt)} = C_{(kt)} - S$$

$$Z_{(k+1t)} = Z_{(kt)} + IE_{(kt)},$$

where

t = the timer interval

k = an integer index which increases by one every interrupt cycle

$E_{(kt)}$ = the error signal sampled at interval kt

$C_{(kt)}$ = the ADC reading of the sensor output at interval kt

S = the user specified digital setpoint

$Z_{(kt)}$ = the voltage applied to the Z piezo electrode at interval kt

I = the user specified integral feedback gain.

Because the output depends only on the previous values of Z (in the sense that new Z values are found from the rectangular approximation integral of the input C) this is an integral feedback algorithm. The major advantage to an integral feedback loop is that it eliminates steady-state error (an offset from the setpoint which is time independent) in the servo. This is an important capability, but it comes at the price of speed. Since the new Z is a sort of rolling average of previous Z values, the integral feedback loop can

be seen to act as a low-pass filter which tends to slow the servo response to transients.

One of the major assumptions made for the integral feedback loop was that the sensor response is linear . This is not always the case and, in fact, one of the most notable exceptions is when the sensor is a tunneling probe. Although integral feedback has been used successfully with such nonlinear sensors, many users prefer to first linearize the tunneling current output with a logarithmic amplifier or in the instrument control software.

The integral feedback loop also serves to illustrate some of the other points concerning the general features of feedback. The first point to be made is that the feedback can be turned off simply by setting the gain (I) to zero. In this case the new Z value is equal to the old Z value and thus Z remains at the last Z value before the feedback was turned off. Another feature of feedback can be seen by considering the effect of too large a gain setting. In this case small errors cause large corrections in Z; if there are time delays in the loop, such as the ADC conversion delay, the phase delay through the anti-aliasing filter or the finite response time of the SPM stage, the loop will tend to overcompensate errors. This leads to oscillations in both the sensor signal and in the feedback response. The requirement of loop stability imposes an upper bound on the rate at which a feedback loop can respond to perturbations. For SPM this means that while scanning, changes in topography can only be followed well if they lie within the bandwidth of the feedback loop. To attain the best performance possible from the feedback loop the gains should be set as high as possible without causing the loop to

oscillate; this makes the loop bandwidth as high as possible and increases the accuracy with which topography is followed.

One should also note that, because the integral feedback loop acts as a low-pass filter, there will be information in the sensor signal that is lost in the Z output. This means that by storing exclusively either the Z output (which is proportional to larger scale image features) or the sensor output (which contains information regarding smaller scale structures) one inherently filters the data in some ill defined manner. Others have noted this distinction between the information in the sensor output and that in the Z output and have created a "new imaging" mode based on recording the fluctuations in the sensor output while maintaining the feedback in the regular manner.[20] While this does give better lateral resolution, it does so at the expense of height information. Thus it may arguably be best to store both types of data and combine them later in post-processing of the data. If this is done no information is lost and a better representation of the sample may be obtained.

PID Feedback

It is possible to improve on some of the limitations of an integral feedback loop by using a more sophisticated algorithm such as proportional-integral-differential feedback. Through the addition of the proportional and differential terms one can increase the speed of the transient response and reduce overshoot and ringing respectively. In our laboratory we use PID feedback because it is easily implemented in a DSP based system and it is a robust algorithm that has proved useful in a wide variety of applications.

Conceptually, PID feedback sums the outputs of three separate feedback loops (Table I). Proportional feedback allows quick response to small features, and is used to increase the bandwidth of the loop, but will not address the problem of steady-state error. Integral feedback, described above, eliminates steady-state error, but does so at the expense of bandwidth and increased overshoot in the transient response. Differential feedback tends to reduce oscillations and overshoot in the transient response, but tends to amplify high frequency noise. By combining all three types of feedback one can tap the strengths of each of the algorithms and arrive at a feedback loop which provides good performance.

Table I. Formulas for Feedback Algorithms

Proportional Feedback	$Z_t = P\,E_t$
Integral Feedback (Trapezoidal Approx.)	$Z_t = Z_{t-1} + I(E_t + E_{t-1})$
Derivative Feedback	$Z_t = D(E_t - E_{t-1})$
P-I-D Feedback	$Zt = P\,E_t + Z_{t-1} + I(E_t + E_{t-1}) + D(E_t - E_{t-1})$

An operational formula for PID feedback (using a trapezoidal approximation integral) is:

$$Z_{(k+1)t} = Z_{kt} + a\,E_{(k+1)t} + b\,E_{kt} + c\,E_{(k-1)t},$$

where $a = P+I+D$; $b = -P+I-2D$; and $c = D$

P = proportional gain I = integral gain D = differential gain

In our software P, I, D and S are set by the user; a, b and c are calculated by the PC. In our experience with AFM and STM, setting P a factor of 10 to 100 times higher than I provides optimum feedback.

Because differential feedback tends to amplify high frequency noise, we use it sparingly. In quiet systems, it does reduce oscillations, but most instruments do not suffer if it is not used. If differential feedback is omitted, the last term in the feedback equation can be dropped, saving processor instruction cycles.

Like integral feedback, the PID algorithm assumes a linear sensor response. Also like integral feedback, increasing any of the gains too much will cause oscillation, but if the gains are properly set, the response of the system is significantly better than if integral feedback alone is used.

Other Feedback Algorithms.

As mentioned previously, a variety of still more sophisticated algorithms exist[21,22] (optimal feedback, for example), but they generally require a mathematical model of the SPM stage response, including the characteristics of the tip-sample interaction. These algorithms enjoy only limited use for SPM because the sensor response can change unpredictably as the sample is scanned or when a different sample is imaged. PID feedback is perhaps the best feedback applicable for SPM because of its ability to tolerate a variety of system characteristics.

Optimizing Feedback Gains

If one endeavors to optimize the feedback gains by looking only at image quality, it is unlikely that a true optimum will be found. While it is true that image quality depends on the feedback gains, image quality is not a very sensitive measure of loop response. Step response curves, which indicate the response of the loop to a perturbation, provide a much more sensitive indicator of gain optimization and a more convenient way to adjust feedback gains.

To generate step response curves, such as shown in Figure E.3, the setpoint is changed by an amount ΔS and the error signal is displayed for a few milliseconds afterward while the feedback adjusts to the new setpoint. (Due to the finite response time of the scanner, changing Z does not produce a real step response curve). The feedback behaves the same during a step response measurement as it would if a step were encountered on the sample and both the tip and the sample were perfectly sharp. By using step response curves, the feedback gains can be optimized either manually or automatically.

Manual Optimization.

To manually optimize the feedback (see Figure E.2), a step response curve is generated and the user adjusts P, I and D to reduce rise time and oscillations. In order to judge whether the new gain settings have decreased rise time and minimized overshot and oscillations another step response curve is generated. This process is repeated until the step response shows an optimal response. On our AFMs and STMs, if tip and sample are good, the feedback settles (as determined by visual inspection of the step response

curves) within 20-50 feedback cycles. This means that the feedback will settle within one data point or less if the scan has 250 points per line and a rate of 4-10 lines/second. Thus, the feedback accurately follows topography as long as the error signal is within the loop bandwidth.

Automatic Optimization.

The step response curve provides a quantitative measure of loop performance and allows automatic optimization of the feedback gains. The optimizer uses the standard deviation of the step response curve compared to an ideal step response as an indicator of loop performance. By using an "evolutionary" algorithm optimal feedback gains can be automatically found.

During automatic optimization nine "mutations" of the "parent" gain factors P, I and D are generated by multiplying them by random numbers between 0.9 and 1.1. A step response curve is then generated for the parent and each mutation, and the curve with the lowest standard deviation is found. The corresponding set of feedback gains become the parent values for the next round of optimization. The entire algorithm is repeated 10-20 times. The evolutionary optimizer works well when the initial PID gains are reasonable and the instrument is not excessively noisy. However, the evolutionary optimization tends to put the feedback on the verge of oscillation. Although this indicates that the feedback is optimized, it also means that if conditions change slightly the instrument may start to oscillate. Therefore we usually reduce P, I and D by about 1% after optimization.

Scanning

In its most basic form, the scan subroutine generates the XY raster and stores incoming data. Useful extensions to the scanning subroutine can provide the ability to rotate the scan, "tilt" the scan and correct for scanner imperfections such as hysteresis and creep.

Basic Scanning

To generate a raster scan pattern digitally, X is repeatedly ramped between selected minimum and maximum values and Y is advanced after each cycle in X. For the XY raster to be useful for SPM both the minimum and maximum values in each scan direction must be adjustable. This variability allows "magnification" and the area scanned to be changed.

Data Averaging

In our software, the scan rate is adjusted by varying the number of timer periods spent at each data point. To keep the scanner motion smooth, the raster advances after each period, rather than after each data point. Furthermore, the data recorded for each point represents an average value over the timer periods spent at that point. Thus data is not discarded at slower scan rates, but averaged to yield improved signal to noise ratio. To illustrate these ideas consider the following example. Assume that a scan has 250 data points per line in each direction. A typical scan rate of 4-10 lines per second then corresponds to 20 to 50 feedback cycles per data point. The maximum scan rate is 200 lines/second, or 1 feed back cycle per data point.

Faster rates would yield fewer than one ADC reading per data point, effectively reducing the number of data points per scan line.

Raster Algorithm

The raster algorithm must avoid two potential pitfalls: 1) cumulative roundoff errors which appear in recursive algorithms; and 2) scan size and rate limitations which can arise in integer based algorithms. The following formula, implemented on a floating point DSP, generates an X raster without these problems. All variables are floating point numbers; a conversion to integer values is done before writing to the DAC.

$$X_t = X_o + t\,\Delta X,$$

where

X_o = starting point of the scan

t = time measured in timer periods

X_t = X position during timer period t

ΔX = X raster increment value (to be added with each timer period).

Although a raster can be generated using fewer instruction cycles, the above formula greatly simplifies programming, especially when implementing some of the features described below. An additional feature of this algorithm is that the term $t\,\Delta X$ eliminates the cumulative error which would result if $X_t = X_{t-1} + \Delta X$ were used.

Scan Rotation

An advantage of DSP raster generation is that the scan direction can be digitally rotated. Rotation is helpful in aligning the scan orientation to match long or narrow features so that the greatest possible pixel density can be acquired over the feature. Rotation is also necessary for AFM, in which friction between the tip and sample can adversely affect the feedback unless the scan direction is aligned perpendicular to the long axis of the cantilever.[23]

Since digital scan rotation is done in software, it is unlike analog scan rotation which requires dedicated hardware construction. Our implementation of digital rotation, which requires only ten instruction cycles, does not introduce additional noise into the scan, and is easily added to the basic scan routine. The algorithm requires advancing both X and Y during each timer period:

$$X'_t = X'_o + t\,\Delta X'$$
$$Y'_t = Y'_o + t\,\Delta Y',$$

where:

$$X'_o = (X_o - X_c)\cos ø + X_c - (Y - Y_c)\sin ø - Y_c$$
$$Y'_o = (X_o - X_c)\sin ø + X_c + (Y - Y_c)\cos ø - Y_c$$
$$(X_c, Y_c) = \text{center of rotation}$$
$$\Delta X' = \Delta X \cos ø$$
$$\Delta Y' = \Delta X \sin ø$$

$ø$ = rotation angle.

The center of rotation is generally the center of the image. However, if the user pans (translates) the image when the rotation is nonzero, the center of rotation should not move with the image. Otherwise the image will pan in the wrong direction.

Sample Tilt Compensation

Compensation for sample tilt can be used to augment normal Z axis feedback or as a substitute for feedback. When sample tilt compensation is used with feedback, images of highly sloped samples can be improved by adding a raster to Z during scanning. This helps the feedback follow sample tilt in X by anticipating what the next Z value should be and adding a correction. As we commented earlier, this can be thought of as a type of slow feedforward correction scheme and acts to keep the errors which require feedback correction small. As implemented in our software this algorithm takes about 5 instruction cycles. The mathematical expression for the algorithm is:

$$Z'_t = Z_{t-1} + \Delta Z.$$

The slope of the raster ΔZ is determined by the PC from analysis of the most recent image, and is inverted with each change in scan direction. Tilt correction is especially useful for "fast scan" imaging, in which the feedback gains are reduced and topography is recorded as fluctuations in sensor output.

Unlike the XY raster, finite word length does not cause a problem with the Z raster because the feedback loop corrects for small errors.

Not all SPMs generate signals that are able to be directly used to control probe-sample proximity. The nearfield scanning optical microscope (NSOM) stands out as an example of a microscope which has no inherent feedback mechanism. To maintain reasonable tip-sample separation while scanning, these instruments require sample tilt compensation in both X and Y. In our work with NSOM we have replaced the feedback loop with the following algorithm (all variables are floating point quantities):

$$Z_t = i\,X_t + j\,Y_t + k.$$

The factors i, j and k are determined by the user from inspection of image sharpness. Although we are planning to add a feedback mechanism (lateral shear force feedback) to the NSOM in the future, the ability to use sample tilt compensation in place of feedback has proved very valuable for instrument development.

Hysteresis Removal

Hysteresis and creep are two imperfections in piezoelectric scanner response which manifest themselves as important artifacts in most SPMs. Hysteresis occurs because the position of a piezoceramic scanner is not a linear function of the applied voltage; the piezo position depends on previously applied voltages. The nonlinearity caused by hysteresis can be as great as 25% of the scanner range.

Another imperfection seen in piezoceramics is creep, which often smears the first few lines of SPM images after panning or zooming. Creep is the continued mechanical motion of the piezo in spite of static electrode voltages. It can be compensated for while scanning and is an ideal candidate

for being eliminated by feedback control of X and Y positioning. Because our systems do not have active XY positioning, we have not attempted to remove creep.

Hysteresis can be removed in four ways: i) using feedback in the X and Y dimensions; ii) generating the XY raster with a lookup table; iii) generating the XY raster with a nonlinear function and iii) warping the image after it is acquired. Although the first option is perhaps the optimal solution for both hysteresis and creep, we have not yet had the opportunity to upgrade our instruments to incorporate XY feedback. Because of its simplicity and ease of implementation, we have chosen to do hysteresis correction as a post image acquisition step.

Lookup Table Method

To compensate for hysteresis , an XY raster generation algorithm can be used to generate a nonlinear raster. This raster can be stored as a lookup table and new X and Y values read from the table before the first timer period of each data point. To provide for other motion periods the DSP can interpolate between lookup table entries. Because hysteresis depends on the recent scan motion history of the scanner, the same nonlinear raster cannot be used for all scans.

Nonlinear Function Method

A somewhat simpler method which requires more processor time is to generate a linear raster and then modify X and Y using a nonlinear function. The coefficients of the function have to change each time the X raster reverses

direction. Unlike lookup tables, nonlinear functions do not permit complex high-order corrections, but for most scanners this type of correction scheme is adequate.

Post-Processing Method

Difficulties can arise when combining the above methods with features such as scan rotation. The method we have chosen simplifies programming by putting hysteresis correction in the PC software. The user-selected scan size and location is modified by the PC to correct for hysteresis. Hysteresis within the scan is eliminated by the image display software, which plots the data points in positions determined from measurements of the hysteresis characteristics of the scanner. The post-processing method has the disadvantage that, after processing, pixel density and scan rate are not constant throughout the scan.

Handling Other Artifacts

Other artifacts such as thermal drift, overall image curvature, and XY nonorthogonality can also be removed by the DSP and active feedback, but we remove them during image display.

Tip-Sample Approach

The DSP subroutine which controls the approach of the tip and sample varies depending on the specific approach mechanism. We have designed two subroutines for application with either continuous approach or

discontinuous approach mechanisms. We have used both subroutines successfully on various instruments in our laboratory.

Continuous Approach

In a continuous approach, a motor slowly turns a screw which determines tip-sample separation. The motor speed is proportional to a voltage set by a DAC. Generally, before starting the approach, the feedback has been turned off and Z set somewhere near the middle of the scanner range. The engage routine sets a DAC to start the motor and then waits for the sensor signal to cross the setpoint. When it does, the feedback is started and the motor shut off.

The engage routine also writes each ADC reading during the approach to a circular buffer. The sensor output for a few milliseconds after achieving feedback can then be plotted, a useful feature which helps the user check for false engages and tip crashes. Using engage plots such as the one in Figure E.4, we have found that simply turning the feedback on when the sensor crosses the setpoint (as opposed to first withdrawing the tip) does not generally cause tip crashes in either STM or AFM.

Discontinuous Approach

In a discontinuous approach, an inchworm, stepper motor, or some other device reduces the gap between the tip and sample in well defined increments, faster than the feedback can respond. The scanner must be set such that tip and sample are at their greatest separation before the approach

mechanism takes a step. After each step, the feedback is turned on. If Z goes out of range, tip-sample separation is still too great and the cycle is repeated.

Modulation Measurements

In a modulation image, the dependence of an input on an output is determined at each point in the scan. For example, in STM, measuring the dependence of tunneling current on Z gives a barrier height image.[24] The dependence of tunneling current on V gives a density of states image.[25] In AFM, the dependence of cantilever deflection on Z gives an elasticity image.[26] Such modulation images can provide valuable information about the physical properties of a sample and give some indication of sample composition. Two types of modulation imaging which have been described in the literature include the difference method[25] and lock-in detection.

Modulation imaging is generally performed using a lock-in amplifier which can cost as much as the construction of an entire air STM. With DSP-systems software emulations of lock-in amplifiers are possible. Such emulations do not require any additional equipment and, within the bandwidth of interest for SPM, achieve signal to noise ratios similar to those of lock-in amplifiers. In fact, in our laboratory we have replaced our lock-in amplifiers with the emulation described below.

Difference Method

One of the simplest ways to take a digital Z modulation measurement is to stop the XY raster momentarily and add a small change to Z, taking the difference between the input signal before and after the change in Z. This

method is effective, but because no averaging (bandwidth limiting) is done, it does not achieve the optimum signal to noise ratio.

Lock-In Detection

For lock-in detection of dC/dZ, a sinusoidal modulation is added to Z at an amplitude and frequency chosen by the user (typically the amplitude is ≈ 1Å and the frequency ≈ 1kHz). Neither the XY raster nor the feedback is interrupted for the modulation. The modulation frequency is set high enough and the feedback gains low enough so that the modulation is outside the bandwidth of the feedback loop. One can express this as:

$$Z'_t = Z_t + Hm_t,$$

where

$$m_t = \sin(\frac{2\pi t}{p})$$

H = peak to peak modulation amplitude

t = time measured in timer periods

p = modulation period measured in timer periods.

Assuming a linear sensor response, the magnitude of the error signal at the modulation frequency is given by:

$$A = \sqrt{A_0^2 + A_{90}^2}$$

$$A_0 = \frac{4}{np} \sum_{t=1}^{np} E_t m_t$$

$$A_{90} = \frac{4}{np} \sum_{t=1}^{np} E_t m_{t+\frac{p}{4}},$$

where:

A = peak to peak magnitude of the error signal

A_0 = amplitude of the component of the error signal in phase with the Z modulation

A_{90} = amplitude of the component of the error signal in quadrature with the Z modulation

n = number of modulation periods per data point.

The factor 4/np provides a peak to peak normalization of the amplitudes (assuming sinusoidal response).

The optimal division of tasks is to have the DSP store A_0 and A_{90} without the normalization factors, and have the PC normalize and take the square root. Note that n must be an integer for the algorithm to work; i.e., there must be an integral number of modulation periods per data point. If a 1 kHz modulation frequency is used the fastest possible scan rate is one period or 1 ms per data point, corresponding to 2 lines/second at 250 point /line. Signal to noise is improved if slower scan rates are used; five or ten periods per point is not unreasonable if the SPM stage has the thermal stability required for such slow imaging.

The above algorithm uses every ADC reading taken during the modulation to yield better signal to noise ratios than difference algorithms which take only two readings per modulation. In addition, the XY raster is not stopped and the feedback is not turned off during the measurement thus avoiding glitches that degrade the data which occur when the feedback or raster are restarted.

The in phase and in quadrature components contain complementary information in a modulation image and so both A_0 and A_{90} should be stored if there will be a need to reconstruct phase as well as magnitude information. However, for basic elasticity or barrier height imaging we have found it sufficient to record only A_0; the 90 ° component provides negligible additional information at the modulation frequencies we use. By not recording the 90 ° component we reduce the amount of processor time required for modulation imaging from 25 to 18 instruction cycles and also halve the amount of data which needs to be stored for each modulation image.

Measurement of the Second Derivative

Digital control systems lend themselves particularly well to spectroscopy experiments.[13] Current-voltage tunneling spectroscopy can benefit from the measurement of both first and second derivative of current with respect to voltage.[27] The first derivative can be measured as described above; the second derivative can be measured simultaneously by detecting components of the error signal at twice the modulation frequency:

$$A_0 = \frac{4}{np} \sum_{t=1}^{np} E_t m_{2t}$$

$$A_{90} = \frac{4}{np} \sum_{t=1}^{np} E_t m_{2t+\frac{p}{4}}.$$

We have found that this technique performs satisfactorily when used in conjunction with the instruments in our laboratory.

Other DSP Functions

Other DSP routines are needed to ramp the X, Y and Z voltages to specified values, move the coarse positioning translators, and measure a step response (by setting the step size to zero, the step response routine can double as a digital oscilloscope). Finally, there needs to be a main menu which calls the other routines in response to PC instructions.

User Interface

The user interface takes instructions from the user, sends data to the DSP, and displays data from the DSP. Implementation of the latter two functions is highly system dependent and does not effect instrument performance. However, the architecture of the instruction parser can contribute greatly to the utility and convenience of an instrument. The instruction parser consists of an input subroutine and a menu. The input subroutine takes instructions from the keyboard. The menu consists of a number of "if" statements, one for each possible instruction.

Input Subroutine

The input subroutine can be easily written to accept up to several hundred instructions, then feed them to the parser one by one. The SPM system is then effectively user programmable, greatly increasing its flexibility and making it possible for the system to perform simple experiments unattended. Conditional instructions, loop and branch instructions, and the ability to define macros which recall stored text files of instructions further increase the utility of the user interface.

Instruction Parser

The user interface is most flexible if each basic operation of the SPM corresponds to an individual instruction. For example, it should be possible to set any of the DACs to a specified voltage from the parser. Conversely, all instructions should be as basic and low level as is reasonable. Commonly used functions, stored as macros, can then be built up from several instructions in such a way that they can be modified to suit the instrument and the operator.

The utility of this approach is illustrated by the ability to acquire a sequence of scans unattended. On instruments with a sample translator, macros can be written to translate, engage and scan repetitively. A sequence of scans with varying conditions or of different areas can be taken automatically. Strings of lithography operations can be performed. Among the macros we find most useful are those to implement circular image buffers, jog the tip-sample approach mechanism up or down until the sample is centered in the piezoceramic range and set parameters for various types of scans.

The macro driven parser simplifies use of the operating system since the beginning user need only know three or four macros to take images. It also makes the system more flexible because a more advanced user can build up low level commands into custom functions. Additionally, the availability of low-level commands is especially useful for testing new instruments, during which the need to perform unexpected operations often arises.

In addition to the word type instruction input, it should also be possible to change feedback and scan parameters with mouse or single keystroke commands while scanning. Real-time parameter updates not only make the software easier to use, but are invaluable for determining what effect various parameters have on image quality.

Another parser function we have found useful is an electronic logbook which keeps a record of important events (approaches, saves, etc.). The events are recorded when the various macros write to the logbook file (i.e., the approach macro records sample tilt, current overshoot, etc.). Such a logbook can be of great help when analyzing data.

Conclusion

A DSP based control system can be constructed quickly and inexpensively, or given sufficient time and money, can be developed into a state of the art SPM control system. With a DSP based system, it is possible to implement in software features such as scan rotation, modulation imaging and hysteresis correction, which would be difficult or expensive to implement with analog techniques. Consisting of just one or two components, a DSP board with integrated or separate analog I/O, the system has an overall conceptual simplicity. This simplicity leads to flexibility which permits a single system to support a wide variety of experiments and adapt to the changing demands of the SPM field.

The authors will gladly provide more detailed information on the algorithms discussed in this appendix to interested readers.

Acknowledgments

Financial support for this work was provided by Ford Motor Company, Abbott Laboratories, Inc., Topometrix, Inc., a National Science Foundation predoctoral fellowship (DRB), a National Institutes of Health Training Grant (GM07617) (SMC) and a Department of Education fellowship (MGY).

Figures -- Appendix E

Figure E.1. Block diagram of a scanned probe microscope control and data acquisition system. The system shown uses a PC/AT computer as the host for the digital signal processor board and has external analog I/O. All electronic details have been omitted for clarity. Other host systems and analog I/O packaging schemes could clearly be used (e.g., workstations and VXI Bus).

Figure E.1

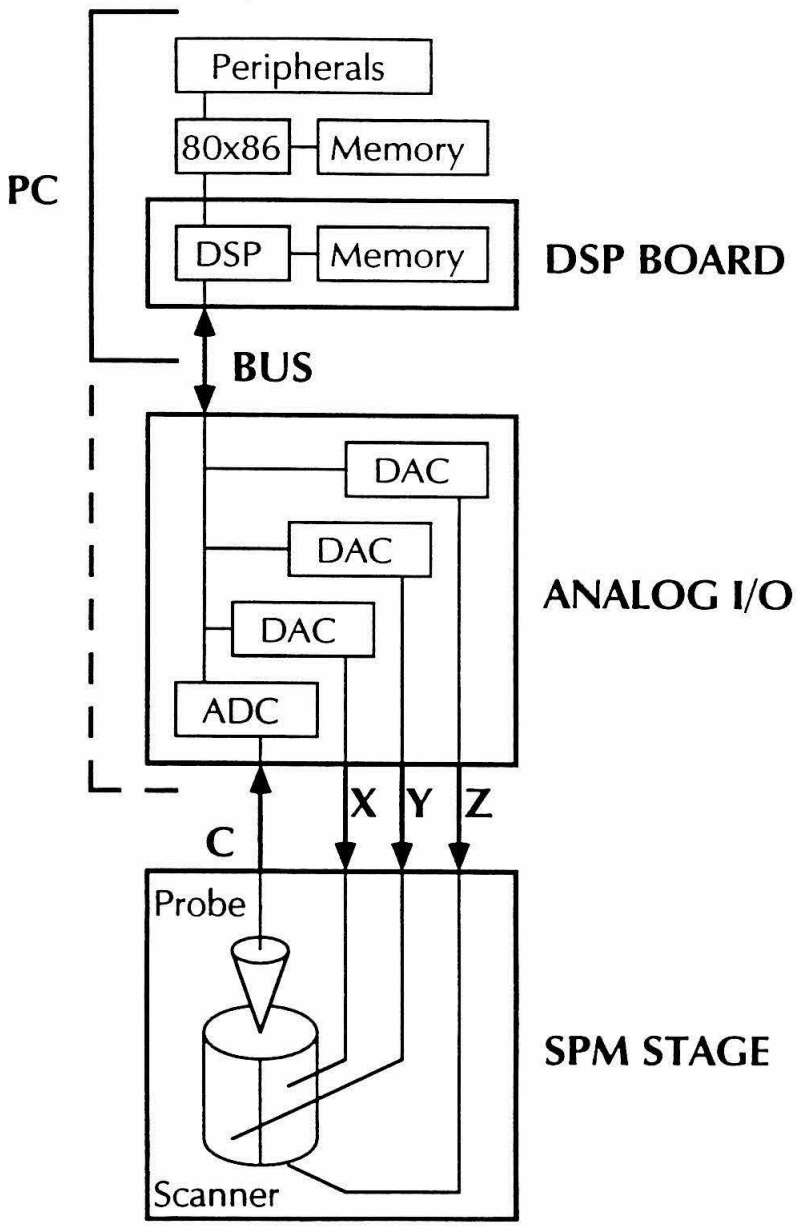
Peripherals
80x86
Memory
PC
DSP
Memory
DSP BOARD
BUS
DAC
DAC
DAC
ADC
ANALOG I/O
X
Y
Z
C
Probe
SPM STAGE
Scanner

Figure E.2. Software algorithms used during one timer period while scanning. Every 10 μs the DSP timer triggers an interrupt, causing the execution of the interrupt service routine (ISR). The software is written so that interrupts only occur after all the operations in the previous ISR call have been completed and the DSP is executing the waiting loop in the scan subroutine. Several portions of the DSP software are not shown: data storage, which occurs less than once per timer period; tip-sample approach routine, which is not used while scanning; and the user interface.

Figure E.2

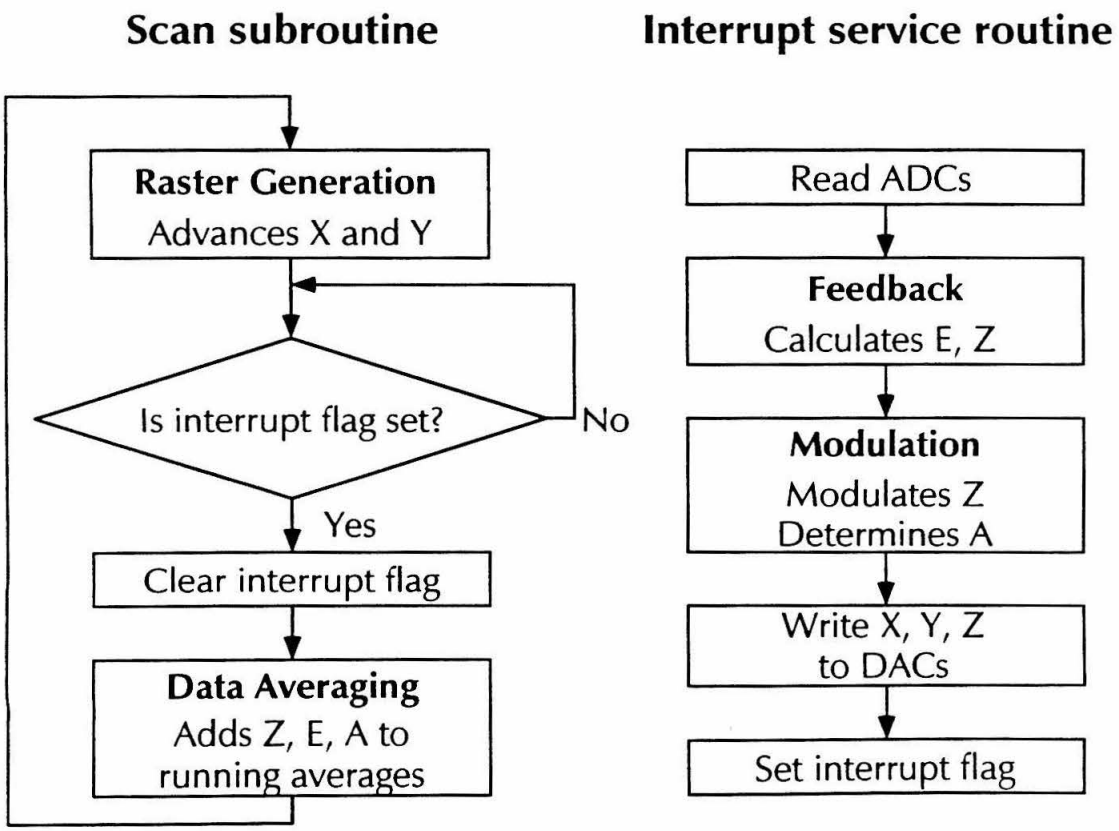
Scan subroutine
Interrupt service routine
Raster Generation
Advances X and Y
Is interrupt flag set?
No
Yes
Clear interrupt flag
Data Averaging
Adds Z, E, A to
running averages
Read ADCs
Feedback
Calculates E, Z
Modulation
Modulates Z
Determines A
Write X, Y, Z
to DACs
Set interrupt flag

Figure E.3. Manual optimization of AFM feedback using step response curves. Curve A) Integral feedback only: I = 0.002, P = D = 0. Curve B) Raising I to 0.003 increases response rate but also increases the amount of overshoot (or oscillation). Curve C) Setting P to 0.03 increases response rate and decreases overshoot. The feedback now settles in about 0.25 ms (this corresponds to one data point or less if there are 250 points / scan line and the scan rate is 8 lines / second or less). For all of the curves $\Delta S = 50$ Å.

Figure E.3

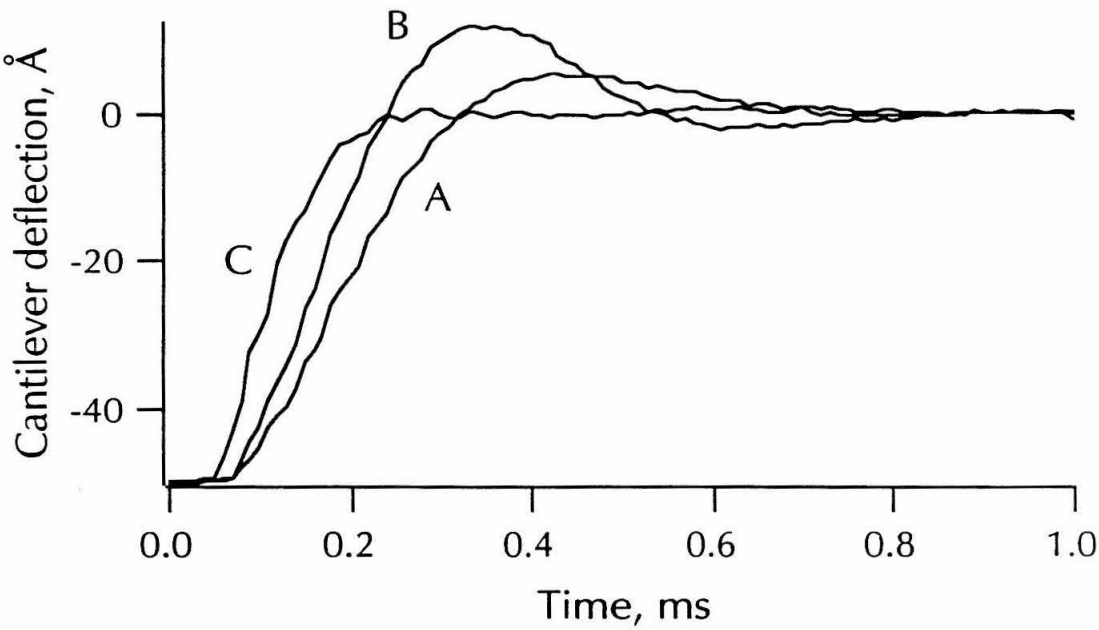

Figure E.4. An AFM tip-sample approach curve taken in air. At t = -2 ms the tip and sample are already in contact with the cantilever deflected downward and the motion of the approach motor is pushing the cantilever up. When the cantilever deflection reaches its setpoint (zero deflection in this case), the feedback is started and the motor is shut off. Since the motor has rotational inertia, it takes about 35 ms to come to rest, and so the cantilever deflection does not immediately settle to the setpoint.

Figure E.4

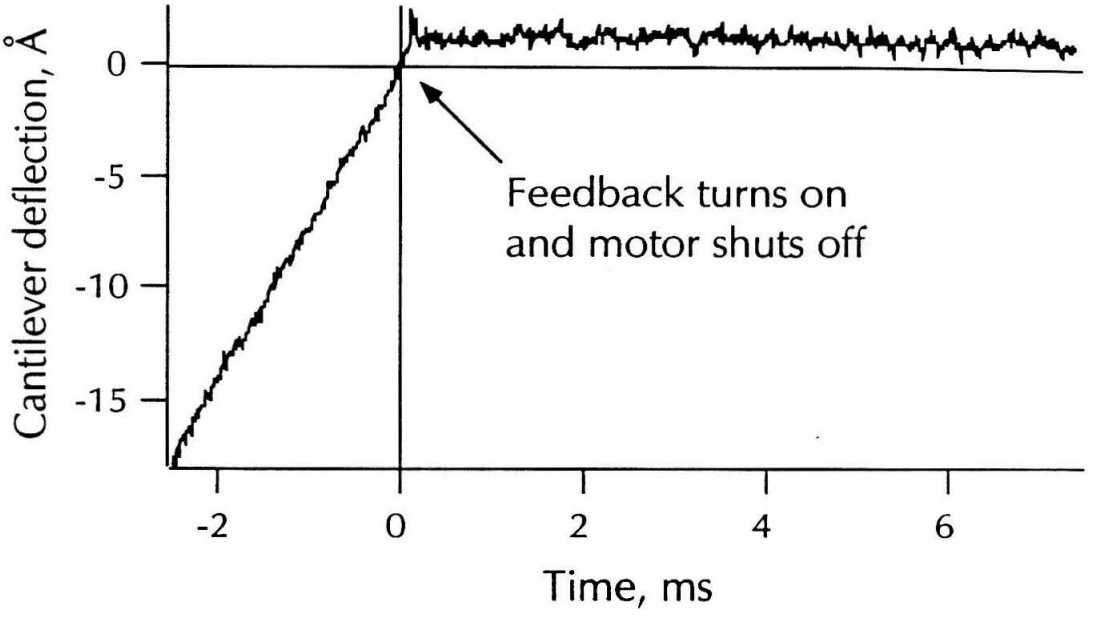
Cantilever deflection, Å
0
-5
-10
-15
-2
0
2
4
6
Time, ms
Feedback turns on
and motor shuts off

References

1. G. Binnig, Ch. Gerber and C. F. Quate, *Phys. Rev. Lett.* **56**, 930 (1986).
2. C. F. Quate, "Scanned probe microscopies", pp. 1-8, American Institute of Physics Conference Proceedings #241, H. Kumar Wickramasinghe , Ed. 1992.

   H. Kumar Wickramasinghe, "Scanned probes old and new", pp. 9-22, American Institute of Physics Conference Proceedings #241, H. Kumar Wickramasinghe , Ed. 1992.
3. O. Marti, S. Gould, P. K. Hansma, *Rev. Sci. Instrum.* **59** (6), 836 (1988).
4. A. Brown, R. W. Cline, *Rev. Sci. Instrum.* **61** (5).1484 (1990).
5. R. S. Robinson, T. H. Kimsey, *J. Vac. Sci. Technol.* **B9** (2), 631 (1991).
6. A. J. Hoeven, E. J. van Loenen, P. J. G. M. van Hooft, K. Oostveen, *Rev. Sci. Instrum.* **61** (6), 1668 (1990).
7. R. Piner, R. Reifenberger, *Rev. Sci. Instrum.* **60** (10), 3123 (1989).
8. S. Park, C.F. Quate, *Rev. Sci. Instrum.* **58** (11), 2010 (1987).
9. A. Hammiche, Y. Wei, I. H. Wilson, R. P. Webb, *Rev. Sci. Instrum.* **62** (2), 3010 (1991).
10. R. Erlandsson, R. Wigren, L. Olson, *Microsc. Microanal. Microstruct.* **1** (5/6), 471 (1991).
11. H. Halling, R. Moeller, A. Schummers, *IEEE Trans. Nuc. Sci.* **36** (1),634 (1989).
12. A. Schummers, H. Halling, K. H. Besocke, G. Cox, *J. Vac. Sci. Technol.* B9 (2), 615 (1991).
13. D. P. DiLella, J. H. Wandass, R. J. Colton, C. R. K. Marrian, *Rev. Sci. Instrum.* **60** (6), 997 (1989).
14. R. C. Barrett and C. F. Quate, *Rev. Sci. Instrum.* **62** (6), 1393 (1991).
15. Spectrum Signal Processing, Inc., #301 3700 Gilmore Way, Burnaby, B.C. V5G4M1, Canada.
16. Texas Instruments, P. O. Box 1443, Houston, TX 77001.
17. For example, Data Translation, 100 Locke Drive, Marlboro, MA 01752.
18. D. Sheingold, ed., Analog-Digital Handbook (Prentice-Hall, Englewood Cliffs, New Jersey, U.S.A., 1986).

19. S. M. Clark, D. R. Baselt, C. F. Spence, M. G. Youngquist, J. D. Baldeschwieler, *Review of Scientific Instruments*, 63, 4296-4307 (1992).
20. C. A. Putman, et al., in Proceeding of the SPIE Volume 1639, Scanning Probe Microscopies, edited by S. Manne, pp. 198-204.
21. Victor J. Bucek, Control Systems (Prentice-Hall, Englewood Cliffs, New Jersey, U.S.A., 1989).
22. G. Franklin and J. Powell, Digital Control of Dynamic Systems (Addison-Wesley, Menlo Park, CA, U.S.A., 1980).
23. A. J. den Boef, *Rev. Sci. Instrum.* **62** (1), 88 (1991).
24. R. Wiesendanger, L. Eng, H. R. Hidber, P. Oelhafen, *Surf. Sci.* **189**, 24 (1987).
25. M. P. Everson, L. C. Davis, R. C. Jaklevic, W. Shen, *J. Vac. Sci. Technol.* **B9** (2), 891 (1991).
26. P. Maivald *et al.*, paper presented at STM ' 90.
27. P. K. Hansma, ed., Tunneling Spectroscopy, Plenum, New York (1982).

Publications

1. Wilmer G. Miller, Michael Youngquist, Samana Chakrabarti, Haiquan Zhao, and Paul Russo, *Polymer Preprints* **27,** 233-4 (1986). Studies on rod-like polymer gels.

2. R. J. Colton, S. M. Baker, R. J. Driscoll, M. G. Youngquist, J. D. Baldeschwieler, and W. J. Kaiser, *J. Vac. Sci. & Technol.* **A 6,** 349-353 (1988). Imaging graphite in air by scanning tunneling microscopy - role of the tip.

3. H. G. Le Duc, W. J. Kaiser, B. D. Hunt, L. D. Bell, R. C. Jaklevic, M . G. Youngquist, *Appl. Phys. Lett.* **54,** 946-948 (1989). Superconducting phonon spectroscopy using a low-temperature scanning tunneling microscope.

4. N. S. Lewis, C. A. Barnes, M. J. Heben, A. Kumar, S. R. Lunt, G. E. McManis, G. M. Miskelly, R. M. Penner, M. J. Sailor, P. G. Santangelo, G. Shreve, B. J. Tufts, M. G. Youngquist, R. W. Kavanagh, S. E. Kellogg, R. B. Vogelaar, T. R. Wang, R. Kondrat, and R. New, *Nature* **340,** 525-530 (1989). Searches for low-temperature fusion of deuterium in palladium.

5. R. J. Driscoll, M. G. Youngquist and J. D. Baldeschwieler, *Nature* **346,** 294-296 (1990). Atomic-scale imaging of DNA using scanning tunnelling microscopy.

6. M. G. Youngquist, R. J. Driscoll, T. R. Coley, W. A. Goddard and J. D. Baldeschwieler, *J. Vac. Sci. & Technol.* **B 9,** 1304-1308 (1991). Scanning tunneling micrsocopy of DNA: Atom-resolved imaging, general observations and possible contrast mechanism.

8. M. G. Youngquist and J. D. Baldeschwieler, *J. Vac. Sci. & Technol.* **B 9,** 1083-1087 (1991). Observation of negative differential resistance (NDR) in tunneling spectroscopy of MoS_2 with a scanning tunneling microscope.

9. M. G. Youngquist, R. J. Driscoll and J. D. Baldeschwieler, *Proc. Microscopical Soc. Canada* **18,** 26-27 (1991). Scanning tunneling microscopy of DNA in UHV.

10. M. G. Youngquist, R. J. Driscoll, T. R. Coley, W. A. Goddard and J. D. Baldeschwieler, Scanned Probe Microscopy, Ed. H. K. Wickramasinghe, AIP Conf. Ser. **241,** 154-158 (1992). STM of DNA in UHV.

11. S. M. Clark, D. R. Baselt, C. Spence M. G. Youngquist, and J. D. Baldeschwieler, *Rev. Sci. Instrum.* **63(10),** 4296-4307 (1992). Hardware for digitally controlled scanned probe microscopes.